E-ISSN: 2667-5846

EXPERIMED

Volume **16** · Issue **2** · 2026

https://experimed.istanbul.edu.tr/

İSTANBUL UNIVERSITY PRESS

E-ISSN: 2667-5846

EXPERIMED

Volume 16 • Issue 2 • 2026

İSTANBUL UNIVERSITY PRESS

Indexing & Abstracting

SCOPUS
Web of Science Core Collection - Emerging Sources Citation Index (ESCI)
Web of Science - Biological Abstracts
Web of Science - BIOSIS Previews
TUBITAK ULAKBIM TR Index
DOAJ (Directory of Open Access Journals)
Chemical Abstracts Service (CAS)
EBSCO Central & Eastern European Academic Source
CAB Abstracts
CABI Global Health
SOBIAD
Gale Cengage

Owner

Prof. Dr. Erdem TÜZÜN

İstanbul University, Aziz Sancar Institute of Experimental Medicine, Department of Neuroscience, İstanbul, Türkiye

Responsible Manager

Prof. Dr. Bedia ÇAKMAKOĞLU

İstanbul University, Aziz Sancar Institute of Experimental Medicine, Department of Molecular Medicine, İstanbul, Türkiye

Correspondence

İstanbul University, Aziz Sancar Institute of Experimental Medicine,

Vakıf Gureba Avenue, 34093, Çapa, Fatih, İstanbul, Türkiye

+90 (212) 414 22 29

experimed@istanbul.edu.tr

https://experimed.istanbul.edu.tr/

Publisher

İstanbul University Press

İstanbul University Press, İstanbul University Central Campus, 34452, Beyazıt, Fatih, İstanbul, Türkiye

+90 (212) 440 00 00

iupress@istanbul.edu.tr

https://iupress.istanbul.edu.tr/

Publication Type

Periodical

Authors bear responsibility for the content of their published articles.

The publication language of the journal is English.

This is a scholarly, international, peer-reviewed and open-access journal published triannually in April, August and December.

İSTANBUL UNIVERSITY PRESS

EXPERIMED

Volume: 16 • Issue: 2 • 2026

Editorial Management

Editor-in-Chief

Prof. Dr. Bedia ÇAKMAKOĞLU

İstanbul University, Aziz Sancar Institute of Experimental Medicine, Department of Molecular Medicine, İstanbul, Türkiye
bedia@istanbul.edu.tr

Co-editors-in-Chief

Prof. Dr. Umut Can KÜÇÜKSEZER

İstanbul University, Aziz Sancar Institute of Experimental Medicine, Department of Immunology, İstanbul, Türkiye
uksezer@istanbul.edu.tr

Prof. Dr. Vuslat YILMAZ

İstanbul University, Aziz Sancar Institute of Experimental Medicine, Department of Neuroscience, İstanbul, Türkiye
vuslat.yilmaz@istanbul.edu.tr

Managing Editor

Prof. Dr. Sema SIRMA EKMEKÇİ

İstanbul University, Aziz Sancar Institute of Experimental Medicine, Department of Genetics, İstanbul, Türkiye
sirmasem@istanbul.edu.tr

Editorial Management Board Members

Asst. Prof. Canan Aysel ULUSOY

İstanbul University, Aziz Sancar Institute of Experimental Medicine, Department of Neuroscience, İstanbul, Türkiye
canan.ulusoy@istanbul.edu.tr

Dr. Barış ERTUĞRUL

İstanbul University, Aziz Sancar Institute of Experimental Medicine, Department of Molecular Medicine, İstanbul, Türkiye
baris.ertugrul@istanbul.edu.tr

Ethical Editor

Prof. Dr. Elif ÖZKÖK

İstanbul University, Aziz Sancar Institute of Experimental Medicine, Department of Neuroscience, İstanbul, Türkiye
eozkok@istanbul.edu.tr

Section Editors

Prof. Dr. Elif Sinem BİRELLER

Acıbadem Mehmet Ali Aydınlar University, Faculty of Pharmacy, Department of Biochemistry, İstanbul, Türkiye
sinem.bireller@acibadem.edu.tr

Assoc. Prof. Ferda PAÇAL

İstanbul University, Aziz Sancar Institute of Experimental Medicine, Department of Lab Animal Science, İstanbul, Türkiye
ferda.pacal@istanbul.edu.tr

Assoc. Prof. Ali Cihan TAŞKIN

İstanbul University, Aziz Sancar Institute of Experimental Medicine, Department of Lab Animal Science, İstanbul, Türkiye
ataskin@istanbul.edu.tr

Assoc. Prof. Timur Hakan BARAK

Acıbadem Mehmet Ali Aydınlar University, Faculty of Pharmacy, Department of Pharmacognosy, İstanbul, Türkiye
timur.barak@acibadem.edu.tr

Statistics Editor

Sevda ÖZEL YILDIZ

İstanbul University, İstanbul Medical Faculty, Department of Biostatistics, İstanbul, Türkiye
sevda@istanbul.edu.tr

İSTANBUL UNIVERSITY PRESS

EXPERIMED

Volume: 16 • Issue: 2 • 2026

Editorial Board Members

Aziz SANCAR (Honorary Member) — *University of North Carolina, School of Medicine, Department of Biochemistry and Biophysics, Chapel Hill, North Carolina, USA*
aziz_sancar@med.unc.edu

Abid HUSSAINI — *Columbia University, Taub Institute, Department of Pathology and Cell Biology, New York, USA*
abid.hussaini@columbia.edu

Ahmet GÜL — *İstanbul University, School of Medicine, Department of Internal Medicine, İstanbul, Türkiye*
agul@istanbul.edu.tr

Ali Önder YILDIRIM — *Helmholtz Zentrum München, Department of Lung Biology and Diseases, München, Germany*
oender.yildirim@helmholtz-muenchen.de

Batu ERMAN — *Sabanci University, Department of Molecular Biology, Genetics and Bioengineering, İstanbul, Türkiye*
batu.erman@boun.edu.tr

Çağla EROĞLU — *Duke University, Department of Cell Biology, North Carolina, USA*
cagla.eroglu@duke.edu

Ebba LOHMANN — *Tübingen University, Department of Neurodegenerative Diseases, Tübingen, Germany*
ebba.lohmann@uni-tuebingen.de

Elif APOHAN — *Inonu University, Department of Biology, Malatya, Türkiye*
elif.apohan@inonu.edu.tr

Erdem TÜZÜN — *İstanbul University, Aziz Sancar Institute of Experimental Medicine, Department of Neuroscience, İstanbul, Türkiye*
erdem.tuzun@istanbul.edu.tr

Gökçe TORUNER — *MD Anderson Cancer Center, Department of Hematology, Houston, Texas, USA*
gatoruner@mdanderson.org

Günnur DENİZ — *İstanbul University, Aziz Sancar Institute of Experimental Medicine, Department of Immunology, İstanbul, Türkiye*
gdeniz@istanbul.edu.tr

Gürol TUNÇMAN — *Harvard University, Department of Genetics and Complex Diseases, Massachusetts, USA*
gtuncman@hsph.harvard.edu

Hannes STOCKINGER — *Vienna School of Medicine, Molecular Immunology Unit, Pathophysiology Center, Vienna, Austria*
hannes.stockinger@meduniwien.ac.at

Hesenov Muşviq CƏLALOGLU — *Azerbaijan Medical University, Department of General Surgery, Baku, Azerbaijan*
hesenov@amu.edu.az

Rukset ATTAR — *Yeditepe University, Department of Obstetrics and Gynecology, İstanbul, Türkiye*
rattar@yeditepe.edu.tr

İhsan GÜRSEL — *İzmir Biomedicine and Genome Center, İzmir, Türkiye*
ihsangursel@bilkent.edu.tr

Numan ÖZGEN — *Baylor University School of Medicine, Department of Pathology and Immunology, Texas, USA*
numan.oezguen@bcm.edu

Serhat PABUÇÇUOĞLU — *İstanbul University-Cerrahpaşa School of Veterinary, Department of Reproduction & Artificial Insemination, İstanbul, Türkiye*
serpab@iuc.edu.tr

Sühendan EKMEKÇİOĞLU — *MD Anderson Cancer Center, Texas University, Houston, Texas, USA*
sekmekcioglu@mdanderson.org

Yusuf BARAN — *İzmir Institute of Technology, Department of Molecular Biology and Genetics, İzmir, Türkiye*
yusufbaran@iyte.edu.tr

İSTANBUL UNIVERSITY PRESS

EXPERIMED

Volume: 16 • Issue: 2 • 2026

Table of Contents

Research Article

Mismatches in Premises and Conclusion Affect Deductive Reasoning: A tDCS-ERP Study **80**

Barış Özdemir, Sacit Karamürsel

Research Article

Detection of *DHRS2*-associated E3 Ubiquitin Ligases in Breast Cancer Cell Lines **90**

Damla Nur ŞAKAR, Burcu SALMAN YAYLAZ, Şeyma PUNAR, Neslihan ABACI

Research Article

The Effect of Verbascoside on DNA Damage and Oxidative Stress in 3T3-L1 Adipocytes **100**

Melek TUNÇ-ATA, Gizem AKAN, Şefike Sude GÜVENÇ, Deniz ÇELEBİ, Selen ŞAFAK, Zeynep Azra ÜNAL, Safa KORKMAZ, Emine KILIÇ-TOPRAK

Research Article

Loss of GON4L Impairs Proliferation and Spheroid Growth in Luminal Breast Cancer Cells **107**

Hande Özkan, Gözde Korkmaz

Research Article

Role of HLA-B Leader Peptides and HLA-E Genetic Variants in HIV Infection **114**

Yeliz Öğret, Çiğdem Kekik Çınar, Arif Atahan Çağatay, Hayriye Şentürk Çiftçi, Kürşat Özdilli, Fatma Savran Oğuz

Research Article

Clinical Outcomes of Cable Grip Plate–Cable Grip Constructs in the Management of Femoral Intertrochanteric Fractures **120**

Ömer Yonga, Behiç Çelik, Faik Altıntaş

Research Article

In vitro Antimicrobial Activity of Salicylic Acid–Loaded Liposomes Against *Cutibacterium acnes*: A Microbiological Approach for Acne Treatment **128**

Gülcan Kuyucuklu-Kazan, Ahmet Doğan Ergin

Research Article

Role of Sodium Phenylbutyrate and Suramin in the Prevention of Ulcerative Colitis Induced by Dextran Sulfate Sodium **137**

Cansu Özal-Coşkun, Ecem Fatma Karaman, Sibel Özden, Engin Kaptan, Pelin Arda

Research Article

Integrated Analysis of OX40/OX40L Genetic Variants and Circulating Soluble Immune Checkpoint Markers in Laryngeal Cancer Recurrence **148**

Maral Farzam, Dilara Sönmez Zor, Ülgen Sever, Cem Horozoğlu, Saime Turan Sürmen, Onur Dülger, Vahid Chaleshi, Mehmet Özkır, Ayşegül Verim, Yusufhan Süoğlu, İlhan Yaylım

Research Article

DNA Methylation Signatures Distinguish Breast Cancer Histological Subtypes and Predict Hormone Receptor Status: A TCGA-Based Integrative Analysis **157**

Özkan Özdemir, Eylül Aydın, Turna Demirci, Karen Telciyan, Alper Akkuş, Emrah Yücesan, Yeşim Eralp, Özden Hatırnaz Ng

İSTANBUL UNIVERSITY PRESS

Experimed 2026, 16 (2): 80–89

https://doi.org/10.26650/experimed.1828892

Submitted: 23.11.2025
Revision Requested: 12.02.2026
Last Revision Received: 06.04.2026
Accepted: 07.04.2026
Published Online 12.08.2026

Experimed

Research Article

Open Access

Mismatches in Premises and Conclusion Affect Deductive Reasoning: A tDCS-ERP Study

Barış Özdemir [1] & Sacit Karamürsel [2]

[1] Maltepe University, Faculty of Humanities and Social Sciences, Department of Psychology, İstanbul, Türkiye
[2] Koç University, School of Medicine, Department of Physiology, İstanbul, Türkiye

Abstract

Objective: This study aimed to examine the interfering effect of mismatches on deductive reasoning, measured both behaviorally and through event-related potentials (ERP), and whether anodal transcranial direct current stimulation (tDCS) applied to the left prefrontal cortex (PFC) reduces this effect.

Materials and Methods: This study involved 27 healthy right-handed participants, including 11 women, with a mean age of 27.21 ± 6.76 years. Anodal stimulation was applied to the left PFC, while a cathode was placed on the right mastoid. All participants completed inference tasks under both sham and anodal stimulation conditions. Within-group comparisons were conducted to analyze behavioral performance and ERP recordings, which were compared between the sham and anodal stimulation conditions.

Results: The results showed that the response rate for deductive inference tasks with the highest levels of mismatch significantly increased after anodal stimulation compared to sham stimulation. However, there was no significant difference in reaction times between the two stimulation methods. Notably, the highest N2 wave in the frontal region was observed during tasks with the greatest level of mismatch. However, no significant differences in N2 amplitude or latency associated with anodal stimulation were detected.

Conclusion: The findings of the study indicated that anodal tDCS has a limited effect on inference tasks that involve different levels of mismatch. This may be due to a ceiling effect caused by selecting a relatively simple form of inference due to the control of confounding variables.

Keywords Effect · Deductive Reasoning · Prefrontal Cortex · Transcranial Electrical Stimulation · Event-Related Potential

Author Note This study was developed from the doctoral dissertation of Barış Özdemir.

Citation: Özdemir, B. & Karamürsel, S. Mismatches in Premises and Conclusion Affect Deductive Reasoning: A tDCS-ERP Study. Experimed 2026; 16(2): 80-89. DOI: 10.26650/experimed.1828892

This work is licensed under Creative Commons Attribution-NonCommercial 4.0 International License.

© 2026. Özdemir, B. & Karamürsel, S.

Corresponding author: Barış Özdemir barisozdemir@maltepe.edu.tr

INTRODUCTION

Deductive reasoning has been considered the keystone of human cognition. Our ability to apply systematic thinking, understand abstract concepts, analyze arguments, and navigate everyday decision-making rests on deductive reasoning skills (1, 2). It is crucial for various everyday activities and holds psychological significance within the repertoire of higher-level cognitive processes. This includes the ability to derive conclusions from prior beliefs, observations, or suppositions and draw necessary inferences from existing knowledge. Consequently, information can remain implicit within previously encoded knowledge and become explicit only when required (3).

Despite being an integral part of human thinking and learning, research has shown that, to a large extent, people fall prey to biases inconsistent with formal logic theories when they reason (4). Among several factors (e.g., the cognitive effort required, the content of the inference, and the emotional load) underlying these biases that cause inferential errors in the form of conditional and syllogistic logic, the mismatch effect is regarded as one of the leading irrational biases (5, 6). When there is a mismatch in the elements of the premises that make up the inference (such as semantic incompatibility, conflicting information, or mismatches in perceptual stimuli), it becomes challenging to make valid logical inferences. Often, this cognitive load and complexity can lead individuals to reasoning errors (7). Studies on this subject have revealed that specific neural networks related to logical information processing are activated during deductive reasoning and that these networks are disrupted in the reasoning process when incompatible situations (e.g., mismatching elements) are perceived (8). This disruption may manifest in increased cognitive load, making it harder for individuals to maintain coherent logical processing. The current study focused on the extent to which electrical stimulation of the prefrontal cortex might reduce cognitive load caused by the mismatch effect (within perceptual features in the premises) and enhance deductive reasoning performance.

The dominant theoretical explanation for the mismatch effect is based on the dual process theory, which distinguishes between fast, heuristic-based nature and intuitive processes (System 1) and slower, rule-based and deliberative processes (System 2) (9-11). The dual-process theory proposes that during deductive inference, two different cognitive systems, System-1 and System-2, which mostly conflict with one another, are activated. System-1 has evolved to respond rapidly, utilizing heuristics, and is responsible for the tendency to reject the inference (even if the inference is correct) in the presence of a mismatch between the conditional premises and the inferential clause. Typically, System-2 enables individuals to inhibit this irrational rejecting tendency by engaging in an analytical thinking process in line with the principles of formal logic. However, since the success rate of System-2 in inhibiting System-1 varies across individuals and contexts, it becomes possible to observe incorrect inferences because of the dominance of System-1 (11, 12). Importantly, when cognitive load increases, individuals tend to rely more heavily on heuristic shortcuts, reducing the opportunity for analytic System 2 monitoring (13). This dynamic is particularly relevant in real-world contexts, where time pressure and task complexity can amplify the influence of intuitive processes on deductive reasoning.

Event-related potential (ERP) studies have provided important insights into the neural basis of the mismatch effect in reasoning. The N2 component is a negative wave that emerges 200–350 ms after a stimulus, usually peaking at approximately 250-275 ms. It indicates the brain's detection of a mismatch, conflict, or the need to inhibit a reflexive-like response (14, 15). When the characteristics of the visual stimulus in the task (including its modality) do not align with expectations, a high-amplitude N2 is recorded, most prominently in the frontocentral scalp regions, such as the Fz, FCz, F3, F4, and Cz electrode areas (15, 16). N2 is also associated with conflict monitoring and consistently exhibits larger amplitudes when individuals process incompatible premises. This increase in N2 reflects the increased cognitive load and conflict resolution demands of mismatched reasoning tasks and frequently contributes to errors or slower decision making (17). Prado et al. (2008) reported two key findings: (i) inference-related mismatch effects were correlated with N2 activity in the frontocentral region, and (ii) N2 amplitude rose proportionally with the number of mismatching elements (0, 1, or 2) (17). Interestingly, individuals with higher reasoning performance showed lower N2 amplitudes under mismatch, implying more efficient processing. Similarly, N2 has been widely studied, particularly in go/no-go paradigms, as a marker of cognitive control and inhibition. Later work refined this view, proposing that N2 reflects cognitive conflict or dilemma rather than inhibition alone (15, 16). Stronger cognitive conflict elicits greater N2 amplitudes, whereas lower amplitudes are associated with better behavioral performance. In the mismatch effect, N2 represents the cognitive effort required as System 2 reasoning overrides System 1 intuitions.

In recent years, transcranial direct current stimulation (tDCS) has been employed in numerous studies to explore how executive functions influence performance on cognitive tasks by manipulating brain stimulation in a laboratory setting. In tDCS, the current provided by electrodes placed on the skull reaches the reference electrode via the active electrode on the scalp, with some of it short-circuited on the skull and the rest passing through brain tissue (18). This method produces neuromodulatory effects that differ depending on the polarity of the stimulation (anodal or cathodal). Anodal tDCS generates a local excitatory effect in the cerebral cortex region beneath the electrode, whereas cathodal tDCS decreases excitability in the targeted area (19). Anodal stimulation causes subthreshold stimulation in the membrane polarization of cortical

neurons perpendicular to the stimulated region, resulting in a depolarizing effect on their resting potentials. This modulatory effect is sufficient to increase the firing frequency of these neurons. In contrast, cathodal stimulation can cause a decrease in neural firing by exerting a hyperpolarizing effect through a similar mechanism (20). Studies have demonstrated that the effects of electrical stimulation can last not only at the moment of stimulation but also for minutes and even hours afterward (21).

In our study, we focused on how anodal stimulation of the relevant area affects cognitive control and inhibition, particularly in logical inferential tasks associated with prefrontal functions, specifically the left prefrontal cortex (PFC). It is important to emphasize that the PFC region was specifically targeted for electrical stimulation to assess the impact of anodal stimulation compared to a condition without stimulation. In summary, the current study is primarily exploratory and seeks to investigate (i) the relationship between deductive reasoning performance and the ERP component N2 in relation to the mismatch effect, (ii) the effectiveness of tDCS on reasoning accuracy, and ultimately (iii) whether improvements in deduction task performance across varying levels of mismatch can be observed through changes in N2 (indicating enhanced inhibition of the mismatch effect) recordings, achieved by stimulating the PFC using tDCS.

MATERIALS AND METHODS

Participants

The study group was comprised of 27 participants (11 women) with a mean age of 27.21 ± 6.76 years, all of whom were either enrolled in or had completed a higher education program. The mean years of education was 14.54 ± 2.34. The inclusion criteria were right-handedness (22), healthy, with no history of psychiatric or neurological disease or chronic pain, not having any visual or hearing disorder that could impair the study, and scoring 19 or below on the Beck Depression Inventory (BDI). The participants' mean BDI score was 11.33 ± 3.82. Participants were instructed not to consume any alcohol, tea, coffee, or nicotine within 6 hours before the session and to arrive with enough sleep and a full stomach. Experimental sessions occurred between 10:00 a.m. and 4:00 p.m. Written informed consent was obtained from the participants before data collection. This study was approved on ethical grounds by the Clinical Research Ethics Committee of Istanbul University (Date:10.02.2015, No:351).

Deductive Inference Task

The inference tasks in the study were derived from both valid and invalid forms of the Modus Ponens (MP) type of conditional reasoning. These tasks featured a conditional rule illustrating the relationship between shape and color (e.g., "If its shape is a pentagon, its color is yellow."). Each trial consisted of a "conditional if-then statement (in Turkish)" paired with a "pictorial target stimulus (a picture of a colorful shape)" This setup aimed to minimize saccades during the inference process while ERP was being recorded. Trials were prepared with varying levels of mismatch, later referred to as task type, determined by whether the shape and color terms in the statements were repeated in the target stimulus. For example, after the statement "If its shape is a square, its color is not yellow," the target stimulus "yellow square" was classified as not involving a mismatch (MM-0) because the terms for both shape and color were preserved. Conversely, following the statement "If its shape is not a square, its color is not yellow," the target stimulus "black circle" was categorized as involving two mismatches (MM-2) because neither the shape nor the color terms matched (Table 1). Negation for shape and color terms in the statements were controlled for each task type, and target stimuli never contained negation for the first term (MP rule) in this study.

Seven shapes (pentagon, triangle, square, circle, star, plus, and trapezoid) and eight colors (red, yellow, blue, green, black, white, purple, and pink) were used in various combinations for the tasks. If the colored shape on the target stimulus confirmed the rule defined in the statement, participants were instructed to press the "correct" button; otherwise, they pressed the "incorrect" button. Participants scored one for correctly resolving the inference task and 0 for incorrectly resolving it. Response rates were calculated based on the average percentage of correct responses, and reaction time was measured as the average correct response latency in milliseconds. Two similar sets were prepared—one for the sham phase and the other for the anodal stimulation phase—each containing 120 inference tasks composed of three different types of mismatch conditions, referred to as "task types" (40 tasks of each kind: MM-0, MM-1, and MM-2). To prevent learning bias, the sets were designed to include an equal number of correct and incorrect inferences. The task order for each task type was randomized within each set, and the order of the phases (sham and anodal stimulation) was counter-balanced across participants.

Stimuli were presented using PsyTask and displayed on a computer screen. The text displayed on the screen was written in black on a white background. Each trial started with a visual fixation mark in the center of the screen for 500 ms (Figure 1). The two parts of the conditional statement then appeared one line at a time, with the first part (e.g., "If its shape is square") appearing at 500 ms and the second part ("its color is not green") appearing at 1500 ms. The entire statement remained on the screen for another 3000 ms. Then, it disappeared, and the central dot reappeared for 500 ms. This was followed by the target stimulus, which remained on the screen until the subjects pressed one of two buttons with their right hand (correct/incorrect response).

Table 1. Examples for each type of Modus Ponens inference conditions used in the study.

Conditional premise	Second premise ∴ Conclusion	Statement	Target stimulus (Conclusion)	Level of mismatch	HIT/CR
If p → q	p ∴ q	If its shape is a square, its color is yellow.		MM-0	HIT
If p → q	p ∴ ¬q	If its shape is a square, its color is *yellow*.		MM-1	CR
If p → ¬q	p ∴ ¬q	If its shape is a square, its color is not *yellow*.		MM-1	HIT
If p → ¬q	p ∴ q	If its shape is a square, its color is not yellow.		MM-0	CR
If ¬p → q	¬p ∴ q	If its shape is not a *square*, its color is red.		MM-1	HIT
If ¬p → q	¬p ∴ ¬q	If its shape is not a *square*, its color is *red*.		MM-2	CR
If ¬p → ¬q	¬p ∴ ¬q	If its shape is not a *square*, its color is not *red*.		MM-2	HIT
If ¬p → ¬q	¬p ∴ q	If its shape is not a *square*, its color is not red.		MM-1	CR

Italic items in the statements (premises) indicate mismatch with the target stimulus (conclusion). MM-0: No mismatching element between premises and conclusion; MM-1: One mismatching element between premises and conclusion; MM-2: Two mismatching elements between premises and conclusion. HIT: Correct affirmative response; CR: Correct negative response.

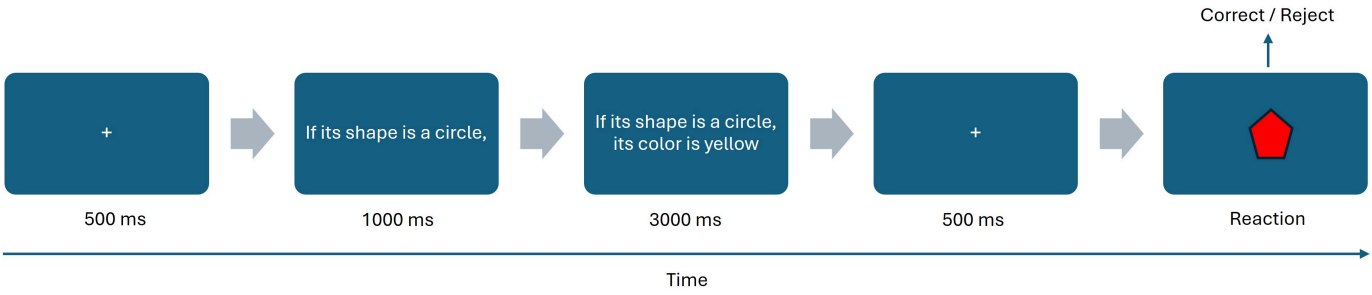


Figure 1. The schema illustrating the inference task used in the study.

Design and Procedure

The study consisted of a single session, including two phases, and all participants attended both phases (sham and anodal stimulation). Once the participants were seated 50 cm away from a 24-inch monitor (2560×1440, 60 Hz), a 10/20 electroencephalography (EEG) cap was placed on them. The anodal tDCS electrodes were connected to the left PFC on the cap, and the reference electrode (via 5x7 cm synthetic sponge) was connected to the right mastoid (Figure 2). It was difficult to place the sponge in the left PFC area with the cap on and to remove it without damaging the EEG cap after stimulation. To fix this, the current from the anodal electrode was spread to the F3, F7, and T3 electrodes on the EEG cap using three extra electrodes (Figure 3). This was done to avoid irritation and pain from delivering all the current through one small area. The EEG cap stayed on the participant during both phases, as tDCS stimulations were given through the cap, but no EEG recordings were performed. The first phase of tDCS stimulation (sham or anodal) lasted 10 minutes. After stimulation, the tDCS electrodes were removed, and EEG recordings were performed during deductive inference tasks.

After completing the first set of tasks, participants were given a 10-minute rest. The tDCS electrodes were then repositioned on the F3, F7, and T3 regions of their caps, followed by a second 10-minute stimulation, which was the reverse of the initial phase. Consequently, each participant experienced two sets: one under the influence of tDCS (following anodal stimulation) and one without the tDCS effect (after sham stimulation). Behavioral performance and EEG recordings were conducted for both sets. The recordings started after 10 exercise trials. To control potential order and practice effects,

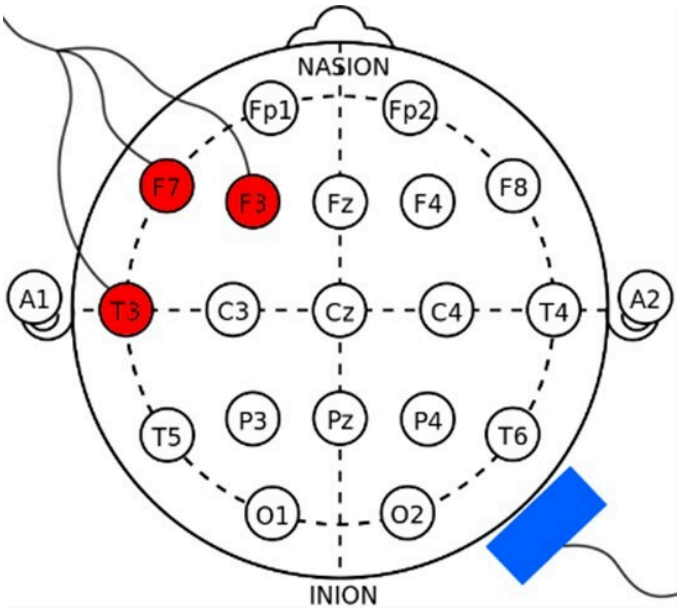


Figure 2. The diagram showing the placement of tDCS electrodes.

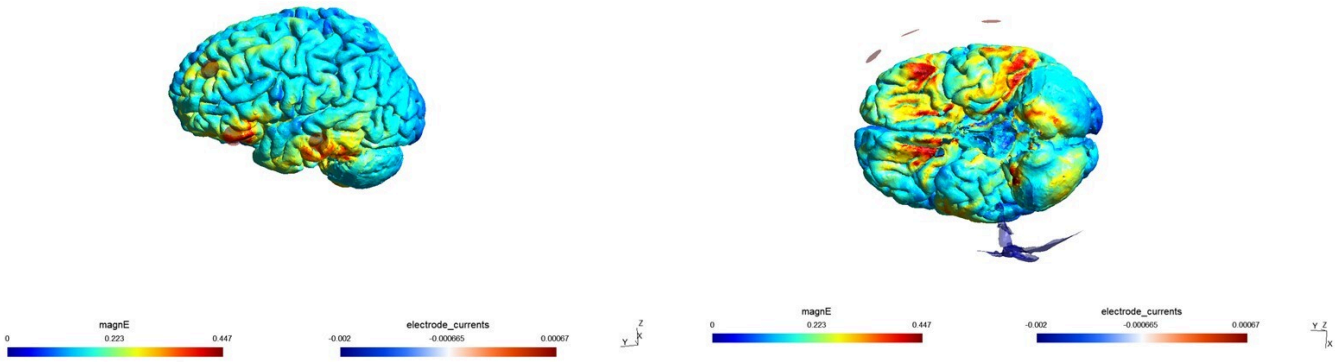


Figure 3. The electric-field modeling based on the final implemented electrode geometry (three anodal injection sites at F3/F7/T3 and the right-mastoid return).

the administration of stimulation was counter-balanced across participants. Experimental sessions lasted for approximately 2 hours in total.

tDCS was administered using a NeuroConn DC-Stimulator (NeuroConn GmbH, Ilmenau, Germany) with a 9-volt battery. During the anodal stimulation, the current ramped up to 2 mA over the first 30 seconds, remained constant at this level for 10 minutes, and then ramped down to 0 mA over the final 30 seconds. For the sham stimulation phase, the current was similarly ramped up to 2 mA, followed by a 30-second ramp down to 0 mA, where it remained for the rest of the duration.

The study design was single-blind: the subjects were naive about when sham/anodal stimulation was applied. At the beginning of the study, the participants were misled by being informed that they would perform tasks under two different types of active stimulation during the same session. At the end of the experiment, the participants were verbally asked whether they had felt the stimulation. None of the participants believed that they had received sham stimulation. The participants were subsequently informed of the deception. The subjects have been informed to begin the inference task after the tDCS has been turned off.

EEG recordings were conducted using a Mitsar-EED amplifier and WinEEG recording and analysis software. These recordings utilized 19 active channels, including Fp1, Fp2, Fz, F3, F4, F7, F8, Cz, C3, C4, T3, T4, T5, T6, Pz, P3, P4, O1, and O2. The electrodes were attached via a cap containing sintered Ag/AgCl electrodes. The active electrodes were referenced to the average of the linked earlobes (A1 and A2). Additionally, vertical (VEOG) and horizontal (HEOG) eye movements were recorded using two electro-oculogram electrodes placed on the nasion and the right exterior canthus of the eye, which helped eliminate artifacts caused by eye movements. The EEG data were

collected at a sampling rate of 512 Hz using a bandpass filter (0.16-100 Hz). Impedances kept below 10 kOhm. To eliminate noise, a 50-Hz notch filter was applied. The epochs were defined as from 200 ms before the time point of stimulus (t=0) to 800 ms after. Baseline correction was applied for the 200-ms pre-stimulus period. Eye blinks and muscle artifacts were removed using independent component analysis. A maximum of 8% of trials for the sham condition and 7% of trials for the anodal stimulation were excluded from the analysis due to artifacts. The ERP's were calculated based on the correct responses. To calculate the amplitudes of N2, the peak values (maximum negative deflection) were determined within the following time windows: 200-300 ms. N2 latency was defined as the peak latency.

Statistical Analyses

The SPSS 25 software package (SPSS Inc. Chicago, IL, USA) was used to perform statistical analyses. The dependent variables included behavioral and ERP responses elicited under inference tasks given following the anodal and sham stimulation phases. The behavioral responses were assessed by calculating the average percentage of correct responses (response rate) and the average latency of these correct responses (reaction time). To analyze the differences in the dependent variables, we conducted a 3 (task type: MM-0, MM-1, and MM-2) × 2 (stimulation type: sham and anodal) repeated-measures ANOVA. For the ERP responses, we calculated averages from data obtained from 9 EEG channels, grouped into three horizontal axes: frontal (F3, Fz, and F4), central (C3, Cz, and C4), and parietal (P3, Pz, and P4). We performed 3 (task type: MM-0, MM-1, and MM-2) x 2 (stimulation type: sham and anodal) x 3 (anteroposterior distribution: frontal, central, parietal) ANOVA. A Greenhouse–Geisser adjustment was used to correct for violations of sphericity. Relevant post hoc comparisons were conducted using Tukey HSD tests, which account for multiple comparisons. The response rate and N2 amplitude differences (anodal-sham) of the participants during the MM-2 task were compared using Pearson correlation. The significance level was considered at $p<0.05$.

RESULTS

Behavioral Results

According to the behavioral analysis, the main effects of task type and stimulation type on response rates were significant, $F(2, 24)=23.99$, $p<0.001$, $\eta^2_p=0.67$, and $F(1, 25)=4.26$, $p=0.05$, $\eta^2_p=0.15$, respectively. Post hoc analyses of task type showed that the response rate was lower for MM-2 (M=0.91 ± 0.01) compared to MM-0 (M=0.95 ± 0.01, p=0.04) and MM-1 (M=0.96 ± 0.01, p=0.03). No significant difference was found between MM-0 and MM-1 (p=0.55). The response rate after anodal stimulation was significantly higher than after sham stimulation (Table 2).

Table 2. Descriptive statistics of response rate and reaction time after sham and anodal tDCS

Task type	Parameters	Sham Mean ± SD	Anodal Mean ± SD	General Mean ± SD
MM-0	Response Rate	0.94 ± 0.01	0.96 ± 0.01	0.95 ± 0.01
	Reaction Time	1217 ± 51	1187 ± 57	1202 ± 51
MM-1	Response Rate	0.97 ± 0.01	0.96 ± 0.01	0.96 ± 0.01
	Reaction Time	1389 ± 73	1359 ± 63	1374 ± 68
MM-2	Response Rate	0.88 ± 0.02	0.93 ± 0.01	0.90 ± 0.01
	Reaction Time	1444 ± 63	1389 ± 67	1417 ± 63
Total	Response Rate	0.93 ± 0.01	0.95 ± 0.01	0.94 ± 0.01
	Reaction Time	1350 ± 58	1312 ± 61	1331 ± 57

Response rates were calculated based on the average percentage of correct responses; reaction time was measured as the average correct response latency in milliseconds. tDCS: Transcranial direct current stimulation; Sham: Sham stimulation; Anodal: Anodal stimulation; General: Combination of sham and anodal stimulations; SD: Standard deviation.

A significant interaction between task type and stimulation type was also observed, $F(2, 24)=3.36$, $p=0.05$, $\eta^2_p=0.22$. Further analyses were conducted to compare the effect of tDCS at each level of mismatch. For MM-2 tasks, anodal stimulation resulted in a significantly higher response rate than sham stimulation ($p<0.05$). In contrast, no significant differences were observed between anodal and sham stimulation for MM-0 ($p=0.45$) or MM-1 ($p=0.62$) tasks (Figure 4).

In the analysis of reaction time, only the main effect of task type was significant, $F(2, 24)=19.48$, $p<0.001$, $\eta^2_p=0.62$. Tukey's HSD post hoc analyses showed that the average reaction time under the MM-0 task was significantly shorter than under the MM-1 ($p<0.01$) and MM-2 tasks ($p<0.001$). No significant difference was observed between the MM-1 and MM-2 tasks ($p=0.64$). The reaction time across deductive inference tasks under sham and anodal stimulation conditions is presented in Table 2. The main effect of stimulation type and the interaction between stimulation type and task type were not significant on reaction times, $F(1, 25)=1.26$, $p=0.27$, and $F(2, 24)=0.22$, $p=0.80$, respectively. No significant correlations were found between the response rate and N2 amplitude differences (anodal-sham) of the participants during the MM-2 task, $r(25)=0.18$, $p=0.37$.

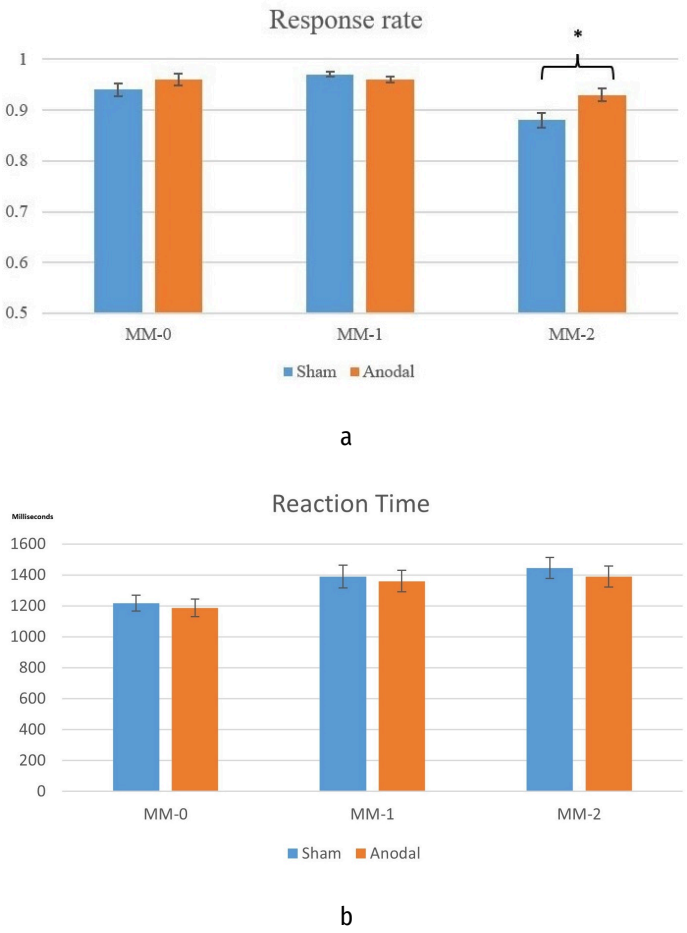


Figure 4. Response rates (based on the average percentage of correct responses) and reaction times (in milliseconds) measured following sham and anodal stimulation. (a) Only for MM-2 tasks, anodal stimulation resulted in a significantly higher response rate compared to sham stimulation; no significant differences were observed between anodal and sham stimulation for MM-0 or MM-1. (b) The reaction time differences were not significant for any task. MM-0: No mismatching element between premises and conclusion; MM-1: One mismatching element between premises and conclusion; MM-2: Two mismatching elements between premises and conclusion. *p<0.05

N2

The main effects of task type and anteroposterior distribution on N2 amplitudes were significant, F(2, 26)=5.19, p=0.01, η^2_p=0.29, and F(2, 26)=9.96, p=0.001, η^2_p=0.43, respectively . Post hoc analyses of task type showed that the highest negativity was observed under the MM-2 task (–1.30 ± 0.58 μV). Negativity recorded under the MM-1 (–0.73 ± 0.82 μV, p<0.05) and MM-0 (–0.35 ± 0.59 μV, p<0.01) tasks was significantly lower than under the MM-2 task. Post hoc analyses of the anteroposterior distribution revealed that the highest negativity was observed at frontal electrodes (–1.86 ± 0.65 μV). Negativity in the central region (–0.66 ± 0.66 μV, p<0.01) and parietal region (0.13 ± 0.51 μV, p<0.01) was significantly lower than in the frontal region. The central and parietal regions did not differ significantly (p=0.09). The main effect of stimulation type was not significant, F(1, 27)=1.05, p=0.32 (Figure 5). The interaction of task type × stimulation type on N2 amplitude was not significant, F(2, 26)=2.26, p=0.12, η^2_p=0.15. Figure 6 illustrates how different types of tasks affect the distribution of N2 amplitude on frontal regions.

Analyses of N2 latency revealed only a significant main effect of task type, F(2, 25)=6.93, p<0.01, η^2_p=0.36. The longest average N2 latency was observed under the MM-2 task (268.62 ± 6.15 ms), whereas latencies under the MM-0 (249.46 ± 6.61 ms, p=0.02) and MM-1 (254.10 ± 7.80 ms, p=0.03) tasks were significantly shorter. The effect of anodal stimulation on N2 latency across task types was not significant, F(2, 25)=0.47, p=0.63 (Figure 6).

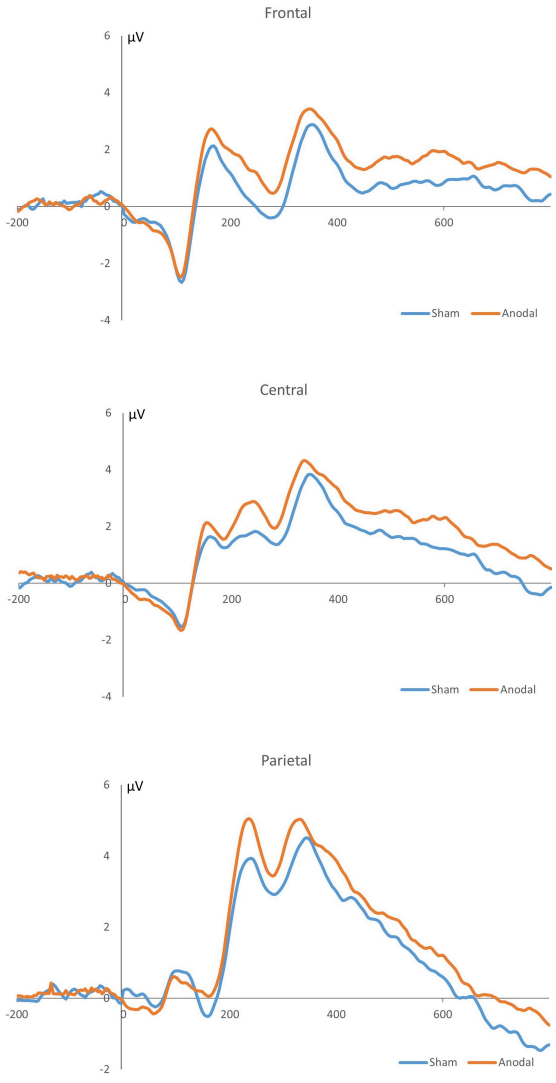


Figure 5. ERP results in response to inference-making tasks after sham and anodal stimulation within the N2 time window (200–300 ms). No significant differences were observed between anodal and sham stimulation.

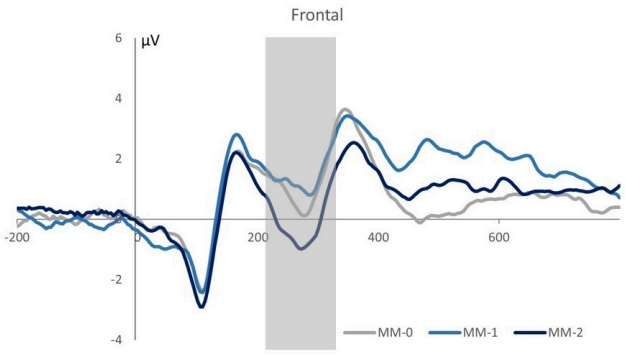


Figure 6. ERP results in response to MM-0, MM-1, and MM-2 tasks at frontal sites within the N2 time window (200–300 ms). No significant differences were observed between tasks. MM-0: No mismatching element between premises and conclusion; MM-1: One mismatching element between premises and conclusion; MM-2: Two mismatching elements between premises and conclusion.

DISCUSSION

This study aimed to compare deductive reasoning performance under different levels of mismatch (between terms in the premises and the conclusion) and under different types of cortical stimulation (sham versus anodal tDCS) when the content is arbitrary. The important originality of this study lies in the fact that the analyses were enriched by including the differences in behavioral and ERP signals associated with tDCS applied to participants.

Behavioral Results

Participants' response rates were slightly but significantly poorer on the task MM-2 (which had the highest level of mismatch between elements in the premises and conclusion), especially under sham stimulation. This was an expected result via the “mismatch effect.” This effect results from the tendency to consider information that matches the lexical content of the premises of deductive inference as logically correct, even if it is logically incorrect, and to consider information that does not match as logically incorrect, even if it is logically correct (23). Previous studies have shown that performance on logical inference tasks decreases when the level of mismatch between the terms in the inference increases (17). Therefore, it could be expected that under the MM-2 task (e.g., premise: "If its shape is not square, its color is not green"; Conclusion: A red circle. The two terms that define the color and shape in the premise and conclusion do not match), there would be an increase in the rate of individuals who give the wrong answer and evaluate the inference as "incorrect" without evaluating the inference via formal logic. In parallel, since the accuracy of inferences made with logical validity is related to the ability to suppress the mismatch effect, participants are expected to spend more cognitive effort and, therefore, more time. In this context, increased reaction times are expected in inference tasks with high mismatches. Indeed, the findings of this study partially support this. Increased reaction times were observed as the level of mismatches increased in the inference task; however, a significant difference was only observed in the MM-2 task. The difference between MM-1 and MM-0 was not significant (this was also the case in the response rate comparison). With anodal stimulation, an improved effect of tDCS on performance was found only in the response rates of the MM-2 task; reaction times in all tasks tended to accelerate with anodal stimulation, but the differences remained insignificant.

The lack of a significant difference in response rate and reaction time between the MM-0 and MM-1 tasks may be due to the participants' perceived ease of the task (ceiling effect). The observed ceiling effect on performance is likely because all tasks used in this study were designed using the modus ponens form of propositional logic, manipulating only the levels of mismatch. This was done to control for the confounding effects of different logical inference forms, namely, Modus Ponens (MP), Modus Tollens (MT), Denying the Antecedent (DA), and Affirming the Consequent (AC), on performance. Previous studies have shown that inferences in the MP form require relatively less cognitive effort than other types of inference. It is the type with the highest average success rates (reaching up to 95%); in other words, it is the easiest type of deduction for individuals (3, 24). The reason for the higher performance on this type of inference is explained by referring to the differential cognitive demands imposed by the number of mental models required to compute in each case (25). In this study, the inclusion of two mismatching elements was sufficient to create a relatively challenging situation for the participants, and a significant level of difficulty was not achieved among the other mismatch levels. Nevertheless, the performance-enhancing effect of anodal tDCS was detected in a relatively challenging cognitive task (MM-2 in this case) and has been demonstrated recently in some studies examining tasks more similar to those in this study, as well as less deviant tasks (26, 27).

Electrophysiological Results

The finding of the highest N2 negativity in the most mismatched task (MM-2) within the frontal region aligns with recent research on deductive inference, which identified N2 waves recorded in the frontocentral region when a conclusion statement directly contradicts the premises held in working memory (17, 28). Dual-processing theory considers frontocentral N2, a marker of cognitive dilemma solving, irrational bias, and heuristic inhibition. According to this theory, as the level of mismatches in inferences increases, N2 negativity should also be expected to increase (6, 29). In other words, the cognitive effort expended by individuals to inhibit the mismatch effect is correlated with N2 negativity. From this perspective, a significant dissociation in terms of negativity should also be expected between the MM-1 and MM-0 tasks; however, no such finding was found in the current study. In addition to the ceiling effect mentioned in the above discussion regarding behavioral findings, another explanation for this could be that the literature has shown

that the N2 wave can occur not only due to mismatches between the terms in the inferences but also, on a larger scale, when the inference result does not match the expected outcome. In other words, N2 has been detected in individuals who give the "false" response when faced with an "incompatible" conclusion following the premises (30). In half of the MM-0 task, despite having no mismatched terms, (e.g., Premise: If the shape is a pentagon, its color is not yellow. Conclusion: A yellow pentagon. Answer: False), false inferences are also present, and the individual is expected to correctly falsify the inference upon seeing the resulting statement. Therefore, it is plausible that half of the problems comprising the MM-0 task elicited a certain level of N2. However, the fact that significantly lower N2 negativity was not elicited compared to MM-1, as observed in behavioral findings, can be explained by the participants' ability to perform these two task types without difficulty. In other words, the mismatch effect may not have been effective in the MM-0 and MM-1 task types; the categorical effect of mismatch in terms of ERP waves appears to have emerged only in MM-2.

One of the main objectives of the present study was to determine whether N2 may be associated with cognitive performance enhancement that may occur with tDCS. Prado et al. (2008) found that those who were most successful in the deductive inference task had the lowest N2 amplitude, meaning that they were mentally prepared for possible inference outcomes after the premises and performed accuracy checks without needing to inhibit matching bias (17). In this study, it should have been expected that the N2 amplitude, indicating the intensity of cognitive inhibition, would increase positively with the exciting effect of tDCS in all tasks (without separating according to mismatch levels) and in the MM-2 task, where only behavioral success enhancement was observed. However, no significant results were found in this direction. Although a greater reduction in MM-2 latency was reported in relation to tDCS compared to other tasks, it was not statistically significant. The conclusion that can be drawn from this is that the improvement in behavioral performance on deductive inference tasks, specifically on the most difficult task in this study, MM-2, cannot be attributed to an increased ability to suppress the cognitive dilemma created by conflicting terms, as predicted by the dual processing theory. Instead, it is more plausible that the performance improvement on the MM-2 task is due to improvements in general working memory, such as a decrease in cognitive load on the participants or increased sustained attention following stimulation of the DLPFC.

CONCLUSION

Overall, the present study provides partial but meaningful evidence regarding how more cognitively challenging inferences with arbitrary content are influenced by varying levels of mismatch and anodal tDCS applied over the frontal cortex. Behaviorally, participants showed clear sensitivity to mismatches only at the highest level (MM-2), consistent with the expected increase in mismatch effect and cognitive demand. Although the easier MP-based structure of all tasks likely created a ceiling effect, limiting the detection of finer differences between MM-0 and MM-1, the study still revealed that anodal stimulation improved response accuracy specifically in the most demanding condition. This indicates that tDCS may facilitate performance when inhibitory control and bias suppression are taxed. Electrophysiologically, the results align with the existing literature showing increased N2 negativity under greater mismatch, reflecting heightened conflict monitoring and heuristic inhibition demands. However, like the behavioral findings, the mismatch effect emerged robustly only for MM-2. The trend toward reduced N2 amplitude and latency under anodal stimulation, although nonsignificant, is consistent with the notion that tDCS may modulate the neural processes involved in bias suppression and cognitive control.

The most important limitation of this study is that the inference tasks were prepared only in the relatively easy MP form. Future studies employing more cognitively demanding inference types or reducing ceiling effects may better clarify the interaction between stimulation, reasoning performance, and associated neural dynamics. One methodological limitation of the study is that, owing to technical difficulties, anodal tDCS stimulation had to be applied not only to the F3 region but also to a broader area encompassing the orbitofrontal and temporal regions, rather than the conventional left dorsolateral prefrontal cortex (DLPFC). This may have disrupted the stimulation x task type interaction effect in the ERP findings. Another limitation of this study is the counter-balanced administration of stimulation types (sham or anodal) to participants. While this approach was selected to mitigate potential order and practice effects, it did not eliminate the confounding carry-over effect associated with anodal stimulation on the performance of participants who received anodal stimulation first. We recommend that future research address this issue by scheduling sessions on separate days. Another limitation is that the number of correct responses in the tasks was balanced only for the total number of HIT and CR responses, but the equivalence of the HIT and CR ratios within the MM-0, MM-1, and MM-2 tasks was not considered. In other words, when inference problems are categorized as HIT and CR, different ratios of MM-0, MM-1, and MM-2 are observed within these categories. Because the focus of the study regarding inference problems was the mismatch level, we excluded an experimental design that would focus on the differences in HIT and CR responses. Numerous studies have observed the mismatch effect on CR responses, particularly in the N2 context, unlike HIT. Future studies could shed light on this issue by comparing the effects of anodal stimulation on mismatches in inference content and those related to CR. Finally, the last limitation of the study is its single-blind design. Future studies should adopt double-blind protocols to rule out potential experimenter expectancy effects in the results.

Ethics Committee Approval: This study was approved on ethical grounds by the Clinical Research Ethics Committee of Istanbul University (Date:10.02.2015, No:351).
Peer Review: Externally peer-reviewed.
Author Contributions: Conception/Design of Study- B.Ö., S.K. Data Acquisition- B.Ö.; Data Analysis/Interpretation- B.Ö., S.K.; Drafting Manuscript- B.Ö.; Critical Revision of Manuscript- B.Ö., S.K.; Final Approval and Accountability- B.Ö., S.K.
Conflict of Interest: The authors have no conflict of interest to declare.
Financial Disclosure: This study was funded by the Istanbul University Scientific Research Projects Unit (Project number: 52423).

Author Details

Barış Özdemir

[1] Maltepe University, Faculty of Humanities and Social Sciences, Department of Psychology, İstanbul, Türkiye

0000-0002-5955-5030 barisozdemir@maltepe.edu.tr

Sacit Karamürsel

[2] Koç University, School of Medicine, Department of Physiology, İstanbul, Türkiye

0000-0002-7534-9392

REFERENCES

1. O'Brien DP, Dias MG, Roazzi A, Braine MD. A case study in the mental models and mental-logic debate: Conditional syllogisms. In MDS Braine & D.P. O'Brien (Eds). Mental logic. Mahwah, New Jersey: Lawrence Erlbaum Associates. 1998; pp. 385-420.
2. Rips LJ. The psychology of proof: Deductive reasoning in human thinking. Mit Press; 1994.
3. Johnson-Laird PN, Byrne RM. Conditionals: a theory of meaning, pragmatics, and inference. Psychol Rev 2002; 109(4): 646-78.
4. Stanovich KE. Balance in psychological research: The dual process perspective. Behav Brain Sci 2004; 27(3): 357-8.
5. Clore GL, Huntsinger JR. How emotions inform judgment and regulate thought. Trends Cogni Sci 2007; 11(9): 393-9.
6. Qiu J, Li H, Huang X, Zhang F, Chen A, Luo Y, et al. The neural basis of conditional reasoning: An event-related potential study. Neuropsychologia 2007; 45(7): 1533-9.
7. Reverberi C, Cherubini P, Frackowiak RS, Caltagirone C, Paulesu E, Macaluso E. Conditional and syllogistic deductive tasks dissociate functionally during premise integration. Hum Brain Mapp 2010; 31(9): 1430-45.
8. Coetzee JP, Monti MM. At the core of reasoning: Dissociating deductive and non-deductive load. Hum Brain Mapp 2018; 39(4): 1850-61.
9. Evans JSB. In two minds: dual-process accounts of reasoning. Trends Cogn Sci 2003; 7(10): 454-9.
10. Stanovich K. Rationality and the reflective mind. Oxford University Press; 2011.
11. Kahneman D. Fast and slow thinking. Allen Lane and Penguin Books, New York; 2011.
12. Evans V. Lexical concepts, cognitive models and meaning-construction. Cogn Linguist 2006; 17(4): 491-534.
13. Evans JSB, Curtis-Holmes J. Rapid responding increases belief bias: Evidence for the dual-process theory of reasoning. Think Reasoning 2005; 11(4): 382-9.
14. Eichele TSK, Moosmann M, Jongsma ML, Quiroga RQ, Nordby H, Hugdahl K. Assessing the spatiotemporal evolution of neuronal activation with single-trial event-related potentials and functional MRI. Proc Natl Acad Sci USA 2005; 102(49): 17798-803.
15. Sabé M, Hyde J, Cramer C, Eberhard AL, Crippa A, Brunoni AR, et al. Transcranial magnetic stimulation and transcranial direct current stimulation across mental disorders: a systematic review and dose-response meta-analysis. JAMA netw Open 2024; 7(5): e2412616.
16. Petruo VA, Zeißig S, Schmelz R, Hampe J, Beste C. Specific neurophysiological mechanisms underlie cognitive inflexibility in inflammatory bowel disease. Sci Rep 2017; 7(1): 13943.
17. Prado J, Kaliuzhna M, Cheylus A, Noveck IA. Overcoming perceptual features in logical reasoning: An event-related potentials study. Neuropsychologia 2008; 46(11): 2629-37.
18. Zaghi S, Acar M, Hultgren B, Boggio PS, Fregni F. Noninvasive brain stimulation with low-intensity electrical currents: putative mechanisms of action for direct and alternating current stimulation. Neuroscientist 2010; 16(3): 285-307.
19. Schlaug G, Renga V, Nair D. Transcranial direct current stimulation in stroke recovery. Arch Neurol-Chicago 2008; 65(12): 1571-6.
20. Nitsche MA, Paulus W. Sustained excitability elevations induced by transcranial DC motor cortex stimulation in humans. Neurology 2001; 57(10): 1899-901.
21. Nitsche MA, Cohen LG, Wassermann EM, Priori A, Lang N, Anta A, et al. Transcranial direct current stimulation: state of the art 2008. Brain Stimul 2008; 1(3): 206-23.
22. Nalçacı E, Kalaycıoğlu C, Güneş E, Çiçek. El tercihi anketinin geçerlik ve güvenilirliği. Turk Psikiyatr Derg 2002; 13(2): 99-106.
23. Evans JSB. The influence of linguistic form on reasoning: The case of matching bias. Q J Exp Psychol 1999; Section A, 52(1): 185-216.
24. Trippas D, Thompson VA, Handley SJ. When fast logic meets slow belief: Evidence for a parallel-processing model of belief bias. Mem Cognition 2017; 45(4): 539-52.
25. Handley SJ, Newstead SE, Trippas D. Logic, beliefs, and instruction: a test of the default interventionist account of belief bias. J Exp Psychol Learn 2011; 37(1): 28.
26. Trémolière B, Maheux-Caron V, Lepage JF, Blanchette, I. tDCS stimulation of the dlPFC selectively moderates the detrimental impact of emotion on analytical reasoning. Front Psychol 2018; 9: 568.
27. Edgcumbe DR, Thoma V, Rivolta D, Nitsche MA, Fu CH. Anodal transcranial direct current stimulation over the right dorsolateral prefrontal cortex enhances reflective judgment and decision-making. Brain Stimul 2019; 12(3): 652-8.
28. Noveck IA, Goel V, Smith KW. The neural basis of conditional reasoning with arbitrary content. Cortex 2004; 40(4-5): 613-22.
29. Qiu J, Li H, Chen A, Zhang Q. The neural basis of analogical reasoning: An event-related potential study. Neuropsychologia 2008; 46(12): 3006-13.
30. Prado J, Noveck IA. How reaction time measures elucidate the matching bias and the way negations are processed. Think Reasoning 2006; 12(3): 309-28.

İSTANBUL UNIVERSITY PRESS

Experimed 2026, 16 (2): 90–99

https://doi.org/10.26650/experimed.1789751

Submitted: 01.10.2025
Revision Requested: 20.02.2026
Last Revision Received: 12.04.2026
Accepted: 27.04.2026
Published Online 12.08.2026

Experimed

Research Article

Open Access

Detection of *DHRS2*-associated E3 Ubiquitin Ligases in Breast Cancer Cell Lines

Damla Nur ŞAKAR [1], Burcu SALMAN YAYLAZ [2], Şeyma PUNAR [1] & Neslihan ABACI [2]

[1] Istanbul University, Institute of Graduate Studies in Health Sciences, Department of Genetics, İstanbul, Türkiye
[2] Istanbul University, Aziz Sancar Institute of Experimental Medicine, Department of Genetics, İstanbul, Türkiye

Abstract

Objective: The ubiquitin system plays a central role in regulating intracellular protein homeostasis and cellular signaling. E3 ubiquitin ligases, in particular, are key modulators of protein degradation and have been implicated in cancer progression, including breast cancer. *DHRS2*, a gene known to suppress *MDM2* activity through its ubiquitin-binding domain, has recently emerged as a potential regulator in tumor biology. This study investigated how *DHRS2* expression influences selected E3 ubiquitin ligase genes in breast epithelial cells.

Materials and Methods: MCF-7 and MCF-10A cell lines were used. *DHRS2* was either overexpressed using a vector-based system, or silenced via siRNA. After transfection, quantitative reverse transcription polymerase chain reaction (qRT–PCR) was performed to evaluate changes in the expression levels of *BRCA1, BARD1,* and *STUB1.*

Results: In MCF-7 cells, *DHRS2* overexpression induced a fourfold increase in *BRCA1* expression, whereas *STUB1* and *BARD1* were downregulated (0.56-fold). In MCF-10A cells with naturally low *DHRS2, STUB1* expression increased 1.5-fold after *DHRS2* knockdown, and *BARD1* expression correlated positively with *DHRS2* levels.

Conclusion: This study highlights a potential regulatory link between *DHRS2* and key E3 ubiquitin ligases-*BRCA1, BARD1,* and *STUB1*. Differential patterns across cell types indicate *DHRS2* as a context-dependent modulator of ubiquitin-mediated pathways, supporting its relevance in biomarker discovery and therapeutic targeting in breast cancer.

Keywords Breast Cancer · DHRS2 · Ubiquitin Ligase Genes · Ubiquitination · Cell Line · qRT–PCR

Citation: ŞAKAR, D. N., SALMAN YAYLAZ, B., PUNAR, Ş. & ABACI, N. Detection of *DHRS2*-associated E3 ubiquitin ligases in breast cancer cell lines. Experimed 2026; 16(2): 90-99. DOI: 10.26650/experimed.1789751

This work is licensed under Creative Commons Attribution-NonCommercial 4.0 International License.

© 2026. ŞAKAR, D. N., SALMAN YAYLAZ, B., PUNAR, Ş. & ABACI, N.

Corresponding author: Neslihan ABACI neslihan.abaci@istanbul.edu.tr

INTRODUCTION

Breast cancer, which is characterized by various biological subtypes, is the most prevalent cancer in women (1, 2). The molecular classification of breast cancer relies on the expression patterns of human epidermal growth factor receptor 2 (HER2), progesterone receptor (PR), and estrogen receptor (ER), which define luminal A, luminal B, HER2-enriched, and triple-negative subtypes (3). Although numerous risk factors for development and progression have been identified, the etiology of breast cancer remains largely elusive. Despite advancements, the survival rates for patients with breast cancer remain inadequate, so novel therapeutic targets are urgently needed (4).

The ubiquitin proteasome system (UPS) is a mechanism by which proteins are degraded in cells. This process involves a cascade of three enzymes, E1, E2, and E3, and the addition of a molecule called ubiquitin to proteins (1). E3 ligases of the UPS have been identified as either oncogenes or tumor suppressors in breast cancer, influencing key factors such as epigenetic regulators, signaling pathways and the DNA damage response (4). *BRCA1, BARD1, FBXW7*, and *STUB1* act as tumor suppressor E3 ligases, whereas *TRIM6* and *MDM2* act as oncogenic E3 ligases (5-7). Therefore, elucidating the mechanisms of UPS and its involvement in breast cancer development and progression holds promise for enhancing cancer therapeutic and immunotherapy efficacy (4).

In breast cancer, p53, often called the "gatekeeper of the genome," is a vital transcription factor that regulates various cellular functions. As an E3 ubiquitin ligase, *MDM2* targets p53 for ubiquitination, thereby directing it to proteasome-mediated degradation (2). DHRS2 (Hep27), a member of the short-chain alcohol dehydrogenase/reductase (SDR) enzyme family, inhibits *MDM2* and activates p53 functions, as well as other essential cellular processes (8).

DHRS2 expression is particularly decreased in ovarian cancer tissues, and its downregulation correlates with adverse patient outcomes (8). Furthermore, suppression of the *LEF1* gene in the Jurkat cell line significantly reduced the gene expression of *DHRS2* (9). DHRS2 has also emerged as a potential marker for breast cancer metastasis. When the function of the cellular mechanism resulting from the suppression of *DHRS2* gene expression was examined in the MCF-7 cell line, a migration-reducing function was shown (10). Given the central role of p53 in regulating oncogenic activity, there is evidence to suggest that overexpressed Myb stabilizes p53 in a *DHRS2*-dependent manner. The ubiquitin-proteasome system plays a key role in cell cycle regulation, signal transduction, and protein quality control. Furthermore, c-Myb plays a role in various types of cancer. Some genes, including c-Myc, contain c-Myb regions in their promoter regions (11). E3 ligases, such as *TRUSS, STUB1*, and *FBXW7*, modulate the stability of the c-Myb protein (12). *FBXW7* also targets *CCNE1* for ubiquitin-mediated degradation (13). Furthermore, *TRIM6* functions as an E3 ubiquitin ligase that plays a role in cell development, apoptosis, and autophagy and interacts with *STUB1* to induce its ubiquitination (7). *STUB1* is a chaperone-associated U-box E3 ligase that binds to chaperones and targets various substrates for degradation via the 26S proteasome (12-14). In breast cancer, *STUB1* suppresses tumor progression by ubiquitinating substrates, such as HER2 and C-terminal binding protein 2 (CtBP2) (15). *BARD1* exhibits low-frequency mutations in breast cancer and interacts with *BRCA1*. The BARD1-BRCA1 complex plays a crucial role in the DNA damage response by inducing the ubiquitination and degradation of damaged proteins, similar to that observed with *BRCA2* in DNA damage repair (16-18). Dysfunction of numerous E3 ubiquitin ligases can significantly impact the behavior of cancer cells, including metastasis in breast cancer (1).

In this study, we provide an overview of E3 ligases. We comprehensively characterized the roles of *BARD1* and *STUB1* E3 ubiquitin ligases in breast cancer and changes in the intracellular expression of the *DHRS2* gene. This study represents the first attempt to elucidate the relationship between *DHRS2* and essential ubiquitin ligases in breast cancer. We also examined the overexpression or inhibition of the *DHRS2* gene in four types of breast cancer cell lines in the presence of several ubiquitin ligase genes (*BRCA1, BARD1, FBXW7, STUB1, TRIM6, MDM2,* and *TRUSS*) via *in silico* analyses.

MATERIALS AND METHODS

Cell Culture and Transfection

Each experimental group for the respective cell lines was seeded in 24-well plates to assess changes in gene expression levels. Transfection procedures were performed using Lipofectamine™ 3000 (ThermoFisher, USA), which facilitated the delivery of *DHRS2* siRNA (Dharmacon OnTarget Plus Smartpool, USA) and expression vector (OriGene, *DHRS2* (NM_182908) Human Tagged ORF Clone, USA) following the manufacturer's recommended protocols. The cells were co-transfected with 30 pmol of siRNA and 0.25 µg of vector.

RNA Isolation and cDNA Synthesis

DHRS2 expression was silenced using siRNA and enhanced via an expression vector in MCF-7, MCF-10A, T47D, and MDA-MB-231 cell lines (ATCC, USA). The cells were maintained under standard culture conditions and stored at −80 °C until subsequent analyses. Total RNA was isolated from these cell lines using the RNeasy Mini Kit (QIAGEN, Hilden, Germany) following the manufacturer's protocol. RNA quantity and purity were assessed using a NanoDrop ND-1000 spectrophotometer (Thermo Scientific, Waltham, MA, USA). Complementary DNA (cDNA) was synthesized from the extracted RNA using the High-Capacity cDNA Reverse Transcription Kit (Thermo Fisher, USA) according to the supplier's guidelines. A flow chart detailing the experimental methodology is provided in the study to facilitate a comprehensive understanding (Figure 1).

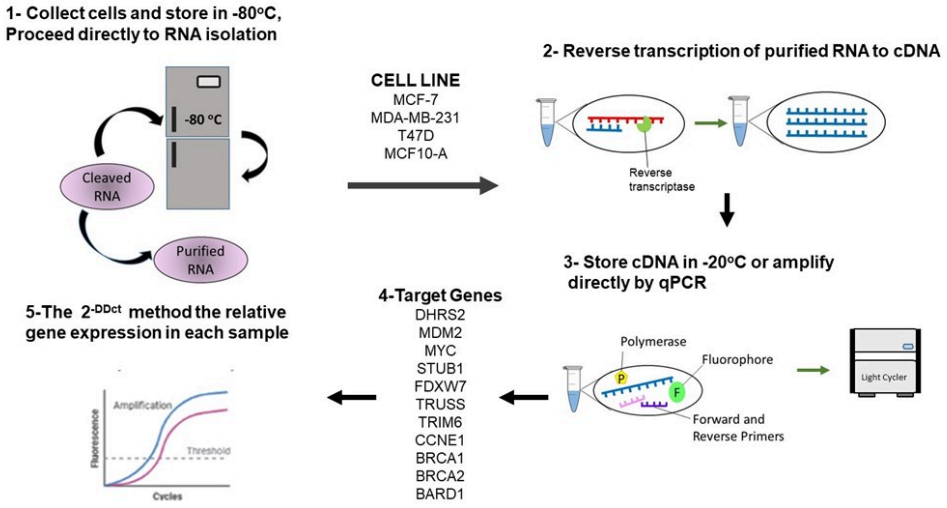


Figure 1. Graphical abstract of the experimental workflow for mRNA expression analysis. The study design consists of five sequential stages: (1) Collection and storage of breast cell lines (MCF-7, MDA-MB-231, T47D, and MCF-10A) at −80°C, followed by automated total RNA isolation. (2) Reverse transcription of the purified RNA into complementary DNA (cDNA) using reverse transcriptase enzyme. (3) Storage of synthesized cDNA at -20°C or direct quantitative polymerase chain reaction (qPCR) amplification utilizing locus-specific forward/reverse primers, DNA polymerase, and fluorophore-based real-time detection. (4) Screening and quantification of target gene panels associated with cellular regulatory pathways, including DHRS2, MDM2, MYC, STUB1, FBXW7, TRUSS, TRIM6, CCNE1, BRCA1, BRCA2, and BARD1. (5) Monitorization of real-time amplification curves across cycles relative to the baseline fluorescence threshold line. Relative mRNA expression levels in each sample were quantified using the comparative $2^{-\Delta\Delta Ct}$ method. cDNA: complementary deoxyribonucleic acid, qPCR: quantitative polymerase chain reaction, Ct: cycle threshold

Transfection efficiency was confirmed 48 hours post-transfection by evaluating *DHRS2* mRNA expression levels via quantitative reverse transcription polymerase chain reaction (qRT–PCR) in relation to the non-targeting control (NTC) group. Successful overexpression was verified by a statistically significant increase in *DHRS2* mRNA levels in the vector group, and knockdown efficiency was confirmed by a significant reduction in *DHRS2* mRNA levels in the siRNA group relative to the NTC. A non-targeting control siRNA (Dharmacon, scrambled sequence with no significant homology to any known mammalian gene) was used as the negative control for all siRNA transfection experiments, whereas an empty vector served as the control for overexpression experiments. All experiments were performed in biological triplicates, and each sample was analyzed in technical duplicates.

Gene Expression Assay

The forward and reverse primer sequences (5'-3') designed for the candidate genes are shown in Table 1. The *TATA-binding protein (TBP)* gene was used as a housekeeping control to normalize the expression of each candidate gene. qRT-PCR was performed using LightCycler 480 SYBR Green I Mix (Roche Diagnostics GmbH, Mannheim, Germany) and LightCycler 480 Instrument II (Roche Diagnostics GmbH, Mannheim, Germany) under the following PCR conditions: 95°C for 5 min, followed by 45 cycles of 95°C for 20 s, 64°C (variable gene-specific) for 20 s, and 72°C for 15 s. Quantification was performed using CT (cycle threshold) values, and relative fold change rates were determined using the $2^{-\Delta\Delta Ct}$ method for subsequent statistical analyses. The *TBP* gene was selected as the reference gene based on its well-established stability in breast cancer cell lines. Ct values for *TBP* showed consistent expression across all experimental groups and cell lines, with no statistically significant variation detected between the vector, siRNA, and NTC groups, confirming its suitability as a housekeeping gene for normalization in the present study.

Table 1. Primer sequences used for qRT-PCR analysis.

FBXW7	Forward	ACTAACTGGAGGCGAGGAGA
	Reverse	GCCTGTGACTGCTGACCAAA
CCNE1	Forward	CCCAAACTCAACGTGCAAGC
	Reverse	TTGCTCGCATTTTTGGCTGC
MYC	Forward	CAGGACTGTATGTGGAGCGG
	Reverse	GCTGTCGTTGAGAGGGTAGG
STUB1	Forward	GAGGCCAAGCACGACAAGTA
	Reverse	ATGTCCTTGCGGTCGTAGGT
BRCA1	Forward	CCGAAGAGGGGCCAAGAAAT
	Reverse	ACAGACACTCGGTAGCAACG
TRIM6	Forward	GGAAGAGAAGAAGGGGCTACG
	Reverse	CAGGGTCCAGAACTCACTCC
TRUSS	Forward	GCAGCTCGCTAATTTCTGCC
	Reverse	TCTGACACCTTTCGAGTCGC
MDM2	Forward	CTACAGGGACGCCATCGAAT
	Reverse	ACTCTCCCCTGCCTGATACA
BRCA2	Forward	CAGCAGACCCAGCTTACCTT
	Reverse	TACGCAACTTCCACACGGTT
BARD1	Forward	CAAACGGTGCCCTCAGAAAA
	Reverse	GGACTAGACATCACTCGCCT
DHRS2	Forward	GCTGTCATCCTGGTCTCTTCC
	Reverse	CTGGAACCACGCAGTTTACC
TBP	Forward	ACTTGACCTAAAGACCATTGCAC
	Reverse	CTTGAAGTCCAAGAACTTAGCTGG

The forward and reverse oligonucleotide primer sequences designed for the quantification of target human genes (*FBXW7, CCNE1, MYC, STUB1, BRCA1, TRIM6, TRUSS, MDM2, BRCA2, BARD1, DHRS2, TBP*) are presented in the 5' → 3' orientation.

Analysis of the Functional Interactions of Candidate Genes

Functional protein interactions were identified using the STRING database (version 11.5; https://string-db.org). The results were visualized using various bioinformatics tools. The UbiNet version 2.0 (Database of E3-Substrate Interactions; http://ubinet2.yinlab.uh.edu) was used to analyze the relationships between E3 ubiquitin ligase genes and substrates. The expression analysis of the samples on biological networks, protein-protein interactions, and functional enrichment related to 10 different genes was performed, and network graphs were generated using the OriginLab software (OriginLab Corporation, Northampton, MA, USA).

Statistical Analyses

Homogeneity tests were performed using SPSS 20.0 (SPSS, Chicago, IL, USA), and the normality of gene expression distributions was assessed. Independent samples t-test was used to evaluate differences between the siRNA and vector groups. Pearson's correlation analysis was used to determine the level of association between groups. Box plots of expression values were generated using GraphPad Prism version 9.5.1 (GraphPad Software, San Diego, CA, USA), whereas heatmap graphs visualizing gene expression values in cell lines were created using the same software. Chord graphs that illustrate the impact of *DHRS2* levels on ubiquitin ligase gene expression were generated using the Flourish data visualization tool online. The outline of the workflow and expression data analysis conducted using bioinformatic strategies in this study is shown in Figure 2. Statistical significance between groups was evaluated using the independent samples t-test, and differences were considered statistically significant at $p<0.05$. Significance levels are denoted in all figures as follows: *$p<0.05$, **$p<0.01$, ***$p<0.001$; ns, not significant. Where differences between groups did not reach conventional significance thresholds, this is indicated accordingly and discussed in relation to the biological variability observed across experimental groups.

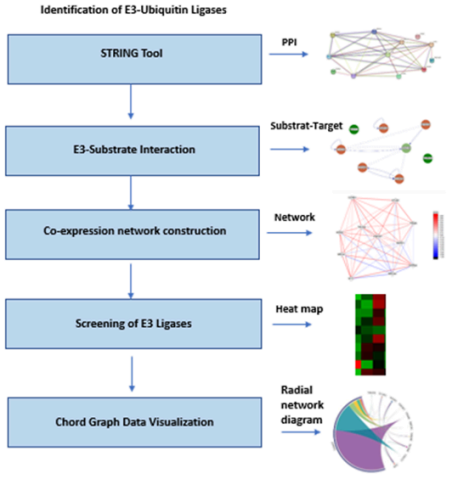


Figure 2. Outline of the workflow and expression data analysis in this study using bioinformatic strategies. The computational pipeline illustrates the systematic identification and characterization of E3-ubiquitin ligases through five core stages: (1) Screening of functional networks via the STRING tool to map protein-protein interactions (PPI). (2) Analysis of E3-substrate interactions to define specific substrate-target profiles. (3) Co-expression network construction to visualize gene expression correlation networks. (4) Systematic screening and filtering of candidate E3 ligases, represented by differential expression profiles in a heat map. (5) Final data visualization of multi-variable genomic or transcriptomic interactions generated as a chord graph (radial network diagram). E3: Ubiquitin ligase E3; PPI: Protein-Protein Interaction; STRING: Search Tool for the Retrieval of Interacting Genes/Proteins.

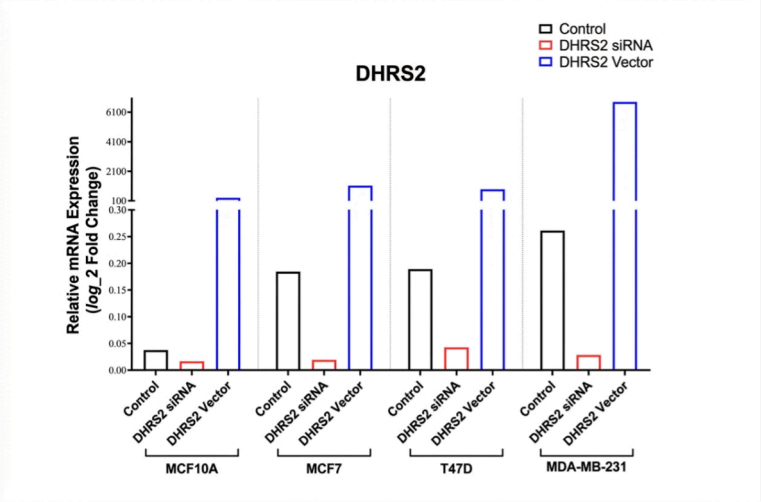


Figure 3. *DHRS2* gene expression levels in experimental groups after optimization

RESULTS

In the initial phase of this study, a broad panel of E3 ubiquitin ligase genes was screened, including *FBXW7, TRIM6, TRUSS, MDM2, BRCA2, MYC, CCNE1, BRCA1, BARD1,* and *STUB1*. Of these, *BRCA1, BARD1,* and *STUB1* showed the most statistically consistent and reproducible expression changes in response to DHRS2 modulation across the cell lines examined and were therefore selected for detailed characterization. Expression data for the full panel across all cell lines are provided in Figure 3. The comprehensive relative fold change ratios for the full target gene panel under DHRS2 vector induction and siRNA knockdown conditions are detailed in Figure 4. Four breast cell lines with distinct molecular profiles were used to evaluate the intracellular effects of *DHRS2* modulation on E3 ubiquitin ligase gene expression. The receptor status, p53 background, and basal *DHRS2* expression levels of these cell lines are summarized in Table 2.

Network Analysis of *DHRS2* Gene Interactions with Candidate E3 Ubiquitin Ligases

The functional associations between *DHRS2* and selected E3 ubiquitin ligase genes were first examined using publicly available interaction databases before experimental validation. The STRING database (version 11.5) was used to evaluate protein interaction networks centered on DHRS2, with MDM2 as the primary known interaction partner. This analysis confirmed the previously established functional association between DHRS2 and MDM2 and identified predicted network connections to BRCA1, BARD1, and STUB1 based on co-expression and co-occurrence data derived from the literature. The UbiNet 2.0 database was additionally used to map E3 ligase–substrate interaction networks relevant to the candidate genes. These database-derived network analyses served as the basis for candidate gene selection and are presented independently from the experimental qRT–PCR expression results described in the following sections.

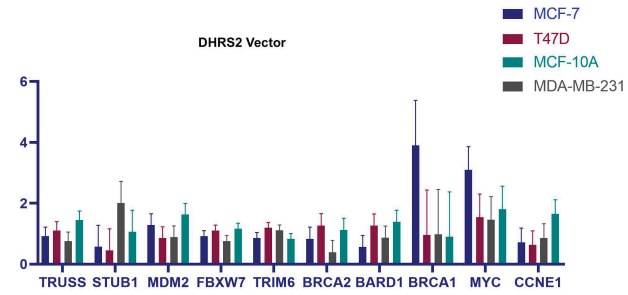
Variable Expression Levels of *DHRS2* in Breast Cell Lines

DHRS2 expression was successfully modulated across MCF-7, MCF-10A, T47D, and MDA-MB-231 cell lines using siRNA-mediated silencing and expression vector enhancement. The silencing rates were recorded as 90% for MCF-7, 89% for MDA-MB-231, 78% for T47D, and 57% for MCF-10A. Concurrently, overexpression assays

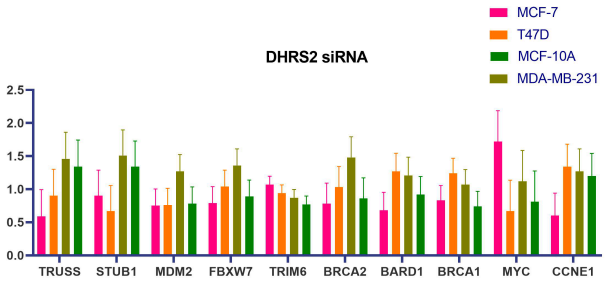
Table 2. Molecular characteristics of breast cell lines used in this study.

Cell line	Subtype	ER	PR	HER2	p53 status	Basal *DHRS2* expression
MCF-7	Luminal A	+	+	–	Wild-type	High
T47D	Luminal B	+	+	–	Mutant (L194F)	Moderate
MDA-MB-231	Triple-negative	–	–	–	Mutant (R280K)	High
MCF-10A	Non-tumorigenic	–	–	–	Wild-type	Low (basal)

ER: Estrogen Receptor; PR: Progesterone Receptor; *HER2*: Human epidermal growth factor receptor 2



a



b

Figure 4. The relative fold change in target gene expression after comparing *DHRS2* expression in MCF-7, MDA-MB-231, T47D and MCF-10A cells **a)** Quantitative gene expression profiles of target panels (including *TRUSS*, *STUB1*, *MDM2*, *FBXW7*, *TRIM6*, *BRCA2*, *BARD1*, *BRCA1*, *MYC*, and *CCNE1*) in MCF-7, T47D, MCF-10A, and MDA-MB-231 cells transiently transfected with the DHRS2 expression vector. **b)** Downregulation effects and subsequent relative mRNA fold changes of the identical target gene panels following treatment with DHRS2-specific small interfering RNA (siRNA) within the respective breast cell lines.

demonstrated increase rates of 26,068.18, 7,885.57, 6,101.72, and 4,608.24 for MDA-MB-231, MCF-10A, MCF-7, and T47D, respectively. The lower silencing rate observed in MCF-10A can be attributed to its naturally lower basal expression levels compared to the cancer cell lines used in this study.

As detailed in the Figure 4, high silencing efficiency was achieved alongside substantial increases in *DHRS2* levels across all experimental groups. The resulting impact on the expression profiles and relative ratios of candidate E3 ubiquitin ligase genes is illustrated in the comparative bar charts provided. In the MCF-7 vecDHRS2 cell line, *BRCA1* expression increased four times compared to that in the control group. However, no significant alterations in *BRCA1* expression were observed between the vector and siRNA groups in other cell lines. The relative expression levels of the *STUB1* and *BARD1* genes were reduced by 44% in MCF-7 cells overexpressing *DHRS2*, and both genes were expressed at the same levels. *STUB1* did not show a fold change in expression in the vector group, whereas *BARD1* showed a 1.5-fold increase in expression in the control MCF-10A cell line.

qRT–PCR Expression Results Confirm *DHRS2*-Associated Changes in Candidate Gene Expression

The following sections present the experimental qRT–PCR expression data obtained from *DHRS2* overexpression and knockdown experiments in breast cell lines. These findings are independent of the *in silico* predictions described, which were derived from publicly available databases and used solely to inform the selection of candidate genes prior to experimentation.

DHRS2 expression levels were evaluated in different breast cell lines, including the fibrocystic MCF-10A breast cell line, luminal A breast cancer groups, and triple negative breast cancer subtype. In particular, DHRS2 exhibited high expression in MDA-MB-231 cells, a metastatic cancer cell line. However, basal expression levels were observed in the MCF-10A cell line, and the highest expression was observed in the nonmetastatic breast cancer cell line MCF-7.

BRCA1 Expression Correlates with Intracellular *DHRS2* Levels in MCF-7 Cells

The relative expression of *BRCA1*, which decreased in MCF-7 siDHRS2 cells and increased approximately fourfold in MCF-7vec DHRS2 cells, is shown in Figure 5. Network analysis revealed a strong positive correlation between the *BRCA1* gene and *DHRS2*, where *BRCA1*

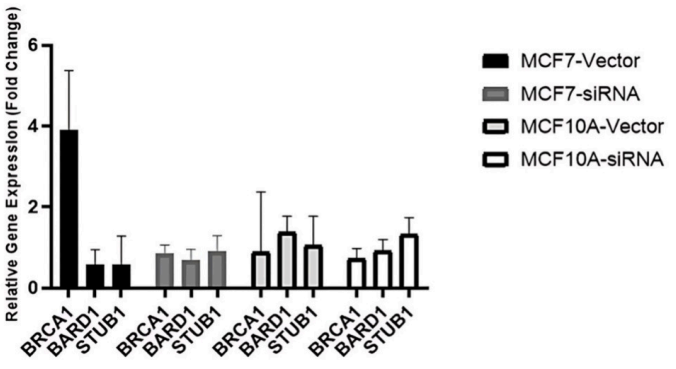


Figure 5. Relative expression rates of *STUB1*, *BARD1*, and *BRCA1* genes in MCF-10A and MCF-7 cell lines

expression increased in the presence of *DHRS2* and decreased in its absence.

The Intracellular Expression Level of *DHRS2* Affects the Expression of *STUB1* and *BARD1* Genes

In Figure 6, network plots were generated based on changes in total expression levels (independent of group differences). Blue lines connect groups with significant mutual effects and opposite expression patterns, whereas red lines connect those with similar values or tendencies. The expression of the *BARD1* and *STUB1* genes was reduced by 32% and 11%, respectively, in the MCF-7 siDHRS2 group compared to the control.

The response of the MCF-7 vecDHRS2 group was greater than that of the NTC group (43%, 36%, respectively). Similarly, *BARD1* and *STUB1* were significantly lower in the MCF-10A siRNA group than in the control group (45% and 34%, respectively), whereas the MCF-10A vector group exhibited a weaker response than the NTC group (25% and 19%, respectively). *DHRS2*, which is highly expressed in MCF-7 cells after transfection of the DHRS2 vector and siRNA, negatively influenced the expression of *BARD1*, whereas a positive interaction was observed in the expression of the *STUB1* gene and *BARD1* in the gene according to network analysis. On the contrary, while the *DHRS2* gene positively affected *BARD1* expression in the MCF-10A human breast epithelium cell line used as a control, a negative interaction was observed between *STUB1* and *BARD1*.

Expression Analysis Across All Four Cell Lines and Candidate Genes

The heatmap in Figure 7 presents a clustering of the normalized Ct values for each cell line and gene. $2^{(\Delta\Delta CT)}$ calculation was conducted to normalize the control group to 1. As shown in the table, the relative expression of *BRCA1* in the MCF-7 cell line increased fourfold in the presence of overexpression of *DHRS2*. In contrast, when *DHRS2* expression was suppressed, *BRCA1* expression decreased by 0.83 times. *BRCA1* expression remained at basal levels in the MCF-10A cell line. The fold change in the expression of *STUB1* and *BARD1* genes in the MCF-7 vecDHRS2 cell line was 0.56. In the absence of *DHRS2* expression in the cell, the relative expression of STUB1 increased 1.5 times in the MCF-10A group, whereas that of *BARD1* was 0.92 fold higher than that of the control but remained unchanged. Notably, the increased expression of *DHRS2* in the T47D cell line corresponded to an increase in the expression of the tumor suppressor *FBXW7*, consistent with the known role of *FBXW7* as a tumor suppressor in luminal breast cancer subtypes. A negative correlative relationship was also observed between *MDM2* and *DHRS2* expression levels in the MDA-MB-231 cell line, further supporting the established

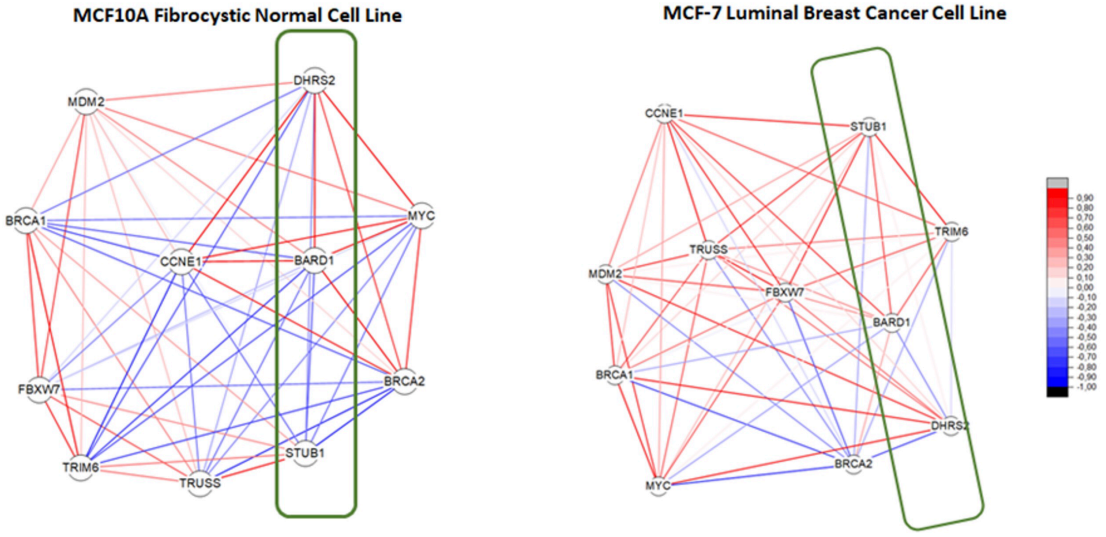


Figure 6. Interaction network of STUB1 and BARD1 genes with DHRS2

inhibitory role of *DHRS2* on *MDM2* activity. The impact of the abundance of *DHRS2* in the cell on overall expression was evident between the two groups in the MDA-MB-231 cell line.

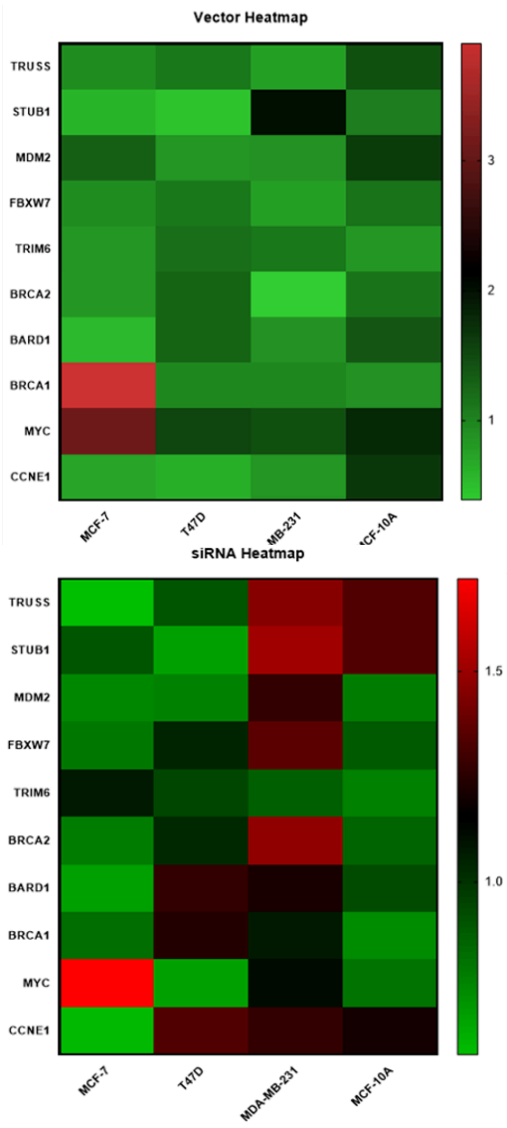


Figure 7. Heatmap analysis of the vector and siRNA groups

Chord Graph Analysis of *DHRS2* Interactions with Candidate Genes

Figure 8 shows that an increase in the *DHRS2* gene in the MCF-7 vector group corresponded to a decrease in the relative expression level of the *STUB1* and *BARD1* genes in the MCF-7 cell line, both genes being expressed equally. In contrast, when the expression of the *DHRS2* gene in the cell was suppressed, the relative expression levels of the *STUB1* and *BARD1* genes in the MCF-7 cell line increased, with both genes being expressed at similar levels. In the control cell line, MCF-10A, the vector and siRNA group, *STUB1* and *BARD1* were expressed inversely.

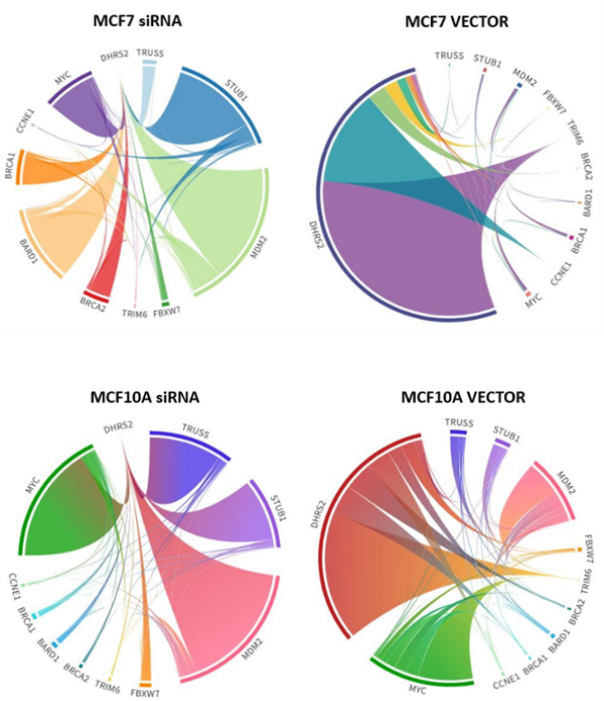


Figure 8. Radial network diagram of the associations of *STUB1* and *BARD1* genes with *DHRS2*.

DISCUSSION

The biological and clinical behavior of breast cancer varies between patients, which presents challenges in disease progression and monitoring patient outcomes. Therefore, biomarkers can help determine the appropriate treatment approach for each patient (3). For years, receptor-based biomarkers, such as estrogen receptor, progesterone receptor, and HER2 status, have been at the forefront of breast cancer treatment. However, targeting p53, which can be mutant or wild-type in different breast cancers, is of clinical significance (2).

The regulation of many cellular events is largely dependent on p53 activity. In particular, the frequency of p53 mutations varies significantly between the different subtypes of breast cancer.

In interpreting the findings of this study, it is important to distinguish between two types of evidence presented. The network analyses in result section are based on publicly available protein interaction databases and represent database-derived predictions.

The expression data in result sections represent original experimental findings obtained from qRT–PCR analyses in transfected breast cancer cell lines. Where both lines of evidence are consistent, this is noted as corroborating; where they diverge, this reflects the recognized gap between computationally predicted and experimentally observed regulatory relationships at the mRNA level.

Most p53 mutations are gain-of-function oncogenic mutations that contribute to a worse prognosis. In wild-type p53-carrying cancers,

abnormal signaling via the p53 pathway usually occurs due to other unusual conditions, such as high expression of *MDM2* (2).

DHRS2, a metabolic enzyme for hormone receptors, plays a vital role in cancer progression and functions as an inhibitor of the *MDM2* gene, an E3 ubiquitin ligase, thus restoring the function of p53 (19-20). This study investigated intracellular changes in *DHRS2* expression in ER^+, PR^+, and $HER2^-$ (MCF-7 and T47D) and triple-negative (MDA-MB-231) breast cancer cell lines, which contain mutant p53 and lack all three receptors. Given that ubiquitin-mediated proteolysis is the primary mechanism to control protein levels of cell cycle regulators, common genetic and expression changes in E3 ligases contribute to the formation of breast tumors (6).

According to our results, in MCF-7 cells in which *DHRS2* expression was suppressed, the relative expression of *BRCA1* decreased, whereas overexpression of *DHRS2* led to approximately a four-fold increase in BRCA1 expression. Additionally, DHRS2 functions are reported as a regulator of cell migration in the MCF-7 cell line (10). The observed increase and decrease in *BRCA1* expression in the presence and absence of DHRS2 suggests that *DHRS2* has a potential regulatory association with *BRCA1*. *BRCA1*, known as an E3 ligase, has been identified as a tumor suppressor in many breast cancer studies (6). The BARD1-BRCA1 complex plays a crucial role in DNA damage by inducing the ubiquitination and degradation of damaged proteins (16).

BARD1 also acts independently of *BRCA1* in the tumor suppressor pathway by interacting with repeats of BCL3 ankyrin and modulating the activity of the transcription factor NFκB (16). Reduced *STUB1* expression has been observed in tumors of patients with breast cancer. *STUB1* degrades the c-Myc protein and may play an essential role in breast cancer by ubiquitinating and degrading substrates such as HER2 and CtBP2 (12, 14-15). In various cancers, including breast cancer, *STUB1* expression is decreased compared to normal tissues. Low *STUB1* expression is associated with decreased survival (15). In the MCF-7 cell line vector group, the level of increase in the intracellular DHRS2 gene led to a simultaneous decrease in the relative expression levels of the *STUB1* and *BARD1* genes in the MCF-7 cell line. Together with chaperones, *STUB1* may play a significant role in breast cancer by promoting the ubiquitination and degradation of the HER2 and ERα proteins (21-22).

When intracellular expression of the DHRS2 gene is suppressed, relative expression levels of *STUB1* and *BARD1* genes increase in the MCF-7 cell line, and these two genes are expressed at similar levels. However, in the MCF-10A fibrocystic cell line, *STUB1* and *BARD1* expression increased in the vector and siRNA groups, and *BARD1* expression decreased with the upregulation of *DHRS2*. Although no apparent relationship was found between *STUB1* and *BARD1 in silico*, our targeted study suggested a possible mechanism in which these two genes interact inversely in non-cancerous cell lines but work together to suppress tumor progression in cancerous cell lines. These findings indicate that the relationship between *DHRS2* and the STUB1–BARD1 axis is context-dependent, differing between tumorigenic MCF-7 and non-tumorigenic MCF-10A cell lines, and may reflect differences in p53 status and receptor expression profiles between these cell lines.

The contrasting expression of *STUB1* in ER-positive HER2-negative MCF-7 cells and non-tumorigenic MCF-10A cells in the presence and absence of DHRS2 suggests a potential link between *DHRS2* and *STUB1*. When the levels of the *DHRS2* gene are modulated, the effect on *STUB1* and *BARD1* appears more pronounced, which may arise from the basal level of *DHRS2* expression in these cells. It is predicted that if its expression is temporarily eliminated using siRNA, responses similar to those in the control group can be obtained, as indicated by our results.

Furthermore, considering the possibility of disruption of DNA repair and ubiquitin mechanisms in cancer cells after intra-group comparisons, changes in expression patterns (one opposite, one similar) were observed in the MCF-10A cell line. Although the relationship between *MDM2* and *STUB1* in cellular aging mechanisms has been demonstrated in the literature (23), our mRNA-level results suggest a potential association between *DHRS2* and *STUB1* expression. We acknowledge that the current findings are based on mRNA expression, and some changes did not reach conventional statistical significance, likely due to biological variance in certain experimental groups. These results represent a preliminary exploration of the DHRS2-E3 ligase axis. Future mechanistic studies involving protein-level validations, such as Western blot and Co-Immunoprecipitation (Co-IP), are required to definitively map the physical interaction sites. Understanding their potential, revealing their relationships with *DHRS2*, a proposed prognostic biomarker for breast cancer, and identifying individual E3 ligases as drug targets may be a promising strategy for breast cancer diagnosis.

CONCLUSION

We investigated the expression of genes that could play roles as inhibitors and activators in the mechanism of action of *DHRS2* in both tumorigenic MCF-7 and non-tumorigenic MCF-10A breast cell lines. By inhibiting *MDM2*, a key E3 ubiquitin ligase, *DHRS2* contributes to the reactivation of p53 and the restraint of tumor development. This study presents the first evidence that *DHRS2* establishes interactions with *MDM2, BARD1, STUB1,* and *BRCA1* within breast cancer cells.

In this study, we explored the expression levels of ubiquitin ligase genes and other associated genes that could serve as prognostic biomarkers in human breast cancer cell lines with increased and decreased expression of *DHRS2*. The relationship between *MDM2*, a ubiquitin E3 ligase gene, and *DHRS2* is known in many cancers. In our study, in addition to this information, we have shown that the expression levels of the *BRCA1, BARD1,* and *STUB1* ubiquitin ligase

genes also change depending on the expression of *DHRS2* at the intracellular level.

Our results point to the potential role of *DHRS2* as a prognostic biomarker in luminal (ER^+, PR^+, and $HER2^-$) breast cancer subtypes, given its correlation with *BRCA1, STUB1,* and *BARD1*.

Acknowledgments: The first author of the manuscript has been awarded a scholarship under the TUBITAK 2210/A General Domestic Graduate Scholarship Program. This study was presented as a poster at the 21st International AEK Cancer Congress, Kassel/Germany

Ethics Committee Approval: This study was performed using commercial cell lines and therefore did not require ethics committee approval.

Peer Review: Externally peer-reviewed.

Author Contributions: Conception/Design of study: D.N.Ş., N.A.; Data Acquisition: D.N.Ş., Ş.P., N.A.; Data Analysis/Interpretation: D.N.Ş., B.S.Y., N.A.; Drafting Manuscript: D.N.Ş.; Critical Revision of Manuscript: N.A.; Final Approval and Accountability : D.N.Ş., B.S.Y., Ş.P., N.A.

Conflict of Interest: The authors declare no competing interests.

Financial Disclosure: This project was funded by the Scientific Projects Coordination Unit of İstanbul University (TYL-2021-38259).

Author Details

Damla Nur ŞAKAR
[1] Istanbul University, Institute of Graduate Studies in Health Sciences, Department of Genetics, İstanbul, Türkiye
0000-0003-4562-7424

Burcu SALMAN YAYLAZ
[2] Istanbul University, Aziz Sancar Institute of Experimental Medicine, Department of Genetics, İstanbul, Türkiye
0000-0002-9144-3899

Şeyma PUNAR
[1] Istanbul University, Institute of Graduate Studies in Health Sciences, Department of Genetics, İstanbul, Türkiye
0000-0002-7722-7401

Neslihan ABACI
[2] Istanbul University, Aziz Sancar Institute of Experimental Medicine, Department of Genetics, İstanbul, Türkiye
0000-0002-9962-4010 neslihan.abaci@istanbul.edu.tr

REFERENCES

1. Wang Y, Dai J, Zeng Y, Guo J, Lan J. E3 ubiquitin ligases in breast cancer metastasis: a systematic review of pathogenic functions and clinical implications. Front Oncol 2021; 11: 752604.
2. Marvalim C, Datta A, Lee SC. Role of p53 in breast cancer progression: an insight into p53 targeted therapy. Theranostics 2023; 13(4): 1421-42.
3. Dai X, Li T, Bai Z, Yang Y, Liu X, Zhan J, et al. Breast cancer intrinsic subtype classification, clinical use and future trends. Am J Cancer Res 2015; 5(10): 2929-43.
4. Han D, Wang L, Jiang S, Yang Q. The ubiquitin-proteasome system in breast cancer. Trends Mol Med 2023; 29(8): 599-621.
5. Zheng N, Shabek N. Ubiquitin ligases: structure, function, and regulation. Annu Rev Biochem 2017; 86: 129-157.
6. Chen C, Seth AK, Aplin AE. Genetic and expression aberrations of E3 ubiquitin ligases in human breast cancer. Mol Cancer Res 2006; 4(10): 695-707.
7. Wei C, Wu J, Liu W, Lu J, Li H, Hai B. Tripartite motif-containing protein 6 facilitates growth and migration of breast cancer through degradation of STUB1. Eur J Histochem 2021; 65(1): 3214.
8. Li Z, Liu H, Bode AM, Luo X. Emerging roles of dehydrogenase/reductase member 2 (DHRS2) in the pathology of disease. Eur J Pharmacol 2021; 898: 173972.
9. Sırma Ekmekci S, Emrence Z, Abacı N, Sarıman M, Salman B, Ekmekci CG, et al. LEF1 induces DHRS2 gene expression in human acute leukemia Jurkat T-cells. Turk J Hematol 2020; 37(4): 226-33.
10. Salman Yaylaz B, Ekmekci SS, Çınar S, Deniz G, Abacı N. DHRS2 is a potential marker of breast cancer metastasis. Gene Rep 2021; 25: 101302.
11. Deisenroth C, Thorner AR, Enomoto T, Perou CM, Zhang Y. Mitochondrial Hep27 is a c-Myb target gene that inhibits Mdm2 and stabilizes p53. Mol Cell Biol 2010; 30(16): 3981-93.
12. Farrell AS, Sears RC. MYC degradation. Cold Spring Harb Perspect Med 2014; 4(3): a014365.
13. Yeh CH, Bellon M, Nicot C. FBXW7: a critical tumor suppressor of human cancers. Mol Cancer 2018; 17(1): 115.
14. Paul I, Ahmed SF, Bhowmik A, Deb S, Ghosh MK. The ubiquitin ligase CHIP regulates c-Myc stability and transcriptional activity. Oncogene 2013; 32(10): 1284-95.
15. Liu Y, Zhou H, Tang X. STUB1/CHIP: new insights in cancer and immunity. Biomed Pharmacother 2023; 165: 115190.
16. Hawsawi YM, Shams A, Theyab A, Abdali WA, Hussien NA, Alatwi HE, et al. BARD1 mystery: tumor suppressors are cancer susceptibility genes. BMC Cancer 2022; 22(1): 599.
17. Wang M, Li W, Tomimatsu N, Yu CH, Ji JH, Alejo S, et al. Crucial roles of the BRCA1-BARD1 E3 ubiquitin ligase activity in homology-directed DNA repair. Mol Cell 2023; 83(20): 3679-91.e8.
18. Wan A, Zhang G, Ma D, Zhang Y, Qi X. An overview of the research progress of BRCA gene mutations in breast cancer. Biochim Biophys Acta Rev Cancer 2023; 1878(4): 188907.
19. Gabrielli F, Tofanelli S. Molecular and functional evolution of human DHRS2 and DHRS4 duplicated genes. Gene 2012; 511(2): 461-9.
20. Shafqat N, Shafqat J, Eissner G, Marschall HU, Tryggvason K, Eriksson U, et al. Hep27, a member of the short-chain dehydrogenase/reductase family, is an NADPH-dependent dicarbonyl reductase expressed in vascular endothelial tissue. Cell Mol Life Sci 2006; 63(10): 1205-13.
21. Xu W, Marcu M, Yuan X, Mimnaugh E, Patterson C, Neckers L. Chaperone-dependent E3 ubiquitin ligase CHIP mediates a degradative pathway for c-ErbB2/Neu. Proc Natl Acad Sci U S A 2002; 99(20): 12847-52.
22. Luan H, Bailey TA, Clubb RJ, Mohapatra BC, Bhat AM, Chakraborty S, et al. CHIP/STUB1 ubiquitin ligase functions as a negative regulator of ErbB2 by promoting its early post-biosynthesis degradation. Cancers 2021; 13(16): 3936.
23. Ullah K, Chen S, Lu J, Wang X, Liu Q, Zhang Y, et al. The E3 ubiquitin ligase STUB1 attenuates cell senescence by promoting the ubiquitination and degradation of the core circadian regulator BMAL1. J Biol Chem 2020; 295(14): 4696-08. Erratum in: J Biol Chem. 2020; 295(32): 11378.

İSTANBUL UNIVERSITY PRESS

Experimed 2026, 16 (2): 100–106

https://doi.org/10.26650/experimed.1892531

Submitted: 19.02.2026
Revision Requested: 02.04.2026
Last Revision Received: 08.04.2026
Accepted: 22.04.2026
Published Online 12.08.2026

Experimed

Research Article

Open Access

The Effect of Verbascoside on DNA Damage and Oxidative Stress in 3T3-L1 Adipocytes

Melek TUNÇ-ATA [1], Gizem AKAN [1], Şefike Sude GÜVENÇ [2], Deniz ÇELEBİ [2], Selen ŞAFAK [2], Zeynep Azra ÜNAL [2], Safa KORKMAZ [1] & Emine KILIÇ-TOPRAK [1]

[1] Pamukkale University, Faculty of Medicine, Department of Physiology, Denizli, Türkiye
[2] Pamukkale University, Faculty of Medicine, Denizli, Türkiye

Abstract

Objective: Obesity involves excessive lipid accumulation in adipose tissue, triggering oxidative stress and DNA damage. This study evaluated the effects of verbascoside doses (50 µM: V50 and 100 µM: V100) on DNA damage and oxidative stress in mature adipocytes.

Materials and Methods: 3T3-L1 cells were differentiated into mature adipocytes and treated with V50 or V100. Oil Red O staining quantified the lipid accumulation. DNA damage was evaluated using the Comet assay. We assessed oxidative stress by calculating the oxidative stress index (OSI) based on total oxidant status (TOS) and total antioxidant status (TAS) measurements.

Results: V100 reduced lipid accumulation compared with the control group. Furthermore, while V50 increased DNA damage (tail intensity and moment), V100 significantly lowered it compared to V50. Additionally, V100 improved oxidative stress markers (increased TAS, decreased TOS, and OSI), whereas V50 had no significant effect on these parameters.

Conclusion: Verbascoside showed dose-dependent effects on mature adipocytes. While V50 increased DNA damage independently of oxidative stress, V100 improved oxidative status and reduced DNA damage. These findings demonstrate that at appropriate doses, verbascoside is a candidate for preventing metabolic disorders, though further molecular studies are needed.

Keywords Adipocyte · DNA Damage · Obesity · Oxidative Stress · Verbascoside · 3T3-L1 Cells

Citation: TUNÇ-ATA, M., AKAN, G., GÜVENÇ, Ş. S., ÇELEBİ, D., ŞAFAK, S., ÜNAL, Z. A., KORKMAZ, S. & KILIÇ-TOPRAK, E. The effect of verbascoside on DNA damage and oxidative stress in 3T3-L1 adipocytes. Experimed 2026; 16(2): 100-106. DOI: 10.26650/experimed.1892531

This work is licensed under Creative Commons Attribution-NonCommercial 4.0 International License.

© 2026. TUNÇ-ATA, M., AKAN, G., GÜVENÇ, Ş. S., ÇELEBİ, D., ŞAFAK, S., ÜNAL, Z. A., KORKMAZ, S. & KILIÇ-TOPRAK, E.

Corresponding author: Emine KILIÇ-TOPRAK ektoprak@pau.edu.tr

INTRODUCTION

Obesity is a widespread health problem worldwide and is associated with structural and functional changes in adipose tissue that affect metabolic diseases (1). As the number and size of fat cells increase, dysfunctional adipocytes develop, and numerous inflammatory processes are triggered (2, 3). This excessive fat accumulation disrupts the hormonal functions of adipose tissue while creating an imbalance between reactive oxygen species (ROS) production and the body's antioxidant defense mechanisms, thereby increasing oxidative stress (4, 5). This oxidative environment within the adipocyte causes significant cellular damage and plays a key role in the pathogenesis of metabolic disorders (6). In particular, excessive lipid accumulation can trigger mitochondrial stress, leading to excessive ROS production and, consequently, the accumulation of DNA damage. This interrelated state of lipid overload and oxidative stress highlights adipocyte dysfunction and elevates the potential for genotoxic risk due to the increased markers of DNA damage and reduced repair capacity observed in obese individuals (7).

To mitigate these obesity-related metabolic disorders, polyphenols have emerged as promising biological molecules due to their potent metabolic regulatory properties (8, 9). Within this group, verbascoside (acteoside)—a polyphenol belonging to the phenolic acid subclass—is of particular interest because of its multifaceted biological activity (10). The primary reason for selecting verbascoside in this study is the multi-targeted biological activity exhibited by this natural polyphenol against obesity and associated metabolic disorders. These activities include anti-adipogenic effects and a protective role against oxidative stress and DNA damage. Verbascoside has been shown to inhibit the adipogenesis process by suppressing key transcription factors (peroxisome proliferator–activated receptors [PPAR] γ and CCAAT/enhancer-binding protein [C/EBP] α) in the 3T3-L1 cell model (7). While this makes it a strong candidate for reducing lipid accumulation, verbascoside's ability to scavenge free radicals and enhance antioxidant enzyme capacity (total antioxidant status [TAS]/total oxidant status [TOS] balance) has also been documented in the literature (11). Additionally, it has been reported that verbascoside possesses genoprotective effects by reducing DNA breaks associated with oxidative stress (12). Despite these known individual effects of verbascoside, its dose-dependent effect on DNA integrity in lipid-rich mature adipocytes has not yet been fully elucidated. In this context, the aim of our study was to evaluate the effect of different verbascoside doses on DNA damage in mature 3T3-L1 fat cells and to investigate the relationship between these effects and cellular oxidative stress markers.

MATERIALS AND METHODS

Differentiation of the 3T3-L1 Adipocyte

This study used the 3T3-L1 cell line (ATCC® CL173™, USA), a fibroblast cell line derived from a mouse (*Mus musculus*) embryo, recognized as a preadipocyte. Cells were cultured in Dulbecco's Modified Eagle Medium (DMEM, Gibco, Waltham, USA) with 25 mM glucose, supplemented with 10% heat-inactivated calf serum (Cegrogen, Germany) and antibiotics (penicillin and streptomycin; Wisent, Saint-Jean-Baptiste, Canada) at 37°C in a humidified atmosphere of 5% CO_2 to establish the experimental group. Upon reaching approximately 80% confluence in the culture dishes, $1x10^5$ cells were subsequently seeded in a 6-well plate following cell counting. The culture medium was subsequently replaced with a differentiation medium containing 3-isobutyl-1-methylxanthine (IBMX, Sigma I5879, USA), dexamethasone (DEX, Sigma D4902, USA), insulin (INS, Sigma I6634, USA), and fetal bovine serum (FBS) (Biowest, South America) to induce the differentiation of preadipocytes into adipocytes. The cells were incubated in this medium (MD1) for 48 h. After the incubation period, the medium containing high glucose, FBS (Biowest, South America), and INS (MD2) was renewed every 2 days, and the cells matured within 8 days. Experiments were conducted on adipocytes that matured on the 10th day after completing differentiation (13). Figure 1 illustrates the details of the experimental timeline.

Lipid Accumulation Evaluation

The lipid staining kit was used for microscopic analysis to confirm the transformation of preadipocytes into mature cells (BioVision Oil Red O, Catalogue No. K580-24; BioVision, Milpitas, CA, USA). Mature adipocytes were fixed in 10% formalin in phosphate-buffered saline (PBS, Wisent, Saint-Jean-Baptiste, Canada) for 1 h. Formalin was

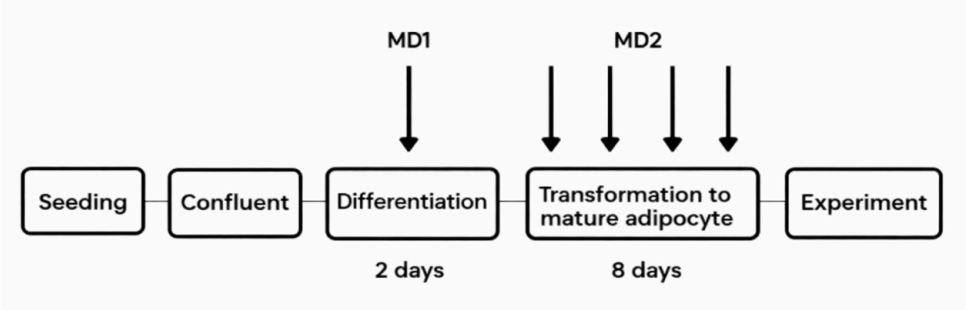


Figure 1. Demonstration of the experimental design. Verbascoside was applied at 50 µM and 100 µM doses. MD1: medium 1, MD2: medium 2.

removed and cells were carefully washed twice with distilled water; after that, add 60% isopropanol (BioVision, K580-24, USA) to each well and incubate for 5 minutes. The isopropanol was eliminated, and the Oil Red O working solution was applied for 30 minutes. Subsequently, the Oil Red O working solution was discarded and washed 2-5 times with distilled water. The optical intensity of the Oil Red O solution was measured at 490 nm using a Thermo Fisher Scientific™ Multiskan™ GO microplate spectrophotometer (Waltham, MA, USA) after being eluted with 100% isopropanol. A microscope (Olympus CKX41, Tokyo, Japan) was used to observe the lipid accumulation at 40X magnification (14).

Administration of Verbascoside

Verbascoside (V4015 ≥99% (HPLC grade), CAS 61276-17-3, $C_{29}H_{36}O_{15}$, Sigma, USA) was dissolved in dimethyl sulfoxide (DMSO) (CAS No: 67-68-5, ChemCruz, USA) to prepare a stock solution, from which intermediate working solutions were prepared. We obtained final concentrations of 50 µM and 100 µM by dilution in the culture medium (15, 16). Mature 3T3-L1 adipocytes were exposed to verbascoside for 24 h at 37 °C in a humidified atmosphere containing 5% CO_2.

Oxidative Stress Parameters

Following the 24 h treatment of 3T3-L1 mature adipocytes with 50 µM and 100 µM verbascoside, the TAS and TOS were determined in the collected culture media. TAS and TOS levels were measured using a Thermo Fisher Scientific™ Multiskan™ GO microplate spectrophotometer (Waltham, MA, USA) at 660 nm and 560 nm, respectively, following the manufacturer's specific instructions regarding reagent incubation and colorimetric reaction. TAS levels were measured based on the antioxidants ability to inhibit the formation of the dianisyl radical, produced through the Fenton reaction-mediated oxidation of o-dianisidine; results were expressed as mmol Trolox Equiv/L (11). TOS levels were quantified colorimetrically by monitoring the oxidation of the ferrous ion-o-dianisidine complex to ferric ions, which subsequently formed a colored complex with xylenol orange in an acidic medium. TOS values were reported as µmol hydrogen peroxide (H_2O_2) Equiv/L (12). Calibration procedures for TAS and TOS were performed using commercially available kits containing Trolox and H_2O_2 standards, respectively. Results for TAS measurements were reported in "mmol Trolox Equiv/L". For TOS measurements, H_2O_2 standards provided ready-to-use by the kit were used, and results were reported as "µmol H_2O_2 Equiv/L". To determine the overall oxidative state, the Oxidative Stress Index (OSI) was calculated using the following formula: OSI (arbitrary unit) = TOS (µmol/L) / TAS (mmol/L) × 100.

Comet Assay

To evaluate DNA integrity, mature adipocytes were rinsed with cold PBS and harvested by centrifugation. The resulting cell pellet was embedded in 0.5% low-melting-point agarose and layered onto slides pre-treated with 1% normal-melting-point agarose, followed by a final overlay of low-melting-point agarose. For proteolysis, slides were incubated overnight in a chilled lysis buffer (pH 10) at +4°C. DNA unwinding was performed in an alkaline electrophoresis buffer for 30 min, followed by electrophoresis at +4°C (21 V and 300 mA) for an additional 30 min. Post-electrophoresis, the slides underwent neutralization, were rinsed with distilled water, and stained using ethidium bromide (CAS No: 1239-45-8, Sigma, USA). Comets were visualized via fluorescence microscopy (Olympus CKX41, Tokyo, Japan, equipped with a fluorescence attachment) and quantified using Comet Assay IV (AutoComet) software (Perceptive Instruments, United Kingdom). DNA damage levels were characterized using head length (µm), tail length (µm), head intensity (AU), tail intensity (AU), and tail moment (AU) (17).

Statistical Analyses

All experimental measurements were performed in triplicate (n=3). Statistical analyses were performed using SPSS 25.0 software (IBM Corporation, Armonk, NY, USA). Continuous variables are presented as mean ± standard deviation (Mean ± SD). Group differences among Control (C), V50, and V100 were evaluated using the Kruskal–Wallis test (KW). A p value <0.05 was considered statistically significant.

RESULTS

The V100 group significantly reduced lipid accumulation in mature 3T3-L1 cells compared to the control group (C: 0.44 ± 0.028 OD; V100: 0.277 ± 0.012 OD; p=0.0001). The V50 group showed a tendency to reduce lipid accumulation compared to the control, but this difference was not statistically significant (Figure 2).

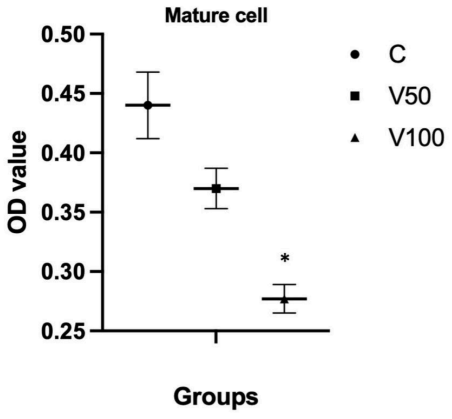


Figure 2. Lipid accumulation results of verbascoside in mature adipocytes. Mean ± SD were used to express the results. Group differences were evaluated using the Kruskal–Wallis test. p<0.05 was considered statistically significant. *: Significantly different from the control group. C: control group; V50: group treated with 50 µM verbascoside; V100: group treated with 100 µM verbascoside.

The V50 group significantly increased DNA damage compared to the control. Figure 3A represents the images of the comet assay parameters. When parameters supporting this general finding were examined, the V50 group significantly reduced head intensity compared to the control (C: 60.249 ± 12.562 AU; V50: 36.416 ± 0.505 AU; p=0.0001). The V50 group significantly increased tail intensity and moment compared to the control (C: 39.744 ± 12.562 AU; 6.722 ± 2.841 AU; V50: 63.91 ± 2.555 AU; 14.222 ± 1.005 AU; p=0.0001, respectively). The V100 group significantly reduced DNA damage compared to the V50 group. When examining the parameters supporting this general finding, head length and intensity were significantly increased in the V100 group compared to the V50 group (V50: 26.546 ± 1.749 µm; 36.416 ± 0.505 AU; V100: 31.545 ± 0.809 µm; 67.383 ± 0.779 AU; p=0.002 and p=0.0001, respectively). Tail length, tail intensity, and tail moment were significantly reduced in the V100 group compared to the V50 group (V50: 48.294 ± 0.964 µm; 63.91 ± 2.555 AU; 14.222 ± 1.005 AU; V100: 34.691 ± 0.978 µm; 32.61 ± 0.797 AU; 4.512 ± 1.178 AU; p=0.006, p=0.0001, and p=0.0001, respectively). No significant difference was observed between the V100 group and the control group in terms of all DNA damage parameters investigated (p>0.05). When examining the parameters in detail, head length and intensity showed a slight non-significant increasing trend in the V100 group compared to the control (C: 29.078 ± 3.387 µm; 60.249 ± 12.562 AU; V100: 31.545 ± 0.809 µm; 67.383 ± 0.779 AU, respectively). Conversely, tail length, tail intensity, and tail moment values in the V100 group were found to be statistically similar to the control levels (C: 41.972 ± 9.091 µm; 39.744 ± 12.562 AU; 6.722 ± 2.841 AU; V100: 34.691 ± 0.978 µm; 32.610 ± 0.797 AU; 4.512 ± 1.178 AU, respectively) (Figure 3A-B).

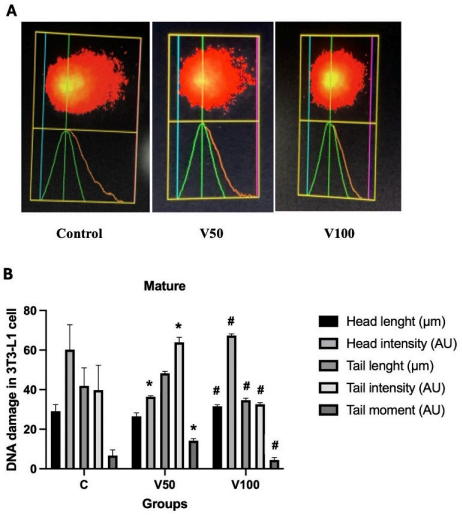


Figure 3. Comet assay images and the determined comet parameters for 3T3-L1 cells. (A) Representative comet assay images for the C, V50, and V100 groups. (B) Determined comet parameters. Mean ± SD were used to express the results. Group differences were evaluated using the Kruskal–Wallis test. p<0.05 was considered statistically significant. *: Significantly different from the control group. #: Significantly different from the V50 group. C: control group; V50: group treated with 50 µM verbascoside; V100: group treated with 100 µM verbascoside; AU: arbitrary unit.

In the V50 group treated with mature 3T3-L1 cells, no significant changes were observed in TAS, TOS, and OSI levels compared to the control. However, in the V100 group, oxidative stress decreased compared to the control. When the parameters supporting this general finding were examined, TAS increased in the V100 group compared to the control (C: 411.471 ± 16.35 mmol Trolox Equiv/L; V100: 861.296 ± 14.587 mmol Trolox Equiv/L; p=0.0001) (Figure 4A). When TOS and OSI values were examined, TOS and OSI values in the V100 group were decreased compared to the control group (C: 72.791 ± 0.716 µmol H_2O_2 Equiv/L; 15.172 ± 1.847 AU; V100: 47.044 ± 0.267 µmol H_2O_2 Equiv/L; 10.284 ± 1.366 AU; p=0.0001, respectively) (Figure 4B, Figure 4C).

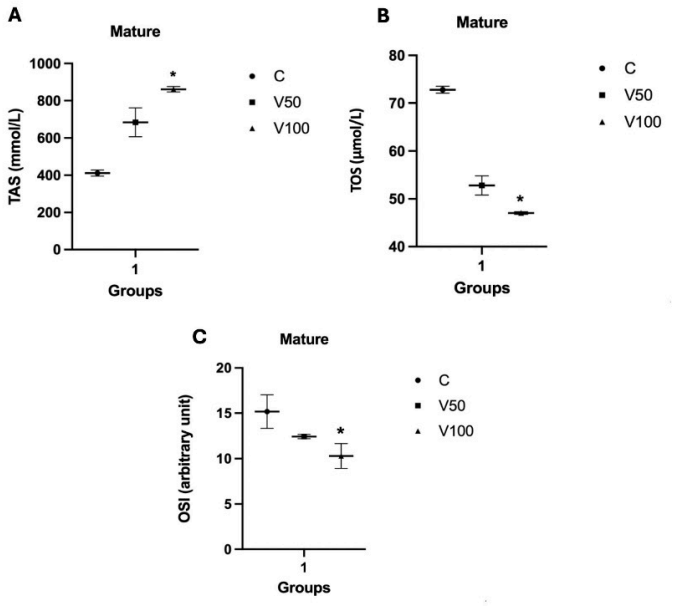


Figure 4. Effects of verbascoside on the oxidative stress status of mature 3T3-L1 adipocytes. (A) TAS, (B) TOS, and (C) OSI levels. Mean ± SD were used to express the results. Group differences were evaluated using the Kruskal–Wallis test. p<0.05 was considered statistically significant. *: Significantly different from the control group. C: control group; V50: group treated with 50 µM verbascoside; V100: group treated with 100 µM verbascoside.

DISCUSSION

Lipid accumulation in adipose tissue, oxidative stress, and DNA damage are interrelated processes, and investigating the effects of verbascoside on these mechanisms is important for understanding the dose-dependent biological responses of polyphenols.

In our study, although a 50 µM dose of verbascoside did not cause a significant change in oxidative stress parameters, DNA damage comet parameters increased markedly. This reveals that low doses of verbascoside may induce genotoxicity at the cellular level through mechanisms independent of oxidative stress. Possible reasons include the disruption of intracellular redox balance at the local level by metabolites of phenolic compounds or the creation of inhibitory effects on DNA repair mechanisms (18, 19).

In the literature, verbascoside (0.05 mM and 0.1 mM) increases chromosomal damage in human lymphocytes. This effect has been reported to be related to pathways involving poly ADP-ribose polymerase-1 (PARP-1) and p53, which are involved in DNA repair. Furthermore, it has been noted that verbascoside can be broken down into caffeic acid, and this metabolite may negatively affect DNA repair by disrupting the intracellular redox balance (19). Therefore, the DNA damage observed at a dose of 50 µM may be due to either the direct genotoxic effect of the polyphenol or the adverse mechanisms caused by the resulting metabolites. Additionally, a study using Barleria (0.43 mg/g) and verbascoside (1.02 mg/g) observed DNA damage in different cell types, particularly in PC3 cancer cells, using the Comet assay (20). These findings support the effect demonstrated by 50 µM verbascoside in our study. Beyond its dose-dependent variations, verbascoside is widely recognized as a potent polyphenolic antioxidant due to its ability to scavenge free radicals and enhance cellular antioxidant enzyme activities. This robust antioxidant capacity plays a crucial role in mitigating oxidative stress-induced damage in various metabolic disorders (21).

Furthermore, the fact that changes observed in DNA damage parameters appear before oxidative biomarkers demonstrates that they may be independent of these effects. This is because the comet assay has the capacity to reveal early and local DNA damage in cells before systemic biomarkers (22). Oxidative stress markers (TAS, TOS, and OSI), on the other hand, indicate more general, systemic responses.

In contrast, the V100 dose reduced oxidative stress and DNA damage compared to the V50 dose. This highlights that verbascoside has not been able to stimulate sufficient antioxidant defense systems at low doses. The 50 µM dose may have posed a threat to the cells; however, as this threat was not sufficiently strong, antioxidant defense mechanisms (e.g., activation of nuclear factor erythroid 2–related factor 2 [Nrf2]) may not have been stimulated to an adequate level. The 'hormetic response' has been frequently described in the literature for polyphenols, whereby low doses stress the cell but do not fully trigger defense responses, whereas higher doses exert a protective effect through the activation of Nrf2/antioxidant response element-mediated antioxidant enzymes. This U-shaped dose-response curve has been demonstrated for numerous phenolic compounds in the literature (23, 24). Therefore, the DNA damage observed at a 50 µM dose may be related to the insufficient stimulation of cellular defense mechanisms. The Nrf2/ARE/HO-1 pathway plays a critical role in maintaining cellular redox homeostasis. Under basal conditions, Nrf2 is sequestered in the cytoplasm by the Keap1 protein and targeted for proteasomal degradation. Upon exposure to antioxidant compounds, critical cysteine residues on Keap1 undergo modification, allowing Nrf2 to escape degradation and translocate from the cytoplasm into the nucleus. In the nucleus, it binds to the ARE sequences located in the promoter regions of target genes. This binding triggers the expression of Phase II antioxidant enzymes, primarily heme oxygenase-1 (HO-1), superoxide dismutase (SOD), and glutathione peroxidase (GPx) (25). In our study, the administered V50 dose may have been insufficient to activate the Nrf2/ARE/HO-1 signaling pathway.

In our study, the inhibitory effect of the V100 dose on lipid accumulation and its role in enhancing antioxidant capacity are consistent with those reported in the literature across both cellular and animal models. Herranz-López et al. reported that verbascoside significantly reduced triglyceride accumulation and ROS generation in hypertrophic adipocytes, a process associated with 5' adenosine monophosphate-activated protein kinase (AMPK) activation and PPAR-α upregulation (26). The systemic manifestation of these cellular defense mechanisms was further validated by Hao et al. in a diabetic mouse model; the researchers demonstrated that acteoside (verbascoside) effectively prevented hepatic steatosis and oxidative stress by activating the Nrf2/HO-1 signaling pathway (27).

In summary, a 50 µM dose of verbascoside can cause genotoxic effects by disrupting intracellular redox balance or suppressing DNA repair mechanisms, whereas at a 100 µM dose, this damage is suppressed by the stimulation of antioxidant defenses and the activation of repair mechanisms. This indicates that verbascoside exhibits a hormetic effect and may elicit dose-dependent biological responses. These results indicate that verbascoside, at an appropriate dose, may be a potential candidate for the prevention of metabolic diseases and support the existence of dose-dependent biological responses to polyphenols.

CONCLUSION

In the present study, the V100 dose exhibited a favorable metabolic effect by suppressing lipid accumulation in mature adipocytes. Furthermore, this concentration augmented TAS while simultaneously reducing TOS and OSI. This outcome fortified the cellular antioxidant capacity and subsequently mitigated DNA damage. Conversely, the observation that the V50 dose intensified DNA damage demonstrates that relatively lower concentrations may trigger divergent metabolic pathways. By unveiling the "Janus-faced" (bi-modal) impact of verbascoside on adipocyte metabolism, this research underscores the critical necessity of precise dose calibration for treating obesity and its associated cellular pathologies. These findings illustrate that a single molecule can function as either a protective shield or a source of cellular stress depending on the dosage, thereby providing a foundational premise for future investigations. A primary limitation of this study is the lack of direct molecular quantification for Nrf2/ARE signaling pathways, leaving the proposed 'hormetic response' mechanism as a hypothetical framework to be validated in future research. Another

limitation of this study is the absence of cytotoxicity assays for the determined doses.

Acknowledgments The authors thank Asst. Prof. Hande Senol for her help in statistical analyses. Part of this work was presented as poster at the 50th National Physiology Congress, 12-16 November 2025, in Antalya, Türkiye.

Ethics Committee Approval Ethical approval was not required, as the study involved only commercial cell lines in an *in vitro* model with no human or animal subjects.

Peer Review Externally peer-reviewed.

Author Contributions Conception/Design of study: E.K.T., M.T.A., G.A.; Data Acquisition: E.K.T., M.T.A., G.A., S.K., Ş.S.G., D.Ç., S.Ş., Z.A.Ü.;Data Analysis/Interpretation: E.K.T., M.T.A., G.A.; Drafting Manuscript: E.K.T., M.T.A., G.A., S.K., Ş.S.G., D.Ç., S.Ş., Z.A.Ü.; Critical Revision of Manuscript: E.K.T., M.T.A., G.A.; Final Approval and Accountability: E.K.T., M.T.A., G.A., S.K., Ş.S.G., D.Ç., S.Ş., Z.A.Ü.

Conflict of Interest The authors have no conflict of interest to declare.

Financial Disclosure This study was supported by TUBITAK under the 2209/A - Research Project Support Programme for Undergraduate Students. Project numbers; 1919B012335425 and 1919B012326675.

Author Details

Melek TUNÇ-ATA
[1] Pamukkale University, Faculty of Medicine, Department of Physiology, Denizli, Türkiye
0000-0002-0384-2356

Gizem AKAN
[1] Pamukkale University, Faculty of Medicine, Department of Physiology, Denizli, Türkiye
0009-0000-3336-102X

Şefike Sude GÜVENÇ
[2] Pamukkale University, Faculty of Medicine, Denizli, Türkiye
0009-0001-8229-0747

Deniz ÇELEBİ
[2] Pamukkale University, Faculty of Medicine, Denizli, Türkiye
0009-0001-0542-1627

Selen ŞAFAK
[2] Pamukkale University, Faculty of Medicine, Denizli, Türkiye
0009-0007-3619-896X

Zeynep Azra ÜNAL
[2] Pamukkale University, Faculty of Medicine, Denizli, Türkiye
0009-0001-7726-3146

Safa KORKMAZ
[1] Pamukkale University, Faculty of Medicine, Department of Physiology, Denizli, Türkiye
0009-0000-2480-5514

Emine KILIÇ-TOPRAK
[1] Pamukkale University, Faculty of Medicine, Department of Physiology, Denizli, Türkiye
0000-0002-8795-0185 ektoprak@pau.edu.tr

REFERENCES

1. World Health Organization. Obesity and overweight. 2025. Available from: https://www.who.int/news-room/fact-sheets/detail/obesity-and-overweight.
2. Liu F, He J, Wang H, Zhu D, Bi Y. Adipose morphology: a critical factor in regulation of human metabolic diseases and adipose tissue dysfunction. Obes Surg 2020; 30(12): 5086-100.
3. Hotamisligil GS. Inflammation and metabolic disorders. Nature 2006; 444(7121): 860–7.
4. Yu J, Qiu J, Zhang Z, Cui X, Guo W, Sheng M, et al. Redox biology in adipose tissue physiology and obesity. Adv Biol (Weinh) 2023; 7(9): e2200234.
5. Włodarczyk M, Nowicka G. Obesity, DNA damage, and development of obesity-related diseases. Int J Mol Sci 2019; 20(5): 1146.
6. Voronkova YS, Voronkova OS, Gorban VA, Holoborodko KK. Oxidative stress, reactive oxygen species, antioxidants: a review. Ecol Noospherol 2018; 29(1): 52-5.
7. Escobar Marcillo DI, Guglielmi V, Privitera GF, Signore M, Simonelli V, Manganello F, et al. The dual nature of DNA damage response in obesity and bariatric surgery-induced weight loss. Cell Death Dis 2024; 15(9): 664.
8. Yahfoufi N, Alsadi N, Jambi M, Matar C. The immunomodulatory and anti-inflammatory role of polyphenols. Nutrients 2018; 10(11): 1618.
9. Boccellino M, D'Angelo S. Anti-obesity effects of polyphenol intake: current status and future possibilities. Int J Mol Sci 2020; 21(16): 5642.
10. Mohammed RA, Kamel AS, Hindam MO, El-Dessouki AM, Hamouda HA, Ramadan NM, et al. Acteoside as a multifunctional natural glycoside: therapeutic potential across various diseases. Inflammopharmacology 2025. https://doi.org/10.1007/s10787-025-01811-0.
11. Erel O. A novel automated method to measure total antioxidant response against potent free radical reactions. Clin Biochem 2004; 37(2): 112–9.
12. Erel O. A new automated colorimetric method for measuring total oxidant status. Clin Biochem 2005; 38(12): 1103–11.
13. Prieto-Hontoria PL, Pérez-Matute P, Fernández-Galilea M, Martínez JA, Moreno-Aliaga MJ. Lipoic acid inhibits leptin secretion and Sp1 activity in adipocytes. Mol Nutr Food Res 2011; 55(7): 1059-69.
14. Dragunow M, Cameron R, Narayan P, O'Carroll S. Image-based high-throughput quantification of cellular fat accumulation. J Biomol Screen 2007; 12(7): 999-1005.
15. Olivares-Vicente M, Sánchez-Marzo N, Encinar JA, de la Luz Cádiz-Gurrea M, Lozano-Sánchez J, Segura-Carretero A, et al. The potential synergistic modulation of AMPK by Lippia citriodora compounds as a target in metabolic disorders. Nutrients 2019; 11(12): 2961.
16. Özbek NE, Kılıç Toprak E, Çört A, Altıntaş F, Tokgün O, Küçükatay V. Verbascoside promotes lipolysis in 3T3-L1 hypertrophic cells through alteration in the expression of lipolysis-related genes. Pam Tıp Derg 2026; 19(1): 13-26.
17. Cevik M, Caker S, Deliorman G, Cagatay P, Gunduz MK, Susleyici B. The effects of glipizide on DNA damage and nuclear transport in differentiated 3T3-L1 adipocytes. Mol Biol Rep 2022; 49(2): 1151-9.
18. León-González AJ, Auger C, Schini-Kerth VB. Pro-oxidant activity of polyphenols and its implication on cancer chemoprevention and chemotherapy. Biochem Pharmacol 2015; 98(3): 371-80.
19. Santoro A, Bianco G, Picerno P, Aquino RP, Autore G, Marzocco S, et al. Verminoside- and verbascoside-induced genotoxicity on human lymphocytes: involvement of PARP-1 and p53 proteins. Toxicol Lett 2008; 178(2): 71-6.
20. Kaewdaungdee S, Sham ZW, Ho HX, Lee SY, Tanee T, Benoit YD, et al. Barleria extracts containing barlerin and verbascoside boost immunity and regulate CYP450 gene in prostate cancer. Sci Rep 2025; 15(1): 21942.
21. Marčetić M, Bufan B, Drobac M, Antić Stanković J, Arsenović Ranin N, Milenković MT, et al. Multifaceted biological properties of verbascoside/acteoside: antimicrobial, cytotoxic, anti-inflammatory, and immunomodulatory effects. Antibiotics (Basel) 2025; 14(7): 697.
22. Collins AR. The comet assay for DNA damage and repair: principles, applications, and limitations. Mol Biotechnol 2004; 26(3): 249-61.

23. Calabrese EJ, Blain R. The occurrence of hormetic dose responses in the toxicological literature, the hormesis database: an overview. Toxicol Appl Pharmacol 2005; 202(3): 289-301.
24. Calabrese EJ, Kozumbo WJ. The hormetic dose-response mechanism: Nrf2 activation. Pharmacol Res 2021; 167: 105526.
25. Li N, Hao L, Li S, Deng J, Yu F, Zhang J, et al. The NRF-2/HO-1 signaling pathway: A promising therapeutic target for metabolic dysfunction-associated steatotic liver disease. J Inflamm Res 2024; 17: 8061-83.
26. Herranz-López M, Barrajón-Catalán E, Segura-Carretero A, Menéndez JA, Joven J, Micol V. Lemon verbena (Lippia citriodora) polyphenols alleviate obesity-related disturbances in hypertrophic adipocytes through AMPK-dependent mechanisms. Phytomedicine 2015; 22(6): 605-14.
27. Hao DD, Zhang L, Liu SL, Sun ZJ, Si RG, Zhang FN, et al. Acteoside inhibits hepatic lipid accumulation and oxidative stress in type 2 diabetic mice via the Nrf2/HO-1 Pathway. J Toxicol Environ Health A 2025; 88(15): 616-25.

İSTANBUL UNIVERSITY PRESS

Experimed 2026, 16 (2): 107–113

https://doi.org/10.26650/experimed.1888162

Submitted: 12.02.2026
Revision Requested: 29.03.2026
Last Revision Received: 27.04.2026
Accepted: 05.05.2026
Published Online 12.08.2026

Experimed

Research Article

Open Access

Loss of GON4L Impairs Proliferation and Spheroid Growth in Luminal Breast Cancer Cells

Hande Özkan [1] & Gözde Korkmaz [1,2]

[1] Koç University Research Center for Translational Medicine (KUTTAM), İstanbul, Türkiye
[2] Koç University, School of Medicine, Department of Medical Sciences, İstanbul, Türkiye

Abstract

Objective: GON-4-like (GON4L) is a nuclear protein described as a putative transcriptional regulator with transcriptional repressive activity. Its oncogenic potential has been reported in bladder cancer through interactions with the transcription factor Yin Yang 1 (YY1), the corepressor SIN3 Transcription Regulator Family Member A (SIN3A), and Histone Deacetylase 1 (HDAC1). However, the functional role of GON4L in breast cancer remains largely unexplored. This study aimed to investigate the contribution of GON4L to breast cancer cell proliferation under both two-dimensional (2D) monolayer and three-dimensional (3D) culture conditions.

Materials and Methods: In this study, GON4L expression in breast cancer was analyzed using publicly available datasets (UALCAN, TNMplot) and quantitative reverse transcription polymerase chain reaction (RT-qPCR) in cell lines. GON4L was knocked-down in the MCF7 breast cancer cell line using the CRISPR-Cas9 gene editing system. The impact of GON4L loss on cellular proliferation was assessed through green fluorescent protein (GFP)-based competition and colony formation assays under 2D conditions, as well as spheroid formation assays in 3D culture systems. Statistical analyses were performed using Student's t-test.

Results: GON4L expression was significantly elevated in breast cancer patient samples, including metastatic tissues. Compared with the non-tumorigenic breast epithelial cell line MCF-12A, GON4L expression was increased in MCF7 cells cultured under both 2D and 3D conditions. Genetic loss of GON4L resulted in a marked reduction in short- and long-term proliferative capacity in 2D culture systems and significantly impaired spheroid formation and growth in 3D cultures. These findings indicate that GON4L is required for sustained proliferation and maintenance of tumor-like architecture in breast cancer cells.

Conclusion: Our results identify GON4L as a functionally important transcriptional regulator supporting proliferative capacity and structural organization in breast cancer cells, particularly under tumor-mimicking 3D conditions. Further investigation of GON4L-dependent regulatory mechanisms may provide insight into its potential relevance in breast cancer progression.

Keywords Breast Cancer · GON4L · CRISPR-Cas9 · Three-dimensional Cell Culture · Spheroid Model

Author Note This study was conducted using the service and infrastructure of Koç University Research Center for Translational Medicine (KUTTAM). G.K. is a recipient of a Turkish Academy of Sciences (TUBA) GEBIP Award (2021) and The Science Academy Young Scientist Award Program (BAGEP-2021).

Citation: Özkan, H. & Korkmaz, G. Loss of GON4L Impairs Proliferation and Spheroid Growth in Luminal Breast Cancer Cells. Experimed 2026; 16(2): 107-113. DOI: 10.26650/experimed.1888162

This work is licensed under Creative Commons Attribution-NonCommercial 4.0 International License.

© 2026. Özkan, H. & Korkmaz, G.

Corresponding author: Gözde Korkmaz gkorkmaz@ku.edu.tr

INTRODUCTION

Breast cancer remains the most frequently diagnosed malignancy among women worldwide, and represents a biologically heterogeneous disease at both the molecular and histopathological levels (1, 2). This heterogeneity underlies significant variability in tumor behavior, therapeutic response, and clinical outcome, highlighting the need for a deeper understanding of the transcriptional regulatory mechanisms that govern cancer initiation and progression (3). In this context, identifying genes that coordinate oncogenic signaling pathways may provide critical insights into the molecular dysregulation driving breast cancer development.

GON-4-like (GON4L) is a nuclear protein that has been described as a putative transcriptional regulator, initially characterized by its roles in controlling proliferation and differentiation during embryonic development in several animal models (4, 5). At the molecular level, GON4L primarily functions as a transcriptional corepressor through its interaction with the DNA-binding protein Yin Yang 1 (YY1), the co-repressor SIN3 transcription regulator family member A (SIN3A), and histone deacetylase 1 (HDAC1). Through these interactions, GON4L is thought to contribute to chromatin remodeling and transcriptional repression in a context-dependent manner (6, 7).

Despite its established role in developmental processes, the involvement of GON4L in cancer biology remains largely unexplored. To date, mechanistic insight into its oncogenic function has been reported primarily in bladder cancer, where GON4L promotes tumor aggressiveness by facilitating the recruitment of YY1 and the androgen receptor (AR) to the *CD24* promoter, leading to enhanced *CD24* expression (8). Importantly, evidence also suggests that GON4L may exert oncogenic effects independent of CD24 and AR signaling, pointing to a broader and more complex role in tumor progression (8).

In vitro functional studies in cancer biology are most commonly conducted using two-dimensional (2D) monolayer cultures. However, such models fail to capture key aspects of solid tumor biology, including tissue architecture, cell–cell interactions, and microenvironment-dependent signaling (9, 10). Three-dimensional (3D) culture systems provide a physiologically relevant context by better reflecting native tumor organization (11).

In this study, we aimed to investigate the oncogenic potential of GON4L in breast cancer by integrating both 2D monolayer and 3D spheroid culture models. We focused on luminal breast cancer and examined the functional role of GON4L in the estrogen receptor–positive MCF7 cell line. Using a CRISPR-Cas9–based gene editing approach, we targeted *GON4L* and assessed its contribution to cellular proliferation under both 2D and 3D growth conditions.

Taken together, existing evidence and our experimental framework support the hypothesis that GON4L may function as an important regulator of cellular fitness in breast cancer. Its capacity to integrate transcriptional repression with epigenetic regulation through YY1/HDAC1-associated complexes underscores its potential relevance in breast cancer progression and warrants further investigation.

MATERIALS AND METHODS

Cell Culture

Human luminal breast cancer cell line MCF7 (ATCC® HTB-22™, USA) and HEK293T (ATCC® CRL-3216™, USA) cell lines were obtained from American Type Culture Collection (ATCC®, USA) and maintained at 37 °C in a humidified incubator with 5% CO_2. MCF7 cells and HEK293T cells were cultured in Dulbecco's Modified Eagle Medium (DMEM)-high glucose (Sigma, USA) supplemented with heat-inactivated 10% fetal bovine serum (FBS) (Biowest, France) and 1% penicillin/streptomycin (Biowest, France).

sgRNA Cloning and Lentivirus Production for GON4L Targeting

For functional experiments of *GON4L*, single guide RNA (sgRNA) sequences targeting distinct exonic regions were selected, along with a non-targeting control sgRNA with no predicted on-target sites in the human genome (Table 1). Corresponding oligonucleotides were synthesized (Macrogen, South Korea) and cloned following the protocol recommended by the Zhang laboratory (12). Phosphorylation and annealing of complementary sgRNA oligos for *GON4L* and control group with non-targeting oligos (CNT) were performed following the recommended protocol for T4 polynucleotide kinase (New England Biolabs, USA). 1 µL of each complementary oligos (100 µM), 0.5 µL T4 PNK, and 1 µL of 10X T4 Ligase Buffer (containing 1 mM ATP) was added and incubated at 37 °C for 30 minutes, followed by heat inactivation at 95 °C for 5 minutes and slow cooling to 25 °C at a ramp rate of 5 °C/min. Annealed sgRNAs were diluted 1:200 in nuclease-free water. For ligation, the pLentiCRISPR-v2 plasmid (Addgene #52961, a gift from Feng Zhang) was first digested with BsmBI-v2 (New England Biolabs, USA) using 5 µg plasmid DNA and 5 µL enzyme, followed by incubation at 55 °C for 3 hours and heat inactivation at 80 °C for 20 minutes. The digested plasmid (12 kb fragment) was purified from agarose gel using the Macherey-Nagel NucleoSpin Gel and PCR Clean-up Kit (Macherey Nagel, Germany). 50 ng of digested pLCV2 was used for ligation reactions established using T4 DNA Ligase (New England Biolabs, USA) for 1 hour incubation at room temperature (12, 13).

Ligated products were transformed into *Escherichia coli* Stbl3 competent bacteria and plated on ampicillin-containing agar plates. Plasmids were isolated using a mini-prep kit (Macherey Nagel, Germany) and verified via Sanger sequencing. Verified sgRNA constructs were used for lentiviral production and subsequent transduction of breast cancer cell lines in downstream experiments.

Table 1. DNA oligonucleotide sequences for cloning of single-guide RNA (sgRNA)

OLIGO NAME	SEQUENCE	COMPLEMENTARY	EXON
sgNT-1	CACCGGTCGTGAAGTGCATTCGATC	AAACGATCGAATGCACTTCACGACC	-
sgNT-2	CACCGGTAGCGAACGTGTCCGGCGT	AAACACGCCGGACACGTTCGCTACC	-
sgNT-3	CACCGGACCGGAACGATCTCGCGTA	AAACTACGCGAGATCGTTCCGGTCC	-
sgRNAGON4L-1	CACCGTGAGAAATTGCCTGGTACCG	AAACCGGTACCAGGCAATTTCTCAC	Exon 30
sgRNAGON4L-2	CACCGCAAGGGCCACGACCACCTGC	AAACGCAGGTGGTCGTGGCCCTTGC	Exon 26
sgRNAGON4L-3	CACCGGGACTCAGGAAGGAAGCAGG	AAACCCTGCTTCCTTCCTGAGTCCC	Exon 30

Lentivirus Production and Infection

HEK293T cells (4×10⁶ per 10 cm² dish) were transfected with pLCV2-sgRNA constructs targeting GON4L, along with packaging plasmids: 10 µg target vector, 5 µg pMDLg/pRRE (Addgene #12251), 2.5 µg pRSV-Rev (Addgene #12253), and 3.5 µg pCMV-VSV-G (Addgene #8454), using 63 µL PEI (Sigma, USA) in serum-free, antibiotic-free DMEM. The transfection mix was incubated for 15 minutes at room temperature before being added to the cells. After 16 hours, the medium was replaced, and the viral supernatant was harvested at 36 hours post-transfection, filtered through a 0.45 µm polyether sulfone (PES) filter, and stored at −80 °C.

For infection, MCF7 cells (4×10⁶ per 10 cm² dish) were seeded and transduced with lentiviruses in the presence of 8 µg/mL polybrene (Sigma, USA). Viral titer was optimized to achieve a multiplicity of infection (MOI) <0.4 to ensure single-copy integration. Following infection, cells were selected with 2 µg/mL puromycin as for 48 h. As control groups, CNT-infected cells were also generated with the same steps and used as controls in all subsequent experiments.

RNA Isolation and RT–qPCR

To verify the efficiency of GON4L gene targeting, total RNA was extracted using TRIzol™ Reagent (Invitrogen™, USA) according to the manufacturer's protocol. Briefly, 0.5–1 million cells were lysed in TRIzol, followed by chloroform phase separation and RNA precipitation using isopropanol. Pellets were washed in 80% ethanol, air-dried, and re-suspended in 50–60 µL nuclease-free water.

Complementary DNA (cDNA) was synthesized from 1 µg total RNA using the iScript™ cDNA Synthesis Kit (Bio-Rad, USA) under the following conditions: 25 °C for 5 min, 46°C for 20 min, and 95 °C for 1 min. The cDNA product was diluted 1:1 with nuclease-free water and used for quantitative PCR with SYBR Green Master Mix (Qiagen, Germany) on a LightCycler 480 II (Roche, Switzerland). β-*Actin* was used as the housekeeping gene, and relative GON4L expression was calculated using the ΔΔCt method with CNT as the reference/calibrator group. CNT cells were generated through the same lentiviral transduction and puromycin selection procedure as the GON4L-targeting groups and therefore serve as the appropriate internal control for normalization. As these processing steps may independently influence gene expression, unmodified MCF7 cells were not used as a reference for fold change calculations. All primer sequences are listed in Table 2.

Table 2. Primer Sequences for RT-qPCR

GENE NAME	PRIMER TYPE	SEQUENCE
ACTB	Forward	CATGTACGTTGCTATCCAGGC
	Reverse	CTCCTTAATGTCACGCACGAT
GON4L	Forward	CCACATCAGTGGAAGCCACCTA
	Reverse	CCTACCTCTCTAGCACCATCAG

Validation Experiments for GON4L Knockdown

To investigate the impact of *GON4L* targeting, MCF7 cells were infected with lentiviruses encoding *GON4L*-targeting sgRNAs in pLCV2. CNT was generated by infection with a non-targeting sgRNA cloned into the same pLCV2 backbone. Lentiviral transduction was performed at a MOI of 0.4. Following infection, cells were subjected to puromycin selection as described above to enrich successfully transduced populations.

GON4L knockdown efficiency was confirmed prior to functional assays with quantitative reverse transcription polymerase chain reaction (RT-qPCR), and validated cell populations were subsequently used to evaluate both short- and long-term proliferation capacity and 3D spheroid growth assays.

GFP-based Competitive Proliferation Assay

To assess the impact of GON4L loss on cell proliferation, a GFP-based competition assay was performed in the MCF7 cell line. Stable GFP-expressing polyclonal lines were first generated by transducing cells with the pLenti-CMV-GFP-Puro vector (Addgene #17448). GFP-positive cells were then mixed with cells transduced with *GON4L*-targeting sgRNAs and simultaneously with non-targeting oligos as the CNT group at a 1:3 ratio. Experiments were constructed as 120,000 cells from the group of GON4L knockdown (KD) or CNT mixed with 60,000 cells cultured in a 12-well plate. Experiment was performed as three biological replicates, each containing three technical replicates. Each assay included a corresponding non-targeting sgRNA CNT. The percentage of GFP⁺ cells was measured at baseline (Day 0) and at regular 72-hour intervals (Day 3, 6, 9, and 12) using a Beckman using a Cytoflex flow cytometer (Beckman Coulter, USA). A total of 10,000 events were collected per sample, and a decline in the

GFP⁺ population over time indicated a proliferative disadvantage associated with GON4L knockdown. In the CNT control group, GFP signal was also measured to ensure the proliferation capacity of CNT was protected, while temporal changes in GON4L-targeted experimental groups indicated competitive growth.

Colony Formation Assay

To evaluate long-term clonogenic potential following *GON4L* targeting, cells were seeded in 6-well plates at a density of 4,000 cells/well in triplicate. Cells were cultured under standard conditions for 14 days, with medium replenished every 3–4 days. Colonies were then washed twice with DPBS, fixed in ice-cold 100% methanol for 20 minutes at +4 °C, and stained with 0.5% crystal violet for 1 hour at room temperature with gentle shaking.

Plates were washed with water, dried, and scanned for visual documentation to determine the colony number and size. Then, long-term proliferation capacity and clonogenic potential were determined in GON4L-knockdown cells relative to the CNT control group. To quantify colony-forming ability, images of the CNT group and each experimental group were acquired, and the total colony area was measured using ImageJ-Fiji (NIH, USA). The results were normalized to the CNT and presented as relative colony formation. All experiments were performed in three independent biological replicates (n=3).

3D Spheroid Growth Assay

To assess the effect of *GON4L* knockdown on 3D spheroid growth, *GON4L*-knockdown cells and CNT control cells were seeded onto ultra-low attachment plates in equal numbers (750,000 cells per plate) containing 10% methylcellulose medium. Spheroid formation was monitored, and images were captured on Day 3 using a Nikon Eclipse Ts2 light/fluorescence microscope. At least 50 spheroids per condition for each biological replicate were imaged using a 20×/0.40 objective lens. Spheroid area was quantified using ImageJ software (NIH, USA): the scale bar was calibrated using the "Set Scale" function, and individual spheroids were outlined using the "Polygon Selections" tool to calculate surface area. Differences in spheroid size were used to infer the impact of GON4L loss on 3D tumor architecture.

Statistical Analyses

All experiments assessing the functional impact of GON4L knockdown were conducted using at least three independent biological replicates, unless otherwise specified. Data are presented as mean ± standard deviation (SD). Statistical analyses were performed using GraphPad Prism version 10.0 for Windows (GraphPad Software, Boston, MA, USA). Comparisons between GON4L-targeting sgRNA groups and corresponding non-targeting controls (CNT) were evaluated using unpaired two-tailed Student's t-test. Statistical significance was defined as follows: *p<0.05; **p<0.01; ***p<0.001, ****p<0.0001.

RESULTS

GON4L Expression is Dysregulated in Breast Cancer

GON4L is located on chromosome 1q22 and encodes a nuclear protein that has been described as a putative transcriptional regulator (4). Its functional relevance has been previously explored in bladder cancer, where interactions involving YY1 have been reported (8). To further support the clinical relevance of GON4L, publicly available patient-derived datasets from the UALCAN portal were used to interpret the data of breast cancer patients into the analysis. UALCAN is a widely used cancer omics platform that provides access to transcriptomic, proteomic, and survival data derived from large-scale datasets, including TCGA and CPTAC (The extension of UALCAN: https://ualcan.path.uab.edu/index.html) (14). These patient-level datasets provide an important translational framework for validating experimental observations and strengthening the biological significance of candidate genes, such as *GON4L*.

GON4L expression was significantly higher in tumor tissues than in normal breast tissue (14) (Figure 1A). In luminal subtypes of breast cancer, the expression of GON4L significantly increased compared to normal tissues (14) (Figure 1B). Furthermore, GON4L expression was elevated in metastatic breast cancer samples relative to primary tumors (Figure 1C), supporting an association between increased GON4L expression and disease progression (15).

To assess GON4L expression dysregulation under different *in vitro* growth conditions, qPCR analysis was performed in both 2D monolayer and 3D spheroid cultures. In both settings, GON4L expression was significantly elevated compared with the non-tumorigenic breast epithelial cell line MCF-12A (Figure 2).

GON4L Loss Reduces Proliferation in MCF7 Breast Cancer Cells

To investigate the functional contribution of GON4L to breast cancer cell proliferation, GON4L was targeted in MCF7 cells using the CRISPR-Cas9 genome editing system. Knockdown efficiency was validated by quantitative PCR (qPCR), which confirmed a significant reduction in *GON4L* transcript levels compared with control cells (Figure 3A).

Cellular proliferation following GON4L loss was assessed using both short- and long-term assays. Long-term proliferative potential was further examined using a colony formation assay under 2D monolayer culture conditions. Consistent with the competition assay results, GON4L loss led to a significant reduction in colony-forming ability compared with control cells (Figure 3B).

Short-term proliferative capacity was evaluated using a GFP-based competition assay, in which *GON4L*-knockdown cells exhibited a marked proliferative disadvantage relative to non-targeting control

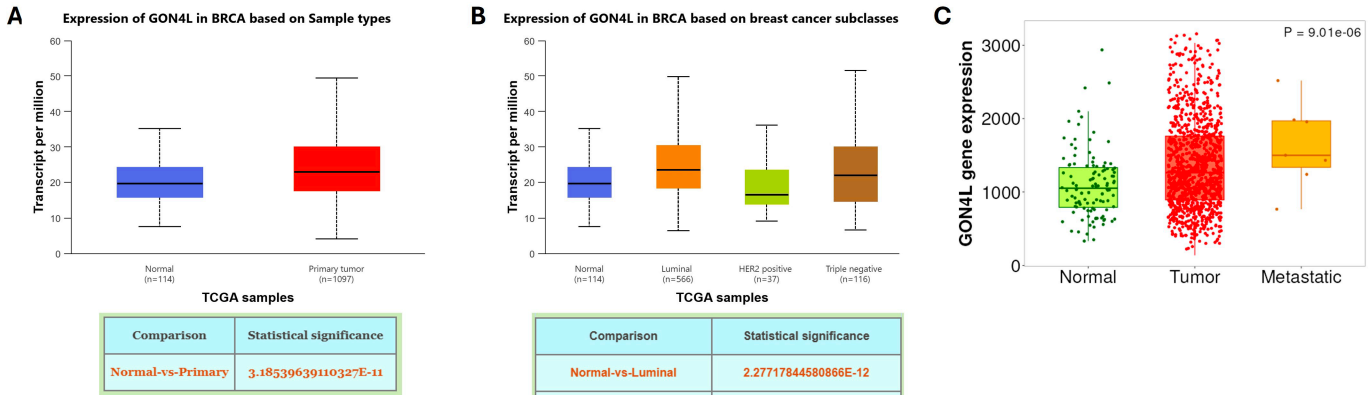


Figure 1: GON4L expression elevated in breast cancer patient samples **(A)** In primary breast tumors, GON4L expression was significantly elevated compared to adjacent normal tissues (UALCAN) (14). **(B)** GON4L expression was significantly increased in luminal subtypes of breast cancer patients (UALCAN) (14). **(C)** In metastasis, GON4L exhibiting an elevated expression might be a critical regulator of breast cancer progression (TNM-plot) (15).

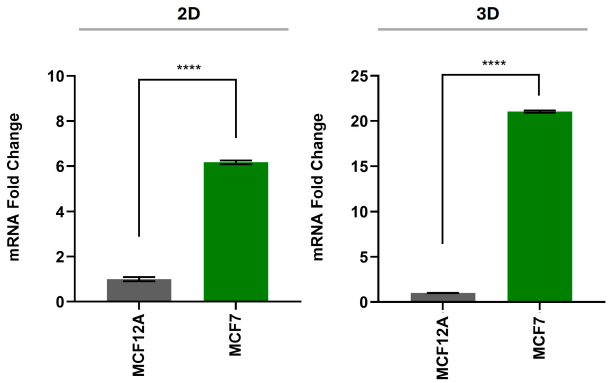


Figure 2: Endogenous gene expression of GON4L in MCF7 cells compared with non-tumorigenic MCF12A cells in 2D monolayered culture and 3D spheroid culture. RT-qPCR was performed to specify differential gene expression by analyzing candidate gene expression normalized to β-Actin housekeeping gene. GON4L expression in breast cancer cells was recorded as 6-fold in 2D and 20-fold in 3D (t-test:****p<0.0001).

cells (Figure 3C and Figure 3D). While control cells maintained stable proliferation, *GON4L*-knockdown cells showed a pronounced decline in relative abundance, falling below 20% over the course of the assay. Together, these findings demonstrate that GON4L is required for sustained proliferative capacity in MCF7 breast cancer cells under 2D culture conditions.

GON4L Is Required for 3D Spheroid Growth of MCF7 Cells

To examine the role of GON4L in tumor-like growth conditions, the proliferative capacity of *GON4L*-knockdown cells was assessed in 3D spheroid cultures. *GON4L* was targeted using the CRISPR-Cas9 system, and knockdown cells were subsequently cultured under 3D spheroid-forming conditions (Figure 4).

Consistent with observations in 2D monolayer cultures, loss of GON4L markedly impaired spheroid formation and growth in 3D culture. *GON4L* knockdown MCF7 cells formed fewer and smaller spheroids than non-targeting control cells (Figure 4A). Quantitative analysis confirmed a significant reduction in spheroid-forming efficiency and overall spheroid growth upon GON4L loss (Figure 4B and Figure 4C).

These findings demonstrate that GON4L is required for efficient tumor-like growth of MCF7 cells under 3D culture conditions.

Collectively, these findings highlight an important role for GON4L in supporting tumor-like growth under 3D culture conditions. In addition to impairing cellular proliferation, loss of GON4L disrupted spheroid integrity, indicating a requirement for GON4L in maintaining both proliferative capacity and structural organization in 3D environments. Given its reported function as a transcriptional repressor and chromatin-associated regulator, GON4L may contribute to the maintenance of oncogenic transcriptional programs in breast cancer cells. Although further studies are required to delineate the precise molecular pathways regulated by GON4L, the present findings suggest that perturbation of GON4L-dependent mechanisms may represent a potential strategy for limiting tumor growth in breast cancer.

DISCUSSION

In this study, GON4L, a putative transcriptional regulator (4), was identified as an important determinant of breast cancer cell proliferation under both 2D monolayer and 3D spheroid culture conditions. Our findings indicate that GON4L supports cellular fitness and growth in breast cancer cells, consistent with its elevated expression observed in breast cancer patient samples, which underscores its potential clinical relevance.

Functional analyses demonstrated that loss of GON4L resulted in a pronounced reduction in proliferative capacity in both short- and long-term assays performed under 2D culture conditions. Notably, this growth impairment was more pronounced in 3D spheroid cultures, suggesting that GON4L may be particularly important

for sustaining tumor-like growth in complex microenvironments. These observations are in line with previous studies showing that transcriptional regulators can exhibit context-dependent activity in 3D settings, where cell–cell and cell–matrix interactions fundamentally reshape gene regulatory programs (16). In 3D culture systems, altered chromatin organization and transcriptional accessibility have been reported, potentially creating distinct regulatory dependencies that are not obvious in conventional 2D models (17).

GON4L interacts with transcriptional and epigenetic corepressor complexes, including YY1, SIN3A, and HDAC1, suggesting a role in the repression of differentiation-associated or anti-proliferative gene programs (7). Disruption of these regulatory interactions may contribute to the impaired proliferative capacity and compromised structural integrity observed in GON4L-deficient spheroids. Moreover, the inability of GON4L-deficient breast cancer cells to maintain cohesive 3D architecture highlights a potential role for GON4L in

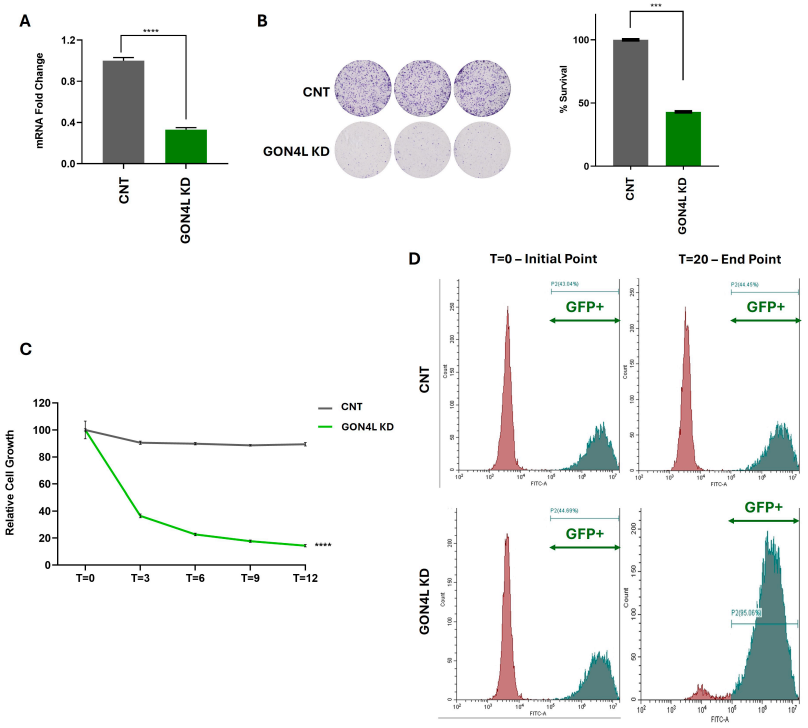


Figure 3: **GON4L targeting significantly prevents the proliferation of MCF7 cells.** **(A)** RT-qPCR to verify the knockdown status of MCF7. **(B)** Colony-forming ability and long-term proliferation capacity significantly declined upon GON4L targeting. **(C)** In a competition assay, GON4L loss in MCF7 short-term proliferation showed a significant decrease in which relative cell growth was reported to decrease to 15% at the end point. **(D)** Representative flow cytometry histograms showed that the GFP signal detected in T = 0 was highly close in the control (CNT) and GON4L knockdown groups, whereas the GFP signal in T = 20 was recorded with an elevated level in the GON4L targeted group (t-test: *** p<0.001, ****p<0.0001).

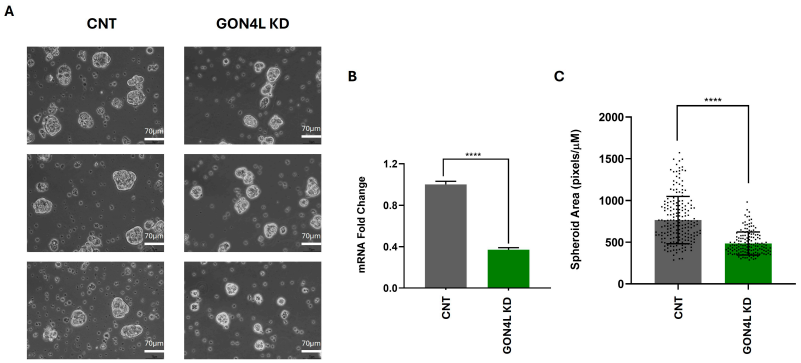


Figure 4: GON4L KD has a significant impact on 3D spheroid growth capacity of MCF7 cells. **(A)** Spheroid growth assay performed in MCF7 cells showed that the GON4L gene plays a crucial role in 3D spheroid formation. **(B)** RT-qPCR to verify the knockdown status of MCF7. **(C)** The area was attenuated upon GON4L blockage significantly, and a certain negative impact was observed on spheroid formation. Scale bar was 70 µm (t-test: ****p<0.0001).

coordinating transcriptional programs required for adaptation to tumor-like spatial organization.

Despite the functional impact observed upon GON4L targeting, several limitations of this study warrant acknowledgement. First, *GON4L* undergoes alternative splicing and produces multiple transcript isoforms; accordingly, the sgRNAs employed here may not effectively target all protein-coding variants. As a result, the observed reduction in *GON4L* mRNA levels most likely reflects partial transcript depletion rather than complete gene ablation, which is consistent with the significant yet incomplete decrease in transcript levels confirmed in our experiments. Second, GON4L protein levels were not directly assessed, which limits the ability to fully correlate transcriptional reduction with functional protein depletion. Third, emerging evidence highlights that transcript isoform diversity can carry distinct biological and clinical implications in breast cancer, with isoform-specific expression patterns potentially serving as more precise biomarkers than total gene expression levels. Although isoform-level characterization of GON4L in luminal breast cancer remains limited, its established role as a transcriptional corepressor interacting with chromatin-modifying complexes raises the possibility that individual transcript variants may differentially regulate downstream gene expression programs (6–8). Therefore, the contribution of specific GON4L isoforms to proliferation and 3D tumor architecture cannot be excluded and deserves dedicated investigation. Future studies incorporating isoform-specific targeting strategies and protein-level validation will be essential to more precisely define the mechanistic contribution of GON4L in breast cancer.

Taken together, our findings position GON4L as a functionally relevant transcriptional regulator in luminal breast cancer, required for both proliferative capacity and structural organization maintenance under tumor-mimicking conditions. While further studies are necessary to define the downstream gene networks controlled by GON4L, the present data suggest that perturbation of GON4L-dependent regulatory mechanisms may limit tumor growth. Future investigations focusing on GON4L-regulated transcriptional programs and their relevance in clinical breast cancer samples will be essential to clarify its potential value as a therapeutic target or biomarker.

Ethics Committee Approval: Ethical approval was not required, as the study involved only commercial cell lines in an *in vitro* model with no human or animal subjects.

Peer Review: Externally peer-reviewed.

Author Contributions: Conception/Design of study: G.K., H.Ö.; Data Acquisition: G.K., H.Ö.; Data Analysis/Interpretation: G.K., H.Ö.; Drafting Manuscript: G.K., H.Ö.; Critical Revision of Manuscript: G.K.; Final Approval and Accountability: G.K.

Conflict of Interest: The authors have no conflict of interest to declare.

Financial Disclosure: This publication has been produced benefiting from the 2232 International Fellowship for Outstanding Researchers Program of TÜBİTAK (Project No: 118C261).

Author Details

Hande Özkan

[1] Koç University Research Center for Translational Medicine (KUTTAM), İstanbul, Türkiye

0009-0007-1611-2268

Gözde Korkmaz

[1] Koç University Research Center for Translational Medicine (KUTTAM), İstanbul, Türkiye

[2] Koç University, School of Medicine, Department of Medical Sciences, İstanbul, Türkiye

0000-0002-3574-1015 gkorkmaz@ku.edu.tr

REFERENCES

1. Siegel RL, Kratzer TB, Giaquinto AN, Sung H, Jemal A. Cancer statistics, 2025. CA Cancer J Clin 2025; 75(1): 10-45.
2. Harbeck N, Penault-Llorca F, Cortes J, Gnant M, Houssami N, Poortmans P, et al. Breast cancer. Nat Rev Dis Primers 2019; 5(1): 66.
3. Harbeck N, Gnant M. Breast cancer. Lancet 2017; 389(10074): 1134-50.
4. Colgan DF, Goodfellow RX, Colgan JD. The transcriptional regulator GON4L is required for viability and hematopoiesis in mice. Exp Hematol 2021; 98: 25-35.
5. Williams MLK, Sawada A, Budine T, Yin C, Gontarz P, Solnica-Krezel L. Gon4l regulates notochord boundary formation and cell polarity underlying axis extension by repressing adhesion genes. Nat Commun 2018; 9(1): 1319.
6. Tsai SM, Chu KC, Jiang YJ. Newly identified Gon4l/Udu-interacting proteins implicate novel functions. Sci Rep 2020; 10(1): 14213.
7. Lu P, Hankel IL, Hostager BS, Swartzendruber JA, Friedman AD, Brenton JL, et al. The developmental regulator protein Gon4l associates with protein YY1, co-repressor Sin3a, and histone deacetylase 1 and mediates transcriptional repression. J Biol Chem 2011; 286(20): 18311-19.
8. Agarwal N, Dancik GM, Goodspeed A, Costello JC, Owens C, Duex JE, et al. GON4L drives cancer growth through a YY1-androgen receptor-CD24 axis. Cancer Res 2016; 76(17): 5175-85.
9. Bloise N, Giannaccari M, Guagliano G, Peluso E, Restivo E, Strada S, et al. Growing role of 3D in vitro cell cultures in the study of cellular and molecular mechanisms: short focus on breast cancer, endometriosis, liver and infectious diseases. Cells 2024; 13(12): 1054.
10. Habanjar O, Diab-Assaf M, Caldefie-Chezet F, Delort L. 3D cell culture systems: tumor application, advantages, and disadvantages. Int J Mol Sci 2021; 22(22): 12200.
11. Barbosa MAG, Xavier CPR, Pereira RF, Petrikaitė V, Vasconcelos MH. 3D cell culture models as recapitulators of the tumor microenvironment for the screening of anti-cancer drugs. Cancers (Basel) 2022; 14(1): 190.
12. Sanjana NE, Shalem O, Zhang F. Improved vectors and genome-wide libraries for CRISPR screening. Nat Methods 2014; 11(8): 783-4.
13. Shalem O, Sanjana NE, Hartenian E, Shi X, Scott DA, Mikkelson T, et al. Genome-scale CRISPR-Cas9 knockout screening in human cells. Science 2014; 343(6166): 84-7.
14. Chandrashekar DS, Karthikeyan SK, Korla PK, Patel H, Shovon AR, Athar M, et al. UALCAN: an update to the integrated cancer data analysis platform. Neoplasia 2022; 25: 18-27.
15. Bartha Á, Győrffy B. TNMplot.com: a web tool for the comparison of gene expression in normal, tumor and metastatic tissues. Int J Mol Sci 2021; 22(5): 2622.
16. Özkan H, Öztürk DG, Korkmaz G. Transcriptional factor repertoire of breast cancer in 3D cell culture models. Cancers (Basel) 2022; 14(4): 1023.
17. Pampaloni F, Reynaud EG, Stelzer EHK. The third dimension bridges the gap between cell culture and live tissue. Nat Rev Mol Cell Biol 2007; 8(10): 839-45.

İSTANBUL UNIVERSITY PRESS

Experimed 2026, 16 (2): 114–119

https://doi.org/10.26650/experimed.1887002

Submitted: 11.02.2026
Revision Requested: 22.04.2026
Last Revision Received: 23.04.2026
Accepted: 25.05.2026
Published Online 12.08.2026

Experimed

Research Article

Open Access

Role of HLA-B Leader Peptides and HLA-E Genetic Variants in HIV Infection

Yeliz Öğret [1], Çiğdem Kekik Çınar [1], Arif Atahan Çağatay [2], Hayriye Şentürk Çiftçi [1], Kürşat Özdilli [3] & Fatma Savran Oğuz [1]

[1] Istanbul University, Istanbul Faculty of Medicine, Department of Medical Biology, İstanbul, Türkiye
[2] Istanbul University, Istanbul Faculty of Medicine, Department of Internal Medicine, Division of Infectious Disease, İstanbul, Türkiye
[3] Medipol University, Medipol Faculty of Medicine, Department of Medical Biology, İstanbul, Türkiye

Abstract

Objective: This study assessed whether human leukocyte antigen (HLA)-B signal peptide dimorphism at position -21 (HLA-B-21) Methionine/Threonine (M/T) and HLA-E polymorphisms are associated with the level of viremia in human immunodeficiency virus (HIV)-positive individuals from the Turkish population.

Materials and Methods: The study cohort comprised 130 HIV–positive patients and 102 healthy controls. HLA typing was achieved through a next-generation sequencing (NGS)–based approach, and HLA-E alleles were determined by Sanger sequencing. HIV-1 level of viremia was measured using the COBAS Ampliprep/TaqMan system. Statistical evaluation included chi-square analysis, nonparametric techniques, and logistic regression modeling.

Results: HLA-E*01:01 and the homozygous E*01:01 genotype were observed significantly more frequently in HIV–positive patients than in controls. No significant relationship was found between HLA-E alleles and viral load. The HLA-B*51:01 allele was significantly more frequent in patients with a higher viral load, whereas HLA-B*44:02 showed a similar trend without reaching statistical significance. In addition, the HLA-B-21 T/T genotype was significantly associated with higher viral load levels.

Conclusion: Our findings indicate that the HLA-B-21 signal peptide polymorphism may play a role in modulating HIV replication, whereas HLA-E polymorphisms alone appear to have a limited impact. This study provides novel immunogenetic data from the Turkish population and highlights the potential of HLA-B-21 polymorphism as a genetic marker influencing HIV disease progression.

Keywords HIV · HLA-B Signal Peptide · HLA-E Polymorphism · Viral Load

Citation: Öğret, Y., Kekik Çınar, Ç., Çağatay, A. A., Şentürk Çiftçi, H., Özdilli, K. & Savran Oğuz, F. Role of HLA-B Leader Peptides and HLA-E Genetic Variants in HIV Infection. Experimed 2026; 16(2): 114-119. DOI: 10.26650/experimed.1887002

This work is licensed under Creative Commons Attribution-NonCommercial 4.0 International License.

© 2026. Öğret, Y., Kekik Çınar, Ç., Çağatay, A. A., Şentürk Çiftçi, H., Özdilli, K. & Savran Oğuz, F.

Corresponding author: Yeliz Öğret yelizdogret@gmail.com

INTRODUCTION

The immune system's ability to control human immunodeficiency virus (HIV) infection is influenced by various immunogenetic factors, particularly those involving major histocompatibility complex (MHC) genes. MHC genes play a central role in presenting foreign peptides to immune cells, and among them, human leukocyte antigen (HLA)-B alleles are particularly critical due to their effect on HIV progression and immune response.

Viral peptides are presented to $CD8^+$ T cells via HLA class I molecules, ensuring that infected cells are destroyed. Natural killer (NK) cells also recognize and eliminate virus-infected cells that do not have the appropriate HLA class I molecules. Among the HLA class I genes, HLA-B is the most polymorphic and has a strong impact on $CD4^+$ T cell counts, viral set point, and consequently the rate of progression to acquired immune deficiency syndrome (AIDS) (1).

The presentation of peptide (9-mer, 3-11 amino acids) epitopes derived from the signal sequences of classical HLA-B molecules is accomplished by HLA-E, a non-classical HLA class I molecule (2, 3). After being transported to the cell surface, the HLA-E/peptide complex engages CD94/NKG2 receptors on NK cells (4). The affinity of the inhibitory NKG2A receptor for the HLA-E-bound peptide is higher than that of the NKG2C receptor (activator) (5-7). Several viruses (HIV-1, cytomegalovirus, etc.) utilize the HLA-E-mediated pathway to escape NK cell-mediated death.

Among the 27 alleles of the HLA-E, HLA-E*01:01 and E*01:03 have been associated with immune function (8). The HLA-E*01:03 allele has been associated with enhanced surface display and improved stability relative to HLA-E*01:01. This difference may result in a more efficient inhibitory function on interaction with the NKG2A receptor, ultimately leading to distinct responses of NK cells to each of these ligands (9).

Two variants are defined by the amino acid present at position 2 (P2) of the 21-residue HLA-B signal peptide—either methionine (P2-M) or threonine (P2-T), resulting in differential interactions with CD94/NKG2 receptors (10, 11). As a result of this polymorphism, three HLA-B P2 genotypes (M/M, M/T, and T/T) are formed. The substitution of P2-M with P2-T leads to labile HLA-E display on the cell surface (12). Studies from two African cohorts have shown that the P2-T variant plays a significant role in immune activation, whereas the presence of P2-M has no effect on the spread of HIV-1 infection. The same studies found that NK-mediated cytolysis was significantly increased in carriers of the P2-T allele (13, 14).

In light of these findings, we aimed to investigate the association between HLA-B signal peptide variants, HLA-E polymorphisms, and viral load in HIV–positive individuals.

MATERIALS AND METHODS

Study Groups

Our study included 130 HIV–positive patients who were presented to the Istanbul Faculty of Medicine, Department of Infectious Diseases and Clinical Microbiology, and 102 healthy volunteers (control group). HIV positivity and level of viremia in the patients were analyzed in the Microbiology Department. Quantitative HIV-1 RNA testing was performed using the COBAS Ampliprep/TaqMan system (Roche Diagnostics, USA). The kit's detection range was between 20 and 10,000,000 copies/mL. The research was reviewed and approved by the Istanbul University, Istanbul Faculty of Medicine, Clinical Research Ethics Committee (Approval No: 2019/246).

Methods

DNA extraction from whole blood was performed using the Qiagen EZ-1 DNA isolation device (Qiagen, Hilden, Germany) and the Qiagen Blood Mini Kit (Qiagen, Hilden, Germany) for both patients and volunteer donors. The HLA typing of the study groups was evaluated using the Illumina MiSeq Sequencing System (Illumina, Inc., San Diego, CA, USA), Omixon Holotype HLA™ analysis (Omixon, Budapest, Hungary), and Omixon HLA Twin software (Omixon, Budapest, Hungary). The change at position 21 of the HLA-B leader peptide (Threonine (T) or Methionine (M)) was confirmed using the tool available at https://www.ebi.ac.uk/ipd/imgt/hla/matching/. Genotypic discrimination between the two HLA-E alleles was performed by Sanger sequencing using TBG HLA-E primers (Texas BioGene, Inc., Richardson, Texas, USA). The results were evaluated using AccuType software (TBG Diagnostics Limited/TBG Biotechnology Corp., Taipei, Taiwan).

Statistical Analyses

Data were analyzed using SPSS version 21.0 software (IBM Corporation, Armonk, NY, USA). p-values were calculated using Yates's correction or Fisher's exact test. The level of viremia was assessed by determining whether the HIV RNA amount was less than or greater than 10,000 copies/mL, and its relationship with HLA-E, M/T frequencies was examined using the chi-square test. Since the level of viremia values did not follow a normal distribution, the relationship between HLA-E, M/T parameters, and viremia levels was compared using nonparametric Kruskal-Wallis analysis. A p-value below 0.05 was considered statistically significant.

RESULTS

Among the 130 HIV–positive patients included in the study, 115 were male and 15 were female, with a mean age of 38.76 years. Of the 102 healthy volunteers in the control group, 46 were male and 56 were female, with a mean age of 28.78 years.

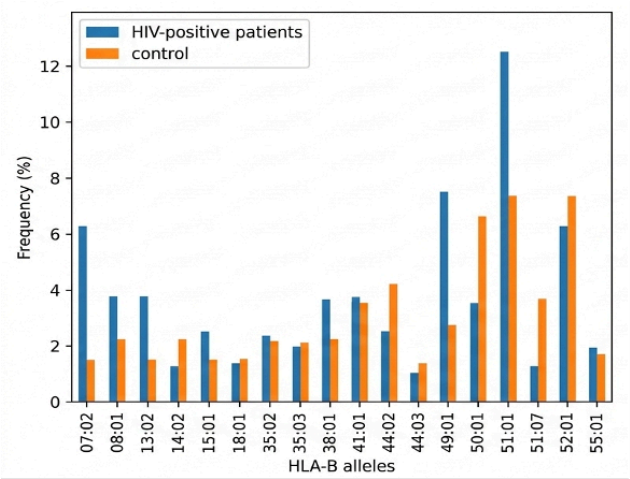


Figure 1. Distribution of HLA-B alleles in HIV-positive patients and healthy controls

In the statistical comparison of HLA allele distributions, the HLA-B*52:01 allele was observed at a higher frequency in the HIV-positive patient group compared to the control group (9/260 vs. 2/204, p=0.123, odds ratio (OR)=3.62). Conversely, the HLA-B*49:01 (8/260 vs. 12/204, p=0.169, OR=0.51) and HLA-B*27:02 (1/260 vs. 4/204, p=0.174, OR=0.19) alleles were observed at higher frequencies in the control group compared to the patient group. Furthermore, the HLA-B*15:08 and HLA-B*53:01 alleles were found exclusively in the control group (2/204) and were not identified in HIV-positive patients (p=0.193) (Figure 1).

The distribution of HLA-E*01:01 and HLA-E*01:03, as well as the -21T and -21M alleles, was in Hardy–Weinberg equilibrium. When HLA-E alleles were evaluated in both groups, the E*01:01 allele was found to be statistically more common in the patient group (p=0.013). However, T and M dimorphisms at position 21 within HLA-B showed no significant difference in distribution between the study groups. When the HLA-E genotype was evaluated, the E*01:01/*01:01 genotype was significantly more common in HIV patients (p=0.037), but no statistical significance was observed for the signal peptide dimorphism genotypes.

Viral load data were available for 108 patients. Analysis of HLA-B allele distribution across low and high viral load categories showed the alleles were more frequently observed in the higher viral load group (Table 1). In particular, the HLA-B*51:01 allele was significantly more frequent in the high viral load group (OR=4.66, p=0.0049). Similarly, the HLA-B*44:02 allele showed a higher frequency in the high viral load group (OR=3.87), although this did not reach statistical significance (p=0.054) (Figure 2). On the other hand, the HLA-B*35:03 allele was also observed more frequently in the high viral load group (n=10 vs. n=5, respectively); however, this difference was not statistically significant (p=0.211). No significant relationship was found between the level of viremia and the patients' HLA-E or P2 alleles. However, the signal peptide T/T genotype was significantly more common in patients with a high level of viremia (p=0.025), whereas no statistical significance was found for the HLA-E genotype. When comparing the level of viremia medians with HLA-E and T/M homozygosity and heterozygosity, borderline insignificance was observed. Nevertheless, the median level of viremia in patients with the T/T homozygous genotype was higher than in those with T/M or M/M genotypes.

Table 1. Distribution of HIV-positive patients according to viral load category

Viral load category	n (%)
<10,000 copies/mL (low viral load)	40 (37.03)
≥10,000 copies/mL (high viral load)	68 (62.96)
Total	108 (100.00)

Logistic regression analysis showed no significant relationship between the level of viremia (cutoff: 10,000 copies/mL) and gender (p=0.999), HLA-E (p=0.959), or M/T genotype (p=0.982).

DISCUSSION

In our study, the effects of HLA class I and class II alleles on viral load in HIV–positive individuals were analyzed in detail. Notably, the HLA-B*51:01 allele was observed at a significantly higher frequency in the high-level viremia category. This finding suggests that the B*51:01 allele may be insufficient in controlling HIV replication and may represent a genetic background that supports disease progression. However, the underlying immunogenetic mechanisms of this association remain unclear (15). Similarly, the HLA-B*44:02 allele was also more common in the high-level viremia category, with a p-value approaching statistical significance. This observation indicates that the B*44:02 allele may also play a disadvantageous role in the control of HIV infection. Both alleles have been associated with similar trends in previous studies conducted in different ethnic groups; however, the results have been inconsistent due to population-specific differences (16). Therefore, validation of the present findings in larger, multicenter studies is warranted.

In particular, studies conducted in Asian and Mediterranean populations have suggested that HLA-B*51:01 may be associated with more rapid disease progression. In this respect, our study represents one of the few investigations in Türkiye confirming a similar pattern among HIV–positive individuals. These findings support the hypothesis that certain HLA alleles can influence viral replication dynamics in HIV infection and suggest that HLA-B*51:01 and HLA-B*44:02, in particular, should be further investigated as potential immunogenetic markers of disease progression.

It is well established that HIV replication is regulated by epigenetic and transcriptional mechanisms. In this context, our study specifically evaluated the association between HLA-B-21 (T/M) polymorphism and viral load. According to our results, the T/T genotype was significantly more frequent in patients with higher levels of viremia, suggesting a potential association with less

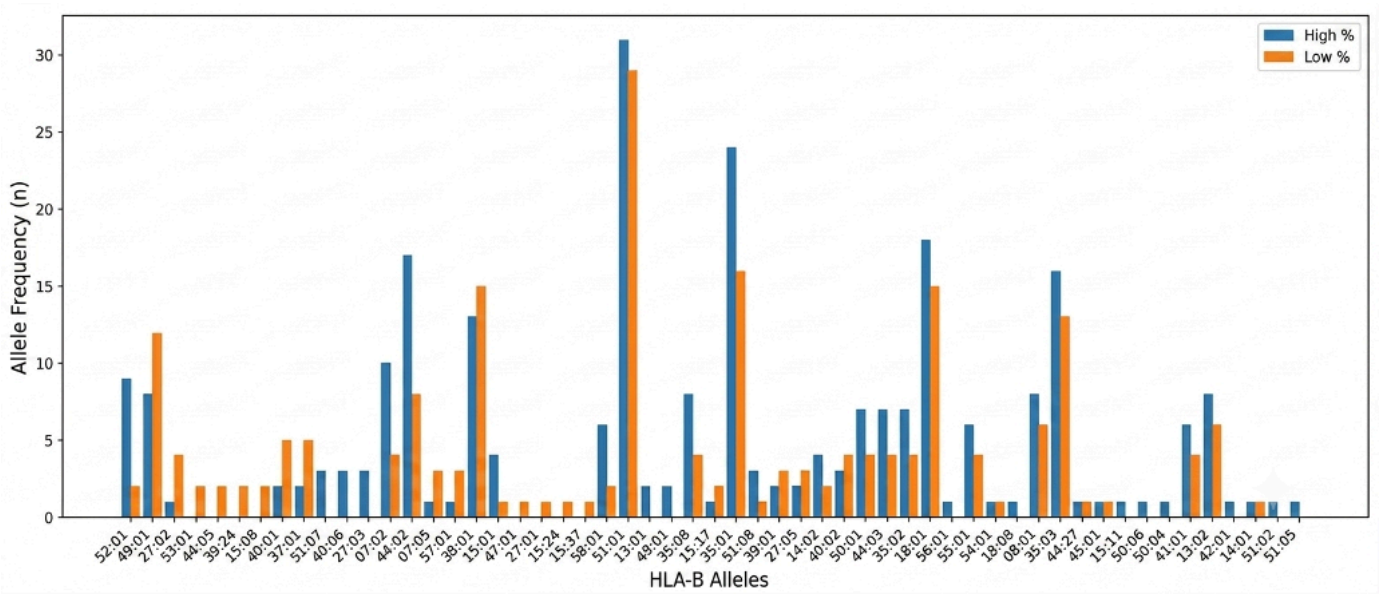


Figure 2. Distribution of HLA-B alleles according to HIV viral load categories.

effective viral control. Although previous studies have suggested that the HLA-B-21 polymorphism may influence immune responses, the exact mechanisms linking this polymorphism to HIV replication remain unclear. Therefore, our findings should be interpreted cautiously and require further functional validation (17). In contrast, the T/M genotype may weaken this control. These findings highlight the potential of HLA-B-21 as a genetic marker during HIV infection.

HLA-E*01:01/01:03 genotypes and Bw4/Bw6 variants are of particular interest in HIV research because of their effects on NK cell responses and antigen presentation. However, in our study, no statistically significant differences were observed between the low and high levels of viremia for either system. These results suggest that these genotypes, on their own, do not exert a decisive influence on the level of viremia control, or that their effects may manifest only in more specific immune profiles (18). International studies on Bw4/Bw6 variants and HLA-E polymorphisms have reported that their influence on HIV progression is limited or variable across individuals (18, 19). Consistent with these contradictory findings, our study did not identify significant differences in these variants.

A major advantage of this investigation is the systematic analysis of important genetic factors in HIV, including HLA-B, HLA-E, and HLA-B-21, within a single patient cohort. Nevertheless, the sample size may have been insufficient to evaluate certain alleles at statistically significant levels. Interpretations regarding rare genotypes, in particular, should therefore be made cautiously. Furthermore, no functional immune response measurements (such as NK cell activity or CTL responses) were performed in parallel with the genetic analyses.

This study is one of the first to comprehensively investigate the relationship between HIV infection and HLA/HLA-B-21 genotypes in the Turkish population. To date, the association between HLA distribution and HIV disease course has not been examined in such detail in this region. Moreover, this work is among the rare studies to demonstrate a statistically significant relationship between the HLA-B-21 T/M polymorphism and the level of viremia. These findings are noteworthy in demonstrating the link between genetic markers and immune control mechanisms. In addition, by separately analyzing both low and high levels of viremia category, the relationship between genotypes and disease progression could be addressed more clearly. In this regard, our study provides a cross-sectional analysis and offers meaningful stratification according to clinical classification.

CONCLUSION

In this study, the relationship between viral load and, HLA-I and II alleles, as well as HLA-B-21 T/M genotypes, was evaluated for the first time in a comprehensive manner specifically within the Turkish population. The findings indicate the genetic markers may influence HIV replication and disease progression.

Notably, the HLA-B*51:01 and B*44:02 alleles were more frequently observed in the high-level viremia category, suggesting that these alleles may confer a disadvantage in the control of HIV infection. In contrast, no significant differences were detected for Bw4/Bw6 variants or HLA-E*01:01/01:03 genotypes. One of the most striking findings was the association between the HLA-B-21 T/M polymorphism and viral load. The HLA-B-21 T/T genotype was significantly more frequent in patients with higher levels of viremia, suggesting a potential role in less effective viral control. Overall, these results provide valuable insights into the influence of genetic factors on the course of HIV infection. They may contribute to the development of genetically based predictions for personalized

treatment strategies and immunotherapies. However, validation of these associations will require larger cohorts and further molecular studies supported by functional analyses.

Limitations

In addition to the small sample size, potential confounding factors such as variability in antiretroviral therapy, duration of infection, and disease stage may have influenced the results. Larger studies are needed to confirm these findings and further investigate the role of HLA-E polymorphisms in viral load regulation. In addition, important clinical variables were not consistently available due to the retrospective design of the study. The absence of these variables may have influenced viral load measurements and limited the ability to perform fully adjusted analyses. Furthermore, no formal power analysis was conducted before the study, and subgroup analyses may be underpowered.

Informed Consent	Written consent was obtained from all patients.
Ethics Committee Approval	The study was approved by the Istanbul University Istanbul Medical Faculty Clinical Research Ethics Committee, Türkiye (2019/246).
Peer Review	Externally peer-reviewed.
Author Contributions	Conception/Design of Study- Y.Ö., Ç.K.Ç., F.S.O.; Data Acquisition- Y.Ö., A.A.Ç., K.Ö.; Data Analysis/Interpretation- Y.Ö., Ç.K.Ç., H.S.Ç.; Drafting Manuscript- Y.Ö. ,Ç.K.Ç.; Critical Revision of Manuscript- Ç.K.Ç., F.S.O., A.A.Ç.; Final Approval and Accountability- Y.Ö., Ç.K.Ç., A.A.Ç., H.S.Ç., K.Ö., F.S.O.
Conflict of Interest	The authors have no conflict of interest to declare.
Financial Disclosure	This publication has been produced benefiting from the 2232 International Fellowship for Outstanding Researchers Program of TÜBİTAK (Project No: 118C261).

Author Details

Yeliz Öğret
[1] Istanbul University, Istanbul Faculty of Medicine, Department of Medical Biology, İstanbul, Türkiye
0000-0001-9732-5474 yelizdogret@gmail.com

Çiğdem Kekik Çınar
[1] Istanbul University, Istanbul Faculty of Medicine, Department of Medical Biology, İstanbul, Türkiye
0000-0003-2098-381X

Arif Atahan Çağatay
[2] Istanbul University, Istanbul Faculty of Medicine, Department of Internal Medicine, Division of Infectious Disease, İstanbul, Türkiye
0000-0002-3051-8199

Hayriye Şentürk Çiftçi
[1] Istanbul University, Istanbul Faculty of Medicine, Department of Medical Biology, İstanbul, Türkiye
0000-0001-5160-5227

Kürşat Özdilli
[3] Medipol University, Medipol Faculty of Medicine, Department of Medical Biology, İstanbul, Türkiye
0000-0002-7129-5024

Fatma Savran Oğuz
[1] Istanbul University, Istanbul Faculty of Medicine, Department of Medical Biology, İstanbul, Türkiye
0000-0002-6018-8936

REFERENCES

1. Singh P, Kaur G, Sharma G, Mehra NK. Immunogenetic basis of HIV-1 infection, transmission and disease progression. Vaccine 2008; 26(24): 2966-80.
2. Lemberg MK, Bland FA, Weihofen A, Braud VM, Martoglio B. Intramembrane proteolysis of signal peptides: an essential step in the generation of HLA-E epitopes. J Immunol 2001; 167(11): 6441-6.
3. Bland FA, Lemberg MK, McMichael AJ, Martoglio B, Braud VM. Requirement of the proteasome for trimming of signal peptide-derived epitopes presented by HLA-E. J Biol Chem 2003; 278(36): 33747-52.
4. Kapp K, Schrempf S, Lemberg MK, Dobberstein B. Post-targeting functions of signal peptides. In: Madame Curie Biosci Database [Internet]. Austin (TX): Landes Bioscience; 2000-13.
5. Petrie EJ, Clements CS, Lin J, Sullivan LC, Johnson D, Huyton T, et al. CD94-NKG2A recognition of HLA-E bound to an HLA class I leader sequence. J Exp Med 2008; 205(3): 725-35.
6. Kaiser BK, Barahmand-Pour F, Paulsene W, Medley S, Geraghty DE, Strong RK. Interactions between NKG2x immunoreceptors and HLA-E ligands display overlapping affinities and thermodynamics. J Immunol 2005; 174(5): 2878-84.
7. Valés-Gómez M, Reyburn HT, Erskine RA, López-Botet M, Strominger JL. Kinetics and peptide dependency of the binding of the inhibitory NK receptor CD94/NKG2-A and the activating receptor CD94/NKG2-C to HLA-E. EMBO J 1999; 18(15): 4250-60.
8. Hannoun Z, Lin Z, Brackenridge S, Kuse N, Akahoshi T, Borthwick N, et al. Identification of novel HIV-1-derived HLA-E-binding peptides. Immunol Lett 2018; 202: 65-72.
9. Hosseini E, Minagar A, Ghasemzadeh M, Arabkhazaeli A, Ghasemzadeh A. HLA-E01:01 genotype confers less susceptibility to COVID-19, while HLA-E01:03 genotype is associated with more severe disease. Hum Immunol 2023; 84(4): 263-71.
10. Llano M, Lee N, Navarro F, García P, Albar JP, Geraghty DE et al. HLA-E-bound peptides influence recognition by inhibitory and triggering CD94/NKG2 receptors: preferential response to an HLA-G-derived nonamer. Eur J Immunol 1998; 28(9): 2854-63.
11. Fellay J, Shianna KV, Ge D, Colombo S, Ledergerber B, Weale M, et al. A whole-genome association study of major determinants for host control of HIV-1. Science 2007; 317(5840): 944-7.
12. Pereyra F, Jia X, McLaren PJ, Telenti A, de Bakker PI, Walker BD, et al. The major genetic determinants of HIV-1 control affect HLA class I peptide presentation. Science 2010; 330(6010): 1551-7.
13. Merino AM, Sabbaj S, Easlick J, Goepfert P, Kaslow RA, Tang J. Dimorphic HLA-B signal peptides differentially influence HLA-E- and natural killer cell-mediated cytolysis of HIV-1-infected target cells. Clin Exp Immunol 2013; 174(3): 414-23.
14. Borrego F, Ulbrecht M, Weiss EH, Coligan JE, Brooks AG. Recognition of HLA-E complexed with HLA class I signal sequence-derived peptides by CD94/NKG2 confers protection from NK cell-mediated lysis. J Exp Med 1998; 187(5): 813-8.
15. Kawashima Y, Pfafferott K, Frater J, Matthews P, Payne R, Addo M, et al. Adaptation of HIV-1 to human leukocyte antigen class I. Nature 2009; 458(7238): 641-5.
16. Cubillos Angulo JM, Castro Cuesta TA, Menezes EP, Pedroso C, Brites C. Influence of HLA-B polymorphisms on HIV-1 mother-to-child transmission: a systematic review. Braz J Infect Dis 2019; 23(1): 53-59.
17. Allouch A, David A, Amie SM, Lahouassa H, Chartier L, Margottin-Goguet F, et al. p21-mediated restriction of HIV-1 in monocyte-derived dendritic cells. J Virol 2013; 87(1): 339-51.

18. Davis ZB, Diedrich CR, Behrens GA, Claas FH. A conserved HIV-1-derived peptide presented by HLA-E renders infected T cells susceptible to attack by NKG2A/CD94-expressing NK cells. PLoS Pathog 2016; 12(2): e1005541.

19. Leslie A, Matthews PC, Listgarten J, Carlson JM, Kadie C, Ndungu T, et al. Additive contribution of HLA class I alleles in immune control of HIV-1 infection. J Virol 2010; 84(19): 9879-88.

İSTANBUL UNIVERSITY PRESS

Experimed 2026, 16 (2): 120–127

https://doi.org/10.26650/experimed.1949327

Submitted: 11.05.2026
Revision Requested: 23.05.2026
Last Revision Received: 24.05.2026
Accepted: 01.07.2026
Published Online 12.08.2026

Experimed

Research Article

Open Access

Clinical Outcomes of Cable Grip Plate–Cable Grip Constructs in the Management of Femoral Intertrochanteric Fractures

Ömer Yonga [1], Behiç Çelik [1] & Faik Altıntaş [1]

[1] Yeditepe University, Faculty of Medicine, Department of Orthopedics and Traumatology, İstanbul, Türkiye

Abstract

Objective: This study aimed to compare functional outcomes, complication rates, and perioperative parameters of Cable Grip Plate and Grip Cable techniques for greater trochanter fixation in elderly patients undergoing partial hip replacement for intertrochanteric femur fractures.

Materials and Methods: This study included 82 patients aged > 60 years treated between January 2020 and December 2023. Greater trochanter fixation was performed using a cable grip plate (n=45) or a grip cable system (n=37). Demographics, operative time, intraoperative blood loss, early and late complications, revision rates, functional outcomes (Harris Hip Score (HHS), Parker Mobility Score (PMS), Visual Analog Scale (VAS)), and walking aid use were compared between groups.

Results: Operative time and blood loss were significantly higher in the cable grip plate group (p=0.001 and p<0.001, respectively). Nevertheless, this group demonstrated superior functional outcomes, including higher HHS (82.7 ± 4.8 vs 79.6 ± 5.5, p=0.008), improved PMS (p=0.006), lower VAS scores (p=0.032), and earlier return to activities of daily living (p=0.009). Late complications were more frequent in the Grip Cable group (p=0.030), whereas revision rates and mortality were similar.

Conclusion: Despite longer operative time and increased blood loss, cable grip plate fixation was associated with better functional recovery and fewer late complications, supporting its use for greater trochanter stabilization in this population.

Keywords Intertrochanteric Fractures · Hip Arthroplasty · Cable Grip System · Trochanteric Fixation · Biomechanical Stability

Citation: Yonga, Ö., Çelik, B. & Altıntaş, F. Clinical Outcomes of Cable Grip Plate–Cable Grip Constructs in the Management of Femoral Intertrochanteric Fractures. Experimed 2026; 16(2): 120-127. DOI: 10.26650/experimed.1949327

This work is licensed under Creative Commons Attribution-NonCommercial 4.0 International License.

© 2026. Yonga, Ö., Çelik, B. & Altıntaş, F.

Corresponding author: Ömer Yonga omer_yonga@hotmail.com

INTRODUCTION

Intertrochanteric femur fractures are common, especially in the elderly population and can be challenging to treat. Partial hip replacement is frequently preferred in the treatment of these fractures, especially in patients with osteoporotic bone structure. Insufficient fixation of the greater trochanter is the most significant clinical challenge in this process (1).

Among the modern methods used in greater trochanter fixation, cable systems and plate combinations are prominent (2). These systems have been developed to support early mobilization and functional recovery. Cable grip plate systems promise greater stability, while grip cables maintain their status as a less invasive option thanks to innovations in this system (3, 4). However, when both patient- and cadaver-focused studies are examined, uncertainty persists regarding the superiority of one technique over the other.

The number of studies comparing the effectiveness of two different methods on patient functionality is quite limited, considering the complexity of the methodology. Most existing studies focus on a single technique or include small patient groups. Considering that these patients requiring greater trochanter fixation are elderly and osteoporotic, the standardization of factors affecting complications and the need for revision also limits the homogeneity of the studies (5).

One important point to consider when examining the success of trochanteric fixation methods is their effect on both short- and long-term functionality. Validated functional outcome measures — including composite scoring systems, such as the Harris Hip Score (HHS) and Parker Mobility Score (PMS), as well as pain scales, such as the Visual Analogue Scale (VAS)— are the most commonly used to assess recovery after trochanteric fixation (6). Return to activities of daily living is an additional clinically meaningful end point. Our main hypothesis was that the cable grip plate system would provide better functional results (HHS and PMS) and lower implant complication rates by providing a more stable fixation.

In this retrospective comparative study, we aimed to compare the clinical results of two different methods (Cable Grip Plate and Grip Cable) used for greater trochanter fixation in patients undergoing partial hip replacement for intertrochanteric femur fracture. In addition, the comparison of both techniques in terms of surgical parameters (operation time and amount of bleeding) was among the secondary objectives of the study.

MATERIALS AND METHODS

Patient Selection and Sampling

Between January 2020 and December 2023, patients who underwent partial hip replacement for femoral intertrochanteric fracture in our clinic and used Cable Grip Plate (Figure 1) or Grip Cable (Figure 2) for greater trochanter fixation were included in the study.



Figure 1. Patient x-ray with cable grip plate applied.

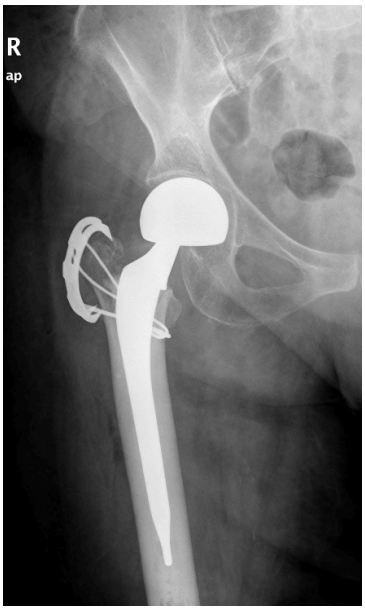


Figure 2. Patient x-ray with a grip cable applied.

Patients with at least one year of follow-up, over 60 years of age, who had fractures due to low-energy trauma on osteoporotic ground were evaluated. Patients with pathologic fractures, fractures caused by high-energy trauma, previously operated on the same hip, neurologic deficits, and patients who did not complete the follow-up were excluded from the study.

This retrospective comparative study was conducted in accordance with the Declaration of Helsinki approved by the Yeditepe University Non-Interventional Clinical Research Ethics Committee (Date: Dec 13, 2024, No: E.83321821-805.02.03-509), with informed consent obtained from all participants.

Surgical Technique

All surgical procedures were performed under general or spinal anesthesia under sterile conditions in the lateral decubitus position, by the same experienced orthopedic surgeons. For antibiotic prophylaxis, 1 gram of cefazolin sodium was administered intravenously 30 minutes before surgery. A posterolateral approach with Gibson incision was preferred. The fascia lata was opened longitudinally after the skin-subcutaneous layer was passed. Gluteus maximus fibers were separated, and the capsule was reached by preserving the external rotator muscles.

Femoral stem placement was performed in all patients. Calcar-supported or unsupported prosthesis systems were selected according to bone quality and anatomic features of the patient. After prosthesis placement, greater trochanter fixation was started. Patients were divided into two groups according to the fixation method used by the treating surgeon: 45 patients received cable grip plate fixation and 37 patients received grip cable fixation.

In the cable grip plate group, a plate suitable for the size of the patient's femur was selected and placed, and at least one and at most three cable grips were applied to the proximal and distal parts. In the Grip Cable group, fixation was provided only with cable systems without using a plate. In both groups, each cable was stretched with a standard torque of 50 Newton-meters using a special tensioning device to ensure optimum stability. After hemostasis control, one hemovac drain was placed, and the folds were closed in anatomical plane(s).

Postoperative Follow-up

In the postoperative follow-up of the patients, a standardized rehabilitation program was applied according to the protocols recommended in the literature and our clinical experience. In-bed isometric quadriceps and active-assistive hip exercises were started on the first postoperative day. Patients were mobilized with walker support under the guidance of a physiotherapist according to pain tolerance. Low-molecular-weight heparin (enoxaparin 40 mg/day subcutaneously) was administered for deep vein thrombosis prophylaxis until the 30th day after discharge. After discharge, patients were called for follow-up visits at 2nd, 6th, and 12th weeks and 6th and 12th months in accordance with the follow-up protocol recommended in the literature. Radiological evaluation was performed by taking standard anteroposterior and lateral hip radiographs at each visit. In addition, validated scoring systems were used for functional evaluation at each visit.

Evaluation Parameters

The evaluation parameters used in our study were determined based on similar studies in the literature. Demographic data (age, gender, and body mass index), ASA scores, fracture side, trauma mechanism, and comorbidities were recorded in detail.

Surgical parameters included time from trauma to surgery, operation time, amount of intraoperative bleeding, type of prosthesis used (with/without calcar support), number of cables used for stabilization, and length of hospital stay. According to the literature, early complications were defined as complications that developed within the first 30 days postoperatively.

VAS (0–10 points) for pain assessment, HHS, and PMS were used to evaluate functional outcomes. To evaluate the mobilization status of the patients, the use of walking aids was recorded, and the time to return to activities of daily living was determined. According to the literature, late complications were defined as complications occurring after the 30th postoperative day.

Statistical Analysis

The statistical analysis of the data examined in the study was performed using IBM SPSS 23.0 software (IBM Corp., Armonk, NY, USA). The mean and standard deviation (SD) were used to define data that followed a normal distribution, whereas the median and interquartile range (IQR) were used to define non-normally distributed data. The Student's t-test was used to compare continuously measured data from two independent groups that followed a normal distribution, whereas the Mann-Whitney U test was used to compare data that did not follow a normal distribution. Chi-square and Fisher's exact test were used to compare categorical data. Survival analysis was performed using the Kaplan–Meier method. Missing data were handled using complete-case analysis; variables with missing values were reported descriptively. Results with a p value below 0.05 were considered statistically significant.

RESULTS

In our study, we analyzed 82 patients who underwent partial hip replacement due to intertrochanteric fracture, divided into two groups as Cable Grip Plate (n=45) and Grip Cable (n=37) according to the method used in greater trochanter fixation. When demographic data were analyzed, the mean age was 80.8 ± 8.6 years in the Cable Grip Plate group and 79.4 ± 8.6 years in the Grip Cable group, and there was no significant difference between the groups (p=0.453). Female patients were predominant in both groups; 77.8% in the cable grip plate group and 86.5% in the grip cable group (p=0.310). The mean body mass index of the patients was similar (26.5 ± 1.8 kg/m² for Cable Grip Plate, 25.9 ± 1.6 kg/m² for Grip Cable group) (p=0.140). In terms of anesthesia risk, patients with ASA II and III scores were the majority in both groups, and the distributions were similar (p=0.971). No significant difference was found between the groups in terms of fracture side and trauma mechanism (p=0.824 and p=0.964, respectively). The most common comorbidity in both groups was hypertension, and the distribution of other comorbidities was similar (Table 1).

Table 1. Demographic and clinical characteristics of patients

Variable	Cable grip plate (n=45)	Grip cable (n=37)	Total (n=82)	p value
Age (years)†	80.8 ± 8.6	79.4 ± 8.6	80.2 ± 8.6	0.453
Gender‡				
· Female	35 (77.8%)	32 (86.5%)	67 (81.7%)	0.310
· Male	10 (22.2%)	5 (13.5%)	15 (18.3%)	
Body Mass Index (kg/m²)†	26.5 ± 1.8	25.9 ± 1.6	26.2 ± 1.7	0.140
ASA Score‡				0.971
ASA I	4 (8.9%)	4 (10.8%)	8 (9.8%)	
ASA II	19 (42.2%)	16 (43.2%)	35 (42.7%)	
ASA III	19 (42.2%)	14 (37.8%)	33 (40.2%)	
ASA IV	3 (6.7%)	3 (8.1%)	6 (7.3%)	
Fracture Side‡				0.824
· Right	22 (48.9%)	19 (51.4%)	41 (50.0%)	
· Left	23 (51.1%)	18 (48.6%)	41 (50.0%)	
Trauma Mechanism‡				0.964
· Simple Fall	38 (84.4%)	31 (83.8%)	69 (84.1%)	
· Fall from Height	4 (8.9%)	3 (8.1%)	7 (8.5%)	
· Motor vehicle accident	3 (6.7%)	3 (8.1%)	6 (7.3%)	
Comorbidities‡*				
· Hypertension	28 (62.2%)	20 (51.4%)	48 (58.5%)	0.455
· Diabetes Mellitus	19 (42.2%)	15 (40.5%)	34 (41.5%)	0.878
· Cardiovascular Disease	7 (15.6%)	7 (18.9%)	14 (17.1%)	0.687
· Cerebrovascular Disease	4 (8.9%)	3 (8.1%)	7 (8.5%)	0.900
· COPD	5 (11.1%)	1 (2.7%)	6 (7.3%)	0.146
· Osteoporosis	14 (31.1%)	18 (48.6%)	32 (39.0%)	0.105
· Other	6 (13.3%)	8 (21.6%)	14 (17.1%)	0.321
Intertrochanteric Fracture Type‡				0.934
· 31A3.1	13 (28.9%)	10 (27.0%)	23 (28.0%)	
· 31A3.2	25 (55.6%)	22 (59.5%)	47 (57.3%)	
· 31A3.3	7 (15.6%)	5 (13.5%)	12 (14.6%)	

Data are presented as mean ± standard deviation or n (%); †: Analyzed using Student's t-test; ‡: Analyzed using the chi-square test or Fisher's exact test; ASA: American Society of Anesthesiologists; COPD: Chronic Obstructive Pulmonary Disease; *: A single patient may have multiple comorbidities.

When the surgical procedures were analyzed in detail, it was seen that all patients underwent partial hip replacement. When the operation times were compared, the duration was significantly longer in the cable grip plate group (110.0 ± 27.6 min for Cable Grip Plate, 93.4 ± 11.9 min for Grip Cable group), (p=0.001). This difference was thought to be due to the additional surgical procedures required for plate placement. Similarly, the amount of intraoperative bleeding was higher in the Cable Grip Plate group than Grip Cable group (311.1 ± 62.1 mL vs. 246.0 ± 59.4 mL, respectively) (p<0.001). Due to the nature of the surgical technique, the number of wires used was higher in the cable grip plate group, and this difference was statistically significant (median 3 vs. 2, p<0.001). There was no significant difference between the groups in terms of length of hospital stay (6.58 ± 1.76 days for Cable Grip Plate, 6.30 ± 2.01 days for Grip Cable group), (p=0.503). When early complications were evaluated, the total complication rate was 22.2% in the Cable Grip Plate group and 18.9% in the Grip Cable group, but the difference did not reach statistical significance (p=0.915) (Table 2).

Table 2. Surgical details and early outcomes

Parameter	Cable grip plate (n=45)	Grip cable (n = 37)	Total (n=82)	p value
Operation Time (minutes)‡	110.0 ± 27.6	93.4 ± 11.9	102.5 ± 23.4	0.001*
Blood Loss (mL)‡	311.1 ± 62.1	246.0 ± 59.4	281.7 ± 68.7	<0.001*
Number of Cables Used†	3 (2)	2 (0)	3 (2)	<0.001*
Prosthesis Type‡				0.805
· Cemented	28 (62.2%)	24 (64.9%)	52 (63.4%)	
· Uncemented	17 (37.8%)	13 (35.1%)	30 (36.6%)	
Length of Hospital Stay (days) ‡	6.58 ± 1.76	6.30 ± 2.01	6.45 ± 1.87	0.503
Early Complications§				0.915
· Superficial surgical site infection	3 (6.7%)	2 (5.4%)	5 (6.1%)	
· Hematoma	3 (6.7%)	1 (2.7%)	4 (4.9%)	
· Delirium	1 (2.2%)	2 (5.4%)	3 (3.7%)	
· Deep vein thrombosis	2 (4.4%)	1 (2.7%)	3 (3.7%)	
· Urinary Tract Infection	1 (2.2%)	1 (2.7%)	2 (2.4%)	

Data are presented as mean ± standard deviation, median (interquartile range), or n (%); †: Analyzed using the Mann-Whitney U test; ‡: Analyzed using Student's t-test; §: Analyzed using Fisher's exact test; *: Statistically significant (p<0.05)

When the functional results were analyzed in detail, although both groups showed significant improvement compared with preoperative values, the cable grip plate group showed superior results. HHS was 82.7 ± 4.8 in the Cable Grip Plate group and 79.6±5.5 in the Grip Cable group at the last follow-up (p=0.008). Parker Mobility Score was also

higher in the Cable Grip Plate group than Grip Cable group (6.0 vs. 5.0, respectively) (p=0.006). In pain assessment, the VAS score was lower in the Cable Grip Plate group (2.7±0.9) than Grip Cable group (3.2±1.0), (p=0.032). During the rehabilitation process, patients in the Cable Grip Plate group returned to activities of daily living earlier (10.2±3.8 weeks) than Grip Cable group (12.4±3.7 weeks), (p=0.009). The Cable Grip Plate group also showed better results in terms of walking aid use; the rate of not using a walking aid at the last follow-up was 46.7% in the cable grip plate group, compared with 21.6% in the Grip Cable group (p=0.049) (Table 3).

Table 3. Functional outcomes of patients

Parameter	Cable grip plate (n=45)	Grip cable (n = 37)	Total (n=82)	p value
Harris Hip Score‡				
· Preoperative	49.5 ± 5.9	49.0 ± 5.8	49.2 ± 5.8	0.705
· Final Follow-up	82.7 ± 4.8	79.6 ± 5.5	81.3 ± 5.3	0.008*
Parker Mobility Score†				
· Preoperative	4.0 (0.0)	4.0 (0.0)	4.0 (0.0)	0.231
· Final Follow-up	6.0 (1.0)	5.0 (1.5)	6.0 (2.0)	0.006*
VAS Pain Score‡				
· Preoperative	7.2 ± 1.1	7.4 ± 1.2	7.3 ± 1.1	0.415
· Final Follow-up	2.7 ± 0.9	3.2 ± 1.0	3.0 ± 1.0	0.032*
Walking Aid Usage				0.049*
· None	21 (46.7%)	8 (21.6%)	29 (35.4%)	
· Cane	20 (44.4%)	22 (59.5%)	42 (51.2%)	
· Walker	4 (8.9%)	7 (18.9%)	11 (13.4%)	
Time to return to daily activities (weeks)	10.2 ± 3.8	12.4 ± 3.7	11.2 ± 3.9	0.009*

Data are presented as mean ± standard deviation, median (interquartile range), or n (%); ‡: Analyzed using Student's t-test; †: Analyzed using the Mann-Whitney U test; *: Statistically significant (p<0.05); VAS: Visual Analog Scale.

In long-term follow-up, late complications were more common in the Grip Cable group than Cable Grip Plate group (27.0% vs. 8.9%, respectively) (p=0.030). Similarly, the need for revision surgery was higher in the Grip Cable group than Cable Grip Plate group (13.5% vs. 4.4%, respectively) (p=0.144), but neither difference reached statistical significance. Implant failure and related revisions were more common in the Grip Cable group (8.1%) compared to Cable Grip Plate group (2.2%), (p=0.218). When the mortality distribution was analyzed, it was observed that deaths occurred mostly in the first 6 months in both groups, but no significant difference was found between the groups in terms of time distribution (p=0.741) (Table 4).

Table 4. Late complications, revision, and mortality rates of patients

Parameter	Cable grip plate (n=45)	Grip cable (n=37)	Total (n=82)	p value
Late Complications†				
· Total	4 (8.9%)	10 (27.0%)	14 (17.1%)	0.030*
· Implant irritation	1 (2.2%)	3 (8.1%)	4 (4.9%)	0.218
· Heterotopic ossification	1 (2.2%)	2 (5.4%)	3 (3.7%)	0.445
· Avascular necrosis	1 (2.2%)	1 (2.7%)	2 (2.4%)	0.888
· Chronic pain	1 (2.2%)	2 (5.4%)	3 (3.7%)	0.445
· Secondary osteoarthritis	0 (0%)	2 (5.4%)	2 (2.4%)	0.114
Revision Surgery†				
· Number of patients requiring revision	2 (4.4%)	5 (13.5%)	7 (8.5%)	0.144
Revision Reasons†				
· Implant Failure	1 (2.2%)	3 (8.1%)	4 (4.9%)	0.218
· Trochanteric Pseudarthrosis	0 (0%)	1 (2.7%)	1 (1.2%)	0.267
· Deep Infection	1 (2.2%)	0 (0%)	1 (1.2%)	0.362
Mortality Distribution				0.741
· First 3 months	1 (2.2%)	2 (5.4%)	3 (3.7%)	
· 3 – 6 months	1 (2.2%)	2 (5.4%)	3 (3.7%)	
· 6-12 months	1 (2.2%)	1 (2.7%)	2 (2.4%)	
Mean Survival Time (months)‡	4.3 ± 1.2	3.2 ± 1.1	3.6 ± 0.8	0.803

Data are presented as mean ± standard deviation and n (%); †: Analyzed using Fisher's exact test; ‡: Analyzed using Kaplan-Meier survival analysis; *: Statistically significant (p<0.05).

Based on the Kaplan – Meier survival analysis, no statistically significant difference was found between the Cable Grip Plate and Grip Cable groups (p=0.803) (Figure 3).

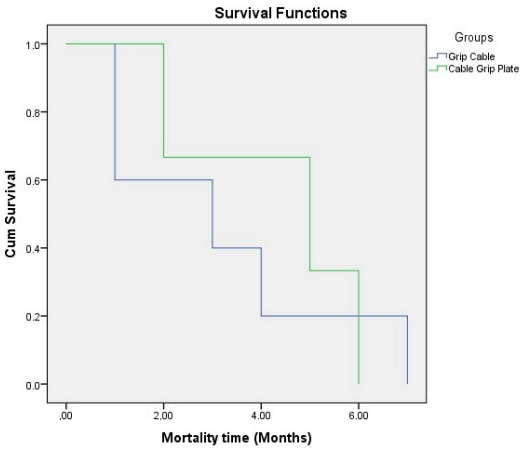


Figure 3. The graphic showing the Kaplan – Meier Survival analysis.

DISCUSSION

In this study, we aimed to compare the results of two different methods used in greater trochanter fixation in patients undergoing partial hip replacement after intertrochanteric femur fracture. Although it was observed that the cable grip plate method prolonged the operation time and increased blood loss, this technique was more successful in functional results. The cable grip plate technique gave more favorable results, especially in terms of patients' return to activities of daily living and pain control.

The cable grip plate technique, which we analyzed in our study, was found to prolong the operation time and increase the amount of intraoperative bleeding. In our study, the operation time in the patient group where the cable grip plate technique was used was longer than in studies where different techniques described in the literature were used (7, 8). This is mainly due to the additional surgical steps required for plate placement. The long operation times observed in the cable grip plate group may be related to the detailed surgical procedures performed to protect the abductor muscle mechanism. It has been observed that cerclage wire techniques used for proper placement and fixation of the trochanteric parts prolong the operation time similar to that of plate systems (9). In addition, this study found that intraoperative blood loss was greater in the group using the plate system. The high amount of intraoperative bleeding is due to the management of complex anatomic structures and the use of more invasive surgical techniques in this method. In the light of these findings, it is important for surgeons to adopt less invasive approaches and use technologies to reduce blood loss. In conclusion, the long operation times and increased blood loss observed in the use of cable grip plates are related to the differences in surgical techniques and the properties of the materials used. Therefore, it is recommended that patient characteristics should be carefully evaluated in surgical planning and the most appropriate method should be selected.

In our study, the cable grip plate system showed more positive results in HHS, PMS, and VAS pain assessments. The time to return to activities of daily living was also significantly shorter. It is also supported in the literature that these systems accelerate the rehabilitation process and improve functional results by strengthening mechanical stability (10). The faster rehabilitation time in the cable grip plate group is most likely due to more effective stabilization and intraoperative technical advantages. Previous studies have demonstrated that multi-fiber cable systems, such as the Dall Miles Cable system, show higher mechanical resistance and shorten the healing process compared with single-fiber systems (11). However, it is important to carefully monitor complications such as metal wear particles and bone resorption that can be seen with these systems (12, 13). These findings support the positive effects of cable grip plate systems in the rehabilitation process. However, the choice of surgical technique and patient characteristics also significantly affect the healing process and functional results.

Our study revealed that late complications and the need for revision surgery were more common in the Grip Cable system, suggesting that this system may be associated with a higher burden of late-term complications. It is known in the literature that cable systems cause problems such as loosening and implant failure over time. Studies have shown that metal wear particles from cable systems accelerate bone resorption (13). It has been reported that mechanical problems such as cable slippage, are common, especially in parts in the trochanteric region (14). In terms of implant revisions, no significant difference was found between the Cable Grip Plate and Grip Cable systems. However, it has been emphasized that cable-plate systems can be used in a wider range of fractures (14). It has been observed that such failures are generally associated with factors such as high body mass index and inadequate fixation. Although loosening and mechanical failures observed in Vancouver B-type fractures increase the need for revision surgery, the risk of complications can be reduced with appropriate surgical fixation techniques and correct implant selection (15).

The higher incidence of requiring revision surgery in the Grip Cable group suggests that this system may have some limitations in terms of implant stability. In the literature, it has been reported that cable systems may cause problems such as loosening, metal fatigue, and implant failure in the long term, especially in elderly and osteoporotic patients (16). In addition, it has been emphasized that the mechanical strength of cable systems is lower than that of plate systems, which may adversely affect stability, especially in areas under intense stress (17). Our findings suggest that cable systems may lead to the need for more frequent revision surgery, and this is a situation that should be considered especially in the early postoperative period.

In our study, mortality rates were similar between the groups. This result reveals that the fixation method used does not have a significant effect on mortality. Studies in the literature analyzing mortality data have not clearly stated the effect of surgical techniques on mortality (18). It has been reported that mortality rates, especially in elderly patients and patients with osteoporosis, are more related to the general health status of the patient, comorbidities, and postoperative complications. Risk assessment models, such as the Almelo Hip Fracture Score (AHFS), have shown that factors such as age, ASA score, and pre-fracture mobility are more determinative than the fixation method in predicting mortality (19). These findings support the similar mortality rates observed in our study. It has been emphasized that the pre-fracture functional level (New Mobility Score) is an important determinant of both mortality rates and in-hospital outcomes (20). Therefore, the similar mortality rates observed in both groups in our study are most likely related to the general health status and pre-fracture functional

capacity of the patients. In summary, it can be said that the general health status and pre-fracture functional level of the patient are more effective on mortality than the choice of fixation method.

Limitations

Firstly, due to its retrospective design, the possibility of bias in patient selection cannot be ruled out. In addition, single-center experience and short follow-up period limit the generalizability of the results. However, the strengths of our study include homogeneous patient groups, standardized surgical technique, and detailed functional assessments. Future multi-center, randomized controlled studies with longer follow-up periods will reveal the long-term results of these techniques more clearly. In particular, there is a need for studies to determine which technique is superior in different patient subgroups (such as osteoporosis severity and activity level).

CONCLUSION

In conclusion, the cable grip plate technique was deemed more efficient, as it demonstrated superior functional outcomes and enhanced preservation of the greater trochanter position in patients with intertrochanteric femur fracture treated with partial hip replacement, despite being associated with longer operative time and increased intraoperative blood loss. This technique significantly shortened the time to return to activities of daily living (10.2 ± 3.8 vs. 12.4 ± 3.7 weeks, p=0.009), improved the HHS (82.7 ± 4.8 vs. 79.6 ± 5.5, p=0.008), and yielded better results in pain control (VAS score 2.7 ± 0.9 vs. 3.2 ± 1.0, p=0.032). Late complication rates (8.9% vs. 27%, p=0.030) and the need for revision surgery (4.4% vs. 13.5%, p=0.144) were numerically lower compared with the Grip Cable method, but these differences did not reach statistical significance. Considering the favorable functional results demonstrated in our study, the cable grip plate technique may be considered a preferable surgical option for greater trochanter fixation in this population.

Acknowledgments: We thank all those who contributed to this manuscript.
Ethics Committee Approval: Ethical Committee approval obtained from Yeditepe University Non-Interventional Clinical Research Ethics Committee (Date: Dec 13, 2024, No: E.83321821-805.02.03-509).
Informed Consent: Informed consent obtained from all participants.
Peer Review: Externally peer-reviewed.
Author Contributions: Conception/Design of Study- Ö.Y., B.Ç., F.A.; Data Acquisition- Ö.Y., B.Ç., F.A.; Data Analysis/Interpretation- Ö.Y., B.Ç.; Drafting Manuscript- Ö.Y., F.A.; Critical Revision of Manuscript- Ö.Y., B.Ç., F.A.; Final Approval and Accountability- Ö.Y., B.Ç., F.A.
Conflict of Interest: The authors have no conflict of interest to declare.
Financial Disclosure: The authors declared that this study has received no financial support.

Author Details

Ömer Yonga
[1] Yeditepe University, Faculty of Medicine, Department of Orthopedics and Traumatology, İstanbul, Türkiye
0000-0002-3872-8836 omer_yonga@hotmail.com

Behiç Çelik
[1] Yeditepe University, Faculty of Medicine, Department of Orthopedics and Traumatology, İstanbul, Türkiye
0009-0001-1779-4500

Faik Altıntaş
[1] Yeditepe University, Faculty of Medicine, Department of Orthopedics and Traumatology, İstanbul, Türkiye
0000-0002-5242-250X

REFERENCES

1. Mei XY, Gong YJ, Safir OA, Gross AE, Kuzyk PR. Fixation options following greater trochanteric osteotomies and fractures in total hip arthroplasty: a systematic review. JBJS Rev 2018; 6(6): e4.
2. Sundaram K, Siddiqi A, Kamath AF, Higuera CA. Trochanteric osteotomy in revision total hip arthroplasty. EFORT Open Rev 2020; 5: 477–85.
3. Sheridan GA, Galbraith A, Kearns SR. Extended trochanteric osteotomy fixation for femoral stem revision in periprosthetic fractures: Dall–Miles plate versus cables. Eur J Orthop Surg Traumatol 2018; 28: 471–6.
4. Kim IS, Pansey N, Kansay RK, Yoo JH, Lee HY, Chang JD. Greater trochanteric reattachment using the third-generation cable plate system in revision total hip arthroplasty. J Arthroplasty 2017; 32: 1965–9.
5. Koyama K, Higuchi F, Kubo M, Okawa T, Inoue A. Reattachment of the greater trochanter using the Dall-Miles cable grip system in revision hip arthroplasty. J Orthop Sci 2001; 6(1): 22–7.
6. Collado A, Arvinius C, Serrano L, Otero J, Moro E, Marco F. Cerclage wire fixation of trochanteric osteotomies in complex hip revision: comparison with cable-plate fixation. Hip Int 2021; 32(5): 672–6.
7. Ogur HU, Tuhanioğlu U, Seyfettinoğlu F, Çiloğlu O, Uslu H, Fidan E. Clinical and functional results of trochanter major fixation in elderly patients undergoing hip arthroplasty for unstable pertrochanteric fractures. J Orthop Trauma Surg Relat Res 2019; 14(2): 1-8.
8. Speranza A, Massafra C, Pecchia S, Di Niccolo R, Iorio R, Ferretti A. Metallic versus non-metallic cerclage cable systems in periprosthetic hip fracture treatment. J Clin Med 2022; 11(6): 1608.
9. Nho JH, Seo GW, Kang TW, Jang BW, Park JS, Suh YS. Bipolar hemiarthroplasty in unstable intertrochanteric fractures with an effective wiring technique. Hip Pelvis 2023; 35(2): 99–107.
10. Tang J, Wu T, Shao H, Zhou Y. Greater trochanter fixation with a claw plate and cable system in complex primary and revision total hip arthroplasty: long-term follow-up. Int Orthop 2022; 46: 2553–60.
11. Dall DM, Miles AW. Re-attachment of the greater trochanter: the use of the trochanter cable-grip system. J Bone Joint Surg Br 1983; 65(1): 55–9.
12. Kelley SS, Johnston RC. Debris from cobalt-chrome cable may cause acetabular loosening. Clin Orthop Relat Res 1992; 285: 140–6.
13. Altenburg AJ, Callaghan JJ, Yehyawi TM, Pedersen DR, Liu SS, Leinen JA, et al. Cemented total hip replacement cable debris and acetabular construct durability. J Bone Joint Surg Am 2009; 91(7): 1664-70.
14. Ricciardi BF, Nodzo SR, Oi K, Lee YY, Westrich GH. Radiographic outcomes of cable-plate versus cable-grip fixation in periprosthetic fractures of the proximal femur. Hip Int 2017; 27(6): 584–8.
15. Ohly NE, Whitehouse MR, Duncan CP. Periprosthetic femoral fractures in total hip arthroplasty. Hip Int 2014; 24(6): 556–67.

16. Liu P, Jin D, Zhang C, Gao Y. Revision surgery due to failed internal fixation of intertrochanteric femoral fracture: current state of the art. BMC Musculoskelet Disord 2020; 21: 573.
17. Faldini C, Grandi G, Romagnoli M, Pagkrati S, Digennaro V, Faldini O, et al. Surgical treatment of unstable intertrochanteric fractures by bipolar or total hip replacement in elderly osteoporotic patients. J Orthop Traumatol 2006; 7: 117–21.
18. Kilci O, Un C, Sacan O, Gamli M, Baskan S, Baydar M, et al. Postoperative mortality after hip fracture surgery: a 3-year follow-up. PLoS One 2016; 11: e0162097.
19. Nijmeijer WS, Folbert EC, Vermeer M, Slaets JPJ, Hegeman JH. Prediction of early mortality following hip fracture surgery in frail elderly patients: the Almelo Hip Fracture Score (AHFS). Injury 2016; 47(10): 2138–43.
20. Kristensen MT, Foss NB, Ekdahl C, Kehlet H. Prefracture functional level evaluated by the New Mobility Score predicts in-hospital outcome after hip fracture surgery. Acta Orthop 2010; 81(3): 296–302.

İSTANBUL UNIVERSITY PRESS

Experimed 2026, 16 (2): 128–136

https://doi.org/10.26650/1884953

Submitted: 23.11.2025
Revision Requested: 12.02.2026
Last Revision Received: 06.04.2026
Accepted: 07.04.2026
Published Online 12.08.2026

Experimed

Research Article

Open Access

In vitro Antimicrobial Activity of Salicylic Acid–Loaded Liposomes Against *Cutibacterium acnes*: A Microbiological Approach for Acne Treatment

Gülcan Kuyucuklu-Kazan [1] & Ahmet Doğan Ergin [2]

[1] Kırklareli University, Faculty of Medicine, Department of Medical Microbiology, Kırklareli, Türkiye
[2] Trakya University, Faculty of Pharmacy, Department of Pharmaceutical Technology, Edirne, Türkiye

Abstract

Objective: This study aimed to comparatively evaluate the antimicrobial activity of free salicylic acid, liposomal salicylic acid, and an arbutin-containing liposomal salicylic acid formulation against *Cutibacterium acnes (C. acnes)*, a key microorganism in the pathogenesis of acne vulgaris, and to assess the contribution of liposomal carrier systems to antimicrobial efficacy.

Materials and Methods: *C. acnes* (ATCC® 6919™) was used as the test strain. Salicylic acid–loaded liposomes were prepared using the thin-film hydration method and characterized for particle size, polydispersity index, zeta potential, encapsulation efficiency, and process yield. Antimicrobial activity was evaluated using broth microdilution and agar dilution methods according to the Clinical and Laboratory Standards Institute (CLSI) M11 guidelines. Ampicillin, ampicillin–sulbactam, meropenem, tetracycline, clindamycin, and vancomycin served as reference antibiotics. Free salicylic acid and liposomal formulations were tested comparatively.

Results: Minimum inhibitory concentration (MIC) values of the reference antibiotics were within CLSI quality control ranges. Free salicylic acid showed an MIC of 0.9 mg/mL, while the liposomal formulation reduced the MIC to 0.45 mg/mL, indicating a twofold enhancement in antimicrobial activity. The arbutin-containing liposomal formulation did not achieve complete inhibition at this concentration but resulted in approximately 50% growth reduction.

Conclusion: Liposomal delivery significantly enhances the antimicrobial activity of salicylic acid against *C. acnes*. Incorporation of arbutin provided partial inhibition, suggesting liposome-based systems as promising topical strategies for acne treatment.

Keywords Salicylic Acid · Liposomes · *Cutibacterium acnes* · Acne Vulgaris

Citation: Kuyucuklu-Kazan, G. & Ergin, A. D. *In vitro* Antimicrobial Activity of Salicylic Acid–Loaded Liposomes Against *Cutibacterium acnes*: A Microbiological Approach for Acne Treatment. Experimed 2026; 16(2): 128-136. DOI: 10.26650/1884953

This work is licensed under Creative Commons Attribution-NonCommercial 4.0 International License.

© 2026. Kuyucuklu-Kazan, G. & Ergin, A. D.

Corresponding author: Ahmet Doğan Ergin adoganergin@trakya.edu.tr

INTRODUCTION

Acne vulgaris is one of the most prevalent dermatological disorders worldwide, with a particularly high incidence during adolescence (1). The pathogenesis of acne is multifactorial and is primarily driven by follicular hyperkeratinization, increased sebum production, inflammation, and colonization by *Cutibacterium acnes (C. acnes)* (2). *C. acnes* proliferates within the lipid-rich pilosebaceous unit and plays a key role in initiating the inflammatory response. Excessive bacterial growth and the subsequent immune activation contribute critically to all stages of acne development, from comedone formation to the progression of inflammatory lesions. Consequently, *C. acnes* is a central target in acne pathogenesis, and a substantial proportion of therapeutic strategies are aimed at reducing the bacterial burden (3).

Salicylic acid (a β-hydroxy acid) has been widely used for the treatment of acne for many years, with well-established comedolytic, antibacterial, and anti-inflammatory effects. Its therapeutic efficacy is primarily attributed to the resolution of follicular obstruction, reduction of free fatty acids, and suppression of *C. acnes*–induced inflammatory processes (4). However, poor solubility and instability under physiological conditions represent key technological challenges in the topical delivery of salicylic acid (5). Dermal absorption of salicylic acid is highly dependent on formulation characteristics, highlighting the need for controlled delivery systems. Therefore, to overcome these limitations, salicylic acid was encapsulated into liposomal drug delivery systems in this study.

Arbutin is a naturally occurring glycoside of hydroquinone that inhibits melanin synthesis and is widely used in cosmetic and dermatological preparations (6). It is particularly effective in reducing post-inflammatory hyperpigmentation following acne lesions. Although data on the direct antibacterial activity of pure arbutin against *C. acnes* are limited, some studies have investigated the effects of arbutin-rich plant extracts on *C. acnes* (7). Given its extensive use in cosmetic formulations, these studies are of particular relevance. Extracts with high arbutin content have been reported to exhibit antibacterial and anti-inflammatory activities against *C. acnes*, suggesting that arbutin may indirectly contribute to the modulation of acne-related microbial growth and inflammation (7, 8).

Liposomes are biocompatible and targetable drug delivery vesicles that exhibit high compatibility with the skin lipid barrier due to their phospholipid-based structure (9). Liposomes are used in targeting the pilosebaceous unit (hair follicle and sebaceous glands) (10). Optimization of their particle size within the range of 300–600 nm enables preferential localization to pilosebaceous units, facilitating the localized delivery of active compounds to the follicular microenvironment where *C. acnes* proliferates (11). Moreover, their controlled release properties may enhance the therapeutic efficacy of active ingredients while reducing the risk of skin irritation. In this context, liposomal carrier systems offer significant potential for overcoming the solubility and penetration limitations of salicylic acid and are a more effective and better-tolerated approach for acne treatment.

The aim of this study was to comparatively evaluate the *in vitro* antimicrobial activity of free salicylic acid, liposomal salicylic acid, and arbutin-combined liposomal systems against *C. acnes* (ATCC® 6919™) and to elucidate the contribution of liposomal carrier systems to the antibacterial potential of these compounds.

MATERIALS AND METHODS

Materials

Salicylic acid and arbutin were obtained from Elito (Türkiye). Soy lecithin (Acros Organics, USA) and cholesterol (Merck, Germany) were used as lipid components. Chloroform (Merck, Germany) was used as the organic solvent, and ultrapure water (İsolab, Türkiye) was used as the aqueous phase. For spectrophotometric analysis, aqueous and phosphate-buffered saline (PBS, dissolution medium) solutions containing 10% (v/v) ethanol were used. Standard solutions of salicylic acid in the concentration range of 2.5–50 µg/mL were prepared. Quantitative measurements were performed at 296 nm in the aqueous medium and at 295 nm in the dissolution medium using an ultraviolet (UV)–visible spectrophotometer (DLAB SP-UV1100 UV Spectrophotometer, China). The analytical method was calibrated and validated before analysis in accordance with International Council for Harmonisation of Technical Requirements for Pharmaceuticals for Human Use (ICH) guidelines.

For microbiological experiments, *C. acnes* (ATCC® 6919™) was cultured in Brucella agar and Brucella broth (Merck, Germany) supplemented with 5% sheep blood, hemin, and vitamin K_1. Anaerobic incubation was performed using AnaeroGen™ gas generation systems (Oxoid, United Kingdom). In accordance with Clinical and Laboratory Standards Institute (CLSI) guidelines, the *in vitro* minimum inhibitory concentration (MIC) values of clindamycin, tetracycline, ampicillin, ampicillin–sulbactam, meropenem, and vancomycin were evaluated as reference antimicrobials.

Preparation of Liposomal Formulations

Salicylic acid–loaded liposomes were prepared using the thin-film hydration method with some modifications (12). Predetermined amounts of soy lecithin, cholesterol, and salicylic acid were dissolved in 5 mL of chloroform using a magnetic stirrer (Weightlab WN-10H-120, Türkiye), and the solvent was removed under reduced pressure using a rotary evaporator (Heidolph, Germany) at 40 °C and 60 rpm to form a thin lipid film. The resulting film was hydrated with 10 mL of ultrapure water, stirred for 2 minutes, and subsequently sonicated for 20 minutes to obtain multilamellar vesicles using

an ultrasonic water bath (WiseClean, Japan). The liposomes were separated by centrifugation at 13500 rpm for 20 min (Daihan, Japan) and stored in dry form after lyophilization (HyperCOOL HC3110, Hanil Scientific Inc., Korea, −80 °C, <0.1 torr, 16 h). To optimize the formulation, eight different liposomal formulations were prepared by varying the lecithin content, salicylic acid dose, and lecithin-to-cholesterol molar ratio by applying multiple linear regression analysis to formulations with F1-F8 codes (STATISTICA 8.0; Stat Soft. Inc., OK, USA) (Table 1, 2).

Table 1. Formulation table of salicylic acid loaded liposomes

	Lecithin (mg)	Salicylic acid (mg)	Lecithin-Cholesterol molar ratio
F-1	100	20	2
F-2	100	20	4
F-3	100	40	2
F-4	100	40	4
F-5	200	20	2
F-6	200	20	4
F-7	200	40	2
F-8	200	40	4

Table 2. Variable level of 2^3 factorial design for liposomes

Variable level	-1 (low)	+1 (high)
Lecithin (mg) (X_1)	100	200
Salicylic acid (mg) (X_2)	20	40
Lecithin-Cholesterol molar ratio (X_3)	2	4

Characterization of Liposomal Formulations

Particle Size Distribution and Polydispersity Index (PDI)

Lyophilized liposomes (5–10 mg) were reconstituted in 10 mL of ultrapure water and dispersed using an ultrasonic water bath (WiseClean, Japan) for 5 min, followed by vortex (Daihan Scientific VM-10, China) mixing for 5 min. No additional dilution step was applied before analysis. Particle size and size distribution were determined by dynamic light scattering (DLS) using a Zetasizer (NanoSeries Nano-ZS, Malvern Instruments, UK). Measurements were performed at 25 °C using a 633-nm He–Ne laser with a scattering angle of 173°. Disposable cuvettes were used, and all measurements were conducted in triplicate (n = 3).

Zeta Potential

Lyophilized liposomes (5–10 mg) were reconstituted in 10 mL of ultrapure water prior to analysis. No additional dilution step was applied. The zeta potential values of the formulations were determined by electrophoretic mobility measurements using a Zetasizer Nano-ZS (Malvern Instruments, UK). Measurements were performed at 25°C using disposable folded capillary zeta cells. All analyses were performed in triplicate, and the results are presented as mean ± standard deviation (n = 3).

Encapsulation Efficiency and Drug Loading

Encapsulation efficiency was determined using an indirect method by quantifying the amount of free salicylic acid in the supernatant obtained after liposome preparation. Drug loading (DL%) was calculated based on the supernatant concentration (Equation 1). For the determination of the active drug content, a direct method was employed. Briefly, 10 mg of liposomes were incubated in ultrapure water for 30 minutes to ensure complete release of the encapsulated drug. DL% was calculated using Equation 2. All analyses were performed in triplicate.

$$\mathrm{EE\%} = \frac{\text{Total SA} - \text{Unloaded SA}}{\text{Total SA}} \times 100 \qquad \text{Eq. 1}$$

$$\mathrm{DL\%} = \frac{\text{Loaded SA}}{\text{Total formulation weight}} \times 100 \qquad \text{Eq. 2}$$

EE: Encapsulation efficiency; SA: Salicylic acid; DL: Drug loading

Process Yield

The process yield of the liposomal formulations was determined gravimetrically. Following lyophilization, the actual weight of the recovered liposomes was compared with the theoretical weight of the formulation, and the process yield was calculated using Equation 3.

$$\mathrm{PY\%} = \frac{\text{Obtained Liposome weight}}{\text{Total ingredients (SA + Lecithin + cholesterol)}} \times 100 \qquad \text{Eq. 3}$$

PY: Process yield; SA: Salicylic acid

Morphological Analyses

The morphological characteristics of the liposomes were evaluated using scanning electron microscopy (SEM). For SEM analysis, the aqueous liposome dispersion (F-8) was dropped onto the sample holder and allowed to dry at room temperature. The dried samples were subsequently coated with a thin conductive layer before imaging. SEM imaging was performed using a Zeiss EVO LS10 microscope (Cambridge, UK) operated at 20 kV under different magnifications.

Release Study

In vitro drug release studies were performed for free salicylic acid and the selected optimum salicylic acid-loaded liposome formulation (F-8) based on previously reported methods with minor modifications (13, 14). Briefly, free salicylic acid and liposomes containing an equivalent amount of salicylic acid (80 µg) were dispersed in 2 mL of PBS (pH 7.4) containing 10% ethanol to maintain sink conditions. The samples were transferred into eppendorf tubes and incubated in a shaking water bath at 37°C and 75 rpm for 24 h. At predetermined time intervals (0, 0.25, 0.5, 1, 2, 4, 7, and 24 h), the tubes were withdrawn and centrifuged at 13,500

rpm for 10 min. Following centrifugation, the supernatants were collected and analyzed spectrophotometrically using a UV–visible spectrophotometer at 295 nm to determine the amount of released salicylic acid. The analytical method used for quantification was previously calibrated and validated. All experiments were performed in triplicate.

Antimicrobial Activity Studies

Broth Microdilution Method

C. acnes (ATCC® 6919™) was used as the test microorganism in antimicrobial activity studies. MIC values were determined using the broth microdilution method recommended by the CLSI for anaerobic bacteria (15). The reference strain was cultured on Brucella agar supplemented with 5% sheep blood, hemin (5 µg/mL), and vitamin K_1 (1 µg/mL) and incubated under anaerobic conditions at 37 °C for 48 h to obtain fresh cultures. Colonies were then suspended in Brucella broth supplemented with hemin and vitamin K_1 and incubated under anaerobic conditions at 37 °C for an additional 48 h.

Bacterial suspensions were adjusted to 0.5 McFarland turbidity (approximately 1.5 × 10^8 CFU/mL) using the same enriched Brucella broth and subsequently diluted to achieve a final inoculum concentration of 5 × 10^5 CFU/mL in the microdilution wells, in accordance with CLSI recommendations. Two-fold serial dilutions of reference antibiotics (ampicillin, ampicillin–sulbactam, meropenem, tetracycline, clindamycin, and vancomycin) and the three test formulations (free salicylic acid, liposomal salicylic acid, and 2% arbutin+ liposomal salicylic acid) were prepared in 96-well microplates. The plates were incubated under anaerobic conditions using AnaeroGen™ gas-generating systems at 35°C–37°C for 48 h (15). The antimicrobial efficacy of free salicylic acid and liposomal formulations (salicylic acid-LIPO and salicylic acid-LIPO-ARB) against *C. acnes* was evaluated using the broth microdilution method according to CLSI recommendations. Serial two-fold dilutions of the formulations were prepared within the concentration range of 0.05625–1.8 mg/mL. MIC/MIC_{50} values were determined based on the inhibition of visible bacterial growth following anaerobic incubation. MIC/MIC_{50} values were interpreted according to CLSI M11 guidelines (15). MIC/MIC_{50} values were interpreted according to CLSI M11 (15) breakpoints, and visual assessment was supported by absorbance measurements when necessary. All experiments were performed in triplicate.

Agar Dilution Method

The agar dilution method, accepted as the reference method for antimicrobial susceptibility testing, was performed in accordance with the CLSI guideline for anaerobic bacteria (CLSI M11) (15). Isolates were cultured on Brucella agar supplemented with 5% sheep blood, hemin (5 µg/mL), and vitamin K_1 (1 µg/mL) and incubated under anaerobic conditions at 37 °C for 48 h to obtain fresh cultures. Bacterial suspensions prepared from fresh colonies were adjusted to 0.5 McFarland turbidity (approximately 1.5 × 10^8 CFU/mL) in Brucella broth supplemented with hemin and vitamin K_1, and then diluted tenfold to achieve a final inoculum density of 1 × 10^5 CFU per 10 µL.

Test formulations and reference antibiotics were prepared as two-fold serial dilutions according to CLSI recommendations and incorporated into Brucella agar supplemented with 5% sheep blood, hemin, and vitamin K_1. Separate agar plates were prepared for each concentration, and drug-free plates were included as controls. Aliquots of 10 µL of the bacterial suspension were applied to the agar surface by spot inoculation, proceeding from the lowest to the highest concentration. After inoculum absorption, the plates were incubated under anaerobic conditions at 37 °C for 48 h. Control plates without antibiotics were incubated under aerobic conditions for contamination control and under anaerobic conditions for growth control.

Following incubation, the MIC was defined as the lowest concentration at which complete inhibition of visible bacterial growth was observed; faint growth or single colonies were not considered indicative of growth. Results were interpreted according to the CLSI M11 criteria (15). All experiments were performed in triplicate.

Statistical Analyses

All experiments were performed in at least three independent replicates, and results are presented as mean ± standard error. Statistical analyses were conducted using Statistica software (STATISTICA 8.0; StatSoft. Inc., OK, USA). In addition to appropriate parametric or nonparametric tests, multivariate regression analysis was performed to evaluate the individual and combined effects of three formulation parameters on the measured responses. A p-value of < 0.05 was considered statistically significant.

RESULTS

Preparation and Characterization of Liposomal Formulations

In this study, a total of eight liposomal formulations were developed using different lecithin amounts, varying salicylic acid doses, and two lecithin-to-cholesterol molar ratios (2:1 and 4:1) and were comprehensively characterized. Particle size, PDI, zeta potential, encapsulation efficiency, drug loading and process yield values of the formulations are presented in Table 3.

Table 3. Results of liposomal formulations containing salicylic acid

Code	Size ± SD (nm) (n=3)	PDI ± SD (n=3)	Zeta Potential ± SD (mV) (n=3)	EE % ± SD (n=3)	DL % ± SD (n=3)	Process Yield%
F-1	427.7 ± 61.56	0.45 ± 0.05	-35.87 ± 0.69	13.31 ± 4.13	11.20 ± 0.70	54.27
F-2	339.6 ± 14.96	0.45 ± 0.01	-35.48 ± 1.01	28.57 ± 1.93	9.73 ± 0.12	62.62
F-3	359.9 ± 62.16	0.60 ± 0.06	-34.47 ± 1.05	30.36 ± 0.91	12.73 ± 0.27	72.22
F-4	396.6 ± 48.98	0.52 ± 0.06	-30.62 ± 0.29	37.69 ± 0.66	10.88 ± 0.12	56.72
F-5	850.8 ± 80.3	0.62± 0.05	-36.79 ± 0.60	17.62 ± 5.97	8.47 ± 1.42	58.85
F-6	169.5 ± 11.97	0.41 ± 0.08	-36.66 ± 2.06	23.57 ± 1.83	12.4 ± 0.84	62.18
F-7	609.4 ± 90.78	0.54 ± 0.05	-35.50 ± 0.77	35.03 ± 4.24	11.3 ± 0.57	61.54
F-8	155.2 ± 11.81	0.42 ± 0.08	-28.55 ± 0.22	36.06 ± 0.47	14.22 ± 0.2	60.96

PDI: Polydispersity index; SD: Standard deviation; EE: Encapsulation efficiency; DL: Drug loading

Particle Size and PDI Evaluation

The particle sizes of the liposomal formulations ranged from 155.2 to 850.8 nm. Formulations containing higher amounts of lecithin (F-5, F-6, F-7, and F-8) generally exhibited larger particle sizes, with F-5 showing the largest mean particle size (850.8 nm). In contrast, increasing the lecithin-to-cholesterol molar ratio from 2:1 to 4:1 did not result in a statistically significant effect on particle size ($p>0.05$). The PDI values of all formulations ranged between 0.41 and 0.62, and since all values were below 0.7, the size distributions were considered homogeneous and acceptable.

Zeta Potential and Colloidal Stability

Zeta potential measurements revealed that all formulations possessed negative surface charges, with values ranging from -28.55 mV to -36.79 mV. These results indicate adequate electrostatic stabilization and confirm the colloidal stability of the liposomal formulations.

Encapsulation Efficiency and Drug Loading

Statistical analysis of encapsulation efficiency revealed that increasing the amount of salicylic acid and the lecithin-to-cholesterol molar ratio to 4:1 had a statistically significant positive effect on encapsulation efficiency ($p<0.05$). The highest encapsulation efficiencies were observed for formulations F-4 (37.69%) and F-8 (36.06%). These formulations exhibited optimal loading profiles due to their higher salicylic acid content (40 mg) combined with a 4:1 lecithin-to-cholesterol molar ratio. The drug loading values ranged from 8.47% to 14.22%, and formulations with higher encapsulation efficiencies also showed higher drug loading.

Process Yield

The process yield of the liposomal formulations ranged from 54.27% to 72.22%. All formulations exhibited acceptable process yields, with the highest yield (72.22%) obtained for formulation F-3.

Morphology of Liposomes

Although SEM images showed relatively smaller primary particles, the mean particle size of the optimized liposome formulation was determined to be approximately 155 nm by DLS analysis (Figure 1). The difference between SEM and DLS results may be attributed to the hydrodynamic diameter measured in the aqueous dispersed state during DLS analysis, which can lead to particle swelling, as well as the partial aggregation observed in the formulation.

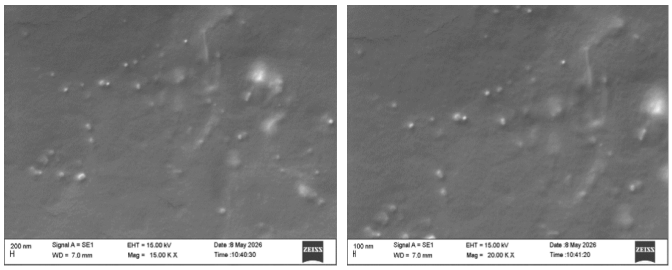


Figure 1. SEM images of liposomes.

Release Study

The *in vitro* release study demonstrated that free salicylic acid exhibited a rapid release profile, reaching approximately 90% release within the first hours. In contrast, the salicylic acid-loaded liposome formulation (F-8) showed a slower and more controlled release behavior, with approximately 65% cumulative release after 24 h. These findings indicate that liposomal encapsulation successfully prolonged the release of salicylic acid compared to the free drug (Figure 2).

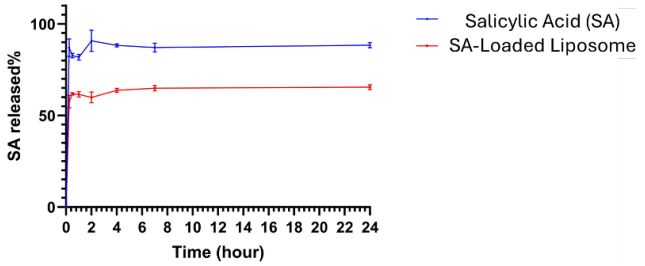


Figure 2. Release study of salicylic acid and salicylic acid-loaded liposomes.

Antimicrobial Activity Results

MIC Values Determined by the Broth Microdilution Method

The antimicrobial activities of free salicylic acid, liposomal salicylic acid, and 2% arbutin-combined liposomal formulations designed to enhance penetration were evaluated against *C. acnes* (ATCC® 6919™) using the broth microdilution method over a concentration range of 0.135–0.001 mg/mL. Free salicylic acid was tested in powder form as salicylic acid (1.8 mg/mL), liposomal salicylic acid was evaluated as salicylic acid-LIPO (1.8 mg/mL), and the arbutin-combined liposomal formulation was tested as salicylic acid-LIPO-ARB (1.8 mg/mL). For comparison, reference antibiotics included ampicillin (AMP, 0.008 mg/mL), ampicillin–sulbactam (SAM, 0.008/0.016 mg/mL), meropenem (MEM, 0.008 mg/mL), tetracycline (TET, 0.0016 mg/mL), clindamycin (CLI, 0.256 mg/mL), and vancomycin (VAN, 0.008 mg/mL). All antimicrobial agents were evaluated against *C. acnes* (ATCC® 6919™) in accordance with CLSI recommendations.

The MIC values determined for *C. acnes* (ATCC® 6919™) were 0.5 µg/mL for ampicillin, 0.25/4 µg/mL for ampicillin–sulbactam, 0.25 µg/mL for meropenem, and 0.5 µg/mL for tetracycline, clindamycin, and vancomycin. These results were consistent with the expected CLSI quality control MIC ranges. Free salicylic acid exhibited an MIC of 0.9 mg/mL against *C. acnes*, whereas this value decreased to 0.45 mg/mL in the liposomal formulation, corresponding to an approximately two-fold reduction in MIC following liposomal encapsulation. In the salicylic acid–arbutin–loaded liposomal formulation (SA-LIPO-ARB), complete inhibition was not achieved at 0.45 mg/mL; however, approximately 50% inhibition of bacterial growth was observed, indicating that the MIC_{50} value was below 0.45 mg/mL (Figure 3). These findings suggest that while the addition of arbutin did not result in complete inhibition, it exerted a partial inhibitory effect. Overall, the results demonstrate that liposomal carrier systems can enhance the antimicrobial activity of salicylic acid against *C. acnes*.

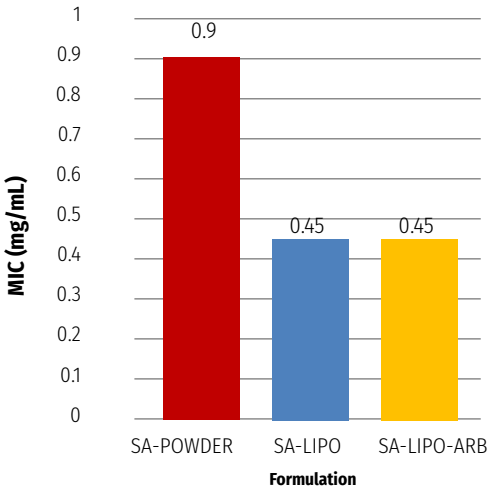


Figure 3. MIC values of free and liposomal salicylic acid formulations against *C. acnes* (ATCC® 6919™). MIC: Minimum inhibitory concentration; SA-Powder: Free salicylic acid; SA-LIPO: liposomal salicylic acid; SA-LIPO-ARB: Arbutin-loaded liposomal salicylic acid.

MIC Values Determined by the Agar Dilution Method

In this study, the antimicrobial susceptibilities of *Cutibacterium* strains were also evaluated using the agar dilution method, which is recommended by the CLSI as the gold standard, against six antibiotics (ampicillin, ampicillin–sulbactam, meropenem, tetracycline, clindamycin, and vancomycin) as well as three test compounds. Susceptibility interpretations were performed according to the CLSI (M11) criteria. Based on the MIC values obtained by the agar dilution method, the susceptibility profiles of the isolates to the tested antibiotics were identical, and no statistically significant differences were observed between the methods. All antibiotic MIC results were within the CLSI-reference breakpoints.

For *C. acnes* (ATCC® 6919™), the MIC values were 0.5 µg/mL for ampicillin, 0.25/4 µg/mL for ampicillin–sulbactam, 0.25 µg/mL for meropenem, and 0.5 µg/mL for tetracycline, clindamycin, and vancomycin, which were consistent with the expected CLSI quality control MIC ranges. Free salicylic acid exhibited an MIC of 0.9 mg/mL against *C. acnes*, whereas this value decreased to 0.45 mg/mL in the liposomal formulation, indicating an approximately two-fold increase in antimicrobial activity. In the SA-LIPO-ARB, complete inhibition was not achieved at 0.45 mg/mL; however, a reduction in colony size was observed (Table 4).

Table 4. MIC values and colony inhibition profiles of salicylic acid and salicylic acid–arbutin–loaded liposomal formulations against *C. acnes* (ATCC® 6919™).

	MIC (mg/mL)	Colony Inhibition
SA	0.90	Complete
SA-LIPO	0.45	Complete
SA-LIPO-ARB	0.45	Partial

MIC: Minimum inhibitory concentration; SA: Salicylic acid; SA-LIPO: Liposomal salicylic acid; SA-LIPO-ARB: Salicylic acid–arbutin–loaded liposomal formulation.

DISCUSSION

Acne vulgaris is a chronic inflammatory disorder of the pilosebaceous unit, in which colonization by *C. acnes* plays a central role in disease pathogenesis (16). The colonization characteristics of this bacterium enable protection against host immune responses and antimicrobial agents, thereby limiting treatment efficacy and facilitating the development of resistance (17). Consequently, therapeutic agents used in acne management should not only exhibit antibacterial activity but also provide targeted delivery with high local tolerability. In the present study, the *in vitro* antimicrobial activities of a novel liposomal formulation used in acne treatment and its arbutin-combined counterpart were comparatively evaluated against *C. acnes* (ATCC® 6919™), demonstrating the effectiveness of liposomal carrier systems.

Salicylic acid has long been employed in acne therapy due to its keratolytic and anti-inflammatory properties; however, when administered in its free form, it presents notable limitations, including poor solubility, instability, and potential for irritation (5, 18). Previous studies have reported MIC_{90} values of approximately 1000 µg/mL and minimum bactericidal concentration (MBC) values around 2000 µg/mL for free salicylic acid against *C. acnes* strains (19). Liposomal encapsulation enhances the local concentration of the drug in the vicinity of bacterial cells, rendering these threshold concentrations biologically relevant. In our study, free salicylic acid exhibited an MIC of 0.9 mg/mL against *C. acnes*, indicating moderate antibacterial activity in its unencapsulated form. In contrast, the MIC value decreased to 0.45 mg/mL following liposomal encapsulation, clearly demonstrating an approximately two-fold enhancement in antimicrobial efficacy. Notably, these MIC values were comparable to those obtained for the reference antibiotics used in the study, suggesting that liposomal salicylic acid formulations exhibit antimicrobial activity consistent with standard antibacterial agents.

The enhanced antimicrobial efficacy observed in this study may be attributed to several advantages of liposomal carrier systems, including their high compatibility with the skin lipid barrier due to their phospholipid-based structure, their ability to provide controlled drug release, and their capacity to facilitate more efficient delivery to the pilosebaceous unit (20, 21). In addition, liposomes protect active compounds from environmental degradation and prolong their residence time within the skin, thereby contributing to increased local antimicrobial activity. Another important factor is the relative stability of salicylic acid's antimicrobial activity in sebaceous environments. Unlike other topical agents, salicylic acid maintains its antibacterial effectiveness in the presence of sebum. For instance, while the activity of benzoyl peroxide (BPO) is markedly reduced in the presence of 50% sebum, the MIC and MBC values of salicylic acid are minimally affected by sebaceous conditions (19). This observation suggests that the lipophilic nature of salicylic acid confers a distinct advantage within the lipid-rich environment of the sebaceous follicle.

In the present study, salicylic acid–loaded liposomes were successfully prepared using a thin-film hydration approach, and the effects of formulation variables on key physicochemical characteristics were systematically evaluated. The results indicate that variations in lecithin content did not result in a statistically significant effect on particle size ($p>0.05$), although formulations with higher lecithin levels tended to exhibit larger vesicle diameters. Similarly, changes in the lecithin-to-cholesterol molar ratio did not significantly influence particle size, suggesting that within the investigated composition range, lipid composition primarily affected membrane organization rather than vesicle growth. All formulations exhibited PDI values below 0.7 and negative zeta potentials, suggesting homogeneous size distribution and sufficient electrostatic stabilization, both of which are critical for colloidal stability in topical delivery systems. In this study, the particle size of SA-loaded liposomes ranged from 155.2 to 850.8 nm, indicating a relatively broad size distribution. Mi et al. prepared SA-loaded nanoliposomes using a similar thin-film hydration method; however, their formulations were subsequently extruded through 400 and 200 nm membranes, resulting in smaller and more uniform vesicles. Therefore, the broader particle size range and higher PDI values observed in our study may be attributed to the absence of an extrusion step. Extrusion can reduce large vesicles, break down multilamellar structures, and improve size homogeneity. Although the particle size of the liposomal formulations varied widely from 155.2 to 850.8 nm, statistical analysis showed that the lecithin amount, salicylic acid amount, and lecithin:cholesterol ratio had no significant effect on particle size ($p > 0.05$). This wide variation may therefore be attributed to formulation composition and process-related factors. The absence of an extrusion or homogenization step may have resulted in heterogeneous vesicle populations, including small unilamellar vesicles, larger multilamellar vesicles, and aggregated structures. Variations during thin-film hydration, sonication efficiency, and sample dispersion before DLS analysis may also have contributed to the broad size range.

The zeta potential values obtained in our study ranged from −28.55 ± 0.221 to −36.79 ± 0.601 mV, indicating relatively high negative surface charge and acceptable colloidal stability of the liposomal formulations. Similar to the findings reported by Mi et al., the

negative zeta potential values may be attributed to the interaction between salicylic acid and phospholipid components within the lipid bilayer (22). In addition, the incorporation of salicylic acid may alter phospholipid arrangement and surface charge density, thereby affecting vesicle stability. Compared with the study of Mi et al., the formulations developed in the present study exhibited comparable or slightly higher negative zeta potential values, suggesting stronger electrostatic repulsion and a lower tendency for particle aggregation.

Statistical analysis of the encapsulation efficiency results revealed that both salicylic acid amount and lecithin:cholesterol ratio had a significant positive effect on encapsulation efficiency ($p<0.05$). Increasing the salicylic acid amount and increasing the lecithin:cholesterol ratio from 2 to 4 enhanced the encapsulation efficiency of the formulations. In particular, formulations containing 40 mg salicylic acid with a lecithin:cholesterol ratio of 4 (F-4 and F-8) exhibited the highest encapsulation efficiency values of 37.69% and 36.06%, respectively. Nevertheless, the encapsulation efficiency values obtained in the present study were lower than those reported by Mi et al. (~73%) and Chandwani et al. (41%–72%) for salicylic acid-loaded liposomal systems (22, 23). These differences may be attributed to variations in preparation methods, lipid composition, drug-to-lipid ratio, and vesicle homogenization processes.

The process yields values of the liposomal formulations ranging from 54.27% to 72.22%. Although statistical analysis indicated that formulation parameters did not significantly affect process yield ($p>0.05$), variations among formulations may be associated with process-related factors occurring during liposome preparation and post-processing steps. Material loss during thin-film formation, hydration, transfer procedures, centrifugation, and lyophilization may have contributed to reduced process yield in some formulations.

The observed positive correlation between encapsulation efficiency and drug loading percentage further supports the effectiveness of the selected formulation strategy. Although the process yield varied among formulations, all values remained within an acceptable range for laboratory-scale liposome production. Taken together, these findings indicate that careful optimization of lipid composition and drug concentration is essential for achieving liposomes with balanced size, stability, and loading properties. Based on the overall characterization profile, formulation F-8 was identified as the optimal system and selected for subsequent release, morphology, and antimicrobial evaluation.

The lack of studies in the literature quantitatively evaluating the antimicrobial activity of conventional salicylic acid–loaded liposomes against *C. acnes* using standard MIC values further enhances the originality of the present work. In the study by Miranda et al. (2024), salicylic acid was formulated within nanostructured lipid carriers (NLCs) and demonstrated growth inhibition against *C. acnes* (ATCC® 6919™); however, standard antimicrobial parameters such as the MIC and MBC were not reported, and antimicrobial efficacy was assessed solely based on percentage growth inhibition (24). Similarly, antibacterial activity against *C. acnes* has been reported for salicylic acid–containing nanogels or supramolecular systems; however, in most of these studies, efficacy was assessed based on percentage inhibition or clinical improvement rather than quantitative MIC-based comparisons (25, 26). In this context, the quantitative MIC data generated in the present study using CLSI-compliant broth and agar dilution methods are particularly significant, as they clearly demonstrate the superiority of salicylic acid–loaded liposomes over the free form.

In the SA-LIPO-ARB, complete inhibition was not achieved at a concentration of 0.45 mg/mL; however, approximately 50% reduction in bacterial growth was observed. This finding suggests that arbutin does not act as a bacteriostatic agent against *C. acnes* per se but rather exerts a partial inhibitory or supportive modulatory effect. The literature indicates that arbutin is primarily recognized for its tyrosinase inhibitory and antioxidant properties, while evidence regarding its direct antibacterial activity remains limited (6). Accordingly, the observation that the MIC_{50} value was below 0.45 mg/mL in the present study suggests that arbutin may function as a modulating component within the liposomal system, contributing indirectly to the overall antimicrobial performance.

CONCLUSION

Overall, this study demonstrates that making salicylic acid within liposomal carrier systems significantly enhances its antimicrobial activity against *C. acnes*, enabling effective inhibition at lower concentrations. This approach appears promising for clinical applications, as it may reduce local irritation and limit reliance on conventional antibiotics. Nevertheless, the *in vitro* nature of the study represents a primary limitation, and the findings should be further validated using biofilm models, *in vivo* experiments, and clinical studies to confirm translational relevance.

Ethics Committee Approval: This study was conducted in accordance with the principles of the Declaration of Helsinki. As the study was based solely on in vitro experiments using a reference bacterial strain and did not involve human participants, human-derived materials, or animal subjects, ethics committee approval was not required.

Peer Review: Externally peer-reviewed.

Author Contributions: Conception/Design of study: G.K.K.; A.D.E.; Data Acquisition: G.K.K.; A.D.E.; Data Analysis/Interpretation: G.K.K.; A.D.E.; Drafting Manuscript: G.K.K.; A.D.E.; Critical Revision of Manuscript: G.K.K.; A.D.E.; Final Approval and Accountability: G.K.K.; A.D.E.

Conflict of Interest: The authors have no conflict of interest to declare.

Financial Disclosure This study was supported by the Trakya University Scientific Research Projects Coordination Unit (TÜBAP) under Project No. 2024/54.

Author Details

Gülcan Kuyucuklu-Kazan

[1] Kırklareli University, Faculty of Medicine, Department of Medical Microbiology, Kırklareli, Türkiye

0000-0003-1596-1659

Ahmet Doğan Ergin

[2] Trakya University, Faculty of Pharmacy, Department of Pharmaceutical Technology, Edirne, Türkiye

0000-0002-9387-0085 adoganergin@trakya.edu.tr

REFERENCES

1. Hazarika N. Acne vulgaris: new evidence in pathogenesis and future modalities of treatment. J Dermatolog Treat 2021; 32(3): 277-85.
2. Harvey A, Huynh TT. Inflammation and acne: putting the pieces together. J Drugs Dermatol 2014; 13(4): 459-63.
3. Marisa Gonzaga da Cunha FD, Carlos D. Apparecida Machado Filho, Glaucia Luciano da Veigave Fernando Fonseca. The relevance of sebum composition in the etiopathogeny of acne. Eur J Biol Res 2018; 8(1): 21-5.
4. Wiśniewska J, Klasik-Ciszewska S, Duda-Grychtoł K. Salicylic acid and its use in cosmetology. Aesth Cosmetol Med 2023; 12: 91-5.
5. Sinha P, Srivastava N, Rai VK, Mishra R, Ajayakumar PV, Yadav NP. A novel approach for dermal controlled release of salicylic acid for improved anti-inflammatory action: Combination of hydrophilic-lipophilic balance and response surface methodology. J Drug Deliv Sci Technol 2019; 52: 870-84.
6. Boo YC. Arbutin as a skin depigmenting agent with antimelanogenic and antioxidant properties. Antioxidants (Basel) 2021; 10(7): 1129.
7. Dell'Annunziata F, Cometa S, Della Marca R, Busto F, Folliero V, Franci G, et al. In vitro antibacterial and anti-inflammatory activity of Arctostaphylos uva-ursi leaf extract against Cutibacterium acnes. Pharmaceutics 2022; 14(9): 1952.
8. Taylor S, Elbuluk N, Grimes P, Chien A, Hamzavi I, Alexis A, et al. Treatment recommendations for acne-associated hyperpigmentation: Results of the Delphi consensus process and a literature review. J Am Acad Dermatol 2023; 89(2): 316-23.
9. Braido B, Rukavina Z, Grimstad Ø, Franzè S, Cilurzo F, Vanić Ž, et al. Liposomes-in-hydrogel for topical drug delivery: Mechanical, kinetic, and biological insights. J Drug Deliv Sci Technol 2025; 113: 107380.
10. Lauer AC, Ramachandran C, Lieb LM, Niemiec S, Weiner ND. Targeted delivery to the pilosebaceous unit via liposomes. Adv Drug Deliv Rev 1996; 18(3): 311-24.
11. Lademann J, Patzelt A, Richter H, Antoniou C, Sterry W, Knorr F. Determination of the Cuticle thickness of human and porcine hairs and their potential influence on the penetration of nanoparticles into the hair follicles. J Biomed Opt 2009; 14(2): 021014.
12. Ergin AD, Oltulu Ç, Türker NP, Demirbolat GM. In vitro hepatotoxicity evaluation of methotrexate-loaded niosome formulation: fabrication, characterization and cell culture studies. Turk J Med Sci 2023; 53(4): 872-82.
13. Sanchez A, Tobio M, Gonzalez L, Fabra A, Alonso MJ. Biodegradable micro- and nanoparticles as long-term delivery vehicles for interferon-alpha. Eur J Pharm Sci 2003; 18(3-4): 221-9.
14. Ergin AD, Üner B, Balcı Ş, Demirbağ Ç, Benetti C, Oltulu Ç. Improving the bioavailability and efficacy of coenzyme Q10 on Alzheimer's Disease through the arginine-based proniosomes. J Pharm Sci 2023; 112(11): 2921-32.
15. Clinical and Laboratory Standards Institute. Methods for antimicrobial susceptibility testing of anaerobic bacteria. Approved standard. 8th ed. CLSI document M11-A8. Wayne (PA): Clinical and Laboratory Standards Institute; 2012.
16. Lee YB, Byun EJ, Kim HS. Potential role of the microbiome in acne: a comprehensive review. J Clin Med 2019; 8(7): 987.
17. Nakatsuji T, Kao MC, Fang JY, Zouboulis CC, Zhang L, Gallo RL, et al. Antimicrobial property of lauric acid against Propionibacterium acnes: its therapeutic potential for inflammatory acne vulgaris. J Invest Dermatol 2009; 129(10): 2480-8.
18. Liu Y, Dan Y, Yang J, He X, Liu J, Yi Y, et al. Clinical efficacy of a salicylic acid-containing gel on acne management and skin barrier function: a 21-day prospective study. J Cosmet Dermatol 2025; 24(7): e70353.
19. Pannu J, McCarthy A, Martin A, Hamouda T, Ciotti S, Ma L, et al. In vitro antibacterial activity of NB-003 against Propionibacterium acnes. Antimicrob Agents Chemother 2011; 55(9): 4211-7.
20. Dragicevic N, Maibach HI. Liposomes and other nanocarriers for the treatment of acne vulgaris: improved therapeutic efficacy and skin tolerability. Pharmaceutics 2024; 16(3): 309.
21. Fang JY, Chou WL, Lin CF, Sung CT, Alalaiwe A, Yang SC. Facile biofilm penetration of cationic liposomes loaded with DNase I/Proteinase K to eradicate Cutibacterium acnes for treating cutaneous and catheter infections. Int J Nanomedicine 2021; 16: 8121-38.
22. Mi Z, Mu H, Han Y, Liu R, Niu B, Wang G, et al. Salicylic acid nanoliposomes treatment alleviates chilling injury in postharvest baby ginger by regulating membrane lipid metabolism. Food Chem 2025; 482: 144137.
23. Chandwani S, Saini TR, Soni R, Paswan SK, Soni PK. Box-Behnken design optimization of salicylic acid loaded liposomal gel formulation for treatment of foot corn. Int J Appl Pharm 2023; 15(3): 220-33.
24. Miranda RG, Martins TS, Almeida LS, Napoleão MO, Lopes PS, Leite-Silva VR, et al. Use of postbiotics and salicylic acid in a nanostructured system to control Cutibacterium acnes. Contrib Cienc Soc 2024; 17(6): e7844.
25. Bilal H, Xiao Y, Khan MN, Chen J, Wang Q, Zeng Y, et al. Stabilization of Acne Vulgaris-associated microbial dysbiosis with 2% supramolecular salicylic acid. Pharmaceuticals (Basel) 2023; 16(1): 87.
26. Ye CX, Yi J, Su Z, Gao X, Jiang X, Yu N, et al. 2% supramolecular salicylic acid hydrogel vs. adapaline gel in mild to moderate acne vulgaris treatment: A multicenter, randomized, evaluator-blind, parallel-controlled trial. J Cosmet Dermatol 2024; 23(6): 2125-34.

İSTANBUL UNIVERSITY PRESS

Experimed 2026, 16 (2): 137–147

https://doi.org/10.26650/experimed.1938986

Submitted: 28.04.2026
Revision Requested: 10.07.2026
Last Revision Received: 13.07.2026
Accepted: 16.07.2026
Published Online 12.08.2026

Experimed

Research Article

Open Access

Role of Sodium Phenylbutyrate and Suramin in the Prevention of Ulcerative Colitis Induced by Dextran Sulfate Sodium

Cansu Özal-Coşkun [1], Ecem Fatma Karaman [2], Sibel Özden [3], Engin Kaptan [4] & Pelin Arda [4]

[1] Biruni University, Faculty of Pharmacy, Department of Biochemistry, İstanbul, Türkiye
[2] Biruni University, Faculty of Pharmacy, Department of Pharmaceutical Toxicology, İstanbul, Türkiye
[3] Istanbul University, Faculty of Pharmacy, Department of Pharmaceutical Toxicology, İstanbul, Türkiye
[4] Istanbul University, Faculty of Science, Department of Biology, İstanbul, Türkiye

Abstract

Objective: Ulcerative colitis is a relapsing inflammatory condition confined to the colonic mucosa in which persistent immune activation is accompanied by oxidative damage and epithelial disruption. This study investigated whether sodium phenylbutyrate (PBA) and suramin could mitigate these pathological changes in a mouse model of experimentally induced colitis.

Materials and Methods: Following induction of colitis with dextran sulfate sodium (DSS), the efficacy of PBA and suramin was evaluated by clinical disease activity and histological scoring. Using immunohistochemical and spectrophotometric approaches, changes in proliferative activity, antioxidant enzymes, and oxidative stress indicators were analyzed. Western blot analysis was performed to assess cytokine, cyclooxygenase-2, and active caspase-3 levels together with histone 3 lysine 9 trimethylation modification; signal transducer and activator of transcription (*STAT*)*1*, *STAT3*, and sirtuin (*SIRT*) gene expression were quantified by quantitative reverse transcription-polymerase chain reaction (qRT-PCR).

Results: DSS aggravated oxidative stress and inflammatory responses while suppressing proliferative activity, anti-inflammatory signaling, and antioxidant defense systems in colon tissue. Treatment with PBA or suramin partially reversed these alterations, improving redox balance and inflammatory status and modulating gene expression and histone modifications.

Conclusion: These results suggest that PBA and suramin exert protective effects against DSS-induced colitis through the modulation of apoptosis, inflammation, and oxidative stress, supporting their potential therapeutic value in inflammatory bowel diseases.

Keywords Sodium Phenylbutyrate · Suramin · Ulcerative Colitis · Dextran Sulfate Sodium · Mice

Citation: Özal-Coşkun, C., Karaman, E., Özden, S., Kaptan, E. & Arda, P. Role of sodium phenylbutyrate and suramin in the prevention of ulcerative colitis induced by dextran sulfate sodium. Experimed 2026; 16(2): 137-147. DOI: 10.26650/experimed.1938986

This work is licensed under Creative Commons Attribution-NonCommercial 4.0 International License.

© 2026. Özal-Coşkun, C., Karaman, E., Özden, S., Kaptan, E. & Arda, P.

Corresponding author: Pelin Arda parda@istanbul.edu.tr

INTRODUCTION

Ulcerative colitis is a relapsing inflammatory disorder of the colon mucosa marked by sustained immune activation, epithelial breakdown, and tissue damage, influenced by genetic susceptibility as well as environmental factors including stress, alcohol, and smoking. Although its pathogenesis is not fully elucidated, increased pro-inflammatory cytokine production, oxidative stress, and decreased antioxidant enzyme activity are key contributors to disease development (1). Current therapies primarily offer symptomatic relief rather than addressing the underlying causes, and prolonged use of anti-inflammatory drugs may result in adverse effects such as diabetes, hepatitis, and hepatotoxicity, underscoring the need for new therapeutic strategies. Experimental colitis triggered by dextran sulfate sodium (DSS) has become a standard model, as it recapitulates key clinical and histopathological aspects of human ulcerative colitis (2).

Histone deacetylase inhibitors (HDACi) induce chromatin relaxation through increased histone acetylation, leading to altered gene expression profiles that regulate immune responses and cellular redox balance, including antioxidant and oxidative stress pathways. Sodium phenylbutyrate (PBA), an orally bioavailable HDAC inhibitor, attenuates inflammatory and oxidative stress responses, reduces pro-inflammatory cytokine expression, upregulates glutathione (GSH), and decreases reactive oxygen species (ROS) generation. (3). Suramin, a class III HDAC (Sirtuin: SIRTs) inhibitor, is also used in the treatment of onchocerciasis and human African trypanosomiasis and has been reported to attenuate inflammatory damage by interfering with cytokine–receptor interactions and reducing cytokine expression (4).

Ulcerative colitis is characterized by a complex interplay among inflammatory signaling, oxidative stress, impaired epithelial regeneration, and epigenetic dysregulation. These processes are closely interconnected through signaling pathways, such as signal transducer and activator of transcription (STAT)1/STAT3, and epigenetic regulators, including SIRTs and histone modifications, which collectively influence inflammatory gene expression, epithelial homeostasis, cellular survival, and antioxidant defense (5, 6). Since HDAC inhibitors can modulate both intracellular signaling pathways and epigenetic mechanisms, an integrated assessment of molecular, biochemical, and histopathological alterations may provide a more comprehensive understanding of the therapeutic mechanisms of PBA and suramin in DSS-induced colitis.

The protective mechanisms of PBA in experimental colitis are still not completely understood. In addition, the impact of suramin in this model has not been extensively studied. The aim of this study was to comparatively evaluate the therapeutic potential of sodium phenylbutyrate and suramin by assessing their effects on colon morphology, cell proliferation, histone modifications, inflammatory mediators, oxidative stress, and antioxidant defenses in DSS-induced colitis.

MATERIALS AND METHODS

In vivo Experimental Model

Ethical approval for all animal experiments was obtained from the Local Ethics Committee for Animal Experiments of Istanbul University (25.02.2016; No: 07). Forty-eight male C57BL/6 mice (20–25 gram and 8–10 weeks) were included in the study. Randomization was used to assign the animals to six groups. Twenty-four hours after the final administration, anesthesia was induced with sodium pentobarbital (150 mg/kg). Mice were exposed to 3% (w/v) DSS (36,000–50,000 Da; MP Biomedicals, California, USA) provided in the drinking water over five days as a means of inducing acute colitis; the solution was prepared daily in sterile autoclaved tap water based on previous protocols (7). Body weight and fluid intake were recorded daily, and injections were administered at a fixed time each day, 0.1 mL per day. The experimental design is summarized in Figure 1. Forty-eight mice were randomly assigned to six groups (n=8 per group): Control, PBA, suramin, DSS, PBA + DSS, and suramin + DSS. Control animals received sterile drinking water, whereas colitis was induced by administration of 3% DSS starting on day 3 and continuing for 5 days. PBA and suramin treatments were initiated on day 1 and administered once daily throughout the 7-day experimental period according to the protocol shown in Figure 1. All injections were performed at the same time each day. Twenty-four hours after the final treatment, mice were anesthetized and colon tissues were collected for subsequent analyses.

Assessment of Changes in Body Weight Percentage and Colon Length

Mice body weight was recorded daily at a consistent time, and percentage weight change was calculated relative to baseline. On the final day, colons were excised under anesthesia, cleared of fecal content, and measured for statistical analysis.

Determination of Disease Activity Index

Disease activity index (DAI) was used for the clinical evaluation of colitis, as described by Cooper et al. (2) (maximum score: 4). Scores were recorded daily in DSS-treated mice, and animals with a final DAI of ≥3 were considered colitis.

Histopathologic Evaluation

Colon tissue samples were fixed in Bouin's solution prior to paraffin embedding. After sectioning at 5 µm, the slides were stained with hematoxylin and eosin (H&E). Histopathological evaluation was conducted using light microscopy (Olympus BX53F, Olympus Corporation, Japan), and images were acquired with a digital imaging system (DP27-CU). Histological damage was assessed according to

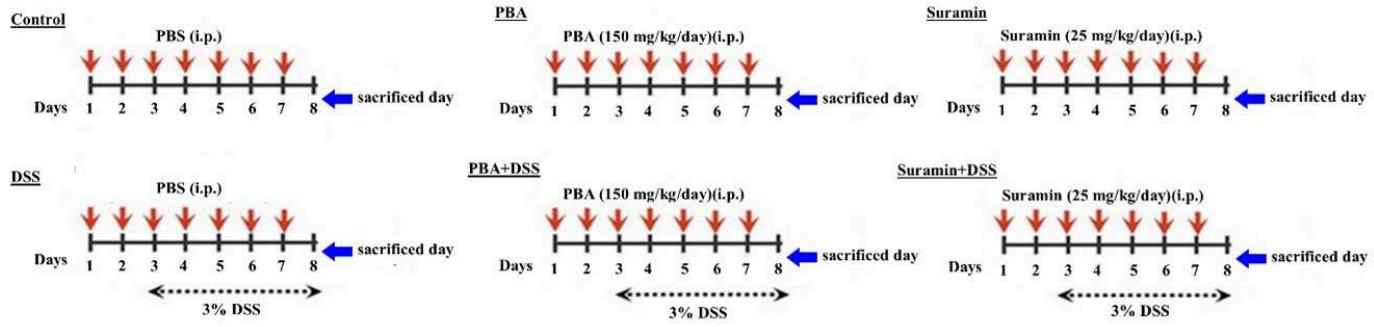


Figure 1. Schematic diagram of experimental design according to groups. PBA: phenylbutyrate; DSS: dextran sulfate sodium; PBS: phosphate buffered saline.

Dieleman et al. (8) (Table 1). Histopathological scoring was performed independently by two observers. Multiple microscopic fields from each tissue section were examined before assigning the final histological score.

Table 1. Colitis scoring system developed by Dieleman et al. (8)

Feature graded	Grade	Description
Severity of Inflammation	0	None
	1	Slight
	2	Moderate
	3	Severe
Spread of inflammation	0	None
	1	Mucosa
	2	Mucosa and submucosa
	3	Transmural
Crypt damage	0	None
	1	Basal 1/3 damaged
	2	Basal 2/3 damaged
	3	Only surface epithelium intact
	4	Entire crypt and epithelium lost
Percent involvement	1	1–25%
	2	26–50%
	3	51–75%
	4	76–100%

Immunohistochemical Analysis

Following fixation in 10% buffered formalin, colon tissues were paraffin-embedded, sectioned at 4 µm, and analyzed for cell proliferation by Ki-67 immunostaining using the streptavidin–biotin–peroxidase method, with Mayer's hematoxylin as a counterstain. The proliferation index was determined by counting 1000 cells in at least five randomly selected, non-overlapping high-power fields (×400 magnification) from each section and expressed as a percentage. Ki-67-positive cells were independently evaluated by two observers.

Biochemical Analyses

Colon tissues were homogenized in physiological saline (0.9% sodium chloride solution) (10 mL/g), centrifuged at 4°C, 10,000 × g for 20 minutes, and the supernatants were collected for spectrophotometric analyses. Total protein was quantified by the Lowry assay (9) using bovin serum albumin (BSA) as a reference standard. Oxidative stress parameters, including malondialdehyde (MDA) (10), and GSH (11), as well as antioxidant enzymes catalase (CAT) (12), glutathione peroxidase (GPx) (13), and superoxide dismutase (SOD) (14), were determined using established biochemical assays.

ELISA

Colon tissue samples (25 mg) were homogenized in 500 µL of lysis buffer and centrifuged at 1500×g for 15 minutes. Myeloperoxidase (MPO) levels were determined using a mouse-specific sandwich ELISA kit (HK210, Hycult Biotech, Netherlands). All ELISA samples were analyzed in duplicate, and the mean of the duplicate measurements was used for statistical analysis. Optical density was measured at 450 nm, and concentrations were derived from a standard curve.

Western Blotting

Western blotting was used to analyze the protein levels of tumor necrosis factor-α (TNF-α), interleukin (IL)-1β, IL-6, IL-10, cyclooxygenase-2 (COX-2), caspase-3, and Histone H3 Lysine 9 trimethylation (H3K9me3) in colon tissues. Tissues were homogenized in radioimmunoprecipitation assay (RIPA) buffer (with protease inhibitor cocktail) (Thermo Fisher Scientific, USA). The Bradford assay was used to determine protein concentrations (15). Electrophoresis was performed on 4–12% Bis-Tris gels (Thermo Fisher Scientific, USA), followed by dry transfer. Blocking was carried out with 5% BSA in tris-buffered saline, 0.1% tween-20 (TBST), and antibody dilutions were prepared with 1% BSA in TBST. Protein expression levels were normalized to glyceraldehyde-3-phosphate dehydrogenase (GAPDH) by densitometric analysis. Antibody dilutions and catalogue numbers are provided in Table 2.

Table 2. Primary and secondary antibodies used in Western blot analysis and their dilution rates

Antibody	Brand / Catalog No.	Dilution
Caspase-3	NOVUS / NB100-56113	1:1000
IL-10	Boster / A00021	1:250
IL-1β	NOVUS / NB600-633	1:1000
IL-6	Boster / A00102-2	1:250
TNF-α	Abcam / ab9739	1:1000
COX-2	NOVUS / NB100-689	1:1000
GAPDH	Santa Cruz / sc-25778	1:1000
H3K9me3	Millipore / 07-442	1:1000
H3	Thermo Fisher / PA516183	1:2000
Goat anti-rabbit IgG-HRP	Santa Cruz / sc-2030	1:5000

Quantitative Reverse Transcription-Polymerase Chain Reaction

Quantitative reverse transcription-polymerase chain reaction (qRT-PCR) was performed to evaluate the expression of *STAT1* and *3*, *SIRT 1, 2, 3*, and *5* using the BioLine SensiFast™ SYBR® No-Rox Kit (Bioline, London, UK) on a LightCycler® 480 Instrument II (Roche Diagnostics, Germany). Table 3 summarizes the primer sequences and annealing temperatures used in this study. β-actin was used as the reference gene for normalization of gene expression levels. No-template controls (replacing cDNA with water) were included in each run. All samples were analyzed in triplicate, and mean Ct values were calculated. Relative mRNA levels were quantified using the ΔΔCt method (16), and the results were expressed as fold changes normalized to the control group.

Table 3. Primers used qRT-PCR analysis of STAT pathway and histone deacetylase genes and their corresponding annealing temperatures

Gene name	Forward (5′–3′) Reverse (5′–3′)	Ta (°C)	Reference
STAT1	F: GACTTCAGACACAGAAATCAACTC R: TTGACAAAGACCACGCCTT	57	(17)
STAT3	F: CATGTCAAACGTGAGCGACT R: GGAAATAACGGTGAAGGTGCT	57	(17)
SIRT1	F: CCTTTCAGAACCACCAAAGC R: TCCCACAGGAGACAGAAACC	58	(18)
SIRT2	F: GGCAGAGATGGACTTCCTGA R: TGTAGCGTGTCACTCCTTCG	60	(18)
SIRT3	F: CAGCTACATGCACGGTCTGT R: AGATCTGCCAAAGCGAAGTC	58	(18)
SIRT5	F: TGGAAATCCACGGAACCTTA R: GGATTCTGGCGTCTTGAGTC	57	(18)
β-Actin	F: GGGAATGGGTCAGAAGGACT R: CTTCTCCATGTCGTCCCAGT	60	(19)

Statistical Analysis

Data were analyzed using SPSS 23.0 software (SPSS Inc., Chicago, IL, USA). DAI was assessed using Kruskal–Wallis and Mann–Whitney U tests, whereas other variables were evaluated by one-way ANOVA with independent t-tests for multiple comparisons. Results are reported as mean ± standard error (SE) of the mean. Values less than $p<0.05$ were considered statistically significant.

RESULTS

Body Weight and Colon Length Alterations in Mice with Acute Colitis

Percentage body weight changes on day 8 are presented in Figure 2A, and statistical comparisons are detailed in the figure legend. Body weight showed a reduction in the DSS group relative to the control group, whereas both the PBA+DSS and suramin+DSS groups showed an increase relative to the DSS group. Colon length data are presented in Figure 2B, and statistical comparisons are provided in the figure legend. Colon length was reduced in the DSS group compared with the control group. In the PBA+DSS group, colon length remained lower than that of the control and PBA groups but increased compared with the DSS group. In the suramin+DSS group, colon length was reduced compared with both the control and suramin groups.

DAI Score Findings

The 5-day changes in DAI following DSS treatment are presented in Figure 2C, and statistical comparisons are provided in the figure legend. DAI values were persistently elevated in the DSS group across all time points relative to controls. Similarly, both the PBA+DSS and suramin+DSS groups exhibited elevated DAI levels compared with controls throughout the observation period, although the magnitude of the increase varied over time. In contrast, DAI values were reduced in the PBA+DSS group compared with the DSS model group on days 4 and 5. A comparable reduction was also observed in the suramin+DSS group relative to the DSS group at the time points.

Histopathological Findings

Histological colitis scores (Figure 2D) were increased in the DSS group versus controls, whereas both the PBA+DSS and suramin+DSS groups showed reductions relative to the DSS group. Statistical comparisons are provided in the figure legend. Control colons exhibited normal histology (Figure 2E). PBA and suramin alone largely preserved normal tissue morphology with minimal inflammatory infiltration. In contrast, DSS treatment induced marked histopathological damage, including inflammatory cell infiltration, epithelial disruption, crypt loss, and mucosal edema. Both PBA+DSS and suramin+DSS groups showed clear histological improvement, with reduced tissue injury

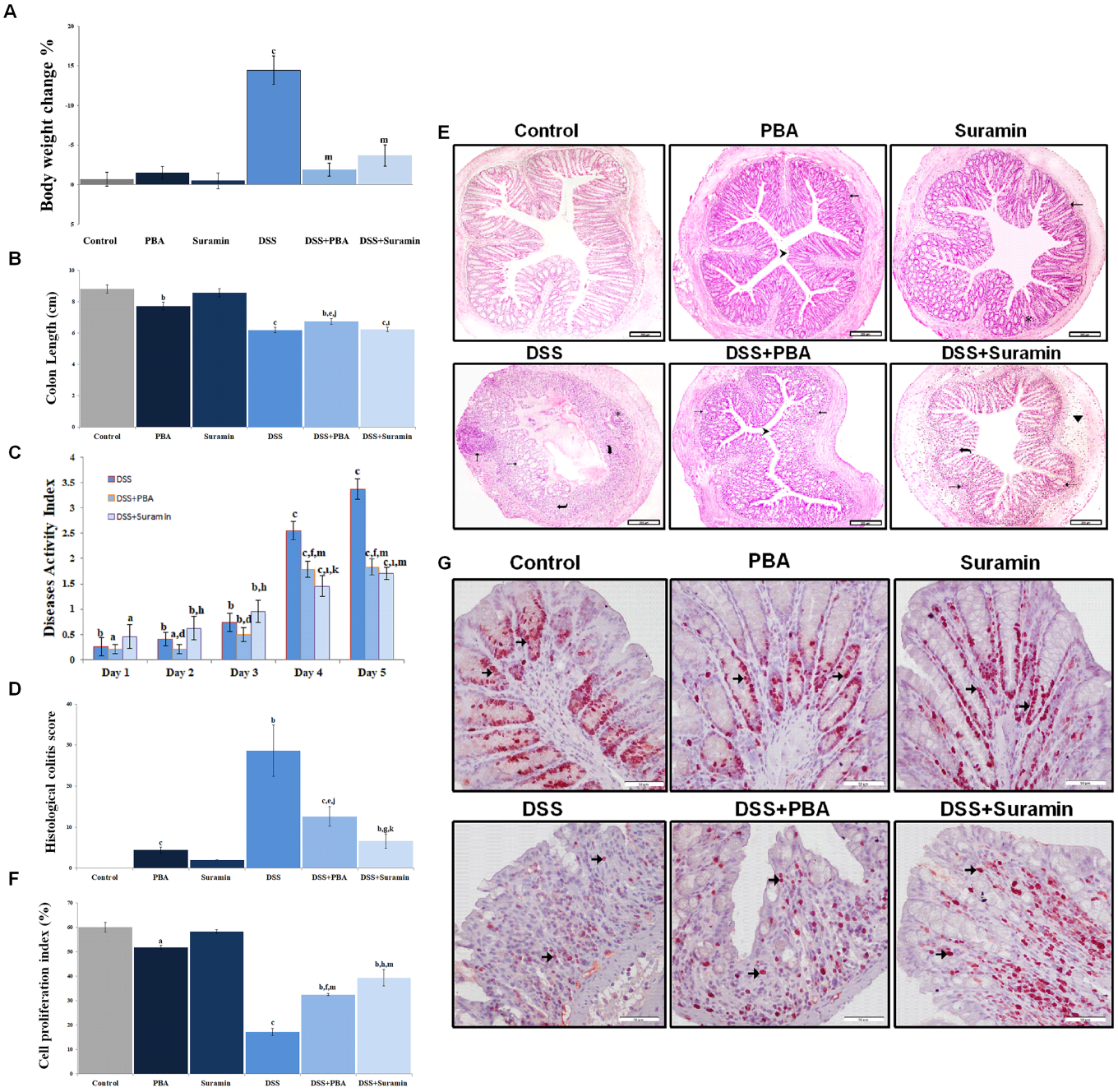


Figure 2. Findings regarding body weight change (A), colon length (B), disease activity index (C) in experimental groups. Alteration in histological colitis score among the groups (D) Hematoxyline & Eosin (H&E) staining in distal colon sections of the mice in different groups. Inflammatory cell infiltration (→), epithelial loss (➢), necrosis (*), vacuolar hydropic degeneration in crypt cells (→), diffuse crypt loss (⇝) and submucosal edema (►). Scale bar is 200 µm (E). Proliferation in colon mucosa. Graph (F) represents changes in cell proliferation index (%) among the groups the index was obtained by Ki-67 immunohistochemistry in the colon tissue of mice (G). Proliferating cells marked with (➡). Scale bar is 50 µm. Images of H&E-stained colon tissue were captured at 100X for overall histology, while Ki-67 sections were shown at 400X to clearly visualize proliferative cells. The data were presented as mean ± standard error (SE). a: ($p<0.05$) vs control group; b: ($p<0.01$) vs control group; c: ($p<0.001$) vs control group; d: ($p<0.05$) vs PBA group; e: ($p<0.01$) vs PBA group; f: ($p<0.001$) vs PBA group; g: ($p<0.05$) vs Suramin group; h: ($p<0.01$) vs Suramin group; ı: ($p<0.001$) vs Suramin group; j: ($p<0.05$) vs DSS group; k: ($p<0.01$) vs DSS group; m: ($p<0.001$) vs DSS group. All statistical tests were performed using ANOVA/t-test, only Kruskal-Wallis, and Mann-Whitney U for E figure. PBA: phenylbutyrate; DSS: dextran sulfate sodium.

and preservation of colon morphology compared with DSS-treated animals.

Immunohistochemical Findings

Ki-67 immunohistochemical staining is presented in Figure 2G, and the proliferation index (%) is shown in Figure 2F. Statistical comparisons are provided in the figure legend. The proliferation

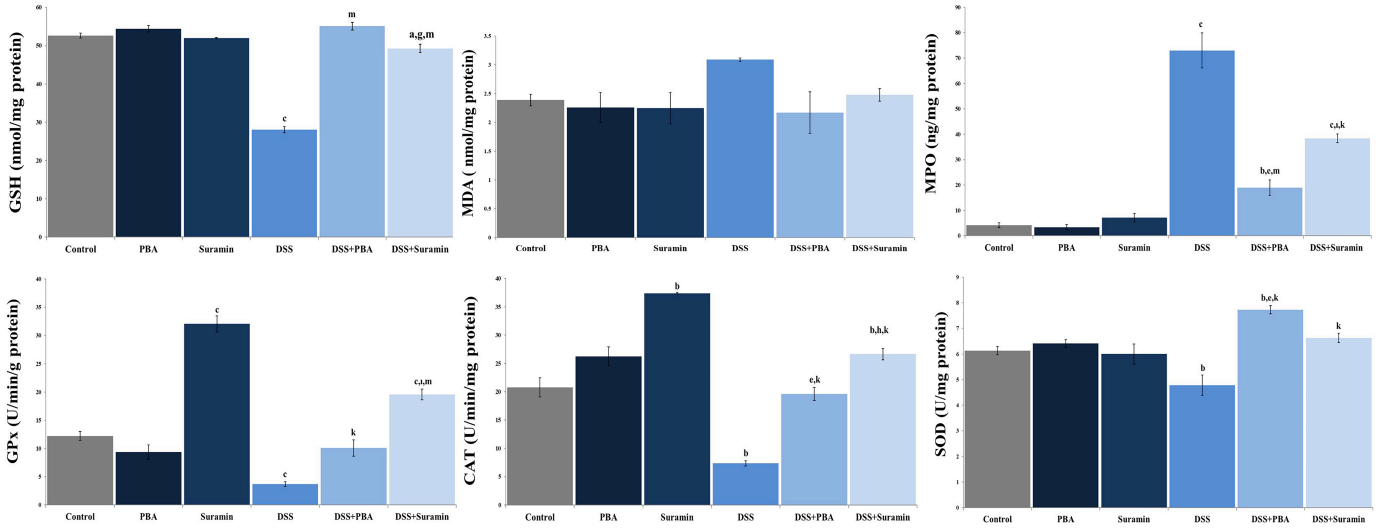


Figure 3. Changes in oxidative stress and antioxidant enzyme activities in the mouse colon homogenates of experimental groups. A dramatic decrease in the GSH level of the DSS-treated group and its decrease in suramin+DSS. Statistically insignificant increase in the MDA level of DSS group. Increased MPO level reduced in PBA+DSS and suramin+DSS. GPx, CAT and SOD enzyme activities were decreased when DSS was treated but their activities elevated when PBA and suramin were injected. The data were presented as mean ± standard error (SE). a: ($p<0.05$) vs control group; b: ($p<0.01$) vs control group; c: ($p<0.001$) vs control group; d: ($p<0.05$) vs PBA group; e: ($p<0.01$) vs PBA group; f: ($p<0.001$) vs PBA group; g: ($p<0.05$) vs suramin group; h: ($p<0.01$) vs suramin group; ı: ($p<0.001$) vs suramin group; j: ($p<0.05$) vs DSS group; k: ($p<0.01$) vs DSS group; m: ($p<0.001$) vs DSS group. All statistical tests were performed using ANOVA/t-test. PBA: phenylbutyrate; DSS: dextran sulfate sodium; GSH: glutathione; MDA: malondialdehyde; MPO: myeloperoxidase; GPx: glutathione peroxidase; CAT: catalase; SOD: superoxide dismutase.

index was reduced in the DSS and PBA groups compared with controls, while no significant alteration was detected in the suramin group. In the PBA+DSS group, Ki-67-positive cells decreased compared with the control and PBA groups but increased compared with DSS. Similarly, the suramin + DSS group showed reduced proliferation compared with the control and suramin groups, yet an increase relative to DSS.

Biochemical Findings

The biochemical findings from colon tissue homogenates are presented in Figure 3, and statistical comparisons are provided in the figure legend. GSH levels and the activities of GPx, CAT, and SOD decreased in the DSS group versus the control group. In both the PBA+DSS and suramin+DSS groups, GSH levels and antioxidant enzyme activities increased relative to the DSS group. GPx activity in the suramin+DSS group remained lower than that in the suramin group. CAT activity increased in the suramin group versus control, whereas the increase observed in the PBA group did not reach statistical significance. SOD activity in the PBA+DSS group increased above the levels observed in both the control and PBA groups. MDA levels increased markedly in the DSS group and decreased in the PBA+DSS and suramin+DSS groups, although these reductions were not statistically significant.

ELISA Analysis Findings

The distribution of MPO levels in colon tissue is presented in Figure 3, and statistical comparisons are provided in the figure legend. MPO levels increased markedly in the DSS group relative to the control group. In both the PBA+DSS and suramin+DSS groups, MPO levels decreased significantly relative to the DSS group. However, MPO levels in the suramin+DSS group remained higher than those observed in the suramin and control groups.

Western Blotting Analysis Findings

The results are presented in Figures 4 and 5, and statistics are reported in the figure legends. Active caspase-3 levels increased across all experimental groups relative to the control group, with the most pronounced elevation observed in the DSS group. In both the PBA+DSS and suramin+DSS groups, active caspase-3 levels decreased relative to the DSS group.

TNF-alpha, IL-1β and IL-6 levels increased markedly following DSS treatment and were reduced in both PBA+DSS and suramin+DSS groups. In contrast, IL-10 levels were lowest in the DSS group and increased after administration of PBA or suramin. IL-10 expression also increased in the PBA and suramin groups compared with controls, with the highest level observed in the suramin + DSS group.

COX-2 expression increased in all experimental groups relative to controls and reached its maximum in the DSS group. Both PBA and suramin attenuated this increase in DSS-treated mice.

H3K9me3 modification (Figure 5) decreased in the DSS group compared with controls. H3K9me3 levels increased in the PBA group, whereas no significant change was observed in the suramin group. In DSS-treated mice, both PBA and suramin increased H3K9me3 expression relative to the DSS group, with the highest level detected in the PBA+DSS group.

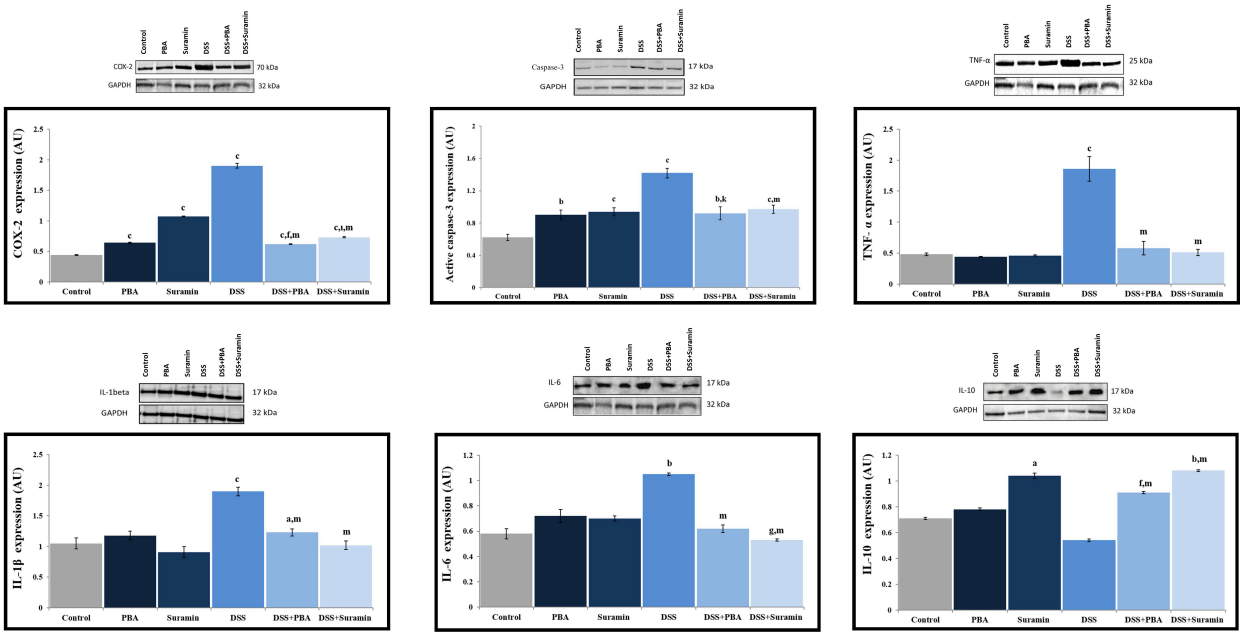


Figure 4. Changes in the level of COX-2 and active caspase-3, and cytokine expressions in different experimental groups analyzed by western blotting. COX-2 and active caspase-3 level increased when DSS was treated in animals but their levels were reversed when PBA and suramin were injected. Analog patterns were also observed in the expression levels of TNF-α, IL-1β and IL-6. The expression of IL-10, an anti-inflammatory cytokine, reduced when DSS was treated in animals but its level was increased in PBA and suramin-injected animals. The data were presented as mean ± standard error (SE). a: ($p<0.05$) vs control group; b: ($p<0.01$) vs control group; c: ($p<0.001$) vs control group; d: ($p<0.05$) vs PBA group; e: ($p<0.01$) vs PBA group; f: ($p<0.001$) vs PBA group; g: ($p<0.05$) vs suramin group; h: ($p<0.01$) vs suramin group; ı: ($p<0.001$) vs suramin group; j: ($p<0.05$) vs DSS group; k: ($p<0.01$) vs DSS group; m: ($p<0.001$) vs DSS group. All statistical tests were performed using ANOVA/t-test. PBA: phenylbutyrate; DSS: dextran sulfate sodium; COX-2: cyclooxygenase-2; TNF-α: tumor necrosis factor-α; IL: interleukin; GAPDH: glyceraldehyde-3-phosphate dehydrogenase.

Quantitative RT-PCR Findings

The results of *STAT1* and *3*, *SIRT1, 2, 3*, and *5* mRNA expression in colon tissue are presented in Figure 6, and statistical comparisons are provided in the corresponding figure legends.

STAT1 expression was reduced in all experimental groups compared with controls, with the lowest level observed in the DSS group (81% decrease). *STAT1* expression was increased in the PBA+DSS group compared with the DSS group, while a slight decrease was observed in the suramin+DSS group relative to the control group.

Among all groups, the highest level of *STAT3* expression was observed in the PBA group (2.62 times) when compared to the control group. *STAT3* was also increased in DSS, PBA+DSS, and suramin+DSS groups versus controls. Compared with the DSS group, *STAT3* expression decreased in the PBA group but increased further in the suramin+DSS group.

SIRT1 expression was increased in the DSS group (2.67-fold), whereas it decreased in the suramin group (48%). Both the PBA+DSS and suramin+DSS groups showed reduced *SIRT1* expression compared with DSS.

SIRT2 expression was reduced in the suramin group relative to the control group (90%), whereas it increased in the DSS group relative to controls. Both PBA+DSS and suramin+DSS groups also showed decreased *SIRT2* expression relative to DSS.

SIRT3 expression was decreased in the sodium phenylbutyrate and suramin groups compared with controls (44% and 58%, respectively), whereas it showed a slight increase in the DSS, PBA+DSS, and suramin+DSS groups compared with controls. However, both treatment groups showed reduced *SIRT3* expression compared with DSS.

SIRT5 expression was increased in the DSS group relative to controls (1.44-fold), while both PBA+DSS and suramin+DSS groups showed decreased *SIRT5* expression relative to DSS (55.55% and 48.61%, respectively).

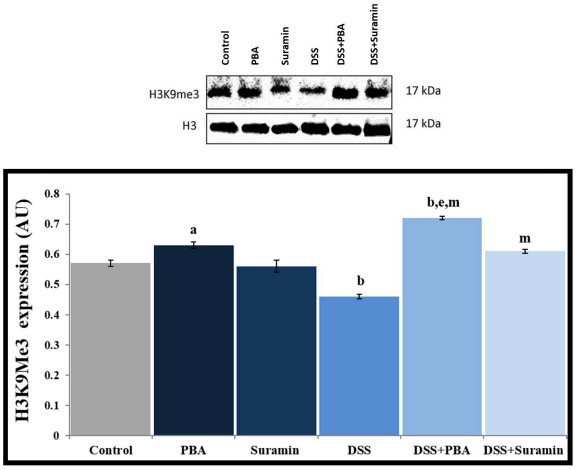


Figure 5. Alterations in H3K9me3 expression levels in colon tissues of experimental groups. DSS treatment reduced H3K9me3 expression but its expression improved when PBA and suramin were injected. The data were presented as mean ± standard error (SE). a: ($p<0.05$) vs control group; b: ($p<0.01$) vs control group; c: ($p<0.001$) vs control group; d: ($p<0.05$) vs PBA group; e: ($p<0.01$) vs PBA group; f: ($p<0.001$) vs PBA group; g: ($p<0.05$) vs suramin group; h: ($p<0.01$) vs suramin group; ı: ($p<0.001$) vs suramin group; j: ($p<0.05$) vs DSS group; k: ($p<0.01$) vs DSS group; m: ($p<0.001$) vs DSS group. All statistical tests were performed using ANOVA/t-test. PBA: phenylbutyrate; DSS: dextran sulfate sodium; H3K9me3: histone H3 Lysine 9 trimethylation.

DISCUSSION

The DSS model of colitis is extensively used because it closely mimics human ulcerative colitis, reproducing both clinical signs and histopathological changes, including mucosal ulceration, crypt loss, inflammatory cell infiltration, and necrosis (20). Five-day exposure to 3% (w/v) DSS resulted in acute colitis in C57BL/6 mice, in agreement with previous reports, as reflected by clinical manifestations, elevated DAI scores, colon shortening, and characteristic histopathological changes (21).

HDACi reduce inflammation by modulating T cells, macrophages, and cytokine signaling involved in colonic inflammation (22). In DSS colitis models, PBA administered intraperitoneally or orally has been shown to attenuate disease severity by reducing DAI scores, preventing colon shortening, decreasing inflammatory cytokines, and improving histopathological damage (23). Consistent with these findings, treatment with PBA (150 mg/kg for 7 days) reduced DSS-induced colitis, as evidenced by lower DAI scores and preservation of colon length. Similarly, suramin at 25 mg/kg significantly reduced DSS-induced disease severity and DAI scores. Suramin modulates nerve excitability and intestinal motility; however, its effects in DSS-induced colitis remain largely unexplored.

Imbalance in the regulation of epithelial cell turnover in the colon contributes to epithelial barrier disruption in ulcerative colitis (24). In this study, DSS exposure significantly decreased epithelial cell proliferation while increasing apoptosis compared with controls. Although HDACi are generally associated with anti-proliferative effects in cancer models and PBA has been reported to suppress proliferation in oncological settings (25), in the present colitis model, PBA increased colonic cell proliferation and reduced caspase-3 expression, suggesting a protective effect on epithelial integrity by limiting apoptosis. Previous studies have demonstrated that suramin exerts antiproliferative effects in cancer cell lines (26), but its effects in ulcerative colitis are not well defined. Here, suramin further enhanced epithelial proliferation, reduced apoptosis more effectively than PBA, and resulted in a higher proliferation index compared with PBA.

Oxidative stress, largely driven by ROS generated by neutrophils and macrophages, plays a key role in the initiation and progression of ulcerative colitis. In DSS-induced colitis, elevated ROS levels and reduced antioxidant enzyme activities have been reported (27), which is consistent with the present findings. PBA has been shown to attenuate oxidative damage by reducing ROS generation and inflammatory cytokine expression (28). However, data on the effects of sodium phenylbutyrate and suramin on oxidative stress remain limited. In this study, both PBA and suramin decreased myeloperoxidase and malondialdehyde levels while increasing GSH levels and SOD, GPx, and CAT activities, indicating antioxidant effects. Suramin induced greater increases in CAT and GPx activities than PBA, suggesting a more pronounced effect on H_2O_2 detoxification,

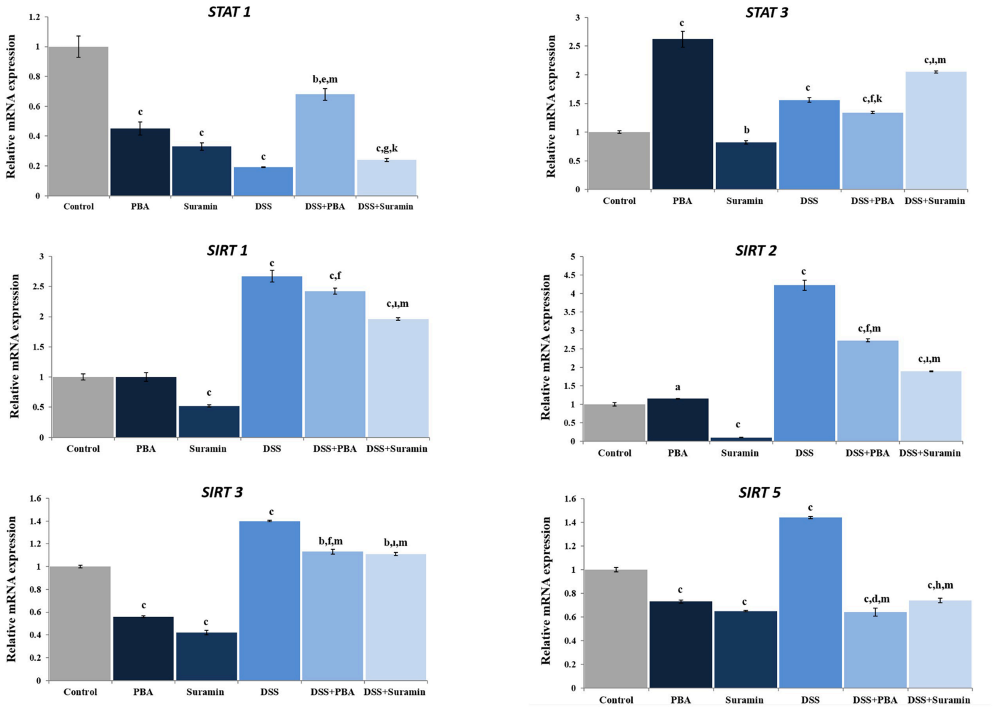


Figure 6. mRNA expressions of *STAT1, STAT3, SIRT1, SIRT2, SIRT3* and *SIRT5* genes based on qRT-PCR analysis of mouse colon tissues in different experimental groups. While DSS treatment decreased *STAT1* mRNA level, PBA injection markedly increased *STAT1* mRNA level. *STAT3* mRNA level decreased in the DSS group when PBA injection decreased its level but suramin injection increased its level in DSS-treated mice. SIRT1, SIRT2, SIRT3 and *SIRT5* mRNA levels were elevated in the DSS-treated group but PBA and suramin injection in DSS-treated mice decreased their levels significantly. The data were presented as mean ± standard error (SE). a: ($p<0.05$) vs control group; b: ($p<0.01$) vs control group; c: ($p<0.001$) vs control group; d: ($p<0.05$) vs PBA group; e: ($p<0.01$) vs PBA group; f: ($p<0.001$) vs PBA group; g: ($p<0.05$) vs suramin group; h: ($p<0.01$) vs suramin group; ı: ($p<0.001$) vs suramin group; j: ($p<0.05$) vs DSS group; k: ($p<0.01$) vs DSS group; m: ($p<0.001$) vs DSS group. All statistical tests were performed using ANOVA/t-test. PBA: phenylbutyrate; DSS: dextran sulfate sodium; *STAT*: signal transducer and activator of transcription; *SIRT:* sirtuin.

whereas PBA exerted a stronger effect on increasing GSH levels and SOD activity. Although differences in MDA reductions between groups were not statistically significant, both treatments improved oxidative stress parameters compared with the DSS group.

Cytokines are essential regulators of inflammatory processes, including their initiation, progression, and resolution (29). PBA has been shown to attenuate inflammation through the inhibition of pro-inflammatory cytokine expression (23). Likewise, suramin has been reported to reduce TNF-α and IL-6 levels in a hepatotoxicity model (30). In this study, suramin reduced TNF-α, IL-1β and IL-6 levels while increasing IL-10 levels in the DSS model group. Overall, suramin demonstrated a stronger anti-inflammatory effect than PBA, with greater suppression of pro-inflammatory cytokines and enhancement of IL-10 in DSS-induced colitis.

COX-2 is an enzyme involved in mucosal repair and prostanoid synthesis, and its expression is induced by cytokines such. In ulcerative colitis, increased IL-1, IL-6, and TNF-α levels are associated with upregulated COX-2 expression, which is also elevated in the DSS-exposed group relative to the control group (31). Consistently, COX-2 expression was significantly increased in DSS-treated mice in this study. However, no previous studies have evaluated the effects of PBA or suramin on colon COX-2 expression in ulcerative colitis. Here, both agents reduced COX-2 expression close to control levels, with comparable effects between the two treatments.

Epigenetic mechanisms, particularly histone modifications, regulate inflammatory responses in a context-dependent manner. H3K9me3 promotes heterochromatin formation and limits transcription factor access to promoters, including NF-κB binding to the IL-6 promoter, and has been associated with the regulation of proinflammatory genes (32). However, H3K9me3 has not yet been investigated in the DSS colitis model. In this study, H3K9me3 levels were decreased in experimental colitis induced by DSS, consistent with increased

inflammatory activity. Treatment with PBA and suramin increased H3K9me3 levels reduced by colitis. These findings suggest that both agents may enhance heterochromatin formation and suppress proinflammatory gene expression through epigenetic regulation. Since epigenetic changes do not always directly correlate with gene activity or disease severity, further studies are required to clarify their role in colitis and therapeutic potential.

STAT activation has been identified as a potential biomarker in intestinal inflammatory diseases, with the *STAT1/3* pathway—particularly *STAT3* upregulation—proposed as a therapeutic target and marker of T cell activation (33).

The present findings showed reduced *STAT1* expression and elevated *STAT3* expression in DSS-induced colitis. PBA increased *STAT1* expression and modestly decreased *STAT3*, whereas suramin did not influence *STAT1* but enhanced *STAT3* expression. Given the established role of phosphorylated *STAT1* and *STAT3* in ulcerative colitis, the observed changes in *STAT1* and *STAT3* mRNA expression may indicate modulation of *STAT* signaling. However, further mechanistic studies, including protein expression and phosphorylation analyses, are needed to establish their functional significance. HDACi have been reported to improve colitis outcomes by enhancing histone acetylation and modulating inflammatory signaling, including *STAT1/3* activity (34). Additionally, altered expression of *SIRT1, 2, 3*, and *5* has been reported in ulcerative colitis, with *SIRT1* dysregulation linked to sustained inflammation and oxidative stress. *SIRT* modulation has also been shown to reduce colitis models (35). In this study, DSS increased *SIRT1, 2, 3*, and *5* expression, while both PBA and suramin reduced these elevations. Notably, suramin demonstrated greater efficacy than PBA in suppressing the expression of *SIRT* genes in DSS-induced colitis.

Overall, the present findings support the proposed therapeutic potential of PBA and suramin in DSS-induced colitis by demonstrating concurrent improvements in histopathological, biochemical, and molecular parameters. The observed attenuation of oxidative stress and inflammatory responses, together with the modulation of HDAC-related molecular pathways, including *STAT* signaling, *SIRT*s, and histone modifications, suggests that these mechanisms collectively contribute to the protective effects of both agents rather than acting through a single molecular target.

Conclusion

Collectively, these findings suggest a previously unrecognized role of suramin in DSS-induced experimental colitis. Both sodium phenylbutyrate and suramin exerted antioxidant and anti-inflammatory effects and were associated with epigenetic changes in a colitis model.

Both agents exhibited cytoprotective effects in colonic tissue by maintaining the proliferative–apoptotic balance, enhancing endogenous antioxidant defenses, and modulating inflammatory responses through suppression of pro-inflammatory cytokines. These combined antioxidant, epigenetic, and immunomodulatory effects suggest that PBA and suramin may represent promising therapeutic candidates for inflammatory diseases associated with oxidative stress.

Ethics Committee Approval: Ethical approval for all animal experiments was obtained from the Local Ethics Committee for Animal Experiments of Istanbul University (Date: 25.02.2016; No: 07).

Peer Review: Externally peer-reviewed.

Author Contributions: Conception/Design of Study- C.Ö.C, P.A.; Data Acquisition- C.Ö.C., E.F.K.; Data Analysis/Interpretation- C.Ö.C.; E.F.K., S.Ö., E.K., P.A.; Drafting Manuscript- P.A.; Critical Revision of Manuscript- C.Ö.C.; E.F.K., S.Ö., E.K., P.A.; Final Approval and Accountability- C.Ö.C.; E.F.K., S.Ö., E.K., P.A.

Conflict of Interest: The authors have no conflict of interest to declare.

Financial Disclosure: This study was supported by the Scientific and Technological Research Council of Turkey (TUBITAK) (Project numbers: KBAG-118Z061), and Scientific Research Projects Coordination Unit of Istanbul University (Project numbers: FDP-2020-36617).

Author Details

Cansu Özal-Coşkun
[1] Biruni University, Faculty of Pharmacy, Department of Biochemistry, İstanbul, Türkiye
0000-0003-1767-6499

Ecem Fatma Karaman
[2] Biruni University, Faculty of Pharmacy, Department of Pharmaceutical Toxicology, İstanbul, Türkiye
0000-0002-1504-4546

Sibel Özden
[3] Istanbul University, Faculty of Pharmacy, Department of Pharmaceutical Toxicology, İstanbul, Türkiye
0000-0002-1662-2504

Engin Kaptan
[4] Istanbul University, Faculty of Science, Department of Biology, İstanbul, Türkiye
0000-0003-0866-8796

Pelin Arda
[4] Istanbul University, Faculty of Science, Department of Biology, İstanbul, Türkiye
0000-0002-7958-6977 parda@istanbul.edu.tr

REFERENCES

1. Sartor RB. Cytokines in intestinal inflammation: pathophysiological and clinical considerations. Gastroenterology 1994; 106(2): 533-9.

2. Cooper HS, Murthy SN, Shah RS, Sedergran DJ. Clinicopathologic study of dextran sulfate sodium experimental murine colitis. Lab Invest 1993; 69(2): 238-49.
3. Ono K, Nimura S, Hideshima Y, Nabeshima K, Nakashima M. Orally administered sodium 4-phenylbutyrate suppresses the development of dextran sulfate sodium-induced colitis in mice. Exp Ther Med 2017; 14(6): 5485-90.
4. Korrapati MC, Shaner BE, Schnellmann RG. Recovery from glycerol-induced acute kidney injury is accelerated by suramin. J Pharmacol Exp Ther 2012; 341(1): 126-36.
5. Yan L, Gu C, Gao S, Wei B. Epigenetic regulation and therapeutic strategies in ulcerative colitis. Front Genet 2023; 14: 1302886.
6. Neurath MF. Strategies for targeting cytokines in inflammatory bowel disease. Nat Rev Immunol 2024; 24(8): 559-76.
7. Arda-Pirincci P, Aykol-Celik G. Galectin-1 reduces the severity of dextran sulfate sodium-induced ulcerative colitis by suppressing inflammatory and oxidative stress response. Bosn J Basic Med Sci 2020; 20(3): 319-27.
8. Dieleman LA, Palmen MJ, Akol H, Bloemena E, Peña AS, Meuwissen SG, et al. Chronic experimental colitis induced by dextran sulphate sodium is characterized by Th1 and Th2 cytokines. Clin Exp Immunol 1998; 114(3): 385-91.
9. Lowry OH, Rosebrough NJ, Farr AL, Randall RJ. Protein measurement with the Folin phenol reagent. J Biol Chem 1951; 193(1): 265-75.
10. Ledwozyw A, Michalak J, Stepień A, Kadziołka A. The relationship between plasma triglycerides, cholesterol, total lipids and lipid peroxidation products during human atherosclerosis. Clin Chim Acta 1986; 155(3): 275-83.
11. Beutler E, Duron O, Kelly BM. Improved method for the determination of blood glutathione. J Lab Clin Med 1963; 61: 882-8.
12. Aebi H. Catalase in vitro. Methods Enzymol 1984; 105: 121-6.
13. Paglia DE, Valentine WN. Studies on the quantitative and qualitative characterization of erythrocyte glutathione peroxidase. J Lab Clin Med 1967; 70(1): 158-69.
14. Sun Y, Oberley LW, Li Y. A simple method for clinical assay of superoxide dismutase. Clin Chem 1988; 34(3): 497-500.
15. Bradford MM. A rapid and sensitive method for the quantitation of microgram quantities of protein utilizing the principle of protein-dye binding. Anal Biochem 1976; 72: 248-54.
16. Karaman EF, Ozden S. Alterations in global DNA methylation and metabolism-related genes caused by zearalenone in MCF7 and MCF10F cells. Mycotoxin Res 2019; 35(3): 309-20.
17. Filgueira LR, Brandt SL, de Oliveira Ramalho TR, Jancar S, Serezani CH. Imbalance between HDAC and HAT activities drives aberrant STAT1/MyD88 expression in macrophages from type 1 diabetic mice. J Diabetes Complicat 2017; 31(2): 334-9.
18. Drew JE, Farquharson AJ, Horgan GW, Williams LM. Tissue-specific regulation of sirtuin and nicotinamide adenine dinucleotide biosynthetic pathways identified in C57Bl/6 mice in response to high-fat feeding. J Nutr Biochem 2016; 37: 20-9.
19. Vandenbon A, Kumagai Y, Lin M, Suzuki Y, Nakai K. Waves of chromatin modifications in mouse dendritic cells in response to LPS stimulation. Genome Biol 2018; 19(1): 138.
20. Kawada M, Arihiro A, Mizoguchi E. Insights from advances in research of chemically induced experimental models of human inflammatory bowel disease. World J Gastroenterol 2007; 13(42): 5581-93.
21. Matos I, Bento AF, Marcon R, Claudino RF, Calixto JB. Preventive and therapeutic oral administration of α,β-amyrin ameliorates dextran sulfate sodium-induced colitis in mice: the relevance of cannabinoid system. Mol Immunol 2013; 54(3-4): 482-92.
22. Glauben R, Siegmund B. Inhibition of histone deacetylases in inflammatory bowel diseases. Mol Med 2011; 17(5-6): 426-33.
23. Ono K, Nimura S, Nishinakagawa T, Hideshima Y, Enjyoji M, Nabeshima K, et al. Sodium 4-phenylbutyrate suppresses the development of dextran sulfate sodium-induced colitis in mice. Exp Ther Med 2014; 7(3): 573-8.
24. Perše M, Cerar A. Dextran sodium sulphate colitis mouse model: traps and tricks. J Biomed Biotechnol 2012; 2012: 718617.
25. Gore SD, Samid D, Weng LJ. Impact of sodium phenylbutyrate and sodium phenylacetate on proliferation, differentiation, and apoptosis of primary neoplastic myeloid cells. Clin Cancer Res 1997; 3(10): 1755-62.
26. Gan Y, Lu J, Yeung BZ, Cottage CT, Wientjes MG, Au JL. Pharmacodynamics of telomerase inhibition and telomere shortening by noncytotoxic suramin. AAPS J 2015; 17(1): 268-76.
27. Liu G, Yu L, Fang J, Hu CAA, Yin J, Ni H, et al. Methionine restriction on oxidative stress and immune response in DSS-induced colitis mice. Oncotarget 2017; 8(27): 44511-20.
28. Bobat F, Wu D, Tu E, Kapoor D, Sharma P, Adams JS, et al. Broad-spectrum therapeutic potential of 4-phenylbutyrate in neurological and systemic diseases of viral and non-viral origin. Front Pharmacol 2025; 16: 1621590.
29. Strober W, Fuss IJ. Proinflammatory cytokines in the pathogenesis of inflammatory bowel diseases. Gastroenterology. 2011;140(6):1756-67.
30. Goto T, Takeuchi S, Miura K, Ohshima S, Mikami KI, Yoneyama K, et al. Suramin prevents fulminant hepatic failure through suppression of NF-κB activity. Cytokine 2006; 33(1): 28-35.
31. Okayama M, Hayashi S, Aoi Y, Nishio H, Kato S, Takeuchi K. Aggravation by selective COX-1 and COX-2 inhibitors of DSS-induced colon lesions in rats. Dig Dis Sci 2007; 52(9): 2095-103.
32. Saccani S, Natoli G. Dynamic changes in histone H3 Lys9 methylation at inducible inflammatory genes. Genes Dev 2002; 16(17): 2219-24.
33. Mudter J, Weigmann B, Bartsch B, Kiesslich R, Strand D, Galle PR, et al. Activation pattern of STAT factors in inflammatory bowel diseases. Am J Gastroenterol 2005; 100(1): 64-72.
34. Glauben R, Batra A, Fedke I, Zeitz M, Lehr HA, Leoni F, et al. Histone hyperacetylation is associated with amelioration of experimental colitis in mice. J Immunol 2006; 176(8): 5015-22.
35. Samant SA, Hyoju SK, Alverdy JC, Gupta MP. The multifaceted role of sirtuins in inflammatory bowel diseases. Am J Physiol Gastrointest Liver Physiol 2025; 329(1): G58-G68.

İSTANBUL UNIVERSITY PRESS

Experimed 2026, 16 (2): 148–156

https://doi.org/10.26650/1964715

Submitted: 15.06.2026
Revision Requested: 30.06.2026
Last Revision Received: 21.07.2026
Accepted: 24.07.2026
Published Online 12.08.2026

Experimed

Research Article

Open Access

Integrated Analysis of OX40/OX40L Genetic Variants and Circulating Soluble Immune Checkpoint Markers in Laryngeal Cancer Recurrence

Maral Farzam [1,2], Dilara Sönmez Zor [2], Ülgen Sever [2], Cem Horozoğlu [3], Saime Turan Sürmen [4], Onur Dülger [5], Vahid Chaleshi [6], Mehmet Özkır [7], Ayşegül Verim [8], Yusufhan Süoğlu [9] & İlhan Yaylım [2]

[1] Istanbul University, Institute of Graduate Studies in Health Sciences, Istanbul, Türkiye
[2] Istanbul University, Aziz Sancar Institute of Experimental Medicine, Department of Molecular Medicine, Istanbul, Türkiye
[3] Haliç University, Faculty of Medicine, Department of Medical Biochemistry, Istanbul, Türkiye
[4] University of Health Sciences, Institute of Health Sciences, Department of Molecular Medicine, Istanbul, Türkiye
[5] Ondokuz Mayis University, Department of Pathology, Samsun, Türkiye
[6] Shahid Beheshti University of Medical Sciences, Research Institute for Gastroenterology and Liver Diseases, Basic and Molecular Epidemiology of Gastrointestinal Disorders Research Center, Tehran, Iran
[7] Yıldız Technical University, Faculty of Science and Literature, Department of Molecular Biology and Genetics, Istanbul, Türkiye
[8] Haydarpasa Numune Education and Research Hospital, Department of Otorhinolaryngology/Head and Neck Surgery, Istanbul, Türkiye
[9] Istanbul University, Istanbul Faculty of Medicine, Department of Otorhinolaryngology, Istanbul, Türkiye

Abstract

Objective: Laryngeal cancer is an aggressive malignancy in which immune regulatory mechanisms play a critical role in tumor progression and recurrence. The OX40/OX40L axis, a member of the tumor necrosis factor superfamily, has been implicated in immune modulation; however, its genetic and soluble profiles in laryngeal cancer remain insufficiently characterized. Beyond cancer susceptibility, the clinical relevance of OX40/OX40L alterations in recurrence biology remains poorly understood.

Materials and Methods: In this study, we investigated the distribution of *OX40* rs17568 and *OX40L* rs1234313 polymorphisms and evaluated their association with serum soluble OX40 (sOX40) and OX40L (sOX40L) levels in 80 patients with laryngeal cancer and 111 healthy controls. Genotyping was performed using polymerase chain reaction-restriction fragment length polymorphism (PCR–RFLP), and soluble protein levels were quantified by enzyme-linked immunosorbent assay (ELISA).

Results: No significant differences in serum sOX40 or sOX40L levels were observed between patients and controls. While *OX40* rs17568 genotype distributions were comparable between groups, a significant difference was detected for *OX40L* rs1234313, with homozygous genotypes (AA and GG) being more frequent in laryngeal cancer patients (p=0.007). Although genotype distributions were not associated with clinicopathological parameters, circulating sOX40 levels were significantly higher in patients with disease recurrence than in those without recurrence (p=0.008).

Conclusion: The findings suggest that alterations in the OX40/OX40L axis may be associated with immune dysregulation during disease progression rather than cancer initiation in laryngeal cancer. Particularly, elevated circulating sOX40 levels were associated with disease recurrence. Given the cross-sectional and exploratory nature of the study, these findings should be interpreted with caution and require validation in larger prospective cohorts.

Keywords Laryngeal Cancer · OX40 · OX40L · Genetic Polymorphism · Recurrence

Citation: Farzam, M., Sönmez Zor, D., Sever, Ü., Horozoğlu, C., Sürmen, S., Dülger, O., Chaleshi, V., Özkır, M., Verim, A., Süoğlu, Y. & Yaylım, İ. Integrated analysis of OX40/OX40L genetic variants and circulating soluble immune checkpoint markers in laryngeal cancer recurrence. Experimed 2026; 16(2): 148-156. DOI: 10.26650/1964715

This work is licensed under Creative Commons Attribution-NonCommercial 4.0 International License.

2026. Farzam, M., Sönmez Zor, D., Sever, Ü., Horozoğlu, C., Sürmen, S., Dülger, O., Chaleshi, V., Özkır, M., Verim, A., Süoğlu, Y. & Yaylım, İ.

Corresponding author: İlhan Yaylım iyaylim@istanbul.edu.tr

INTRODUCTION

Laryngeal cancer is the most common malignancy among head and neck cancers, and its origin is generally the mucosal layer. At the same time, squamous cell carcinoma is the most common and well-differentiated histological subtype (1). Although laryngeal cancer accounts for 0.7% of newly diagnosed cancer cases and 0.6% of mortality, the number of cases continues to increase due to increased air pollution, alcohol, and tobacco use (2, 3). Although surgical intervention, antineoplastic agents, and radiotherapy are effective treatment approaches in early-stage laryngeal cancer, even multimodal approaches combining these strategies may be inadequate in advanced-stage cases (4).

Recent research has shown that the molecular processes of cancer are influenced not only by tumor cells but also by the surrounding tissues and cells (5). Therefore, modern therapeutic strategies have increasingly targeted these micro-environmental factors that influence the initiation and progression of cancer. Tumor development and metastasis are influenced by components of the dynamic tumor microenvironment. This microenvironment facilitates tumor cell immune evasion and contributes to the development of treatment resistance. Although some pathophysiological mechanisms in laryngeal cancer remain unclear, critical relationships between molecules involved in immune modulation and genetic variants have been identified (6, 7).

In humans, 29 receptors belonging to the tumor necrosis factor (TNF) receptor superfamily (TNFRSF), which play a role in regulating immune responses, have been identified. Nineteen ligands that interact with these receptors are classified as the members of the TNF ligand superfamily (TNFSF) and contribute to the initiation of costimulatory signaling in the immune system by activating their corresponding receptors (8). One such ligand-receptor pair, OX40 (TNFRSF4) and its ligand OX40L (TNFSF4), plays a crucial role in immune cell interactions. OX40L is a type II transmembrane protein encoded by the *TNFSF4* gene and is expressed in various immune cells, such as dendritic cells, macrophages, and T and B lymphocytes. When it binds to its receptor, OX40, immune cell activation is triggered (9). The *OX40 (TNFRSF4)* and *OX40L (TNFSF4)* genes are located in chromosomal regions 1p36 and 1q25, respectively. *OX40* encodes a protein comprising 277 amino acids with a molecular weight of approximately 29.3 kDa, while *OX40L* encodes a protein comprising 183 amino acids with a molecular weight of approximately 21 kDa (10, 11).

The inhibitory effects of anti-OX40 agonistic monoclonal antibodies on the development of both immunogenic and non-immunogenic solid tumors have been demonstrated in various studies (12, 13). These antibodies are the focus of many early-phase clinical trials aimed at evaluating their potential as immunotherapeutic agents for various malignancies, including head and neck cancers (12, 14). Single-nucleotide polymorphisms (SNPs) have significant effects on disease susceptibility, etiology, and treatment response. The precise clinical identification of SNPs provides critical insights for personalized treatment strategies and prognostic evaluations, making them fundamental components of modern biomedical research (15). Genetic variation studies on the *OX40/OX40L* axis have found associations with many chronic diseases, including systemic sclerosis, atherosclerosis, myocardial infarction, asthma, and cancers (10, 16-20). Especially for *OX40L*, potential roles in pathophysiological processes in head and neck cancers, bladder cancer, and breast cancer have been shown in studies (18, 21-23). Among the reported variants, *OX40* rs17568 and *OX40L* rs1234313 were selected because of their potential functional relevance and previous associations with immune-mediated diseases and malignancies. The *OX40* rs17568 polymorphism is a nonsynonymous coding variant that may influence receptor structure or downstream signaling, thereby affecting T-cell activation and immune regulation. In contrast, *OX40L* rs1234313 is located within the regulatory region of the *TNFSF4* gene and has been suggested to influence gene transcription and OX40L expression. Both polymorphisms have been investigated in autoimmune diseases, cardiovascular disorders, and several solid tumors, suggesting that genetic variation within the OX40/OX40L signaling pathway may contribute to altered immune surveillance and disease susceptibility. These observations provided the biological rationale for evaluating these variants in patients with laryngeal cancer. In this context, the potential therapeutic effects of genetic variants and their prognostic and predictive value will support an individualized treatment approach (24). For example, our study aims to examine the distribution of *OX40* rs17568 and *OX40L* rs1234313 genetic variants along the *OX40/OX40L* axis, their effects on soluble levels, and their correlation with clinicopathological findings in laryngeal cancer. Although the *OX40/OX40L* axis is known to play a role in immune regulation and has been studied in various cancers, its genetic and soluble immunoprofile in laryngeal cancer is still not well understood. OX40/OX40L alterations specifically associated with disease recurrence in laryngeal cancer are lacking. These polymorphisms have previously been investigated in autoimmune diseases, cardiovascular disorders, and bladder cancer, but their contribution to laryngeal cancer susceptibility and recurrence has not yet been explored. To our knowledge, this is one of the first studies to evaluate both *OX40/OX40L* genetic variations and circulating soluble protein levels in the same laryngeal cancer group.

MATERIALS AND METHODS

Samples

In this cross-sectional study, 80 patients diagnosed with laryngeal cancer and 111 healthy individuals were included. The participants were recruited from the Department of Otorhinolaryngology/Head and Neck Surgery, Istanbul Education and Research Hospital, and

Table 1. Primer sequences and restriction fragment length polymorphism (RFLP) patterns for *OX40* rs17568 and *OX40L* rs1234313 polymorphisms

Gene	SNP		Primer Sequence	Length of product	Restriction Enzyme	RFLP fragments (bp)
OX40	rs17568	Forward	TTCAGCAGTGGCAGTGGTAG	359 bp	BsmAI	GG: 359 AG: 359, 198, 161 AA: 198, 161
		Reverse	TGGGAAAGTGGAACTGGTCT			
OX40L	rs1234313	Forward	TGTGGTAGATGCTGCCTGTG	329 bp	BmrI	AA: 329 AG: 329, 176, 153 GG: 176, 153
		Reverse	CCCTTCTCCTATTCGGGTTG			

the Department of Otorhinolaryngology, Istanbul Faculty of Medicine, Istanbul University, between 2020 and 2021. The patient group comprised 80 individuals (6 women, 74 men), while the control group consisted of 111 individuals (52 women, 59 men). All participants had provided written informed consent for this study before the sampling procedure. The study protocol conformed to the ethical guidelines of The Declaration of Helsinki (1975) and was approved by the Clinical Research Ethics Committee of Istanbul University, Türkiye (approval no: 29.01.2020-165).

Genotyping

Peripheral blood samples were collected from all participants. Samples collected in EDTA tubes were used for genomic DNA isolation, whereas blood collected in serum tubes was centrifuged to obtain serum for enzyme-linked immunosorbent assay (ELISA) analysis. Serum aliquots were stored at −80°C until further use. Genomic DNA was isolated from blood samples using the PureLink® Genomic DNA Kit (Invitrogen, USA), following the manufacturer's protocol. The purity and concentration of the isolated DNA were measured using a spectrophotometer (Applied Biosystems, USA). Genotyping was performed using a multi-step process comprising polymerase chain reaction (PCR) followed by restriction fragment length polymorphism (RFLP) analysis. Detailed information on the primers and the restriction enzyme used for both PCR and RFLP procedures is provided in Table 1. PCR amplification was conducted using the T100™ Thermal Cycler (Bio-Rad INC., USA). The process began with an initial denaturation at 94°C for 10 minutes, followed by 35 cycles of denaturation at 95°C for 45 seconds, annealing at 61°C for 30 seconds, and extension at 72°C for 40 seconds. A final extension was carried out at 72°C for 10 minutes. PCR products were then digested with a restriction enzyme (New England Biolabs, USA) at 37°C for 5 hours. Digested products were separated on a 2.5% agarose gel, stained with ethidium bromide, and visualized under UV illumination (Vilber Lourmat, France). Band patterns and reaction conditions are shown in Table 1.

ELISA

The concentrations of human soluble OX40 (sOX40) and soluble OX40L (sOX40L) in serum samples from both patients and healthy controls were quantified using ELISA. For the measurements, commercially available ELISA kits were used: The Human Soluble OX40L ELISA Kit (Cat. No: EH356RB Invitrogen, USA) and the GENLISA™ Human TNFRSF4/OX40 ELISA Kit (Cat. No: KBH3356 KRISHGEN BioSystems, USA), both supplied by ARP American Research Products, Inc. All procedures followed the manufacturers' protocols. Absorbance was read at 450 nm using an ELISA plate reader, and concentrations were calculated in pg/mL. The sensitivity of the sOX40L kit was reported as <1.8 pg/mL, while the sOX40 kit had a sensitivity of <0.1 pg/mL.

Statistical Analyses

Statistical analyses were performed using SPSS software (version 22.1; IBM Corp., Armonk, NY, USA). Fisher's exact test or the chi-square test was used to analyze genotype and allele frequency distributions. Mann–Whitney U tests were used to compare serum sOX40 and sOX40L levels between groups. A two-sided p-value <0.05 was considered statistically significant. Linkage disequilibrium analysis was performed using Haploview software (version 4.2, Broad Institute, England). In addition, SNPs in both patients and healthy controls were tested for Hardy–Weinberg equilibrium.

RESULTS

sOX40 and sOX40L Levels and Genetic Variant Distributions Among Groups

The demographic characteristics of the study population are summarized in Table 2. Patients with laryngeal cancer were significantly more likely to be male than healthy controls (92.5% vs. 53.2%, p<0.001), whereas the mean age did not differ significantly between the groups (61.0 ± 1.10 vs. 57.4 ± 1.65 years, p=0.07). Serum sOX40 and sOX40L levels were measured in laryngeal cancer patients (32.17 ± 1.66 pg/mL and 17.57 ± 4.78 pg/mL, respectively) and healthy controls (33.96 ± 3.41 pg/mL and 31.71 ± 14.35 pg/mL, respectively). No statistically significant differences were observed in serum sOX40 or sOX40L levels between the two groups (p>0.05).

Table 2. Demographic characteristics of laryngeal cancer patients and healthy controls

Characteristic	Patients (n = 80)	Controls (n = 111)	p value
Age (years; mean ± SE)	61.0 ± 1.10	57.4 ± 1.65	0.07
Sex			
– Male, n (%)	74 (92.5%)	59 (53.2%)	< 0.001
– Female, n (%)	6 (7.5%)	52 (46.8%)	

Genotype and allele frequency distributions of the *OX40* rs17568 polymorphism were comparable between laryngeal cancer patients and controls, with no statistically significant differences detected (Table 3). Similarly, allele frequencies did not significantly differ between groups.

Table 3. Distribution of genotypes and alleles for the polymorphism

Genotype / Allele	Patients (n = 80)	Controls (n = 111)	p value
AA	42 (52.5%)	49 (44.1%)	
AG	28 (35.0%)	44 (39.6%)	0.50
GG	10 (12.5%)	18 (16.2%)	
A allele	112 (70.0%)	139 (62.6%)	0.13
G allele	48 (30.0%)	83 (37.4%)	

Data are presented as numbers (percentage). Differences between groups were evaluated using the chi-square or Fisher's exact test, as appropriate.

In contrast, the genotype distribution of the *OX40L* rs1234313 polymorphism differed significantly between laryngeal cancer patients and controls (p=0.007). Homozygous genotypes (AA and GG) were more frequently observed in the patient group than the heterozygous AG genotype (Table 4). However, allele frequency distributions did not significantly differ between the groups. Hardy–Weinberg equilibrium analysis showed that *OX40* rs17568 was in equilibrium in both the patient (p=0.136) and control (p=0.140) groups. *OX40L* rs1234313 was also in Hardy–Weinberg equilibrium in the patient group (p=0.673), but deviated significantly in controls (p<0.001).

Table 4. Genotype and allele frequency distributions of *OX40L* rs1234313 in laryngeal cancer patients and healthy controls

Genotype / Allele	Patients (n = 80)	Controls (n = 111)	p value
AA	10 (12.5%)	5 (4.5%)	
AG	39 (48.8%)	78 (70.3%)	**0.007**
GG	31 (38.8%)	28 (25.2%)	
A allele	59 (36.9%)	88 (39.6%)	0.86
G allele	101 (63.1%)	134 (60.4%)	

Data are presented as numbers (percentage). Statistically significant results are indicated in bold.

Distribution of Clinicopathological Findings According to *OX40* and *OX40L* Genetic Variants

The distribution of clinicopathological parameters according to *OX40* rs17568 and *OX40L* rs1234313 genotypes was further evaluated in laryngeal cancer patients. Statistically significant difference was found only in the *OX40* genotype distribution in terms of positive or negative recurrence (p=0.048). No significant associations were observed between genotype distributions and clinicopathological features, including tumor stage, lymph node involvement, perineural invasion, differentiation status, smoking, alcohol consumption, reflux, family history, or distant metastasis (Supplementary Tables S1 and S2).

Combined genotype analysis of *OX40* rs17568 and *OX40L* rs1234313 did not reveal any significant differences between laryngeal cancer patients and controls (Supplementary Table S3). Similarly, haplotype analysis showed no statistically significant association between laryngeal cancer and haplotype frequencies of the investigated polymorphisms (Supplementary Tables S4 and S5).

Distribution of sOX40 and sOX40L Levels According to Clinicopathological Findings

Serum sOX40 and sOX40L levels were further evaluated according to selected clinicopathological parameters in patients with laryngeal cancer (Table 5). Although sOX40 levels tended to be higher in patients with advanced tumor stage, lymph node involvement, and perineural invasion, these differences did not reach statistical significance (p>0.05). Recurrence data were available for 79 of the 80 patients included in the study, as recurrence information was unavailable for one patient. Among these, 8 patients experienced disease recurrence, whereas 71 remained recurrence-free during follow-up. Among all clinicopathological parameters evaluated, disease recurrence was the only variable significantly associated with circulating sOX40 levels, which were significantly higher in patients with recurrence than in those without (p=0.008).

Table 5. Serum sOX40 and sOX40L levels according to selected clinicopathological parameters in laryngeal cancer patients

Parameter	Category	Levels (pg/mL)	p value
Tumor stage	T1–T2	31.43 ± 3.17	0.59
	T3–T4	33.36 ± 1.82	
Lymph node	N0	31.74 ± 2.31	0.59
	N1–N3	33.76 ± 2.67	
Perineural invasion	Negative	31.56 ± 2.11	0.44
	Positive	34.60 ± 3.11	
Recurrence	Negative	30.71 ± 1.49	**0.008**
	Positive	43.82 ± 0.89	
Tumor stage	T1–T2	32.07 ± 9.65	0.32
	T3–T4	15.76 ± 5.02	
Lymph node	N0	18.52 ± 5.88	0.84
	N1–N3	16.38 ± 8.88	
Recurrence	Negative	18.65 ± 6.35	0.77
	Positive	15.41 ± 8.34	

Values are presented as mean ± standard error (SE). Comparisons were performed using the Mann–Whitney U test. Statistically significant results are indicated in bold.

No statistically significant differences in sOX40L levels were observed according to tumor stage, lymph node involvement, perineural invasion, or recurrence status (all p>0.05).

DISCUSSION

Genetic variations, such as SNPs, contribute to the modulation of gene expression, particularly in hotspot regions. Immune checkpoint molecules, including PD-1 and CTLA-4, are well-characterized in cancer immunotherapy, while other members, such as OX40, are increasingly being evaluated with respect to their immunomodulatory roles in cancer (25). OX40/OX40L is a member of the TNF superfamily and functions as a costimulatory pathway; experimental evidence indicates that dysregulation of OX40L expression is associated with decreased antitumoral immune activity in the tumor microenvironment (26).

In this study, the genotype distribution of *OX40* rs17568 did not significantly differ between laryngeal cancer patients and controls. This is consistent with reports indicating that rs17568, an exonic variant, may influence gene expression or immune-related phenotypes, yet its association with cancer susceptibility may vary between populations and disease contexts (22–30). Moreover, in squamous cell carcinomas of the paranasal sinuses, an increased risk associated with *OX40* variants has been reported, supporting the possibility that this axis may be relevant in squamous malignancies under chronic inflammatory pressure (22, 31–33).

In contrast, *OX40L* rs1234313 showed a significant difference in genotype distribution between patients and controls in our cohort. Notably, homozygous mutant (GG) and wild-type (AA) genotypes were more frequent than the heterozygous (AG) genotype among laryngeal cancer patients. Previous studies have implicated *OX40L* variants, including rs1234313, in several malignancies and immune-inflammatory disorders. For example, rs1234313 has been suggested as a potential independent risk factor in sporadic breast cancer (20), and polymorphisms in *OX40/OX40L* have also been associated with bladder cancer in a Turkish population (18). In cardiovascular and atherosclerotic contexts, rs1234313 has been evaluated as a risk-associated variant linked to carotid calcification and atherosclerotic phenotypes, highlighting its broader relevance to chronic inflammation (34). Taken together, our findings support the hypothesis that alterations in *OX40L* rs1234313 may contribute to immune dysregulation in laryngeal cancer, potentially affecting immune surveillance during carcinogenesis.

Regarding soluble molecules, we observed no significant differences in sOX40 and sOX40L levels between laryngeal cancer patients and controls. However, sOX40 levels were significantly higher in patients with disease recurrence than in patients without recurrence. This finding is consistent with reports in other malignancies showing that soluble OX40 levels may be associated with advanced disease features. Increased sOX40 levels have been reported in advanced gastric adenocarcinoma and are correlated with cancer progression (35), and high sOX40 levels have been associated with metastatic gastric cancer (36). Similarly, in colorectal cancer, soluble OX40 has been evaluated in relation to tumor immune contexture, and higher circulating sOX40 levels have been linked to adverse clinical outcomes, including reduced survival in advanced colorectal cancer (37, 38). Therefore, the elevated circulating sOX40 levels observed in patients with disease recurrence may reflect alterations in immune activation associated with recurrent disease. Given the cross-sectional design of the present study and the lack of information regarding the temporal relationship between sample collection and recurrence, these findings should be interpreted as an association rather than evidence of a prognostic or predictive biomarker. Prospective longitudinal studies with serial sample collection are required to determine whether elevated sOX40 levels precede recurrence or simply reflect disease status at the time of sampling.

In contrast, sOX40L has been studied less extensively in oncology, and available data are limited. In metastatic gastric cancer, sOX40L did not show a clear association with histological subtypes or case–control differences (36). Beyond cancer, peripheral OX40/OX40L profiles have been evaluated in immune-mediated diseases; in myasthenia gravis, OX40/OX40L dynamics (including soluble forms) were discussed in relation to relapse and remission, underscoring the relevance of this axis in immune regulation (39). In our cohort, although sOX40L did not show statistically significant differences across clinicopathological strata, its variation alongside recurrence-related changes in sOX40 suggests that the *OX40/OX40L* axis may be more involved in progression and recurrence biology than in early carcinogenic events.

In this study, neither the rs17568 nor the rs1234313 genotype distributions showed significant associations with most clinicopathological parameters. Nevertheless, the significant difference in *OX40L* rs1234313 genotype distribution between cases and controls, together with the increase in sOX40 levels in patients with disease, recurrence supports the view that the *OX40/OX40L* profile may contribute to immune escape mechanisms during advanced disease processes. Unlike previous studies that primarily focused on cancer susceptibility or individual genetic polymorphisms, our study integrates both *OX40/OX40L* genetic polymorphisms and circulating soluble immune checkpoint molecules within the same laryngeal cancer cohort. This integrated approach provides a more comprehensive perspective on *OX40/OX40L* dysregulation than evaluating either genetic or soluble biomarkers alone. Overall, our findings suggest that alterations in the *OX40/OX40L* axis may be more closely associated with disease progression and recurrence than with tumor initiation. In particular, elevated circulating sOX40 may represent a potential recurrence-associated marker; however, this observation should be considered exploratory and requires validation in larger, prospective cohorts before any clinical application can be considered. Given the growing interest in OX40-targeted immunotherapy, further validation of

OX40/OX40L-related biomarkers may contribute to improved patient stratification and disease monitoring in the future.

This study has several limitations that should be considered when interpreting the findings. First, the sex distribution differed significantly between the patient and control groups, reflecting the well-known male predominance of laryngeal cancer. Although this imbalance largely reflects the disease's epidemiology, sex-related differences in immune responses may have influenced the observed associations. Given the relatively limited sample size of this study, multivariable analyses adjusted for potential confounding factors were not performed. Therefore, residual confounding cannot be excluded. Second, the relatively small number of patients with disease recurrence limited the statistical power of subgroup analyses, and these findings should therefore be considered exploratory. In addition, the cross-sectional design precludes conclusions regarding temporal or causal relationships between circulating sOX40 levels and disease recurrence; thus, the observed association should not be interpreted as evidence that circulating sOX40 predicts recurrence or has established prognostic value. Furthermore, disease-free and overall survival analyses were not performed, limiting the evaluation of the prognostic significance of *OX40/OX40L* alterations. Finally, the deviation from the Hardy–Weinberg equilibrium observed for *OX40L* rs1234313 in the control group should be considered when interpreting the observed genetic association. Overall, these findings should be validated in larger, prospective, and preferably sex-balanced cohorts.

CONCLUSION

The findings of this study suggest that alterations in the *OX40/OX40L* axis may be more closely associated with disease progression and recurrence than with the initiation of laryngeal cancer. While no significant differences in serum sOX40 and sOX40L levels were observed between patients and controls, elevated sOX40 in recurrent cases suggests a potential association with disease course. The predominance of homozygous genotypes for *OX40L* rs1234313 among patients may indicate the involvement of this immune regulatory pathway; however, these findings require confirmation in larger, well-controlled functional studies before clinical interpretation.

Acknowledgement: We would like to express our heartfelt gratitude to all the patients who generously participated in this study.

Ethics Committee Approval: Ethical approval was obtained from the Clinical Research Ethics Committee of Istanbul University, Türkiye (approval number: 29.01.2020-165). The protocol conforms with the ethical guidelines of The Declaration of Helsinki (1975).

Peer Review: Externally peer-reviewed.

Author Contributions: Conception/Design of Study- İ.Y., C.H., V.C.; Data Acquisition- Y.S., A.V., M.F.; Data Analysis/Interpretation- S.T.S., İ.Y., D.S.Z.; Drafting Manuscript- M.F., Ü.S., O.D., M.Ö.; Critical Revision of Manuscript- Y.S., A.V., İ.Y.; Final Approval and Accountability- İ.Y., M.F.

Conflict of Interest: The authors have no conflict of interest to declare.

Financial Disclosure: The present study was supported by the Istanbul University Scientific Research Projects Unit (Project No: TYL-2020-36727).

Author Details

Maral Farzam
[1] Istanbul University, Institute of Graduate Studies in Health Sciences, Istanbul, Türkiye
[2] Istanbul University, Aziz Sancar Institute of Experimental Medicine, Department of Molecular Medicine, Istanbul, Türkiye
0000-0003-0397-6992

Dilara Sönmez Zor
[2] Istanbul University, Aziz Sancar Institute of Experimental Medicine, Department of Molecular Medicine, Istanbul, Türkiye
0000-0002-4962-5330

Ülgen Sever
[2] Istanbul University, Aziz Sancar Institute of Experimental Medicine, Department of Molecular Medicine, Istanbul, Türkiye
0000-0002-9754-0446

Cem Horozoğlu
[3] Haliç University, Faculty of Medicine, Department of Medical Biochemistry, Istanbul, Türkiye
0000-0001-8998-2028

Saime Turan Sürmen
[4] University of Health Sciences, Institute of Health Sciences, Department of Molecular Medicine, Istanbul, Türkiye
0000-0002-7748-0757

Onur Dülger
[5] Ondokuz Mayis University, Department of Pathology, Samsun, Türkiye
0000-0002-1155-7790

Vahid Chaleshi
[6] Shahid Beheshti University of Medical Sciences, Research Institute for Gastroenterology and Liver Diseases, Basic and Molecular Epidemiology of Gastrointestinal Disorders Research Center, Tehran, Iran
0000-0001-5355-8866

Mehmet Özkır
[7] Yıldız Technical University, Faculty of Science and Literature, Department of Molecular Biology and Genetics, Istanbul, Türkiye
0000-0003-4687-710X

Ayşegül Verim
[8] Haydarpasa Numune Education and Research Hospital, Department of Otorhinolaryngology/Head and Neck Surgery, Istanbul, Türkiye
0000-0002-6649-0837

Yusufhan Süoğlu
[9] Istanbul University, Istanbul Faculty of Medicine, Department of Otorhinolaryngology, Istanbul, Türkiye
0000-0002-4547-5320

İlhan Yaylım
[2] Istanbul University, Aziz Sancar Institute of Experimental Medicine, Department of Molecular Medicine, Istanbul, Türkiye
0000-0003-2615-0202 iyaylim@istanbul.edu.tr

REFERENCES

1. Liberale C, Soloperto D, Marchioni A, Monzani D, Sacchetto L. Updates on larynx cancer: risk factors and oncogenesis. Int J Mol Sci 2023; 24(16): 12913.
2. Bodd MH, McCammon SD. Laryngeal cancer and the end of life (as we know it). Otolaryngol Clin North Am 2023; 56(2): 403-12.
3. Nishimura G, Takahashi H, Sano D, Arai Y, Hatano T, Kitani Y, et al. Risk factors of secondary cancer in laryngeal, oropharyngeal, or hypopharyngeal cancer after definitive therapy. Int J Clin Oncol 2024; 29(2): 103-14.
4. Bassani S, Lee YK, Campagnari V, Eccher A, Monzani D, Nocini R, et al. From hype to reality: a narrative review on the promising role of artificial intelligence in larynx cancer detection and transoral microsurgery. Crit Rev Oncog 2023; 28(3): 21-4.
5. Gonzalez-Pons M, Cruz-Correa M. Colorectal cancer biomarkers: where are we now? Biomed Res Int 2015; 2015: 149014.
6. Suzuki HI, Katsura A, Matsuyama H, Miyazono K. MicroRNA regulons in tumor microenvironment. Oncogene 2015; 34(24): 3085-94.
7. Yu YR, Ho PC. Sculpting tumor microenvironment with immune system: from immunometabolism to immunoediting. Clin Exp Immunol 2019; 197(2): 153-60.
8. Dadas O, Ertay A, Cragg MS. Delivering co-stimulatory tumor necrosis factor receptor agonism for cancer immunotherapy: past, current and future perspectives. Front Immunol 2023; 14: 1147467.
9. An J, Ding S, Li S, Sun L, Chang X, Huang Z, et al. Enhancement of the soluble form of OX40 and OX40L costimulatory molecules but reduction of the membrane form in type 1 diabetes (T1D). J Immunol Res 2019; 2019: 1780567.
10. Jahromi AS, Erfanian S, Roustazadeh A. Association of OX40L gene polymorphism with multiple sclerosis in Iranians. Heliyon 2024; 10(6): e27304.
11. Jahromi AS, Shojaei M, Erfanian S, Maalhagh M, Ghobadifar MA. Lack of Association between OX40L gene polymorphism rs3850641 and the risk of premature myocardial infarction in Iranian population. Int J Pharm Res Allied Sci 2016; 5(2): 528-36.
12. Bell RB, Leidner RS, Crittenden MR, Curti BD, Feng Z, Montler R, et al. OX40 signaling in head and neck squamous cell carcinoma: overcoming immunosuppression in the tumor microenvironment. Oral Oncol 2016; 52: 1-10.
13. Bulliard Y, Jolicoeur R, Zhang J, Dranoff G, Wilson NS, Brogdon JL. OX40 engagement depletes intratumoral Tregs via activating FcgammaRs, leading to antitumor efficacy. Immunol Cell Biol 2014; 92(6): 475-80.
14. Rancoule C, Vallard A, Espenel S, Guy JB, Xia Y, El Meddeb Hamrouni A, et al. Immunotherapy in head and neck cancer: Harnessing profit on a system disruption. Oral Oncol 2016; 62: 153-62.
15. Matsuda K. PCR-based detection methods for single-nucleotide polymorphism or mutation: Real-Time PCR and its substantial contribution toward technological refinement. Adv Clin Chem 2017; 80: 45-72.
16. Wang X, Luan Y, Zhang C. A meta-analysis on correlations of OX40L variants with atherosclerotic disorders. J Cell Biochem 2019; 120(6): 9624-30.
17. Fu Y, Lin Q, Zhang ZR. Association of TNFSF4 polymorphisms with systemic lupus erythematosus: a meta-analysis. Adv Rheumatol 2021; 61: 59.
18. Bilen O, Verim L, Tosun C, Yuksel O, Sever U, Sonmez D, et al. Relationship between bladder cancer and polymorphisms of OX40 (rs17568) and OX40L (rs1234313) genes in a Turkish population. Biotechnol Biotechnol Equip 2023; 37(1): 2245923.
19. Liu S, Xu Z. A meta-analysis on the association between TNFSF4 polymorphisms (rs3861950 T>C and rs1234313 A>G) and susceptibility to coronary artery disease. Front Physiol 2020; 11: 539288.
20. Weiguang Y, Dalin L, Lidan X, Yonggang C, Shuang C, Yanhong L, et al. Association of OX40L polymorphisms with sporadic breast cancer in northeast Chinese Han population. PLoS One 2012; 7(8): e41277.
21. Faghih Z, Taherifard E, Daneshmand A, Talei A, Erfani N. OX40 genetic variations in patients with breast cancer: a case-control study. Br J Biomed Sci 2021; 78(1): 44-46.
22. Faghih Z, Abtahi S, Khademi B, Nikfarjam F, Erfani N. Association of OX40 gene polymorphisms (rs17568G/A and rs229811A/C) with head and neck squamous cell carcinoma. Mol Biol Rep 2019; 46(3): 2609-16.
23. Erfanian S, Rahmanian F, Jahromi AS, Hojjat-Farsangi M. Non-association between rs17568 OX40 Gene Polymorphism and Type-2 Diabetes Mellitus, West-south of Iran. J Int Transl Med 2020; 8(1): 19-22.
24. Miller JE, Veturi Y, Ritchie MD. Innovative strategies for annotating the "relationSNP" between variants and molecular phenotypes. BioData Mining 2019; 12(1): 1-22.
25. Deng J, Zhao S, Zhang X, Jia K, Wang H, Zhou C, et al. OX40 (CD134) and OX40 ligand, important immune checkpoints in cancer. Onco Targets Ther 2019; 12: 7347-53.
26. Zaini J, Andarini S, Tahara M, Saijo Y, Ishii N, Kawakami K, et al. OX40 ligand expressed by DCs costimulates NKT and CD4+ Th cell antitumor immunity in mice. J Clin Invest 2007; 117(11): 3330-38.
27. Ria M, Eriksson P, Boquist S, Ericsson CG, Hamsten A, Lagercrantz J. Human genetic evidence that OX40 is implicated in myocardial infarction. Biochem Biophys Res Commun 2006; 339(3): 1001-06.
28. Souza HS, Elia CC, Spencer J, MacDonald TT. Expression of lymphocyte-endothelial receptor-ligand pairs, alpha4beta7/MAdCAM-1 and OX40/OX40 ligand in the colon and jejunum of patients with inflammatory bowel disease. Gut 1999; 45(6): 856-63.
29. Yoshioka T, Nakajima A, Akiba H, Ishiwata T, Asano G, Yoshino S, et al. Contribution of OX40/OX40 ligand interaction to the pathogenesis of rheumatoid arthritis. Eur J Immunol 2000; 30(10): 2815-23.
30. Olofsson PS, Söderström LA, Wågsäter D, Sheikine Y, Ocaya P, Lang FÖ, et al. CD137 is expressed in human atherosclerosis and promotes development of plaque inflammation in hypercholesterolemic mice. Circulation 2008; 117(10): 1292-1301.
31. Chen Y, Zhang L, Huang H, Liu R, Li X, Qiang O, et al. Association of OX40 and OX40L gene polymorphisms with acute coronary syndrome in a Han Chinese population. DNA Cell Biol 2011; 30(8): 597-602.
32. Yue LY, Xu Y, Tao B, He CS. Association of TNFSF4 gene polymorphisms and plasma TNFSF4 level with risk of systemic lupus erythematosus in a Chinese population. Immunol Invest 2022; 51(2): 316-30.
33. Huang Q, Yang QD, Tan XL, Feng J, Tang T, Xia J, et al. Absence of association between atherosclerotic cerebral infarction and TNFSF4/TNFRSF4 single nucleotide polymorphisms rs1234313, rs1234314 and rs17568 in a Chinese population. J Int Med Res 2014; 42(2): 436-43.
34. Jiang Y, Liu X, Du Y, Zhou S. rs1234313 and rs45454293 are risk factors of cerebral arterial thrombosis, large artery atherosclerosis, and carotid plaque in the Han Chinese population: a case-control study. BMC Neurol 2019; 19(1): 31.
35. Lima CAC, Martins MR, Dos Santos RL, da Silva LM, Da Silva JPA, Forones NM, et al. Soluble levels of 4-1BB (CD137) and OX40 (CD134) are associated with cancer progression in gastric adenocarcinoma. J Surg Oncol 2024; 130(4): 734-40.
36. Lima CAC, Martins MR, Dos Santos RL, da Silva LM, Silva JPA, Torres LC, et al. High soluble OX40 levels correlate with metastatic gastric cancer. J Surg Oncol 2022; 126(1): 139-43.
37. Zor DS, Hakan MT, Özgür E, Horozoglu C, Yörüker EE, Kulle CB, et al. Plasma levels of kynurenine, soluble OX40 and mir-138-5p are associated with tumor-infiltrating lymphocytes in colorectal cancer: an exploratory study. Anticancer Res 2023; 43(7): 3281-88.
38. Sawada R, Arai Y, Sagawa Y, Nagata Y, Nishimura T, Noguchi M, et al. High blood levels of soluble OX40 (CD134), an immune costimulatory molecule, indicate reduced survival in patients with advanced colorectal cancer. Oncol Rep 2019; 42(5): 2057-64.
39. Zhou X, Wang X, Gu Y, Chen L, Shen Y, Tian J, et al. Clinical significance of OX40 and OX40 ligand in the peripheral blood of patients with myasthenia gravis. J Immunol Res 2022; 2022: 4337399.

APPENDIX

Supplementary Materials

Table S 1. The genotype frequency distribution of *OX40* rs17568 among larynx cancer patients/control group based on tumor histopathological characteristics

Histopathological Information		OX40 Genotypes			
		AA	GG	AG	p
Perineural Invasion	Positive	9 (52.9%)	4 (23.5%)	4 (23.5%)	0.227
	Negative	29 (52.7%)	5 (9.1%)	21 (38.2%)	
Tumor Stage	T1+T2	8 (42.1%)	1 (5.3%)	10 (52.6%)	0.134
	T3+T4	30 (56.6%)	8 (15.1%)	15 (28.3%)	
Lymph Node	No	17 (44.7%)	6 (15.8%)	15 (39.5%)	0.332
	N1–N3	21 (62.8%)	3 (8.8%)	10 (29.4%)	
Recurrence	Positive	1 (12.5%)	2 (25.0%)	5 (62.5%)	**0.048**
	Negative	41 (57.7%)	7 (9.9%)	23 (32.4%)	
Distant Metastasis	Positive	2 (100%)	–	–	0.398
	Negative	36 (51.4%)	9 (12.9%)	25 (35.7%)	
Alcohol Consumption	Yes	21 (51.2%)	6 (14.6%)	14 (34.1%)	0.819
	No	17 (54.8%)	3 (9.7%)	11 (35.5%)	
Reflux	Positive	17 (54.8%)	4 (12.9%)	10 (32.3%)	0.919
	Negative	25 (51.0%)	6 (12.2%)	18 (36.7%)	
Family History	Positive	12 (48.0%)	4 (16.0%)	9 (36.0%)	0.776
	Negative	30 (54.5%)	6 (10.9%)	19 (34.5%)	
Differentiation	Low	3 (42.9%)	2 (28.6%)	2 (28.6%)	0.599
	Moderate	22 (50.0%)	6 (13.6%)	16 (36.4%)	
Smoking	Yes	21 (58.3%)	2 (5.6%)	13 (36.1%)	0.226
	No	21 (47.7%)	8 (18.2%)	15 (34.1%)	

Recurrence data were unavailable for one patient; therefore, recurrence analyses were performed on 79 patients. Statistically significant results are indicated in bold.

Table S 2. The genotype frequency distribution of *OX40L* rs1234313 among larynx cancer patients/control group based on tumor histopathological characteristics

Histopathological Information		*OX40L* Genotypes			
		AA	GG	AG	p
Perineural Invasion	Positive	1 (5.9%)	9 (52.9%)	7 (41.2%)	0.727
	Negative	7 (12.7%)	26 (47.3%)	22 (40.0%)	
Tumor Stage	T1+T2	3 (15.8%)	12 (63.2%)	4 (21.1%)	0.135
	T3+T4	5 (9.4%)	23 (43.4%)	25 (47.2%)	
Lymph Node	No	5 (13.2%)	19 (50.0%)	14 (36.8%)	0.752
	N1–N3	3 (8.8%)	16 (47.1%)	15 (44.1%)	
Recurrence	Positive	2 (25.0%)	4 (50.0%)	2 (25.0%)	0.480
	Negative	8 (11.3%)	35 (49.3%)	28 (39.4%)	
Distant Metastasis	Positive	–	2 (100%)	–	0.337
	Negative	8 (11.4%)	33 (47.1%)	29 (41.4%)	
Alcohol Consumption	Yes	3 (7.3%)	20 (48.8%)	18 (43.9%)	0.462
	No	5 (16.1%)	15 (48.4%)	11 (35.5%)	
Reflux	Positive	4 (12.9%)	15 (48.4%)	12 (38.7%)	0.996
	Negative	6 (12.2%)	24 (49.0%)	19 (38.8%)	
Family History	Positive	2 (8.0%)	11 (44.0%)	12 (48.0%)	0.458
	Negative	8 (14.5%)	28 (50.9%)	19 (34.5%)	
Differentiation	Low	0 (0%)	3 (42.9%)	4 (57.1%)	0.306
	Moderate	4 (9.1%)	27 (61.4%)	13 (29.5%)	
Smoking	Yes	4 (9.1%)	26 (59.1%)	14 (31.8%)	0.118
	No	6 (16.7%)	13 (36.1%)	17 (47.2%)	

Recurrence data were unavailable for one patient; therefore, recurrence analyses were performed on 79 patients.

Table S 3. Combined genotyping results of *OX40* rs17568 and *OX40L* rs1234313

Groups	Genotype Combinations								
	AAAA	AAAG	AAGG	AGAA	AGAG	AGGG	GGAA	GGAG	GGGG
Patients	4 (5%)	21 (26.2%)	17 (21.2%)	3 (3.8%)	16 (20%)	9 (11.2%)	2 (2.5%)	3 (3.8%)	5 (6.2%)
Controls	4 (3.6%)	31 (27.9%)	14 (12.6%)	1 (0.9%)	33 (29.7%)	10 (9%)	0 (0%)	14 (12.6%)	4 (3.6%)

Table S 4. Haplotype analyses of rs17568 and rs1234313 polymorphisms

Block Haplotype	Frequencies	Patients, Control Ratio	Chi-square	p
AG	0.411	0.445, 0.386	1.303	0.25
AA	0.254	0.255, 0.253	0.002	0.96
GG	0.205	0.187, 0.217	0.535	0.46
GA	0.131	0.113, 0.143	0.726	0.39

Table S 5. Haplotype evaluation between rs17568 and rs1234313

SNP Reference	Minor allele	Patients, Control Ratio	Chi-square	p
rs17568	A	0.700, 0.640	1.52	0.21
rs1234313	G	0.631, 0.604	0.30	0.58

İSTANBUL UNIVERSITY PRESS

Experimed 2026, 16 (2): 157–176

https://doi.org/10.26650/experimed.1930098

Submitted: 14.04.2026
Revision Requested: 10.06.2026
Last Revision Received: 22.06.2026
Accepted: 27.07.2026
Published Online 12.08.2026

Experimed

Research Article

Open Access

DNA Methylation Signatures Distinguish Breast Cancer Histological Subtypes and Predict Hormone Receptor Status: A TCGA-Based Integrative Analysis

Özkan Özdemir [1,2,3], Eylül Aydın [2], Turna Demirci [2], Karen Telciyan [4], Alper Akkuş [2,3], Emrah Yücesan [5], Yeşim Eralp [6] & Özden Hatırnaz Ng [1,2,3]

[1] Acıbadem Mehmet Ali Aydınlar University, School of Medicine, Department of Basic Sciences, Department of Medical Biology, İstanbul, Türkiye
[2] Acıbadem Mehmet Ali Aydınlar University, Graduate School of Health Sciences, Department of Translational Medicine, İstanbul, Türkiye
[3] Acıbadem Mehmet Ali Aydınlar University, Rare Disease and Orphan Drugs Application and Research Center (ACURARE), İstanbul, Türkiye
[4] Acıbadem Mehmet Ali Aydınlar University, Graduate School of Health Sciences, Department of Genome Studies, İstanbul, Türkiye
[5] İstanbul University-Cerrahpaşa, Institute of Neurological Sciences, Department of Neurogenetics, İstanbul, Türkiye
[6] Acıbadem Mehmet Ali Aydınlar University, Acıbadem Research Institute of Senology, İstanbul, Türkiye

Abstract

Objective: DNA methylation alterations contribute to breast cancer heterogeneity, yet their utility for distinguishing histological subtypes remains underexplored. This study aimed to identify genome-wide methylation signatures across breast cancer subtypes and develop compact probe panels for molecular classification.

Materials and Methods: HumanMethylation450 (HM450) data from 99 samples (40 infiltrating ductal carcinoma (IDC), 40 infiltrating lobular carcinoma (ILC), 14 metaplastic, 5 medullary) and 1,098 clinical samples from The Cancer Genome Atlas (TCGA) breast invasive carcinoma (BRCA) were analyzed. Differentially methylated positions (DMPs) were identified using limma with Benjamini-Hochberg false discovery rate correction. Support vector machine classifiers with minimal probe panels were developed for hormone receptor endpoints.

Results: Of the 404,059 quality-filtered CpG probes, 88,909 (22.0%) were differentially methylated across subtypes (False discovery rate (FDR)<0.05). The ILC-metaplastic comparison yielded the largest divergence (58,661 DMPs). Classifiers achieved area under the curve (AUC) values of 0.935, 0.934, and 0.866 for estrogen receptor (ER), triple-negative breast cancer (TNBC), and progesterone receptor (PR) status, respectively, using 8-bit polymerase chain reaction (PCR). Fifteen CpG probes in internal cross-validation.

Conclusion: Histological subtypes harbor distinct methylation landscapes dominated by global hypomethylation in metaplastic carcinoma. Compact CpG probe panels predict hormone receptor status with high accuracy in internal cross-validation, suggesting the potential of methylation-based diagnostic assays as a complementary approach to immunohistochemistry (IHC), pending external validation.

Keywords DNA Methylation · Breast Neoplasms · Machine Learning · Biomarkers · Receptors

Citation: Özdemir, Ö., Aydın, E., Demirci, T., Telciyan, K., Akkuş, A., Yücesan, E., Eralp, Y. & Hatırnaz Ng, Ö. DNA methylation signatures distinguish breast cancer histological subtypes and predict hormone receptor status: a TCGA-based integrative analysis. Experimed 2026; 16(2): 157-176. DOI: 10.26650/experimed.1930098

This work is licensed under Creative Commons Attribution-NonCommercial 4.0 International License.

2026. Özdemir, Ö., Aydın, E., Demirci, T., Telciyan, K., Akkuş, A., Yücesan, E., Eralp, Y. & Hatırnaz Ng, Ö.

Corresponding author: Özkan Özdemir ozkan.ozdemir@acibadem.edu.tr

INTRODUCTION

Breast cancer remains the most diagnosed malignancy and a leading cause of cancer-related death among women globally, with an estimated 2.3 million new cases and 670,000 deaths in 2022 (1, 2). It is increasingly recognized not as a single entity but as a collection of molecularly and histologically distinct diseases with divergent clinical trajectories, treatment sensitivities, and prognostic profiles (3). Although the majority of invasive breast cancers are classified as infiltrating ductal carcinoma not otherwise specified (IDC-NOS, approximately 80%), infiltrating lobular carcinoma (ILC) constitutes 10-15%, while rare subtypes, including metaplastic carcinoma (0.2–1%) and medullary carcinoma (<1%), present unique biological characteristics that are poorly captured by standard molecular profiling (4, 5).

The current clinical framework relies on immunohistochemistry (IHC) for estrogen receptor (ER), progesterone receptor (PR), and human epidermal growth factor receptor 2 (HER2), supplemented by gene expression-based assays such as prediction-analysis-of-microarray-50 (PAM50) for intrinsic molecular subtyping (LuminalA, LuminalB, HER2-enriched, basal-like, normal-like) (6). While the framework has transformed treatment stratification, IHC-based assessment remains subject to inter-laboratory variability and semi-quantitative interpretation in 10-20% of HER2 testing (7, 8). Gene expression profiling requires high-quality RNA, constraining its applicability to formalin-fixed paraffin-embedded (FFPE) specimens, the predominant practice used in clinical pathology.

DNA methylation offers an alternative biomarker modality. Methylation patterns exhibit chemical stability, are well-preserved in FFPE tissue, and can be detected and analyzed from as little as 50 ng of input DNA (9). Epigenetic alterations are among the earliest molecular events in breast carcinogenesis, regulating tumor-suppressor gene silencing (e.g., *BRCA1*, *RASSF1A*, *GSTP1*), oncogene activation, epithelial-mesenchymal transition (EMT), and immune evasion (10, 11). The clinical feasibility of methylation-based diagnostics has been demonstrated in neuro-oncology, where genome-wide methylation profiling serves as the reference standard for central nervous system (CNS) tumor classification (12).

The Cancer Genome Atlas (TCGA) has assembled comprehensive datasets for over 1,000 breast invasive carcinoma specimens, including Illumina Infinium HumanMethylation450 (HM450) BeadChip data interrogating approximately 485,000 CpG sites (13). While seminal TCGA-based studies have characterized methylation differences between PAM50 molecular subtypes (14, 15), a systematic analysis focusing on histological subtype discrimination, particularly including rare subtypes, and interpretation of the observed differences into diagnostic classifiers has been absent.

The study had two main objectives: (i) to characterize genome-wide DNA methylation differences across four breast cancer subtypes using TCGA-BRCA HM450 data, including subtype-specific signatures, differentially methylated regions (DMRs), and pathway enrichment; and (ii) to develop and internally validate minimal probe panels for accurate prediction of ER, PR, and triple-negative breast cancer (TNBC) status.

MATERIALS AND METHODS

Data Acquisition and Study Population

DNA methylation beta-value matrices and clinical annotations were obtained from the National Cancer Institute (NCI) Genomic Data Commons (GDC) portal for the TCGA-BRCA project (NCI, United States). Methylation data were generated using the Illumina Inc. (California, United States) InfiniumHM450-BeadChip (485,577 CpG-sites) and processed through the GDC harmonization pipeline employing the SEnsible Step-wise Analysis of Methylation data (SeSAMe) (NCI, United States) workflow, which incorporates p-value of out-of-band array hybridization (pOOBAH) detection masking, non-linear dye-bias correction, and background subtraction, aligned to the Genome Reference Consortium HumanBuild38 (GRCh38/hg38) reference genome (National Center for Biotechnology Information (NCBI), United States) (16). Data were retrieved using the TCGAbiolinks (Bioconductor, United States/Italy) R package (17).

For the histological subtype analysis, 99 samples were curated: IDC (n=40; International Classification of Diseases for Oncology, Third Edition [ICD-O-3] code 8500/3), ILC (n=40; code 8520/3), metaplastic carcinoma (n=14; code 8575/3), and medullary carcinoma (n=5; code 8510/3). For clinical endpoint classifier development, the full TCGA-BRCA cohort was used (n=638-1,098 depending on endpoint availability). TCGA biospecimens were collected from primary surgical resections before systemic therapy; however, incomplete annotation of neoadjuvant treatment status prevents confirmation that all samples are treatment-naïve.

Data Preprocessing and Quality Control

Raw beta values (486,427 probes) were subjected to multi-step quality control (QC). Probes were removed based on the following criteria: (i) detection p-value >0.01 in >5% of samples; (ii) mapping to the X/Y chromosome; (iii) known cross-reactivity; or (iv) overlap with common single-nucleotide polymorphisms (SNPs; minor-allele-frequency [MAF] >0.01). After filtering, 404,059 probes (83.1%) were retained.

Differential Methylation Analysis

Differentially methylated positions (DMPs) were identified using a two-stage framework. First, one-way analysis of variance (ANOVA) was conducted across the four subtypes using Benjamini-Hochberg (BH) false discovery rate (FDR) correction. Second, pairwise comparisons between all six subtype pairs were performed using the limma package (Melbourne, Australia), which employs empirical

Bayes moderation of standard errors (18). Probes with FDR<0.05 and absolute mean beta difference (Δβ)>0.1 were classified as differentially methylated. Because the four histological subtypes differ in clinical composition (e.g., hormone-receptor status and age at diagnosis), methylation associated with available clinical covariates (age and race) was additionally characterized separately; the primary subtype and endpoint contrasts were modeled univariably, and residual confounding by unmodelled clinical variables cannot be fully excluded (see Limitations).

For clinical endpoints, DMPs were identified by limma-based two-group comparison for ER status (ER+ vs. ER−; n=837), PR status (PR+ vs. PR−; n=832), HER2 status (HER2+ vs. HER2−; n=638), and TNBC (TNBC vs. non-TNBC; n=698).

Differentially Methylated Regions (DMRs)

DMRs were identified using the differentially methylated regions from the CpG array and Transcriptome package (Sydney, Australia), which applies a kernel-smoothing approach to aggregate DMP-level signals into regional calls (19). Kernel bandwidth was set to 1,000 base pairs (bp), with DMRs retained if they contained ≥3 probes and mean |Δβ|>0.1.

Gene Annotation and Pathway Enrichment

Significant DMPs were annotated using the HM450 manifest (IlluminaHumanMethylation450kanno.ilmn12.hg19). Because Infinium probe identifiers are fixed, platform-level annotations that are independent of the genome build, the GRCh38-aligned GDC beta-value matrices were linked to manifest annotations by probe identifier rather than by genomic coordinate. Therefore, probe-to-gene assignment is unaffected by the build of the annotation manifest, and no cross-build coordinate matching is performed. Genomic coordinates reported in this study were lifted over to GRCh38 (UCSC liftOver; California, United States) to maintain consistency with the alignment reference build. The top 500 DMPs per endpoint were submitted to the Enrichr (New York, United States) platform for pathway enrichment against six databases: Kyoto Encyclopedia of Genes and Genomes (KEGG; Kyoto, Japan) 2021, Gene Ontology (United States) Biological Process (GO-BP) 2023, Gene Ontology Molecular Function (GO-MF) 2023, Reactome (United States; United Kingdom) 2022, WikiPathway (The Netherlands, United States) 2023, and Molecular Signatures Database (MSigDB) Hallmark (United States) 2020 (20). Full pathway enrichment results are provided in Supplementary Table S1.

Machine Learning Classifier Development

Classifiers for ER, PR, HER2, and TNBC status were built using support vector machines (SVMs) with radial basis function kernels in a nested cross-validation framework. Two model variants were evaluated: baseline (default hyperparameters) and enhanced (inverse class-frequency weighting plus synthetic minority oversampling technique [SMOTE] for imbalance ratio>3:1). We assessed performance using AUC with 10-fold stratified cross-validation and calculated 95% confidence intervals (CIs) from 1,000 bootstrap replicates. We determined the minimal probe panels using recursive feature elimination (RFE). Classifiers were categorized into evidence tiers based on AUC thresholds: Tier 1 (high-performance, AUC≥0.85), Tier 2 (research-validated, 0.70≤AUC<0.85), and Tier 3 (exploratory, AUC<0.70). These tier labels denote internal cross-validation performance thresholds only and do not imply clinical validation, which would require confirmation in independent external cohorts.

Principal Component Analysis

Principal component analysis (PCA) was performed at two stages to distinguish the global methylation structure from the subtype-specific signal. In the first stage ("before feature extraction"), PCA was applied to the full set of remaining 404,059 quality-filtered probes to assess overall methylation variance without any prior feature selection. In the second stage ("after feature extraction"), PCA was restricted to 88,909 ANOVA-significant probes (FDR<0.05) to evaluate whether feature selection enhanced subtype separation. Variance explained by each principal component (PC), cumulative variance, and subtype centroids with standard deviations (SDs) in the PC space were computed. Subtype clustering quality was quantified using the pseudo-F-statistic, which compares between-group to within-group variance in the PC space.

Statistical Analyses

All analyses were conducted in R version 4.4 within the Bioconductor 3.20 environment. TCGAbiolinks version 2.32.0 was used for data retrieval, limma version 3.62.0 for differential methylation analysis, DMRcate version 3.2.0 and minfi version 1.52.0 for DNA methylation analyses, and caret version 6.0-94 and pROC version 1.18.5 for classifier development and receiver operating caracteristic curve analyses. Multiple testing correction used the BH-FDR method. Two-sided p<0.05 (or FDR<0.05) was the significance threshold. Classifier metrics were computed using the caret (version 6.0-94, USA) and pROC (version 1.18.5, Switzerland) packages. Descriptive statistics are reported as mean±SD or median (interquartile range). Categorical variables are presented as counts and percentages.

RESULTS

Cohort Characteristics and Data Quality

The histological subtype cohort comprised 99 female patients: 40 IDC, 40 ILC, 14 metaplastic carcinoma, and 5 medullary carcinoma (Table 1). Mean age at diagnosis ranged from 50 years (medullary) to 60 years (ILC), reflecting the age-at-presentation patterns. ER positivity was highest in ILC (90%) and lowest in medullary and metaplastic carcinomas (0% and 15%, respectively), consistent with

Table 1. Demographic characteristics of the four-subtype cohort (n=99 histologically characterized samples).

Subtype	n	Female (%)	Mean Age	ER+ (%)	PR+ (%)	HER2+ (%)	TNBC (%)
IDC	40	100	58	75	65	15	15
ILC	40	100	60	90	70	5	5
Metaplastic	14	100	57	15	10	5	70
Medullary	5	100	50	0	0	0	100
Total	**99**	**100**	**58**	**68**	**59**	**11**	**27**

IDC: infiltrating ductal carcinoma; ILC: infiltrating lobular carcinoma; ER: estrogen receptor; PR: progesterone receptor; HER2: human epidermal growth factor receptor 2; TNBC: triple-negative breast cancer (ER-/PR-/HER2-).

luminal versus basal-like molecular assignments. The broader TCGA-BRCA clinical cohort included up to 1,098 subjects, with sample sizes varying by endpoint (n=638-1,098) due to differential availability of hormone receptor, HER2, and vital status annotations. After QC-filtering, 404,059 of 486,427 HM450 probes (83.1%) were retained, consistent with the expected SeSAMe pipeline retention rates.

Genome-Wide Differential Methylation Across Histological Subtypes

ANOVA across the four histological subtypes identified 88,909 significantly differentially methylated CpG positions (22.0% of 404,059 filtered probes; FDR<0.05), with 50,598 remaining significant at FDR<0.01. Pairwise comparisons strikingly revealed asymmetric methylation divergence between subtype pairs (Table 2; Figure 1).

The ILC-metaplastic comparison yielded the greatest number of DMPs (n=58,661), with a pronounced directional bias toward

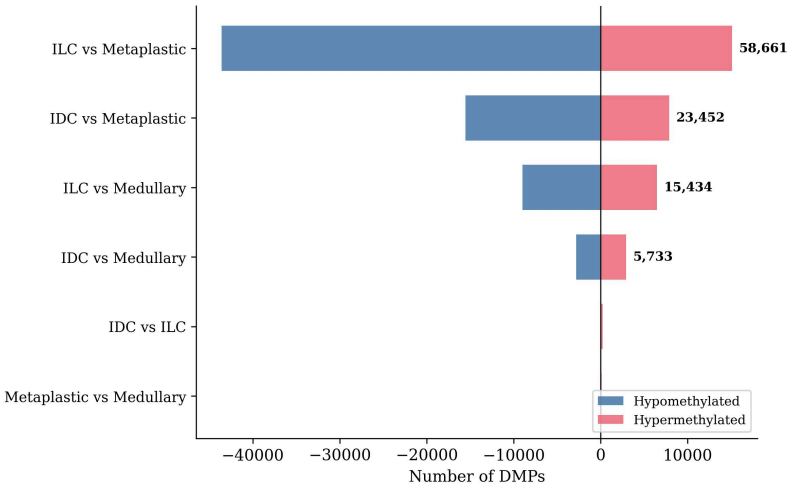


Figure 1. Pairwise DMPs between histological subtypes. Diverging bars show hypomethylated probes (blue, left) and hypermethylated probes (coral, right) relative to the second subtype listed. DMPs: differentially methylated positions; IDC: infiltrating ductal carcinoma; ILC: infiltrating lobular carcinoma.

Table 2. Pairwise DMPs between breast cancer histological subtypes

Comparison	Total DMPs	Hypermethylated	Hypomethylated	Ratio (H/L)	Filtered (%)
ILC vs Metaplastic	58,661	15,099	43,562	0.35:1	14.52
IDC vs Metaplastic	23,452	7,886	15,566	0.51:1	5.80
ILC vs Medullary	15,434	6,461	8,973	0.72:1	3.82
IDC vs Medullary	5,733	2,920	2,813	1.04:1	1.42
IDC vs ILC	227	204	23	8.87:1	0.06
Meta vs Medullary	132	89	43	2.07:1	0.03

Δβ indicates the difference in mean β values between the compared subtypes. Hyper and Hypo indicate the numbers of hypermethylated and hypomethylated DMPs, respectively. Filtered (%) indicates the proportion of quality-filtered probes meeting the DMP criteria (FDR <0.05 and |Δβ| >0.1; 404,059 probes). DMP: differentially methylated position; FDR: false discovery rate; IDC: infiltrating ductal carcinoma; ILC: infiltrating lobular carcinoma; Meta: metaplastic carcinoma; H/L: hypermethylated-to-hypomethylated ratio.

hypomethylation in metaplastic tumors (43,562 hypomethylated vs. 15,099 hypermethylated; ratio 2.9:1). In contrast, IDC and ILC showed remarkably few DMPs (n=227), reflecting their shared luminal origin. The corresponding volcano plots for all six pairwise comparisons are provided in Supplementary Figure S1.

Most Significant Differentially Methylated Sites

The ten most statistically significant DMPs across subtypes are presented in Table 3 with their genomic coordinates, F-statistics, and nearest gene annotations (the complete list of the top 1,000 DMPs is provided in Supplementary Table S2). All ten probes achieved FDR values below 1.2×10^{-9}. Notably, metaplastic carcinoma consistently displayed the most divergent methylation values. The top-ranked probe, cg08734853, maps to *GAIP*-interacting protein, C terminus 1 (*GIPC1*) on chromosome 19 and showed a mean β of 0.739 in metaplastic tumors compared with 0.918 in IDC and 0.935 in ILC (Δβ=−0.196). The largest maximum pairwise difference (Δβ=−0.452) was observed at cg19274341 (chr1, long non-coding RNA locus), where metaplastic carcinoma exhibited near-complete demethylation (β=0.290). Probe cg27090078, mapping to *CAPG* (capping actin protein, gelsolin-like) on chromosome 2, exhibited the reverse pattern, with metaplastic carcinoma showing hypermethylation (mean β=0.800) relative to IDC (0.466) and ILC (0.433; Δβ=+0.367), suggesting locus-specific regulatory divergence. Two probes mapped to *STARD13* and *NAXD* on chromosome 13, while others involved *TRAF3IP2* (chr6), *ZNRF1* (chr16), and *IFIT1B* (chr10), genes implicated in immune signaling, protein ubiquitination, and interferon response, respectively. The genomic coordinate (GRCh38) and regulatory context (promoter, gene body, or intergenic) of each probe are provided in Table 3. Notably, although these top-ranked positions are individually strong single-CpG signals, several genes map to genes showing coordinated multi-probe methylation across the promoter; the clearest example is *STARD13*, where nine promoter-associated probes are concordantly altered in metaplastic carcinoma. More broadly, the subtype methylation signatures resolve into multi-probe differentially methylated regions (mean 3.6-4.2 probes per region) that are predominantly promoter-associated, indicating cumulative, regionally coordinated methylation change rather than uniformly isolated single-CpG alterations.

Principal Component Analysis

PCA on All Quality-Filtered Probes

PCA was first performed on the complete set of 404,059 quality-filtered CpG probes without prior feature selection to assess the extent to which global methylation variance captures histological subtype identity. In this analysis, the first five PCs explained a modest cumulative proportion of total variance, reflecting the high dimensionality and noise inherent in the full HM450 probe set. While a general trend of metaplastic carcinoma separation was observable along PC1, the four histological subtypes overlapped substantially, and IDC, ILC, and medullary samples formed a largely intermixed cloud (Figure 2).

The 95% confidence intervals for all four subtypes showed extensive overlap, particularly between IDC and ILC. This indicates that most CpG-level variance in the unfiltered dataset is driven by inter-individual biological variation, stochastic methylation noise, and technical factors rather than by histological subtype identity.

PCA on ANOVA-Significant Probes

PCA was then repeated using only the 88,909 ANOVA-significant probes (FDR<0.05), representing the feature-extracted probe set. This analysis revealed a dramatic improvement in subtype separation (Figure 3).

Table 3. Top 10 most significantly differentially methylated CpG positions across four breast cancer histological subtypes ranked by F-statistic.

Probe ID	Coordinate (GRCh38)	Gene	F-stat	FDR	β IDC	β ILC	β Meta	δβ Max	Feature
cg08734853	chr19:14,487,533	*GIPC1*	39.8	3.8×10^{-11}	0.918	0.935	0.739	−0.196	Promoter
cg09246897	chr3:34,036,994	Intergenic	36.9	1.4×10^{-10}	0.838	0.889	0.638	−0.300	Intergenic
cg13370010	chr13:33,169,510	*STARD13*	35.9	1.8×10^{-10}	0.920	0.935	0.707	−0.228	Promoter
cg27090078	chr2:85,394,971	*CAPG*	35.3	2.0×10^{-10}	0.466	0.433	0.800	+0.367	Gene body
cg02607915	chr16:75,080,416	*ZNRF1*	34.7	2.6×10^{-10}	0.919	0.929	0.735	−0.194	Gene body
cg19274341	chr1:8,083,831	lncRNA	33.0	6.6×10^{-10}	0.711	0.742	0.290	−0.452	Intergenic
cg16704530	chr6:111,568,736	*TRAF3IP2*	32.9	6.6×10^{-10}	0.837	0.844	0.707	−0.137	Promoter
cg05640533	chr13:110,634,652	*NAXD*	32.6	7.4×10^{-10}	0.829	0.887	0.713	−0.174	Gene body
cg18044543	chr10:89,385,038	*IFIT1B*	31.8	1.1×10^{-9}	0.866	0.899	0.673	−0.226	Gene body
cg03309393	chr6:12,491,151	Intergenic	31.6	1.1×10^{-9}	0.813	0.855	0.450	−0.405	Intergenic

β values represent mean methylation levels within each subtype. Δβ Max represents the signed difference between the two subtypes with the largest absolute pairwise difference across all four subtypes. Positive and negative values indicate higher and lower methylation, respectively, in metaplastic carcinoma relative to the most divergent subtype. Medullary carcinoma was included in the Δβ Max calculation but is not displayed. Coordinate (GRCh38): genomic position of the probe in the Genome Reference Consortium Human Build 38; Gene: nearest or associated annotated gene; Feature: genomic context of the probe relative to the annotated gene; F-stat: F-statistic; FDR: False discovery rate; IDC: infiltrating ductal carcinoma; ILC: infiltrating lobular carcinoma; Meta: metaplastic carcinoma; lncRNA: long non-coding RNA.

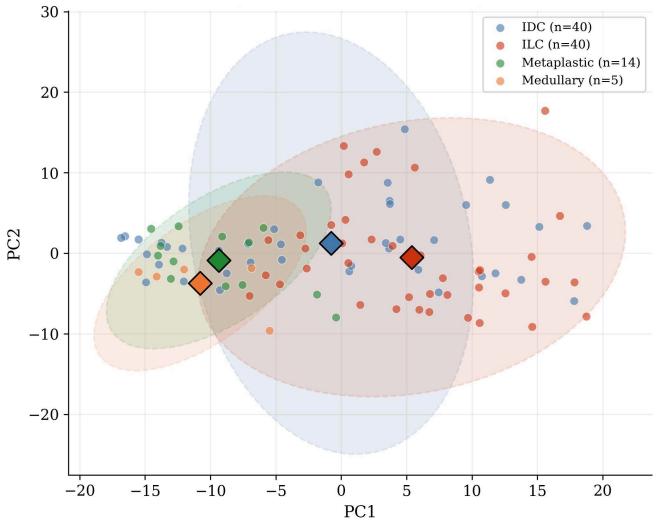


Figure 2. PCA of DNA methylation before feature extraction. PCA on all 404,059 quality-filtered CpG probes showing substantial overlap between histological subtypes. Large diamond markers indicate subtype centroids; dashed ellipses represent 95% confidence intervals. Color-coded by histological subtype: IDC (blue), ILC (red), metaplastic (green), medullary (orange). PCA: principal component analysis; PC: Principal component; IDC: infiltrating ductal carcinoma; ILC: infiltrating lobular carcinoma.

The first five PCs now explained 28.8%, 8.5%, 6.6%, 3.6%, and 3.1% of the variance, respectively, yielding a cumulative 50.6% in just five components, which is a substantially higher proportion than observed in the first, unfiltered analysis. PC1 (28.8%) primarily separated metaplastic carcinoma from all other subtypes, consistent with its globally hypomethylated profile. PC2 (8.5%) distinguished ILC from IDC and medullary tumors. Medullary carcinoma occupied an intermediate position between IDC and metaplastic clusters along PC1, consistent with its basal-like molecular assignment. The 95% confidence intervals after feature extraction showed markedly reduced overlap, with metaplastic and medullary clusters becoming visually distinct from the luminal subtypes.

Subtype Centroids and Clustering Quality

Subtype centroids in PC1-PC2 space were computed to quantify inter-subtype separation (Table 4; Supplementary Table S3). Medullary carcinoma exhibited the most negative PC1 centroid (-10.80 ± 4.43), followed by metaplastic carcinoma (-9.37 ± 4.48), IDC (-0.77 ± 10.70), and ILC (+5.40 ± 7.07). The large SD of IDC along PC1 reflects its molecular heterogeneity, encompassing all PAM50 subtypes. The pseudo-F statistic for subtype clustering was 10.55, confirming that the observed PCA structure is driven by biological subtype differences rather than batch effects. The variance distribution of the

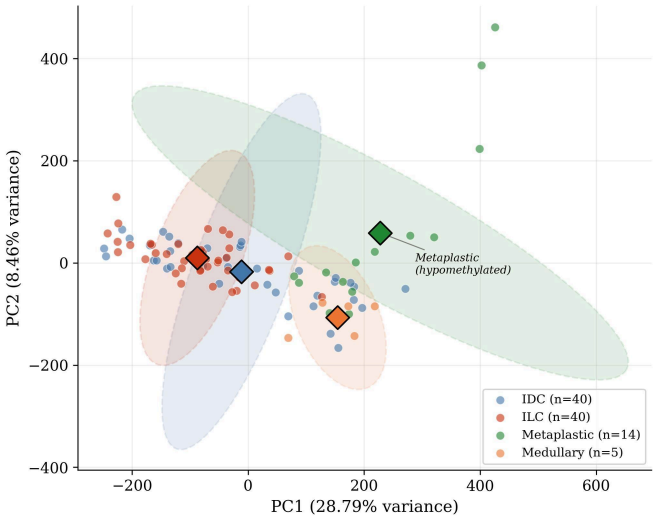


Figure 3. PCA of DNA methylation after feature extraction. PCA restricted to 88,909 ANOVA-significant probes (FDR < 0.05) showing improved separation of the selected subtype-associated methylation patterns, particularly for metaplastic carcinoma. Large diamond markers indicate subtype centroids; dashed ellipses represent 95% confidence intervals. PCA: principal component analysis; PC: Principal component; IDC: infiltrating ductal carcinoma; ILC: infiltrating lobular carcinoma.

Table 4. Subtype centroids and dispersion in PCA space after feature extraction (88,909 ANOVA-significant probes).

Subtype	n	PC1 (Mean ± SD)	PC2 (Mean ± SD)	PC1 Range	Separation
IDC	40	−0.77 ± 10.70	+1.26 ± 4.45	−16.8 to +18.8	Broad / heterogeneous
ILC	40	+5.40 ± 7.07	−0.49 ± 6.68	−7.0 to +18.8	Luminal cluster
Metaplastic	14	−9.37 ± 4.48	−0.88 ± 3.51	−14.5 to −0.4	Distinct / compact
Medullary	5	−10.80 ± 4.43	−3.72 ± 3.31	−15.5 to −5.5	Basal-like cluster

PCA: principal component analysis; IDC: infiltrating ductal carcinoma; ILC: infiltrating lobular carcinoma; PC: principal component; SD: standard deviation; ANOVA: one-way analysis-of-variance.

first five principal components is provided in Supplementary Figure S2.

Subtype-Specific Methylation Signature

Subtype-specific methylation signatures varied dramatically in magnitude. The methylation heatmap of the top 30 differentially methylated CpG sites across subtypes (Figure 4) illustrates the distinct methylation blocks. Metaplastic carcinoma exhibited 22,888 DMPs (16,062 hypomethylated vs. 6,826 hypermethylated; 2.4:1 ratio), consistent with the global hypomethylation phenotype of basal-like/mesenchymal tumors (21). ILC possessed 5,869 DMPs dominated by hypermethylation (79.1%), which indicates a methylation-gain phenotype associated with lobular differentiation. Medullary carcinoma showed a balanced signature (4,150 DMPs), while IDC lacked a unique signature (0 DMPs), reflecting its heterogeneous composition spanning all PAM50 subtypes (Figure 5).

Pathway enrichment of the metaplastic signature revealed EMT, Wnt/β-catenin signaling, and extracellular matrix organization. The ILC signature was enriched for cell adhesion molecules and cadherin binding (GO-MF), consistent with *CDH1* (E-cadherin) loss (22). The medullary signature showed enrichment for interferon signaling and antigen processing, reflecting its dense lymphocytic infiltrate. Enrichment analysis using Enrichr identified 5 significant WikiPathway terms for the ER signature (top: Th17 Cell Differentiation), 4 GO-BP terms and 4 GO-MF terms for HER2 (top: Regulation of Leukocyte Proliferation; Sequence-Specific Double-Stranded DNA Binding), and 2 MSigDB Hallmark terms for PR (top: Estrogen Response Early). The PR signature additionally showed enrichment for dosage compensation by X chromosome inactivation (GO-BP, adjusted $p<0.05$), consistent with known X-linked regulatory mechanisms in hormone receptor signaling. Full pathway enrichment results are provided in Supplementary Table S1.

Clinical Endpoint Classifiers

The number of DMPs ranged from 1,035 (HER2) to 41,397 (TNBC) across endpoints (Figure 6). The SVM classifier performance is summarized in Table 5 and Figure 7.

The ER classifier achieved AUC=0.935 with 10 CpG probes (sensitivity 94.3%, specificity 82.2%). The TNBC classifier (AUC=0.934, 8 probes) and PR classifier (AUC=0.866, 15 probes) also exceeded the predefined high-performance AUC threshold (Tier 1, AUC ≥ 0.85). The HER2 classifier showed Tier 2 performance (AUC=0.852 baseline) with 30 probes, reflecting the predominantly genomic basis rather than epigenomic of HER2 overexpression.

Classifier gene annotation revealed GATA binding protein 3 (*GATA3)*, progesterone receptor (*PGR)*, and homeobox A3 (*HOXA3)* in the ER panel, stem cell differentiation pathways in TNBC, and growth factor receptor-bound protein 7 (*GRB7)* events in Erb-B2 receptor tyrosine kinase 2 (*ERBB2)* signaling (Reactome) for HER2, providing biological plausibility for these features (27,28). The complete methylation signature summary for all 14 classifiers, including panel sizes, AUC values, and tier assignments, is provided in Supplementary Table S4.

Differentially Methylated Regions

DMR analysis identified contiguous genomic intervals of coordinated methylation change. The number and total probe content of DMRs varied substantially across endpoints and subtype signatures (Table 6). The metaplastic subtype signature yielded the largest number of DMRs (102 regions, 403 probes), followed by ILC (86 DMRs, 346 probes) and HER2 status (32 DMRs, 124 probes). Vital status showed no DMRs, consistent with the poor performance of the survival classifier. To characterize DMR topology, each region was classified by its position relative to the nearest gene as promoter-associated (within a transcription start site window, TSS1500/TSS200, or 5′UTR/first exon), gene-body/intragenic, or intergenic; the distribution of these categories for each endpoint and subtype signature is summarized in the Genomic context column of Table 6.

For the Tier 1-2 clinical endpoints, the most prominent TNBC-associated DMRs included a hypomethylated region on chromosome 5 (chr5:43,017,458-43,020,524; 13 probes; mean Δβ=−0.347) mapping to long non-coding RNAs (lncRNAs) CTD-2035E11.3 and CTD-2201E18.3 and a region on chromosome 1 (chr1:171,841,159-171,841,327; gene *DNM3*;5 probes; mean Δβ=−0.364). For HER2 status, the largest DMR mapped to aldehyde dehydrogenase 1 family member L1 (*ALDH1L1;* chr3:126,180,526-126,181,081; 10 probes; mean Δβ=−0.145), followed by *STAC2* (chr17; 7 probes) and glutathione S-transferase pi 1 (*GSTP1;* chr11;5 probes; mean Δβ=−0.142). Because each of these DMRs aggregates multiple neighboring CpG probes, the observed differences represent cumulative regional methylation changes spanning the gene and its flanking regulatory elements; several

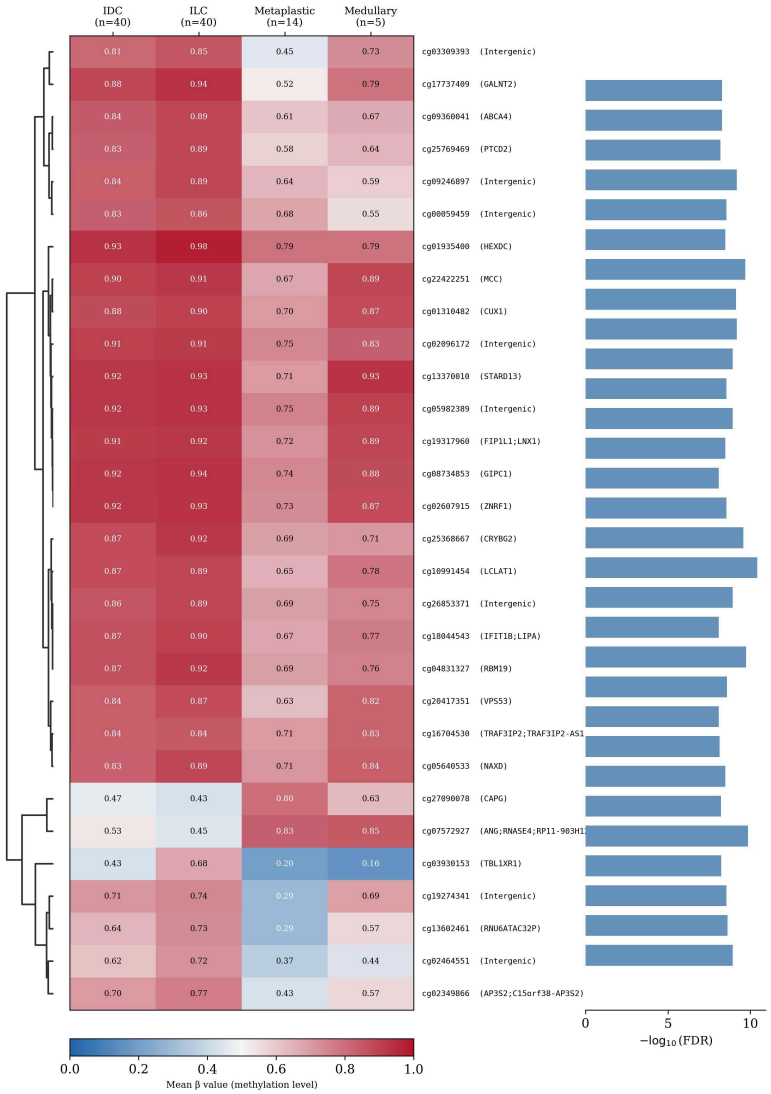


Figure 4. Methylation Heatmap of the Top 30 Differentially Methylated CpG Sites. Mean β values across four histological subtypes, with hierarchical clustering dendrogram (Ward's method). Cell values indicate mean methylation levels (0 = unmethylated, 1 = fully methylated). Rightmost bars show statistical significance (-log10 FDR). The hypomethylated block in metaplastic carcinoma is clearly visible. CpG: cytosine-phosphate-guanine; FDR: false discovery rate; IDC: infiltrating ductal carcinoma; ILC: infiltrating lobular carcinoma.

map to promoter-associated regions (annotated in Table 6 and Supplementary Table S2), where coordinated promoter methylation is most likely to influence transcription.

Integration with Known Breast Cancer Genes

Cross-referencing with 15 established breast cancer genes confirmed *GSTP1* (5 probes, associated with HER2 status), *TP73* (p53-family; 3 probes), estrogen receptor 1 (*ESR1*; 7 probes), and concordant methylation-expression relationships for vimentin (*VIM;* an EMT marker) and *GATA3* (a luminal differentiation master regulator). The finding that *ESR1* did not reach significance in individual endpoint classifiers indicates that ER protein status is governed by upstream epigenomic programming, involving *GATA3* and *FOXA1* networks, rather than direct *ESR1* promoter methylation alone.

DISCUSSION

This study yields three main findings: (i) breast cancer subtypes exhibit distinct methylation landscapes, with metaplastic carcinoma showing extensive hypomethylation (>22,000 CpGs); (ii) inter-subtype differences span three orders of magnitude (132-58,661 DMPs), indicating an epigenomic hierarchy; and (iii) compact 8-15 CpG panels classify ER, PR, and TNBC status with AUC>0.86 in internal cross-validation.

The marked divergence between ILC and metaplastic carcinoma (58,661 DMPs) versus minimal IDC-ILC differences (227 DMPs) indicates fundamentally distinct epigenomic programs. *CDH1* loss in a luminal context indicates that ILC, whereas mesenchymal transdifferentiation involving EMT and Wnt/β-catenin activation characterizes metaplastic carcinoma (21, 22). The observed hypomethylation bias aligns with global DNA hypomethylation

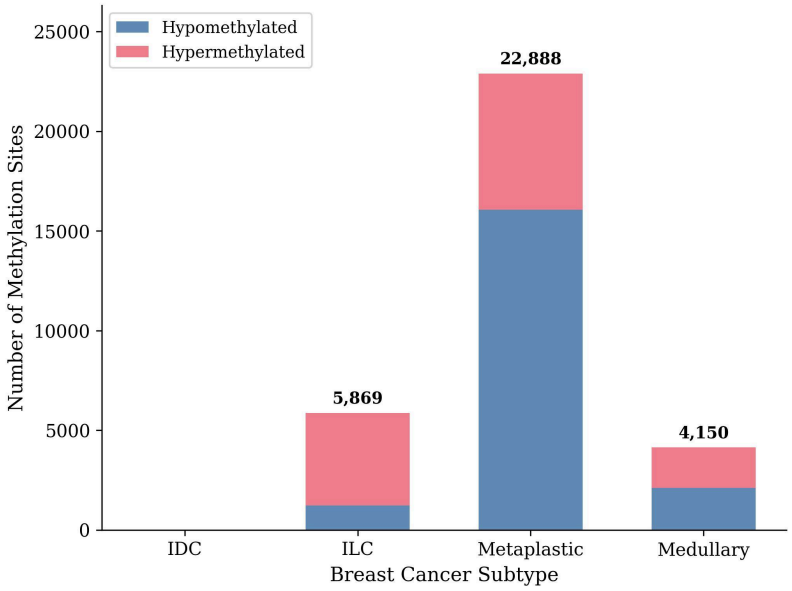


Figure 5. Subtype-Specific Methylation Signatures. Stacked bars show hypermethylated (coral) and hypomethylated (blue) probes unique to each subtype. Metaplastic carcinoma dominates with 22,888 DMPs. DMPs: differentially methylated positions; IDC: infiltrating ductal carcinoma; ILC: infiltrating lobular carcinoma.

Table 5. SVM classifier performance for clinical endpoints.

Endpoint	n	Class Ratio	Baseline AUC	Enhanced AUC	Panel	DMPs	Tier
ER Status	837	646:191	0.923	0.935	10 CpGs	36,953	Tier 1
TNBC	698	592:106	0.940	0.934	8 CpGs	41,397	Tier 1
PR Status	832	563:269	0.866	0.862	15 CpGs	18,580	Tier 1
HER2 Status	638	530:108	0.852	0.834	30 CpGs	1,035	Tier 2

Class Ratio indicates the majority-to-minority class ratio. Baseline and Enhanced AUC refer to model performance before and after class-imbalance correction, respectively. Panel indicates the number of selected CpG probes, and Tier was assigned according to Enhanced AUC. SVMs: support vector machines; AUC: area under the receiver operating characteristic curve; Panel: CpG probes in the minimal diagnostic set. DMPs: differentially methylated positions. Tier: evidence tier; ER: estrogen receptor; TNBC: triple-negative breast cancer; PR: progesterone receptor; HER2: human epidermal growth factor receptor 2.

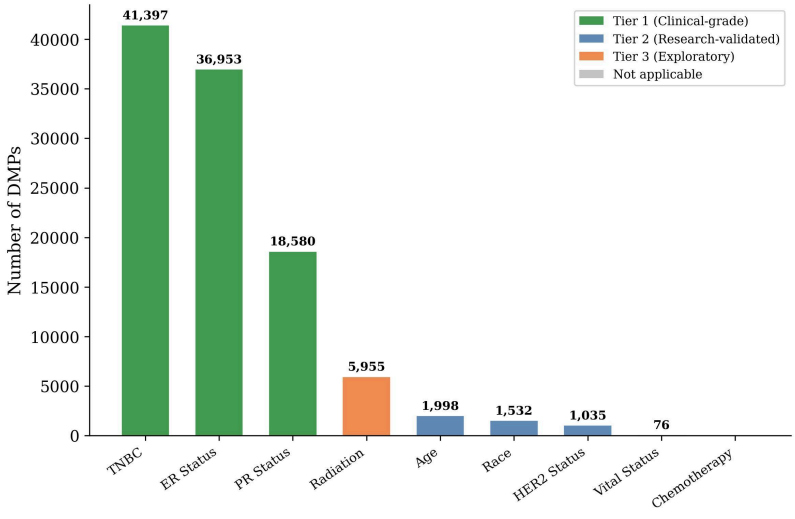


Figure 6. DMPs by Clinical Endpoint. Bars color-coded by evidence tier: Tier 1/high-performance (green), Tier 2/research-validated (blue), and Tier 3/exploratory (orange). DMPs: differentially methylated positions; ER: estrogen receptor; PR: progesterone receptor; HER2: human epidermal growth factor receptor 2; TNBC: triple-negative breast cancer.

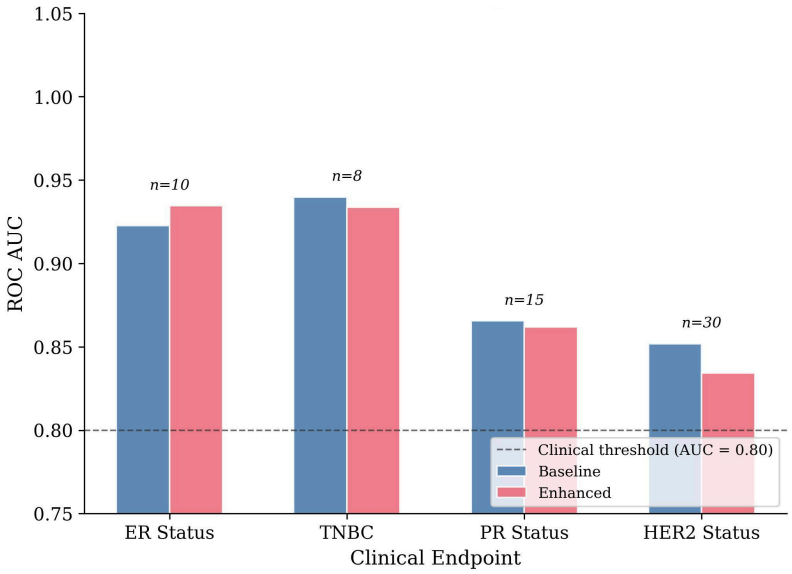


Figure 7. Methylation-Based Classifier Performance. Grouped bars show baseline and enhanced AUC for four clinical endpoints. Dashed lines indicate the AUC=0.80 reference level; Tier 1 (high-performance) classifiers reach AUC≥0.85. Minimal probe panel sizes (n) annotated above the bars. AUC: area under the receiver operating characteristic curve; ER: estrogen receptor; PR: progesterone receptor; HER2: human epidermal growth factor receptor 2; TNBC: triple-negative breast cancer.

linked to *DNMT3B* downregulation and loss of H3K9me3-associated heterochromatin (23, 24).

Unlike the other subtypes, IDC yielded no unique methylation signature (0 subtype-specific DMPs). This is considered a biologically expected result rather than a technical artifact. IDC of no special type is a diagnosis of exclusion spanning the full range of intrinsic molecular subtypes (luminal A/B, HER2-enriched, and basal-like), so its methylation profile is a heterogeneous admixture in which subtype-defining signals average out. Consistent with this, IDC showed the broadest PC1 dispersion of any subtype (largest within-group SD; Table 4), implying that it is better classified at the molecular subtype (e.g., PAM50) than at the histological level.

The two-layered PCA approach integrating the feature extraction demonstrates the critical importance of feature selection for methylation-based subtyping. While the full 404,059-probe PCA showed overlapping subtype distributions, restricting analysis to the 88,909 significant probes yielded four-subtype separation with 43.8% cumulative variance in three components and a pseudo-F statistic of 10.55. This finding practically implies that methylation-based

Table 6. DMRs identified by endpoint, with key characteristics.

Endpoint/Signature	n DMRs	Total Probes	Mean Probes/DMR	Top Gene	Top δβ	Direction	Genomic context
Sig. Metaplastic	102	403	4.0	Multiple	Variable	Hypo-dominant	Predominantly promoter (73%)
Sig. ILC	86	346	4.0	Multiple	Variable	Hyper-dominant	Predominantly promoter (73%)
Sig. Medullary	36	138	3.8	Multiple	Variable	Balanced	Predominantly promoter (83%)
HER2 Status	32	124	3.9	*ALDH1L1*	−0.145	Hypo	Predominantly promoter (81%)
Age	30	116	3.9	*DNAH10*	+0.138	Hyper	Predominantly promoter (77%)
Race	27	103	3.8	Multiple	Variable	Mixed	Promoter-enriched (56%)
PR Status	15	54	3.6	*ESR1*	−0.164	Hypo	Predominantly gene body (60%)
TNBC	12	50	4.2	*DNM3*	−0.364	Hypo	Gene body-enriched (42%)
ER Status	10	39	3.9	Multiple	Variable	Mixed	Predominantly gene body (60%)
Radiation	9	34	3.8	Multiple	Variable	Mixed	Promoter-enriched (56%)

DMRs were detected using DMRcate with kernel bandwidth = 1,000 bp and minimum 3 probes per region. Genomic context: classification of each region set by its relationship to the nearest gene into promoter-associated (TSS1500/TSS200/5′UTR/first exon), gene-body/intragenic, or intergenic categories. DMRs: differentially methylated regions; ILC: infiltrating lobular carcinoma; ER: estrogen receptor; TNBC: triple-negative breast cancer; PR: progesterone receptor; HER2: human epidermal growth factor receptor 2; TSS: transcription start site; UTR: untranslated region. n DMRs indicates the number of detected regions, and Mean Probes/DMR indicates the mean number of CpG probes per region. Top signed Δβ indicates the methylation difference for the top DMR; positive and negative values indicate hypermethylation and hypomethylation, respectively, in the target group relative to its comparator.

diagnostic assays should incorporate a prior feature selection step rather than using all available probes.

The compact classifier panels are, in principle, compatible with existing commercial methylation assay formats, including targeted bisulfite pyrosequencing, methylation-specific multiplex ligation-dependent probe amplification (MS-MLPA), and nanopore-based single-molecule detection, all of which are performable on FFPE tissue (25, 26). The identification of *GATA3* in the ER classifier supports the biological basis of the *GATA3* methylation state, reflecting the entire luminal differentiation program encompassing *ER* expression (27). *GSTP1* hypermethylation associated specifically with HER2 status corroborates known mechanistic connections between detoxification gene silencing and HER2-driven tumorigenesis (28).

A key clinical question is why methylation-based classification is needed when IHC for ER, PR, and HER2 is widely available and cost-effective. Rather than replacing IHC, methylation profiling complements it by addressing key limitations. IHC is semiquantitative and variable, particularly in ER-low cases (1-10%) (7, 8), and depends on tissue antigenicity, which may be compromised in degraded samples. In contrast, methylation is chemically stable and objectively measurable. A single assay can also simultaneously assess ER, PR, and TNBC status from limited material. In equivocal or discordant cases, methylation profiling may provide an orthogonal readout of the underlying epigenomic regulation.

Beyond receptor classification, subtype-specific methylation signatures have implications for personalized treatment stratification. ILC, despite high ER positivity (90% in this cohort), shows heterogeneous responses to endocrine therapy and late recurrences poorly captured by current prognostic tools (22). The ILC methylation signature (5,869 DMPs, 79.1% hypermethylated), enriched for cell adhesion and cadherin-binding pathways, may enable refined risk stratification within this group. Identifying patients with divergent methylation profiles could guide decisions on adjuvant chemotherapy, extended endocrine therapy, or *CDK4/6* inhibitors. Metaplastic carcinoma, with 70% TNBC frequency and the most divergent methylation landscape (22,888 DMPs), remains a therapeutic challenge due to poor chemotherapy response. The EMT and Wnt/β-catenin pathway enrichment observed in the metaplastic methylation signature suggests that these tumors may not be candidates for immune checkpoint inhibitors, given the established link between EMT programs and resistance to PD-1 inhibitors, despite a positive feedback loop with increased PD-1 expression and EMT programming (29, 30), and may instead be enrolled in clinical trials for emerging Wnt-pathway-targeted agents. Overall, methylation-based subclassification may support the selection of patients for targeted therapies.

This study has several limitations that should be considered. First, rare subtypes had limited sample sizes (metaplastic n=14, medullary n=5), increasing the risk of overfitting and rendering these results exploratory. In addition, the marked class imbalance (40:40:14:5) may inflate Type-I-error in ANOVA contrasts involving smaller groups. Most importantly, the classifiers were evaluated using internal 10-fold cross-validation without external validation; this lack of external validation is the principal limitation of the study, and the reported classifier metrics should be regarded as estimates of internal performance that require confirmation in independent external cohorts before any clinical use is considered. In addition, the primary subtype and endpoint analyses were not adjusted for clinical covariates (e.g., age, stage, and intrinsic molecular subtype); although covariate-associated methylation was characterized separately, residual confounding cannot be fully excluded. Furthermore, the HM450 array interrogates only approximately 1.7% of genomic CpG sites, whereas the newer EPICv2 array provides broader coverage. The predominance of North American and European populations in the TCGA cohort may also limit the generalizability of our findings to other ethnic groups. Batch effects were assessed but not formally corrected due to unavailable metadata. Moreover, neoadjuvant treatment status was not uniformly annotated, so treatment-induced epigenetic effects cannot be excluded, particularly in metaplastic and medullary cases. Finally, classifiers for clinical stage (AUC=0.594) and overall survival (AUC=0.648) showed limited performance, reflecting the anatomical basis of staging and the limitations of binary survival analysis without accounting for censoring.

Building on the findings of this study, future work should prioritize external validation of the 8-15 probe panels in FFPE cohorts, direct comparison with IHC, extension to EPIC arrays and long-read sequencing, clustered regularly interspaced short palindromic repeats (CRISPR)-based functional validation of key CpG sites, and clinical utility studies assessing impact on treatment decisions.

CONCLUSION

This study provides a genome-wide characterization of DNA methylation across four breast cancer histological subtypes and demonstrates that compact panels of 8-15. Ten CpG probes achieve AUC>0.93 for ER and TNBC classification in internal cross-validation. The 88,909 differentially methylated positions, distinct hypomethylated profile of metaplastic carcinoma, and structured PCA evidence for feature-extraction-dependent subtype separation support the potential of DNA methylation as a translational diagnostic modality, pending external validation. Upon external validation, these signatures may refine breast cancer subtyping and personalized therapeutic decision-making.

Ethics Committee Approval: This study is based entirely on publicly available, deidentified TCGA data and does not involve human subject recruitment or identifiable patient information. Therefore, ethics committee approval was not required.

Peer Review: Externally peer-reviewed.

Author Contributions: Conception/Design of Study- Ö.Ö., E.A., Y.E., Ö.H.N.; Data Acquisition- Ö.Ö., E.A., T.D., K.T., A.A.; Data Analysis/Interpretation- Ö.Ö., E.A., E.Y.; Drafting Manuscript- Ö.Ö., E.A., T.D., K.T., A.A.; Critical Revision of Manuscript- E.Y., Y.E., Ö.H.N.; Final Approval and Accountability- Ö.Ö., E.A., T.D., K.T., A.A., E.Y., Y.E., Ö.H.N.

Conflict of Interest: The authors have no conflict of interest to declare.

Financial Disclosure: The authors declared that this study has received no financial support.

Author Details

Özkan Özdemir
[1] Acıbadem Mehmet Ali Aydınlar University, School of Medicine, Department of Basic Sciences, Department of Medical Biology, İstanbul, Türkiye
[2] Acıbadem Mehmet Ali Aydınlar University, Graduate School of Health Sciences, Department of Translational Medicine, İstanbul, Türkiye
[3] Acıbadem Mehmet Ali Aydınlar University, Rare Disease and Orphan Drugs Application and Research Center (ACURARE), İstanbul, Türkiye
0000-0002-2647-6416 ozkan.ozdemir@acibadem.edu.tr

Eylül Aydın
[2] Acıbadem Mehmet Ali Aydınlar University, Graduate School of Health Sciences, Department of Translational Medicine, İstanbul, Türkiye
0009-0005-3982-5303

Turna Demirci
[2] Acıbadem Mehmet Ali Aydınlar University, Graduate School of Health Sciences, Department of Translational Medicine, İstanbul, Türkiye
0000-0003-4971-7494

Karen Telciyan
[4] Acıbadem Mehmet Ali Aydınlar University, Graduate School of Health Sciences, Department of Genome Studies, İstanbul, Türkiye
0009-0003-4877-8997

Alper Akkuş
[2] Acıbadem Mehmet Ali Aydınlar University, Graduate School of Health Sciences, Department of Translational Medicine, İstanbul, Türkiye
[3] Acıbadem Mehmet Ali Aydınlar University, Rare Disease and Orphan Drugs Application and Research Center (ACURARE), İstanbul, Türkiye
0009-0005-8696-0284

Emrah Yücesan
[5] İstanbul University-Cerrahpaşa, Institute of Neurological Sciences, Department of Neurogenetics, İstanbul, Türkiye
0000-0003-4512-8764

Yeşim Eralp
[6] Acıbadem Mehmet Ali Aydınlar University, Acıbadem Research Institute of Senology, İstanbul, Türkiye
0000-0001-9603-4755

Özden Hatırnaz Ng
[1] Acıbadem Mehmet Ali Aydınlar University, School of Medicine, Department of Basic Sciences, Department of Medical Biology, İstanbul, Türkiye
[2] Acıbadem Mehmet Ali Aydınlar University, Graduate School of Health Sciences, Department of Translational Medicine, İstanbul, Türkiye
[3] Acıbadem Mehmet Ali Aydınlar University, Rare Disease and Orphan Drugs Application and Research Center (ACURARE), İstanbul, Türkiye
0000-0001-7728-6527

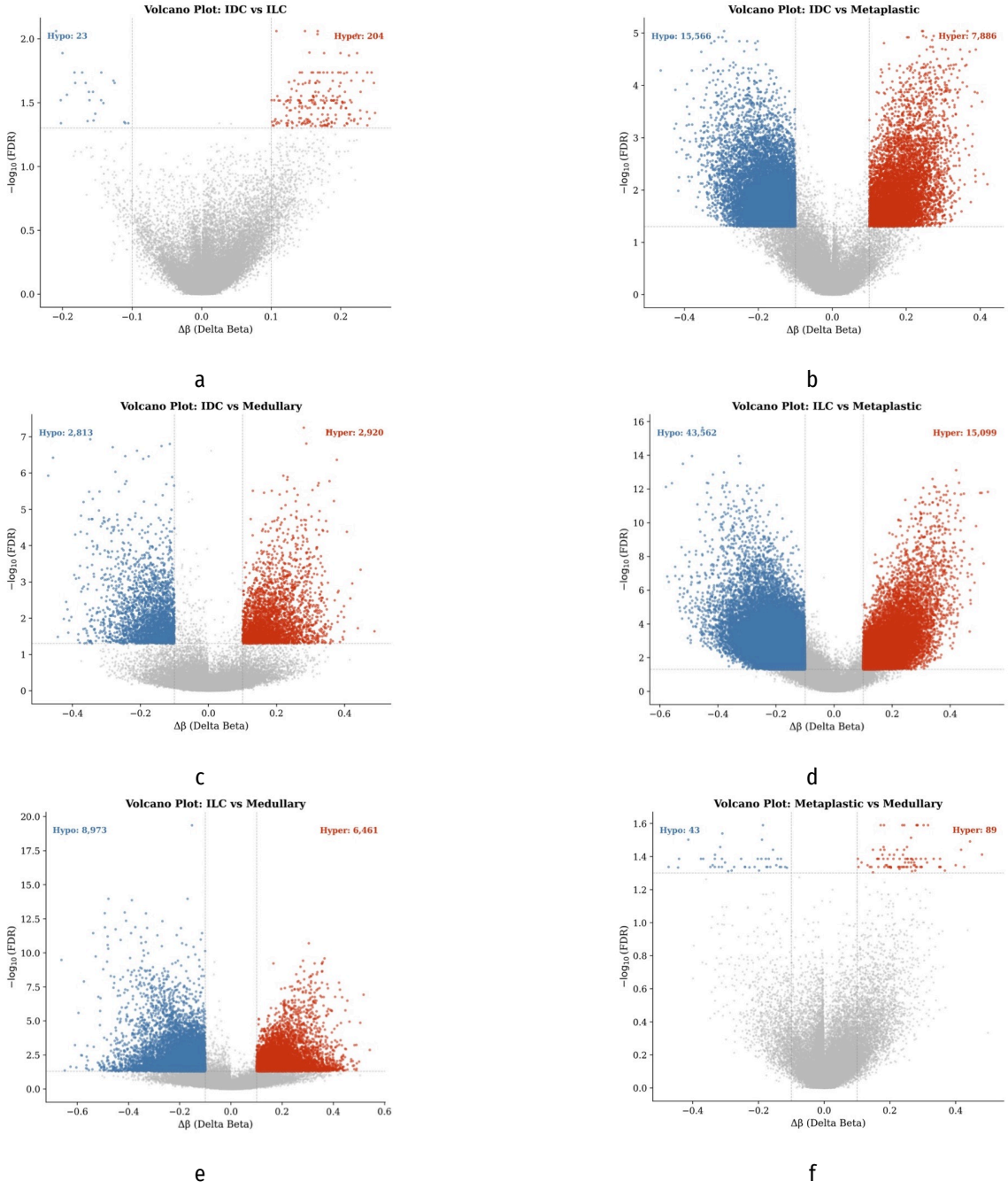
REFERENCES

1. Sung H, Ferlay J, Siegel RL, Laversanne M, Soerjomataram I, Jemal A, et al. Global Cancer Statistics 2020: GLOBOCAN Estimates of Incidence and Mortality Worldwide for 36 Cancers in 185 Countries. CA Cancer J Clin 2021; 71(3): 209-49.
2. Bray F, Laversanne M, Sung H, Ferlay J, Siegel RL, Soerjomataram I, et al. Global cancer statistics 2022: GLOBOCAN estimates of incidence and mortality worldwide for 36 cancers in 185 countries. CA Cancer J Clin 2024; 74(3): 229-63.
3. Perou CM, Sørlie T, Eisen MB, van de Rijn M, Jeffrey SS, Rees CA, et al. Molecular portraits of human breast tumours. Nature 2000; 406(6797): 747-52.
4. Li CI, Anderson BO, Daling JR, Moe RE. Trends in incidence rates of invasive lobular and ductal breast carcinoma. JAMA 2003; 289(11): 1421-4.
5. Weigelt B, Geyer FC, Reis-Filho JS. Histological types of breast cancer: how special are they? Mol Oncol 2010; 4(3): 192-208.
6. Parker JS, Mullins M, Cheang MC, Leung S, Voduc D, Vickery T, et al. Supervised risk predictor of breast cancer based on intrinsic subtypes. J Clin Oncol 2009; 27(8): 1160-7.
7. Hammond ME, Hayes DF, Dowsett M, Allred DC, Hagerty KL, Badve S, et al. American Society of Clinical Oncology/College of American Pathologists guideline recommendations for immunohistochemical testing of estrogen and progesterone receptors in breast cancer. J Clin Oncol 2010; 28(16): 2784-95.
8. Viale G. The current state of breast cancer classification. Ann Oncol 2012; 23(Suppl 10): x207-10.
9. Laird PW. Principles and challenges of genome-wide DNA methylation analysis. Nat Rev Genet 2010; 11(3): 191-203.
10. Baylin SB, Jones PA. Epigenetic determinants of cancer. Cold Spring Harb Perspect Biol 2016; 8(9): a019505.
11. Feinberg AP, Koldobskiy MA, Göndör A. Epigenetic modulators, modifiers and mediators in cancer etiology and progression. Nat Rev Genet 2016; 17(5): 284-99.
12. Capper D, Jones DTW, Sill M, Hovestadt V, Thota N, Lettmann M, et al. DNA methylation-based classification of central nervous system tumors. Nature 2018; 555(7697): 469-74.
13. The Cancer Genome Atlas Network. Comprehensive molecular portraits of human breast tumors. Nature 2012; 490(7418): 61-70.
14. Stefansson OA, Moran S, Gomez A, Sayols S, Arribas-Jorba C, Sandoval J, et al. A DNA methylation-based definition of biologically distinct breast cancer subtypes. Mol Oncol 2015; 9(3): 555-68.
15. Holm K, Hegardt C, Staaf J, Vallon-Christersson J, Jönsson G, Olsson H, et al. Molecular subtypes of breast cancer are associated with characteristic DNA methylation patterns. Breast Cancer Res 2010; 12(3): R36.
16. Zhou W, Triche TJ Jr, Laird PW, Shen H. SeSAMe: reducing artifactual detection of DNA methylation by Infinium BeadChips in genomic deletions. Nucleic Acids Res 2018; 46(20): e123.
17. Colaprico A, Silva TC, Olsen C, Garofano L, Cava C, Garolini D, et al. TCGAbiolinks: an R/Bioconductor package for integrative analysis of TCGA data. Nucleic Acids Res 2016; 44(8): e71.

18. Ritchie ME, Phipson B, Wu D, Hu Y, Law CW, Shi W, et al. limma powers differential expression analyses for RNA-sequencing and microarray studies. Nucleic Acids Res 2015; 43(7): e47.
19. Peters TJ, Buckley MJ, Statham AL, Pidsley R, Samaras K, Lord RV, et al. De novo identification of differentially methylated regions in the human genome. Epigenetics Chromatin 2015; 8: 6.
20. Kuleshov MV, Jones MR, Rouillard AD, Fernandez NF, Duan Q, Wang Z, et al. Enrichr: a comprehensive gene set enrichment analysis web server 2016 update. Nucleic Acids Res 2016; 44(W1): W90-7.
21. Weigelt B, Reis-Filho JS. Histological and molecular types of breast cancer: is there a unifying taxonomy? Nat Rev Clin Oncol 2009; 6(12): 718-30.
22. Ciriello G, Gatza ML, Beck AH, Wilkerson MD, Rhie SK, Pastore A, et al. Comprehensive molecular portraits of invasive lobular breast cancer. Cell 2015; 163(2): 506-19.
23. Ehrlich M. DNA hypomethylation in cancer cells. Epigenomics 2009; 1(2): 239-59.
24. Bediaga NG, Acha-Sagredo A, Guerra I, Viguri A, Albaina C, Ruiz Diaz I, et al. DNA methylation epigenotypes in breast cancer molecular subtypes. Breast Cancer Res 2010; 12(5): R77.
25. Mikeska T, Craig JM. DNA methylation biomarkers: cancer and beyond. Genes 2014; 5(3): 821-64.
26. Tost J, Gut IG. DNA methylation analysis by pyrosequencing. Nat Protoc 2007; 2(9): 2265-75.
27. Asselin-Labat ML, Sutherland KD, Barker H, Thomas R, Shackleton M, Forrest NC, et al. Gata-3 is an essential regulator of mammary-gland morphogenesis and luminal-cell differentiation. Nat Cell Biol 2007; 9(2): 201-9.
28. Rønneberg JA, Fleischer T, Solvang HK, Nordhagen G, Edvardsen H, Orlova R, et al. Methylation profiling with a panel of cancer-related genes: association with estrogen receptor, TP53 mutation status and expression subtypes in sporadic breast cancer. Mol Oncol 2011; 5(1): 61-76.
29. Dimari G, Hu Y, Frenzel A, Fuchs A, Wurm AA, Fischer-Friedrich E. Mesenchymal-epithelial transition reduces proliferation but increases immune evasion in tumor spheroids. iScience 2025; 28(8): 113023.
30. Alsuliman A, Colak D, Al-Harazi O, Fitwi H, Tulbah A, Al-Tweigeri T, et al. Bidirectional crosstalk between PD-L1 expression and epithelial to mesenchymal transition: significance in claudin-low breast cancer cells. Mol Cancer 2015; 14: 149.

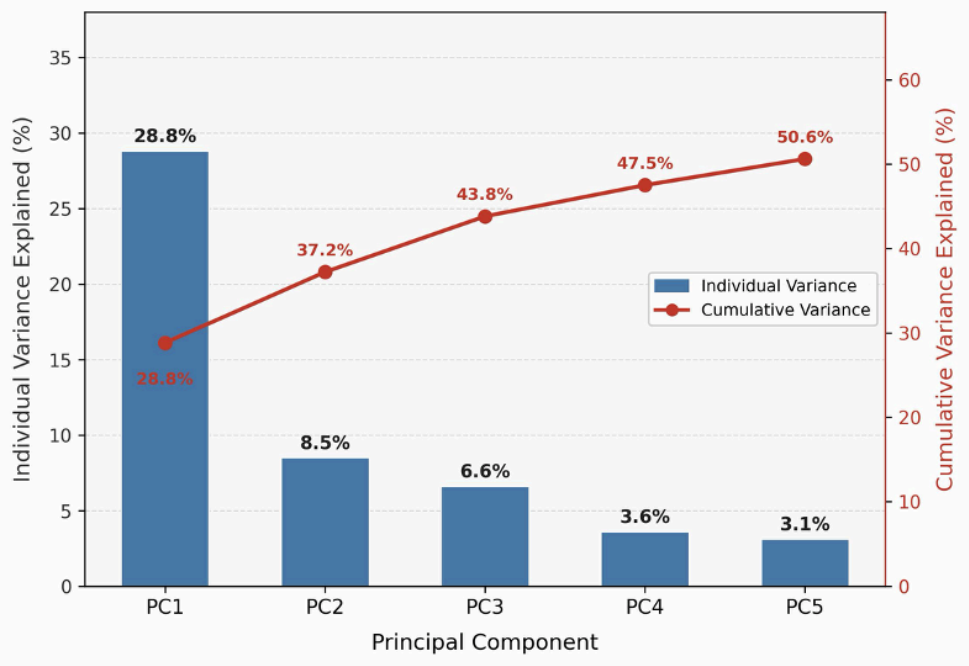
APPENDIX

SUPPLEMENTARY MATERIALS



Supplementary Figures S1.a-f. Individual pairwise volcano plots of differential DNA methylation between breast cancer histological subtypes.

Each panel displays $-\log_{10}$(FDR) versus Δβ (Delta Beta) for one pairwise comparison between histological subtypes. Significantly hypomethylated CpG positions (Δβ<-0.1, FDR<0.05) are shown in blue; significantly hypermethylated positions (Δβ>0.1, FDR<0.05) are shown in red; non-significant probes are shown in grey. The horizontal dashed line indicates the FDR significance threshold ($-\log_{10}(0.05) \approx 1.30$). Vertical dashed lines indicate the $|\Delta\beta|=0.1$ effect size threshold. DMP counts per direction are annotated in the upper corners of each panel. S1.a: IDC vs. ILC (total DMPs=227; Hypo: 23, Hyper: 204); b: IDC vs. Metaplastic (total DMPs=23,452; Hypo: 15,566, Hyper: 7,886); c: IDC vs. Medullary (total DMPs=5,733; Hypo: 2,813, Hyper: 2,920); d: ILC vs. Metaplastic (total DMPs=58,661; Hypo: 43,562, Hyper: 15,099); e: ILC vs. Medullary (total DMPs=15,434; Hypo: 8,973, Hyper: 6,461); f: Metaplastic vs. Medullary (total DMPs=132; Hypo: 43, Hyper: 89). IDC: infiltrating ductal carcinoma; ILC: infiltrating lobular carcinoma; DMP: differentially methylated position; FDR: false discovery rate.



Supplementary Figure S2. PCA variance distribution after feature extraction.

Individual variance explained (blue bars) and cumulative variance (red line) for the first five principal components computed from 88,909 ANOVA-significant CpG probes (FDR<0.05). PC1 explains 28.8% of variance, with cumulative variance reaching 50.6% across five components. This figure corresponds to the PCA results described in Section 3.4.2 of the main text. PCA: principal component analysis; ANOVA: one-way analysis of variance; FDR: false discovery rate; PC :principal component.

Supplementary Table S1. Pathway enrichment results for top 500 DMPs per endpoint using the Enrichr platform.

Endpoint	Database	n Sig	Top Enriched Term
ER Status	KEGG 2021	0	Th17 cell differentiation
ER Status	GO-BP 2023	0	Lymphocyte Migration (GO:0072676)
ER Status	GO-MF 2023	0	Transcription Coactivator Binding (GO:0001223)
ER Status	Reactome 2022	0	SUMOylation Of Intracellular Receptors R-HSA-4090294
ER Status	WikiPathway 2023	5	Th17 Cell Differentiation Pathway WP5130
ER Status	MSigDB Hallmark	0	IL-2/STAT5 Signaling
PR Status	KEGG 2021	0	Signaling pathways regulating pluripotency of stem c...
PR Status	GO-BP 2023	1	Dosage Compensation By Inactivation Of X Chromosome ...
PR Status	GO-MF 2023	1	Transcription Coregulator Binding (GO:0001221)
PR Status	Reactome 2022	0	Interleukin-12 Family Signaling R-HSA-447115
PR Status	WikiPathway 2023	0	Mesodermal Commitment Pathway WP2857
PR Status	MSigDB Hallmark	2	Estrogen Response Early
HER2 Status	KEGG 2021	0	Maturity onset diabetes of the young
HER2 Status	GO-BP 2023	4	Regulation Of Leukocyte Proliferation (GO:0070663)
HER2 Status	GO-MF 2023	4	Sequence-Specific Double-Stranded DNA Binding (GO:19...
HER2 Status	Reactome 2022	1	GRB7 Events In ERBB2 Signaling R-HSA-1306955
HER2 Status	WikiPathway 2023	1	17Q12 Copy Number Variation Syndrome WP5287
HER2 Status	MSigDB Hallmark	0	Reactive Oxygen Species Pathway
TNBC	KEGG 2021	0	Cellular senescence
TNBC	GO-BP 2023	0	Regulation Of Stem Cell Differentiation (GO:2000736)
TNBC	GO-MF 2023	1	Transcription Coactivator Binding (GO:0001223)
TNBC	Reactome 2022	0	Signaling By Receptor Tyrosine Kinases R-HSA-9006934
TNBC	WikiPathway 2023	0	Mammary Gland Development Pathway Puberty Stage 2 Of...

Supplementary Table S1 continued.

TNBC	MSigDB Hallmark	0	Estrogen Response Late
Histology (ANOVA)	KEGG 2021	0	PPAR signaling pathway
Histology (ANOVA)	GO-BP 2023	0	Regulation Of Glial Cell Proliferation (GO:0060251)
Histology (ANOVA)	GO-MF 2023	0	Mitogen-Activated Protein Kinase Binding (GO:0051019)
Histology (ANOVA)	Reactome 2022	0	Signaling By RNF43 Mutants R-HSA-5340588
Histology (ANOVA)	WikiPathway 2023	1	Vitamin D In Inflammatory Diseases WP4482
Histology (ANOVA)	MSigDB Hallmark	0	Adipogenesis
ILC Signature	KEGG 2021	0	Human T-cell leukemia virus 1 infection
ILC Signature	GO-BP 2023	0	CRD-mediated mRNA Stabilization (GO:0070934)
ILC Signature	GO-MF 2023	3	Double-Stranded DNA Binding (GO:0003690)
ILC Signature	Reactome 2022	0	Insulin-like Growth Factor-2 mRNA Binding Proteins (...
ILC Signature	WikiPathway 2023	0	Primary Focal Segmental Glomerulosclerosis FSGS WP2572
ILC Signature	MSigDB Hallmark	0	Wnt-beta Catenin Signaling
Metaplastic Signature	KEGG 2021	0	Transcriptional misregulation in cancer
Metaplastic Signature	GO-BP 2023	0	Odontogenesis (GO:0042476)
Metaplastic Signature	GO-MF 2023	6	Sequence-Specific Double-Stranded DNA Binding (GO:19...
Metaplastic Signature	Reactome 2022	0	POU5F1 (OCT4), SOX2, NANOG Repress Genes Related To ...
Metaplastic Signature	WikiPathway 2023	0	Metabolic Pathways Of Fibroblasts WP5312
Metaplastic Signature	MSigDB Hallmark	1	UV Response Dn
Medullary Signature	KEGG 2021	0	Nicotine addiction
Medullary Signature	GO-BP 2023	0	Oligodendrocyte Differentiation (GO:0048709)
Medullary Signature	GO-MF 2023	0	Amyloid-Beta Binding (GO:0001540)
Medullary Signature	Reactome 2022	0	Signaling To P38 Via RIT And RIN R-HSA-187706
Medullary Signature	WikiPathway 2023	0	Neural Crest Differentiation WP2064
Medullary Signature	MSigDB Hallmark	0	UV Response Dn
Survival	KEGG 2021	0	Synaptic vesicle cycle
Survival	GO-BP 2023	0	Modulation Of Chemical Synaptic Transmission (GO:005...
Survival	GO-MF 2023	0	3′–5′ RNA Helicase Activity (GO:0034458)
Survival	Reactome 2022	0	Transport Of Small Molecules R-HSA-382551
Survival	WikiPathway 2023	0	Type II Interferon Signaling WP619
Survival	MSigDB Hallmark	0	KRAS Signaling Up

Six databases were queried. Endpoints with 0 significant terms still list the top-ranked term by combined score. Full Enrichr output with p-values, odds ratios, and gene lists is available in the code repository. n Sig: number of significantly enriched terms (adjusted p<0.05). Top Term: the most enriched pathway or biological process.

Supplementary Table S2. Top 50 differentially methylated CpG positions across four breast cancer histological subtypes, ranked by F-statistic from one-way ANOVA.

Probe ID	Coordinate (GRCh38)	Gene	F-stat	FDR	β IDC	β ILC	β Meta	β Med	Feature
cg08734853	chr19:14,487,533	*GIPC1*	39.82	3.79e-11	0.918	0.935	0.739	0.877	Promoter
cg09246897	chr3:34,036,994	Intergenic	36.91	1.35e-10	0.838	0.889	0.638	0.589	Intergenic
cg13370010	chr13:33,169,510	*STARD13*	35.90	1.81e-10	0.920	0.935	0.707	0.927	Promoter
cg27090078	chr2:85,394,971	*CAPG*	35.33	2.01e-10	0.466	0.433	0.800	0.634	Gene body
cg02607915	chr16:75,080,416	*ZNRF1*	34.66	2.59e-10	0.919	0.929	0.735	0.872	Gene body
cg19274341	chr1:8,083,831	*RP11-431K24.1*	32.96	6.62e-10	0.711	0.742	0.290	0.693	Intergenic
cg16704530	chr6:111,568,736	*TRAF3IP2*	32.89	6.62e-10	0.837	0.844	0.707	0.826	Promoter
cg05640533	chr13:110,634,652	*NAXD*	32.56	7.37e-10	0.829	0.887	0.713	0.839	Gene body
cg18044543	chr10:89,385,038	*IFIT1B*	31.77	1.14e-9	0.866	0.899	0.673	0.771	Gene body
cg03309393	chr6:12,491,151	Intergenic	31.62	1.14e-9	0.813	0.855	0.450	0.732	Intergenic

Supplementary Table S2 continued.

cg20417351	chr17:521,118	*VPS53*	31.53	1.14e-9	0.838	0.872	0.628	0.824	Gene body
cg19317960	chr4:53,586,439	*FIP1L1*	31.40	1.16e-9	0.914	0.921	0.724	0.893	Promoter
cg17737409	chr1:230,114,263	*GALNT2*	30.32	2.41e-9	0.884	0.936	0.524	0.786	Gene body
cg02096172	chr6:6,893,930	Intergenic	30.11	2.62e-9	0.906	0.912	0.746	0.833	Intergenic
cg04831327	chr12:113,861,271	*RBM19*	29.93	2.74e-9	0.868	0.916	0.688	0.757	Gene body
cg25368667	chr1:26,349,299	*CRYBG2*	29.86	2.74e-9	0.873	0.918	0.689	0.710	Intergenic
cg09360041	chr1:94,122,349	*ABCA4*	29.75	2.74e-9	0.841	0.887	0.607	0.667	Promoter
cg03930153	chr3:177,151,108	*TBL1XR1*	29.72	2.74e-9	0.431	0.675	0.200	0.165	Promoter
cg01935400	chr17:82,435,248	*HEXDC*	29.40	3.28e-9	0.930	0.976	0.792	0.787	Gene body
cg07572927	chr14:20,687,520	*ANG*	29.31	3.28e-9	0.532	0.445	0.833	0.849	Promoter
cg26853371	chr4:1,789,840	Intergenic	29.29	3.28e-9	0.856	0.889	0.690	0.747	Intergenic
cg02464551	chr2:231,617,860	Intergenic	28.66	5.07e-9	0.616	0.724	0.366	0.439	Intergenic
cg02349866	chr15:89,848,645	*AP3S2*	28.57	5.23e-9	0.704	0.768	0.433	0.568	Gene body
cg25769469	chr5:72,348,014	*PTCD2*	28.40	5.69e-9	0.834	0.886	0.579	0.643	Gene body
cg00059459	chr1:8,283,515	Intergenic	28.30	5.94e-9	0.832	0.861	0.676	0.554	Intergenic
cg13602461	chr8:54,153,757	*RNU6ATAC32P*	28.13	6.53e-9	0.644	0.732	0.289	0.567	Intergenic
cg22422251	chr5:113,034,494	*MCC*	27.94	7.29e-9	0.895	0.914	0.673	0.886	Gene body
cg05982389	chr3:106,120,375	Intergenic	27.76	7.99e-9	0.924	0.934	0.755	0.895	Intergenic
cg10991454	chr2:30,611,808	*LCLAT1*	27.73	7.99e-9	0.874	0.891	0.651	0.783	Gene body
cg01310482	chr7:101,952,860	*CUX1*	27.64	8.16e-9	0.876	0.898	0.704	0.871	Gene body
cg05429448	chr3:101,940,786	*RP11-221J22.1*	27.62	8.16e-9	0.682	0.726	0.319	0.610	Promoter
cg26780125	chr8:124,376,565	Intergenic	27.48	8.84e-9	0.615	0.684	0.287	0.533	Intergenic
cg07285237	chr6:139,126,532	Intergenic	27.36	9.18e-9	0.590	0.699	0.243	0.483	Intergenic
cg26112871	chr5:171,893,716	*FBXW11*	27.35	9.18e-9	0.785	0.855	0.453	0.618	Gene body
cg23280294	chr1:8,662,405	*RERE*	27.21	9.52e-9	0.871	0.890	0.675	0.888	Promoter
cg01527307	chr6:14,500,210	Intergenic	27.20	9.52e-9	0.905	0.903	0.722	0.850	Intergenic
cg19654142	chr4:3,476,337	*DOK7*	27.20	9.52e-9	0.816	0.854	0.653	0.639	Gene body
cg27056501	chr1:180,151,565	Intergenic	27.09	1.02e-8	0.901	0.923	0.733	0.861	Intergenic
cg07438246	chr3:14,405,137	*SLC6A6*	27.05	1.02e-8	0.868	0.907	0.719	0.844	Promoter
cg23146741	chr8:42,857,169	*RNF170*	26.92	1.05e-8	0.836	0.855	0.567	0.808	Gene body
cg12542656	chr2:43,042,330	*AC016735.3*	26.91	1.05e-8	0.691	0.731	0.369	0.553	Intergenic
cg03376089	chr17:17,936,095	*TOM1L2*	26.89	1.05e-8	0.798	0.855	0.631	0.732	Gene body
cg02502233	chr6:85,669,885	*SNHG5*	26.89	1.05e-8	0.462	0.628	0.108	0.108	Intergenic
cg11742688	chr1:229,538,494	*ABCB10*	26.76	1.05e-8	0.953	0.960	0.914	0.897	Gene body
cg21585138	chr3:50,607,675	*CISH*	26.76	1.05e-8	0.409	0.423	0.753	0.520	Gene body
cg18885540	chr14:63,856,050	*SYNE2*	26.76	1.05e-8	0.551	0.508	0.825	0.681	Promoter
cg07711192	chr12:14,274,060	Intergenic	26.76	1.05e-8	0.822	0.879	0.559	0.741	Intergenic
cg04499514	chr12:8,066,424	*C3AR1*	26.76	1.05e-8	0.656	0.712	0.294	0.474	Promoter
cg26938676	chr14:72,737,418	*DPF3*	26.62	1.13e-8	0.423	0.353	0.753	0.766	Gene body
cg27181148	chr12:45,425,524	*ANO6*	26.62	1.13e-8	0.899	0.916	0.673	0.896	Gene body

β values are subtype means. The complete list of 1,000 DMPs is available in the data repository. Coordinate (GRCh38): genomic position of each probe in the GRCh38 reference build; Feature: regulatory context of the probe relative to the nearest gene (promoter, gene body, or intergenic). Coordinate and Feature values can be populated in bulk from the annotated probe table exported by the analysis pipeline.

Supplementary Table S3. Principal component coordinates for all 99 samples in the histological subtype cohort, computed from 404,059 quality-filtered CpG probes.

Subtype	PC1	PC2	PC3
IDC	12.581	6.030	2.140
IDC	−16.533	2.139	4.152
IDC	−5.153	3.006	−7.543
IDC	13.768	−3.278	6.606
IDC	3.641	0.600	−3.362
IDC	17.818	−5.928	2.710
IDC	−13.340	0.813	3.038
IDC	−9.370	0.367	7.792
IDC	−6.953	−1.100	−4.832
IDC	−12.147	0.618	1.241
IDC	−13.956	−1.382	2.640
IDC	−9.296	−4.567	−3.275
IDC	9.545	6.031	−0.286
IDC	3.385	1.307	−6.370
IDC	−16.826	1.949	−0.799
IDC	−4.542	−0.789	−4.351
IDC	3.700	6.543	6.848
IDC	0.604	−2.239	1.468
IDC	4.499	1.728	−6.319
IDC	5.882	−2.028	−0.315
IDC	3.716	6.139	4.608
IDC	15.151	3.311	3.204
IDC	−13.753	1.327	−0.213
IDC	−8.758	−2.477	−6.091
IDC	−15.495	1.732	1.893
IDC	11.787	−2.488	−6.864
IDC	−1.754	8.798	−2.323
IDC	7.445	−4.832	−4.106
IDC	3.543	8.794	−0.633
IDC	10.758	−2.810	−2.079
IDC	0.769	−1.561	−6.385
IDC	−4.622	1.114	−8.199
IDC	7.099	1.643	1.276
IDC	−7.148	1.198	12.213
IDC	−14.851	−0.118	3.675
IDC	−14.930	−3.598	−3.432
IDC	11.378	9.122	4.752
IDC	4.853	15.422	−0.830
IDC	18.800	3.419	4.588
IDC	−12.046	−3.466	−3.739
ILC	14.545	−0.412	−2.781
ILC	0.195	13.351	−1.077
ILC	−7.015	−5.269	8.835
ILC	10.499	−2.218	3.294

Supplementary Table S3 continued.

ILC	−5.779	−2.723	−4.418
ILC	10.593	−2.067	−1.118
ILC	0.571	9.815	−4.143
ILC	15.614	−3.516	1.632
ILC	1.457	−6.386	4.540
ILC	5.958	−6.986	−2.122
ILC	14.588	−9.122	4.269
ILC	−0.768	3.542	−5.317
ILC	17.831	−3.579	4.350
ILC	−4.686	−3.815	−4.177
ILC	6.067	−0.226	−4.377
ILC	1.742	11.288	−3.068
ILC	3.923	0.933	−0.634
ILC	18.751	−7.820	3.567
ILC	9.694	−7.979	0.281
ILC	5.620	10.638	−1.841
ILC	−5.592	1.653	−4.910
ILC	15.591	17.702	4.173
ILC	6.768	−5.045	−2.299
ILC	7.767	−3.056	2.042
ILC	2.300	1.740	−4.918
ILC	2.704	12.620	−0.704
ILC	−3.131	2.247	−5.810
ILC	16.711	4.658	−1.208
ILC	4.200	−6.906	−3.022
ILC	6.716	−7.289	−2.556
ILC	10.529	−4.245	−0.806
ILC	8.103	−5.132	−2.158
ILC	0.547	−1.198	−3.955
ILC	10.587	−8.625	−0.577
ILC	0.309	4.193	−2.967
ILC	5.185	−5.439	−1.149
ILC	−2.749	0.630	−6.518
ILC	−2.655	−1.851	−4.592
ILC	12.554	−4.965	1.855
ILC	0.076	1.251	−4.517
Medullary	−15.500	−2.326	−3.176
Medullary	−14.123	−2.860	1.392
Medullary	−12.026	−1.982	1.035
Medullary	−5.481	−9.602	3.598
Medullary	−6.857	−1.812	−5.785
Metaplastic	−0.405	−7.965	7.916
Metaplastic	−7.560	−3.921	−0.072
Metaplastic	−7.053	1.366	14.715
Metaplastic	−8.853	−4.084	−1.502

Supplementary Table S3 continued.

Metaplastic	−13.831	0.935	3.880
Metaplastic	−9.116	2.084	5.833
Metaplastic	−13.041	−3.155	−1.236
Metaplastic	−14.550	3.064	1.627
Metaplastic	−5.947	3.156	17.216
Metaplastic	−9.677	−0.779	−2.081
Metaplastic	−12.834	−0.986	0.595
Metaplastic	−14.022	−0.281	−1.864
Metaplastic	−1.860	−5.108	7.610
Metaplastic	−12.434	3.379	6.703

PC1–PC3 values represent each sample's position in the reduced-dimensionality methylation space.

Supplementary Table S4. Methylation signature summary for all 14 classifiers.

Signature	Type	DMPs	Genes	Hyper	Hypo	Panel	AUC	Tier
ER Status	Hormone Receptor	36953	414	297	203	10	0.9347	T1: High-performance
PR Status	Hormone Receptor	18580	417	276	224	15	0.8657	T1: High-performance
HER2 Status	Hormone Receptor	1035	362	37	463	30	0.8519	T2: Research-validated
TNBC	Hormone Receptor	41397	398	282	218	8	0.9398	T1: High-performance
Vital Status	Prognosis	76	69	15	61	10	0.7141	T3: Exploratory
Survival-Associated (Kaplan-Meier)	Prognosis	500	454	0	0	0	N/A	T4: Preliminary
Age-Associated	Prognosis	1998	386	469	31	30	N/A	T2: Research-validated
Radiation Therapy	Treatment	5955	407	387	113	30	N/A	T3: Exploratory
Chemotherapy	Treatment	0	0	0	0	0	N/A	Not applicable
Race-Associated	Demographic	1532	397	289	211	30	N/A	T2: Research-validated
ILC Subtype	Histology	5869	441	445	55	30	N/A	T2: Research-validated
IDC Subtype	Histology	0	0	0	0	0	N/A	Not applicable
Metaplastic Subtype	Histology	22888	403	208	292	30	N/A	T2: Research-validated
Medullary Subtype	Histology	4150	391	217	283	30	N/A	T2: Research-validated

Tier definitions: Tier 1 (high-performance, AUC≥0.85), Tier 2 (research-validated, 0.70≤AUC<0.85), Tier 3 (exploratory, AUC<0.70), Tier 4 (preliminary, insufficient data). DMPs: total differentially methylated positions; Genes: number of mapped genes; Hyper/Hypo: count of hyper- and hypomethylated probes in the top 500; Panel: number of CpG probes in the minimal diagnostic panel; AUC: area under the ROC curve (10-fold cross-validation); Tier: evidence classification.